Jun 5th, 12:00 AM - Jun 8th, 12:00 AM

Proceedings of the 8th International Junior Researcher and Engineer Workshop on Hydraulic Structures

International Association for Hydro-Environmental Engineering and Research

Proceedings of the 8th International Junior Researcher and Engineer Workshop on Hydraulic Structures

Table of Contents

Foreword to Proceedings of the 8th International Junior Researcher and Engineer Workshop on Hydraulic Structures

S. Erpicum[1], S. Mulligan[2], and B. M. Crookston[3]
[1] Urban and Environmental Engineering Research Unit - HECE Research Group,
Liege University
BELGIUM
[2] VorTech Water Solutions Ltd and the National University of Ireland Galway
IRELAND
[3] Civil & Environmental Engineering Dept., Utah Water Research Laboratory
Utah State University
Logan UT 84321
UNITED STATES
E-mail: S.Erpicum@uliege.be

Abstract: *The Proceedings of the 8th International Junior Researcher and Engineer Workshop on Hydraulic Structures (8th IJREWHS) of the International Association of Hydro-environmental Engineering and Research (IAHR) cover many aspects of hydraulic structures engineering, ranging from weirs and spillways to scour and sediment transport as well as hydropower and flood and drought management. The event organisation motivated the sharing of information and experience between junior and senior hydraulic structures researchers and engineers with different origins and backgrounds. This event also has a strong mentorship component as participants represent the next generation of engineers and scientists. This paper presents the proceedings peer-review process, the proceedings content as well as the event organisation. The reviewers are also acknowledged.*

Keywords: *Hydraulic structures; Experience mixing; Peer-review process; Proceedings.*

1. INTRODUCTION

Hydraulic structures engineering is one of the most important fields of civil and environmental engineering with challenges arising from new and complex issues for upgrades or replacement of aging infrastructure or innovative designs for new builds (Felder et al., 2021). It is also an evolving science in an ever-changing environment with increasing water disasters and rising demands due to population growth (Erpicum et al., 2021). Such challenges and context require the combined efforts of both researchers and practitioners in future years. In this respect, the IAHR International Junior Researcher and Engineer Workshop on Hydraulic Structures (IJREWHS) series aims to bring together young scientists and engineers to discuss hydraulic structure designs, new research and practical solutions.

The objective of IJREWHS is to provide an opportunity for young researchers and engineers to gain international exposure by presenting and discussing their research to current and future international research leaders and experts in the field of hydraulic structures. In a friendly mentoring environment, authors and presenters receive constructive feedback from their peers and a committee of senior researchers on their paper and presentation. Based on that feedback, authors submit a manuscript, which then undergoes a review by peers (both junior workshop participants and senior researchers). Once revised and accepted, the paper is published, ensuring large exposure to the international community.

The 8th IJREWHS was the latest event to date of a successful series organized by the IAHR Hydraulic Structures Committee. The 2021 workshop was hosted online as a virtual event by the National University of Ireland, Galway and attracted 36 junior and senior participants. Previous workshops were held in Montemor-o-Novo, Portugal (2006), Pisa, Italy (2008), Edinburgh, Scotland (2010), Logan, Utah USA (2012), Spa, Belgium (2014), Lübeck, Germany (2016) and Denver, Colorado USA (2019).

This short paper explains the review process of the 8th IJREWHS Proceedings, which have been published open access with a Digital Object Identifier by Digital Commons Utah State University. It also lists the proceedings content and workshop organisation and acknowledges the reviewers.

2. 8TH IJREWHS PROCEEDINGS

2.1. Peer review process and topics

Papers published in the Proceedings of the 8th IAHR International Junior Researcher and Engineer Workshop on Hydraulic Structures have been peer-reviewed for technical content through a formal and rigorous process, as detailed below. The proceedings are hosted by the University Library at Utah State University publication. Each paper was allocated a direct object identifier (DOI) and is accessible open access at the Utah State University Institutional Repository DigitalCommons@USU {https://digitalcommons.usu.edu/}. Each work is available to users through DigitalCommons@USU pursuant to a Creative Commons Attribution-NonCommercial CC BY 4.0 License.

Following the workshop (held online due to the Covid-19 virus pandemic) in July 2021, the Scientific Committee received 23 full papers out of the 26 junior participants presentations. The Panel of Reviewers was drawn from the IAHR Hydraulic Structures Committee community and other international experts in the field, and it also included all the junior researchers and engineers who submitted a full paper. The submitted papers have been peer-reviewed by two independent senior reviewers and two junior reviewers, according to an evaluation sheet whose criteria were established by the Scientific Committee. Authors were then requested to revise their manuscript in accordance with the reviewers' comments and editorial recommendations, and to submit a revised version with a rebuttal letter responding point by point to all reviewers' comments for final review before inclusion in the proceedings. The final number of papers accepted for publication was 20. The symposium proceedings were edited by the Chair of the Scientific Committee, Sebastien Erpicum, the Chair of the Organizing Committee, Sean Mulligan, and the Chair of IAHR Hydraulic Structures Technical Committee, Brian Crookston.

The Authors of the papers published in the proceedings come from 20 different countries on the 6 inhabited continents. The scope of the 8th IJREWHS proceedings is broad, with three papers on weirs, six studies focusing on flow past varied types of hydraulic structures, three papers on sediment transport and four papers on scour processes, but also two papers on hydropower and pumps and two papers on floods and droughts. The topics encompass advanced multidisciplinary subjects such as air-water flows, flow-vegetation interactions, sediment processes and fish passages. The papers are based on field, numerical modelling, or experimental investigations. For sure, these proceedings showcase the wide and growing scope of hydraulics structures engineering challenges, methodologies and solutions.

2.2. Referencing

The papers published in the proceedings are available open access at DigitalCommons@USU {https://digitalcommons.usu.edu/}. DigitalCommons@USU is the institutional repository of the Utah State University.

The full bibliographic reference of the 8th IJREWHS proceedings is:

Erpicum S., Mulligan S., and Crookston B. (2022). "8th IAHR International Junior Researcher and Engineer Workshop on Hydraulic Structures (8th IJREWHS)". *Proceedings of the 8th IAHR International Junior Researcher and Engineer Workshop on Hydraulic Structures – 8th IJREWHS*, 5-8 July 2021, Galway, Ireland. Utah State University, Logan, Utah, USA (ISBN 978-0-578-37416-1).

Each paper of the proceedings must be referenced as, for example:

Paulo F. A., and Teixeira E. D. (2022). "Flow Distribution in Slotted Pipe Bottom Outlets" in "8th IAHR International Junior Researcher and Engineer Workshop on Hydraulic Structures (8th IJREWHS)".

Proceedings of the 8th IAHR International Junior Researcher and Engineer Workshop on Hydraulic Structures – 8th IJREWHS, 5-8 July 2021, Galway, Ireland. Erpicum S., Mulligan S., and Crookston B., Editors. Utah State University, Logan, Utah, USA, 8 pages (DOI: 10.26077/ed65-7234) (ISBN 978-0-578-37416-1).

2.3. Statistical summary

20 peer-reviewed papers written by 56 authors from 20 countries and 6 continents. 5 keynote lectures published as video files.

3. WORKSHOP ORGANISATION AND REVIEWERS

The 8th IAHR International Junior Researcher and Engineer Workshop on Hydraulic Structures was scheduled to take place on 5-8 July 2021 at the National University of Ireland, Galway, Ireland. Because of the exceptional circumstances worldwide induced by the Covid-19 virus pandemic, it was not possible to hold the workshop physically and it was therefore held fully online using a virtual workshop platform. The workshop was held on the same dates but with an adapted schedule to accommodate, as much as possible, the time differences between the various locations of the authors.

3.1. Workshop organizing committee

- Sean Mulligan (Chair), National University of Ireland, Galway, Ireland
- Daniel B. Bung (Vice-Chair), Aachen University of Applied Sciences, Germany
- Stephen Nash, National University of Ireland, Galway, Ireland
- Eoghan Clifford, National University of Ireland, Galway, Ireland
- Michael Hartnett, National University of Ireland, Galway, Ireland
- Daniel Valero, IHE Delft Institute for Water Education, Delft, Netherlands
- Peter Leonard (administrator), National University of Ireland, Galway, Ireland
- Ronan Cooney (administrator), National University of Ireland, Galway, Ireland
- Alan Carty (administrator), VorTech Water Solutions, Galway, Ireland

3.2. Senior Experts-Reviewers

- Jose Adriasola, Chili
- Zulfequar Ahmad, India
- Ismail Albayrak, Switzerland
- Robert Boes, Switzerland
- Fabian Bombardelli, USA
- Daniel Bung, Germany
- Rita Carvalho, Portugal
- Hubert Chanson, Australia
- Eoghan Clifford, Ireland
- Brian Crookston (Editor), USA
- Giovanni De Cesare, Switzerland
- Sebastien Erpicum (Chair - Editor), Belgium
- Roger Falconer, United Kingdom
- Stefan Felder, Australia
- Michael Hartnett, Ireland
- Valentin Heller, United Kingdom
- Robert Janssen, Australia
- Rebekka Kopmann, Germany
- Jorge Matos, Portugal

- Sean Mulligan (Editor), Ireland
- Stephen Nash, Ireland
- Mario Oertel, Germany
- Michele Palermo, Italy
- Blake Tullis, USA
- Daniel Valero, The Netherlands
- David Zhu, Canada

4. ACKNOWLEDGEMENTS

The organization of the workshop would not have been possible without the active involvement of all the members of the organizing committee. We would also like to thank all the reviewers for their valuable support in reviewing the manuscripts and all the Authors for their contributions. We also acknowledge the support of the University Library of Utah State University for the production and publication of the proceedings.

Such very specialized event, involving a small number of participants, is only financially possible with some level of support from various institutions. We would like to acknowledge the support of our sponsors, Energy Systems Integration Partnership Programme (ESIPP), Ward and Burke Construction Ltd and VorTech Water Solutions Ltd.

5. REFERENCES

Erpicum, S., Crookston, B., Bombardelli, F., Bung, D.B., Felder, S., Mulligan, S., Oertel, M. and Palermo, M. (2021). Hydraulic structures engineering: An evolving science in a changing world. WIREs Water. 8(2), e1505.

Felder, S., Erpicum, S., Mulligan, S., Valero, D., Zhu, D. and Crookston, B. (2021). Hydraulic structures at a crossroads towards the Sustainable Development Goals. IAHR White Paper Series, 2021, 2, Madrid, Spain and Beijing, China.

8th International Junior Researcher and Engineer Workshop on Hydraulic Structures
ISBN: 978-0-578-37416-1
https://doi.org/10.26077/ed65-7234

Flow Distribution in Slotted Pipe Bottom Outlets

Felipe Azevedo Paulo[1], Eder Daniel Teixeira[1]
[1]Instituto de Pesquisas Hidráulicas
Universidade Federal do Rio Grande do Sul
Porto Alegre, Rio Grande do Sul
BRAZIL
E-mail: felipe.azevedo.paulo@gmail.com

Abstract: *Reservoir sedimentation is a major threat to dam operation. It can reduce water storage capacity, clog water intakes, and damage turbine components. Flushing operations by bottom outlets are a mitigation measure that allows removing sediment deposited near the dam. Unfortunately, the effect of such structures is localized if no water level draw down takes place; therefore, investigations of new designs that improve sediment removal have emerged recently. In this work, we present our current results on the investigation of the slotted pipe bottom outlet obtained through numerical modeling. The flow patterns were characterized for different water levels, showing that discharges and mean velocities at the slots grow in the downstream direction. In addition, analyzing the effect of geometric elements of the structure showed that wider slots can convey greater discharges with smaller velocities except if they are close to the pipe entrance. Finally, based on the results obtained, a first step is taken into the optimization of this structure, where the discharges in all openings of the slotted pipe could be enhanced by removing the slot closer to the pipe entrance and widening the remaining slots.*

Keywords: *Reservoir sedimentation, bottom outlet, FLOW-3D, pressure flushing.*

1. INTRODUCTION

Reservoirs protect against floods and droughts besides benefits related to navigation, hydroelectricity, and recreation. However, their ability to deliver these services tends to diminish over time due to deposition of sediments transported by the rivers that form the reservoir. Sedimentation causes average values of 1% of annual loss of water storage capacity worldwide (George *et* al., 2017). Therefore, sedimentation is a major threat to dam operation and one of the limiters of its life expectancy (Schleiss *et* al., 2016). Despite their negative impacts (such as degradation of the riverbed downstream of the reservoir, reduction of flood peaks that may be important for fish breeding, interruption of the transport of nutrients related to sediments, among others), reservoirs possess undeniable socioeconomic relevance that makes the sedimentation problem arise as a global concern (Kondolf *et* al., 2014), particularly if we consider demographic growth and increasing energy demand. Therefore, the use of reservoirs is inevitable and its life expectancy should be maximized. This is crucial since the construction of new reservoirs face obstacles such as being bound to extensive processes of environmental licensing and depend on the existence of suitable places that are increasingly scarce (Shen, 1999). Mitigation and prevention of sedimentation is essential to achieve this objective.

Bottom outlets are a means of removing sediment deposited close to the dams, if flushing operations are carried out in the reservoir. The literature regarding sediment removal by bottom outlets shows theoretically, experimentally, and by field observations that its effect is limited to a region close to the bottom outlet intake if they are activated without water level draw down (White & Bettess, 1984; Emamgholizadeh *et* al., 2006; Sawadogo *et* al., 2019). This fact forces water intakes to be placed near bottom outlets if desilting is necessary. Several studies have been conducted regarding traditional bottom outlets (orifices placed in the upstream face of the dam). However, recent research has been oriented to the development of new structures that provide greater efficiency and sediment removal (Madadi *et* al., 2016, 2017; Haghjouei *et* al., 2021). In this fashion, Paulo *et* al. (2021) proposed a new structure called a slotted pipe bottom outlet that allows sediment removal in the direction parallel to the dam axis, providing more freedom in the placement of water intakes (Figure 1). These authors conducted a physical model study of the slotted pipe bottom outlet to verify its ability to scour deposited non-cohesive sediments, showing that this structure can be used for desilting water intakes.

In addition, they proposed a dimensionless equation for the prediction of the scour extent caused by the slots. However, no information exists yet regarding design criteria or if the sediment removal capacity of the slotted pipe could be enhanced with variations in its geometry. In this paper, we present our current advances in the investigation of the geometry that maximizes the discharge provided by the structure. We employed the recognized computational fluid dynamics (CFD) package FLOW-3D to characterize the flow pattern throughout the slotted pipe bottom outlet and investigated the influence of its geometry (slot width and placing) to obtain insights that may lead to an optimized configuration.

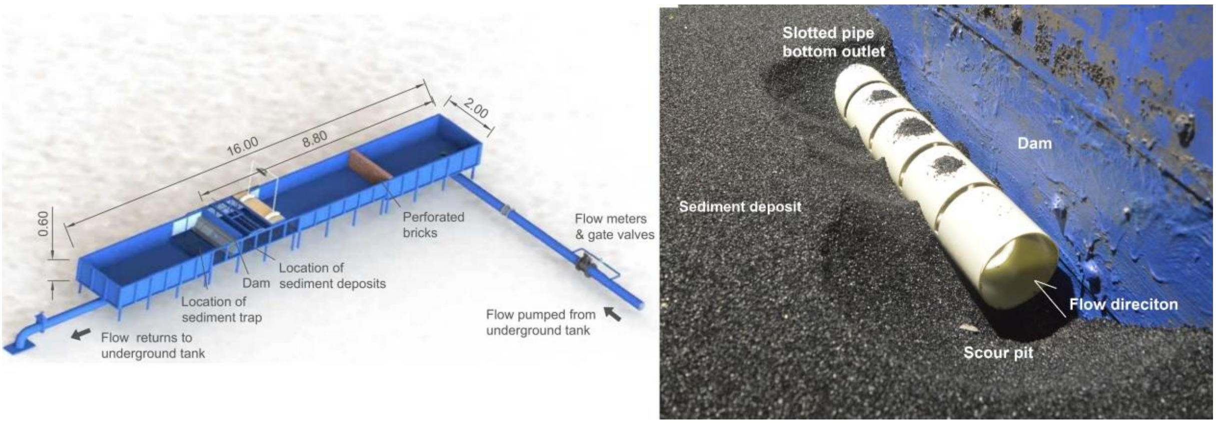

Figure 1 – Physical model of the slotted pipe bottom outlet (Pa*ulo et* al., 2021).

2. METHODS

2.1. Numerical Model

FLOW-3D is a commercial CFD software capable of solving the RANS equations by the finite volume method (FVM) to model multi-scale, multi-physics flows and to obtain transient, three-dimensional solutions. The computational domain is discretized in a 3D structured, staggered mesh of cubic cells. Most of the terms in the equations are solved explicitly, although several implicit methods may be used. However, pressures and velocities are coupled implicitly. The model uses the Volume of Fluid (VOF) method to track the free surface and the proprietary FAVOR (fractional area/volume) method for incorporating geometry effects into the equations (Flow Science, 2018). The main models used in this work were: default VOF, a second-order monotonicity preserving numerical scheme for the advection of momentum, GMRES method for pressure-velocity coupling, and the k-w turbulence model. The fluid considered was the default water at 20°C (density of 998.2 kg/m^3 and dynamic viscosity of 0.001 kg/m/s).

2.2. Set of Simulations

Two series of simulations were conducted. Series A consisted of four simulations to characterize the flow pattern across the bottom outlet for increasing upstream water level. Series B consisted of four simulations to understand the influence of the slots in the discharge and head loss and one simulation of an optimized geometry based on the results of the previous four simulations. Here, the head loss is considered as the energy losses due to friction of the flow with the walls of the pipe and due to local energy losses at the openings of the slotted pipe. No head loss was calculated in this work, however, considering Bernoulli's equation and the same boundary conditions, the alternative that conducts the greater discharge has the lower total head loss.

The dimensions of the slotted pipe simulated were chosen to represent full-scale dimensions of the physical model employed by Pa*ulo et* al. (2021). In their research, the physical model did not represent any specific prototype in reduced scale, being an experimental physical model rather than a reduced scale physical model. Despite simulating the structure proposed by Pa*ulo et* al. (2021), no calibration based on their physical model results was carried out. Due to the preliminary nature of the numerical simulations performed for this work, no sediment deposits were considered. The main objective was to characterize the flow patterns along with the structure and not to evaluate its sediment removal capacity, although the former influences the latter.

Series A

In Series A, only the original geometry proposed by Pa*ulo et* al. (2021) was simulated. This configuration is defined in terms of the hydraulic radius (R_h) of the conduit cross-section: the slots are separated by a distance of $4R_h$ and their width is $0.4R_h$ (Figure 2-a). Only half the pipe was considered in the first three simulations (SA-1, SA-2, and SA-3) of this series to reduce computational cost following the assumption of axisymmetric flow along the longitudinal axis of the structure (Figure 2-c). A fourth simulation (SA-4) took place considering the entire structure to verify the assumption of axisymmetric flow. In this case, the domain shown in Figure 2-c was mirrored. The cell size varied along with the domain (finer cells around the structure and progressively bigger cells in the upstream direction, see Table 1) as shown in Figure 2-b.

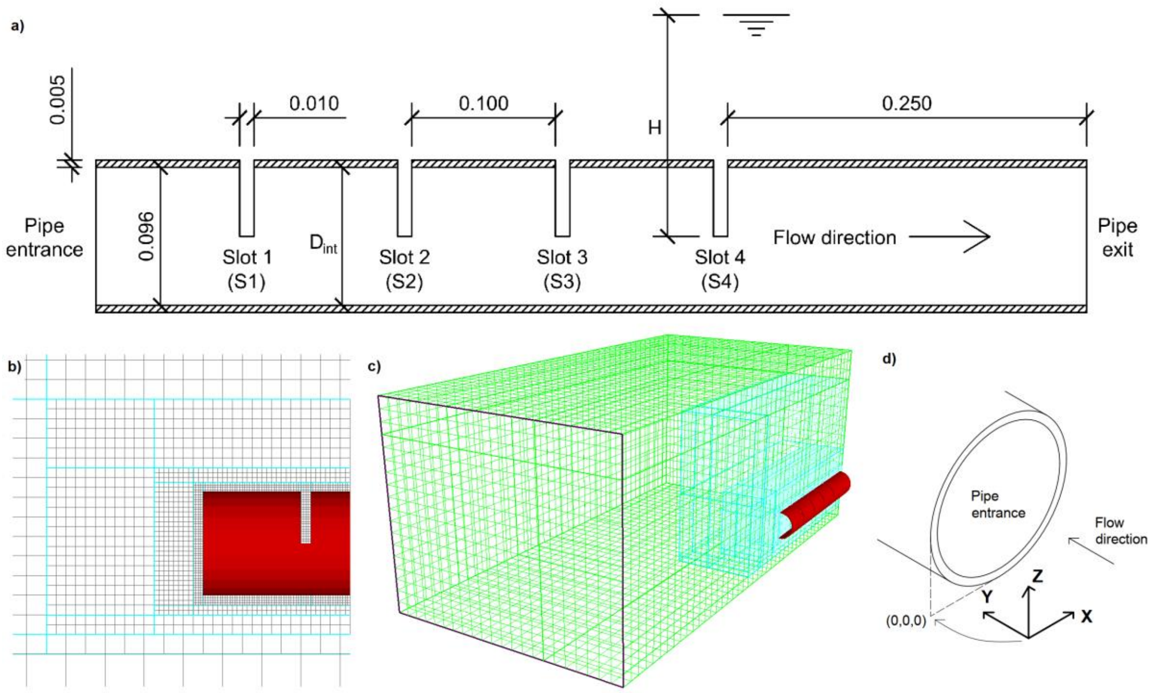

Figure 2 – Original geometry of the slotted pipe bottom outlet (a), mesh cell sizes (b), computational domain (c), and coordinate system (d). All dimensions are in meters.

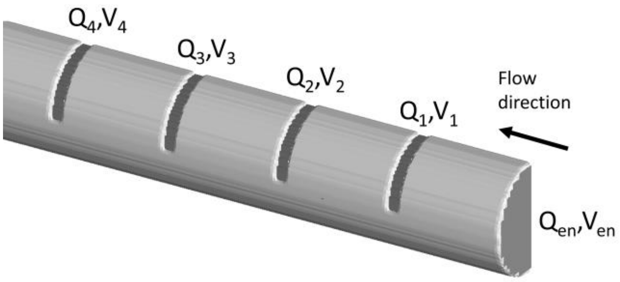

Figure 3 – Flux surfaces (dark grey) where discharges and velocities were measured at the slotted pipe (light grey).

The boundary conditions were defined in the bigger mesh block that represents the reservoir and in a mesh block downstream of the pipe exit. Upstream conditions were defined as stagnation pressure (water level) and the downstream boundary conditions were defined as outflow, to represent a free discharge. Initial conditions considered fluid occupying the entire domain in the reservoir at the same level as the boundary conditions. Figure 3 shows the flux surfaces set to measure discharge and mean velocity at each opening of the slotted pipe. The mean velocity at the pipe exit was measured at that section with a flux surface similar to the one placed at the pipe entrance. The discharge at the pipe exit (total discharge, Q_{ex}) was calculated as the sum of Q_{en}, Q_1, Q_2, Q_3, and Q_4. The values measured were employed for characterizing the flow patterns. Three water levels were simulated comprising the range of the ratio between the water column above the bottom outlet axis (H) and internal diameter (D_{int}) tested by Paulo *et* al. (2021), who tested values of H/D_{int} ranging from 3.12 to 13.79. The water levels simulated correspond to these limits and an intermediate value of 8.45.

Series B

In this series, the computational domain was the same as in Series A, but the geometry varied for each simulation to evaluate the effect of the slots. The water level was kept constant for all simulations (H = 0.347 m). This value was chosen because it is one of the possible values in the range of H/D_{int} tested by Paulo *et* al. (2021), considering the diameter of the slotted pipe simulated (Figure 2-a). A first simulation (SB-original) was executed with the same setup of Series A's simulations to have the comparison basis for the following simulations (SB-1 to SB-4). All the geometries, their changes concerning the original geometry, and their purpose can be seen in Figure 4.

- Original geometry
- Objective: basis of comparison for other simulations

- S2 merged with S3
- Objective: evaluate effect of slot widening away from pipe entrance

- S4 halved and S1's width increased 1.5 times
- Objective: evaluate slot widening near the pipe entrance and the effect of slot shortening

- S4 halved and S2's width increased 1.5 times
- Objective: evaluate slot interference with the pipe entrance (by comparing with the results of SB-1 and SB-2)

- S1 removed and S2's and S3's width increased 1.5 times
- Objective: enhance discharges based on the previous results

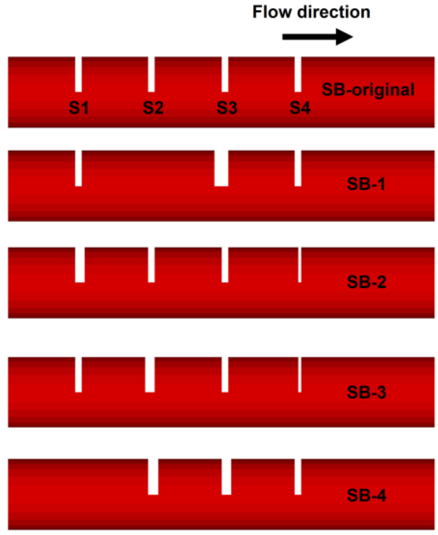

Figure 4 – Geometries considered in Series B simulations.

Table 1 – Simulations parameters.

<table>
<tr><th colspan="4">Mesh</th><th colspan="2" rowspan="2">Bottom outlet</th></tr>
<tr><th>Series</th><th>SA-1 to 3</th><th>SA-4</th><th>SB</th></tr>
<tr><td>Type</td><td colspan="3">Structured</td><td>Z coordinate of pipe centerline</td><td>0.05 m</td></tr>
<tr><td>Cell shape</td><td colspan="3">Cubic</td><td>X coordinate of pipe centerline</td><td>0.055 m</td></tr>
<tr><td>Cell size</td><td colspan="3">0.25 cm to 4.00 cm</td><td>Y coordinate of pipe centerline</td><td>Parallel to Y-axis</td></tr>
<tr><td>Cell count</td><td>565,868</td><td>1,384,670</td><td>544,110</td><td>Wall thickness</td><td>5 mm</td></tr>
<tr><td>Limits in X direction</td><td>-0.825 m to 0.055 m</td><td>-0.625 m to 0.735 m</td><td>-0.825 m to 0.055 m</td><td>Absolute roughness</td><td>1.5×10^{-3} mm (PVC)</td></tr>
<tr><td>Limits in Y direction</td><td colspan="3">-0.91 m to 0.81 m</td><td colspan="2" rowspan="2">–</td></tr>
<tr><td>Limits in Z direction</td><td>-0.1 m to 1.42 m</td><td colspan="2">-0.1 m to 0.5 m</td></tr>
<tr><th colspan="6">Boundary conditions</th></tr>
<tr><td>Simulation</td><td>SA-1</td><td>SA-2</td><td>SA-3</td><td>SA-4</td><td>SB</td></tr>
<tr><td>H (upstream)</td><td>0.300 m</td><td>0.515 m</td><td>1.300 m</td><td>0.402 m</td><td>0.347 m</td></tr>
</table>

To ensure a fair comparison between the original geometry and its variations, the pipe entrance area and the total area of the slots remained constant in all cases. The setup for each simulation is summarized in Table 1. We verified, in a previous simulation, that the flow reaches a steady-state (mean discharges and velocities do not vary with time) at approximately 1 s of simulation. All following simulations were run for 5 s and all presented results are averaged values obtained from 1.5 s to 5.0 s.

3. RESULTS AND DISCUSSIONS

3.1. Series A

Results show that the mean flow velocity in the slots increases in the downstream direction and that recirculation zones form downstream of slots at the conduit's upper inner elevation (Figure 5 and Table 2). More than one-third of the total discharge comes from the pipe entrance and both mean velocity and discharge in a slot are, on average, 1.31 times superior to the same values of a slot immediately upstream. The mean velocity at the pipe entrance is lower than the slot velocities; however, its discharge is superior due to its greater area. These patterns repeat in all three simulations and confirm the assumption of Pa*ulo et* al. (2021) that the discharge in the pipe entrance is superior to the discharge of one slot and the group of slots. This is valid at least for the cases where the total slot area is inferior to the pipe entrance area (in all simulations the latter is 4.8 times greater than the former). Nonetheless, these results indicate that the assumption by the same authors that discharge and velocities are approximately constant for all slots was wrong. The greatest pressure drop occurs in S4 and coincides with the velocity increment in this region. The minimum pressure values were observed downstream of S4 at the conduit's upper inner elevation in a distance up to approximately $1D_{int}$ in the flow direction. Flow distribution in SA-4 is practically the same as observed in the other simulations. Therefore, the assumption of axisymmetric flow is valid and may be used to reduce the computational cost of simulations.

Table 2 – Series A's results.

	Entrance (i = en)	**Slot 1 (i =1)**	**Slot 2 (i = 2)**	**Slot 3 (i = 3)**	**Slot 4 (i = 4)**	**Exit (i = ex)**
SA-1						
Q_i (l/s)	2.231	0.617	0.807	1.050	1.362	6.066
Q_i/Q_{ex} (%)	36.772	10.179	13.295	17.307	22.448	–
V_i (m/s)	0.579	0.633	0.809	1.055	1.379	1.705
V_i/V_{ex} (%)	33.971	37.143	47.448	61.905	80.895	–
SA-2						
Q_i (l/s)	2.920	0.828	1.099	1.450	1.860	8.158
Q_i/Q_{ex} (%)	35.794	10.153	13.472	17.777	22.804	–
V_i (m/s)	0.758	0.835	1.108	1.462	1.875	2.274
V_i/V_{ex} (%)	33.321	36.724	48.726	64.300	82.476	–
SA-3						
Q_i (l/s)	4.935	1.412	1.870	2.422	3.135	13.774
Q_i/Q_{ex} (%)	35.830	10.252	13.574	17.583	22.761	–
V_i (m/s)	1.278	1.422	1.882	2.441	3.164	3.820
V_i/V_{ex} (%)	33.459	37.218	49.258	63.903	82.833	–
SA-4						
Q_i (l/s)	4.890	1.419	1.902	2.504	3.270	13.985
Q_i/Q_{ex} (%)	34.970	10.147	13.598	17.904	23.381	–
V_i (m/s)	0.612	0.715	0.958	1.262	1.648	2.076
V_i/V_{ex} (%)	31.262	36.561	48.994	64.508	84.238	–

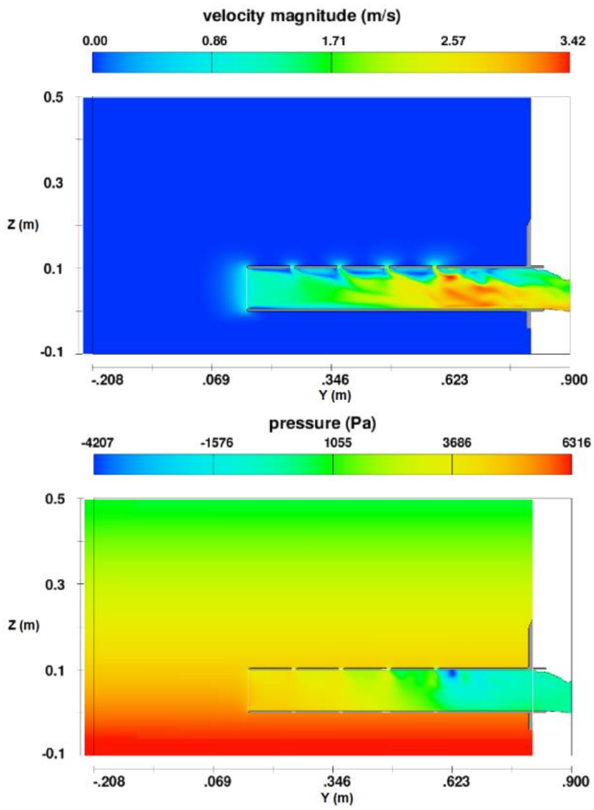

Figure 5 – Velocities and pressures (relative, atmospheric pressure is zero) along the conduit centerline in SA-2.

3.2. Series B

Series B results are summarized in Table 3. Flow distribution in SB-original follows the same pattern observed in Series A. In SB-1, there was an increase in discharge for all openings in the structure. The same can be said about the flow velocity, except for S3, where flow velocity decreased despite the discharge increment. We believe that this happens because the influence of the walls decreases as the slot width increases, leading to lower head loss across the slot. This lower head loss reflects a lower energy gradient for the flow passing through S3, which causes lower velocities. However, the discharge increased due to the greater area. Moreover, the discharge in S3 is lower than the sum of the discharges in S2 and S3 in SB-original.

In SB-2, an increment of 50% in slot area caused an increment of 50% in discharge for S1, although the decrease in flow velocity observed for S3 in SB-1 was not recorded in this case. The shortening of S4 led to a decrease of almost 48% in discharge (which is consistent since the area was halved), but to an increase in flow velocity as well. This reinforces the previously mentioned influence of the walls on the head loss across the slot (a narrower path requires a greater energy gradient, and hence greater velocity, to be overcome).

In SB-3, an increment of 50% in slot area caused an increment of 56% in discharge for S2, while the same area increment for S1 in SB-2 led to a smaller discharge increment. This indicates that there is some interference between the pipe entrance and the slots close to it, since the increment in discharge is greater for the same increment in the area as the slot in consideration is farther from the pipe entrance.

The results of the previous simulations suggest that it may be interesting to move the slots away from the pipe entrance due to the interference between them. In SB-4, the removal of S1 and the distribution of its area evenly between S2 and S3 resulted in discharge increases in all sections of the bottom outlet, thus reducing the head loss across the structure. Although the total discharge did not change much, the increase in discharge for the pipe entrance is beneficial since it may promote more sediment removal for water intakes closer to the reservoir margins.

Despite the preliminary nature of the results (since no calibration has taken place), in all simulations, we observed the formation of a *vena contracta* downstream the pipe entrance, which is a phenomenon known to happen at conduit entrances. Moreover, we have also observed that the flow velocity decreases rapidly in the upstream direction inside the reservoir. This behavior of the flow field upstream of orifices and conduit entrances is widely documented (White & Bettess, 1984; Sham*maa et* al., 2005; Powell & Khan, 2015). Therefore, the results indicate at least a minimal coherence with the real flow that would take place in the slotted pipe bottom outlet.

Table 3 – Series B's results; values in parentheses are the variation from the original geometry's results.

	Entrance (i = en)	**Slot 1 (i =1)**	**Slot 2 (i = 2)**	**Slot 3 (i = 3)**	**Slot 4 (i = 4)**	**Exit (i = ex)**
			SB-original			
Q_i (l/s)	2.319	0.656	0.873	1.154	1.506	6.509
Q_i/Q_{ex} (%)	35.631	10.075	13.418	17.735	23.141	–
V_i (m/s)	0.601	0.660	0.878	1.161	1.516	1.803
V_i/V_{ex} (%)	33.344	36.615	48.675	64.399	84.039	–
			SB-1			
Q_i (l/s)	2.524 (+8.9%)	0.724 (+10.3%)	–	1.763 (+52.8%)	1.569 (+4.2%)	6.580 (+1.1%)
Q_i/Q_{ex} (%)	38.354	10.996	–	26.801	23.849	–
V_i (m/s)	0.655 (+8.9%)	0.729 (+10.4%)	–	0.888 (-23.6%)	1.582 (+4.4%)	1.833 (+1.7%)
V_i/V_{ex} (%)	35.710	39.779	–	48.410	86.270	–
			SB-2			
Q_i (l/s)	2.303 (-1.3%)	0.982 (+49.8%)	0.982 (+12.4%)	1.260 (+9.1%)	0.779 (-48.0%)	6.306 (-3.0%)
Q_i/Q_{ex} (%)	36.516	15.581	15.566	19.977	12.360	–
V_i (m/s)	0.597 (-0.7%)	0.660 (-0.2%)	0.989 (+12.7%)	1.270 (+9.3%)	1.575 (+3.9%)	1.830 (-0.5%)
V_i/V_{ex} (%)	32.635	36.038	54.055	69.369	86.061	–
			SB-3			
Q_i (l/s)	2.293 (-1.1%)	0.643 (-1.9%)	1.362 (+56.0%)	1.254 (+8.6%)	0.783 (-48.0%)	6.335 (-2.7%)
Q_i/Q_{ex} (%)	36.199	10.151	21.502	19.793	12.355	–
V_i (m/s)	0.595 (-0.4%)	0.648 (-1.7%)	0.915 (-7.6%)	1.264 (-0.4%)	1.582 (+0.4%)	1.818 (+0.8%)
V_i/V_{ex} (%)	32.721	35.652	50.301	69.514	87.013	–
			SB-4			
Q_i (l/s)	2.488 (+7.3%)	–	1.024 (+17.2%)	1.655 (+43.4%)	1.518 (+0.8%)	6.685 (+2.7%)
Q_i/Q_{ex} (%)	37.222	–	15.312	24.763	22.703	
V_i (m/s)	0.646 (+7.3%)	–	0.687 (-21.8%)	1.111 (-4.3%)	1.530 (+0.9%)	1.868 (+3.6%)
V_i/V_{ex} (%)	34.565	–	36.800	59.512	81.911	

4. CONCLUSIONS

Bottom outlets are a means of mitigating sediment deposition near the dam. A slotted pipe bottom outlets are a new design of bottom outlets that provides sediment removal in the direction parallel to the dam axis, allowing the desilting of water intakes that are near the reservoir margins. We employed numerical modeling to verify the possibility of increasing the discharge capacity of the structure, characterizing its flow patterns, and evaluating the influence of its geometric elements. Results demonstrated that discharges and flow velocities in the slots grow in the downstream direction. In addition, slot width is shown to be a relevant variable in head loss across the slots. We did not observe a great increase in total discharge by varying slot width and placement, but the increase in discharge at the pipe entrance is beneficial to promoting more sediment removal in water intakes near the reservoir banks. We made the first attempt in geometry optimization and the results showed that it is possible to increase flow discharges along with the structure by changing the slot width. However, we would have to perform more tests to know how far the slots can be displaced without compromising the sediment removal in the region between them and the pipe entrance.

The next steps in our research must be the calibration of the numerical model, the consideration of a sediment deposit around the structure, and the search for an optimized design that must be validated using a physical model.

5. ACKNOWLEDGMENTS

This work was partially supported by the Brazilian agency CAPES.

6. REFERENCES

Emamgholizadeh, S., Bina, M., Fathi Moghadam, M. and Ghomeyshi, M. (2006), *Investigation and Evaluation of the Pressure Flushing Through Storage Reservoir*, ARPN Journal of Engineering and Applied Sciences, 1 (4), 7–16.

Flow Science, I. (2018) *FLOW-3D® Version 12.0 Users Manual*, FLOW-3D [Computer software].

George, M. W., Hotchkiss, R. H. and Huffaker, R. (2017), *Reservoir sustainability and sediment management*, Journal of Water Resources Planning and Management, 143 (3).

Haghjouei, H., Rahimpour, M., Qaderi, K. and Kantoush, S. A. (2021), *Experimental study on the effect of bottomless structure in front of a bottom outlet on a sediment flushing cone*, International Journal of Sediment Research, 36 (3), 335-347.

Kondolf, G. M., Gao, Y., Annandale, G. W., Morris, G. L., Jiang, E., Zhang, J., Cao, Y., Carling, P., Fu, K., Guo, Q., Hotchkiss, R., Peteuil, C., Sumi, T., Wang, H., Wang, Z., Wei, Z., Wu, B., Wu, C. and Yang, C. T. (2014), *Sustainable sediment management in reservoirs and regulated rivers: Experiences from five continents*, Earth's Future, 2 (5), 256–280.

Madadi, M. R., Rahimpour, M. and Qaderi, K. (2016), *Sediment flushing upstream of large orifices: An experimental study*, Flow Measurement and Instrumentation, 52, 180-189.

Madadi, M. R., Rahimpour, M. and Qaderi, K. (2017), *Improving the Pressurized Flushing Efficiency in Reservoirs: an Experimental Study*, Water Resources Management, 31 (14), 4633–4647.

Paulo, F. A., Abreu, A. S., Dai Prá, M., Endres, L. A. M., Ferla, R. and Teixeira, E. D. (2021), *Experimental study of pressure flushing of non-cohesive sediment through slotted pipe bottom outlet*, Revista Brasileira de Recursos Hídricos, 26 (01).

Powell, D. N. and Khan, A. A. (2015), *Flow Field Upstream of an Orifice under Fixed Bed and Equilibrium Scour Conditions*, Journal of Hydraulic Engineering, 141 (2).

Sawadogo, O., Basson, G. R. and Schneiderbauer, S. (2019), *Physical and coupled fully three-dimensional numerical modeling of pressurized bottom outlet flushing processes in reservoirs*, International Journal of Sediment Research, 34 (5), 461–474.

Schleiss, A. J., Franca, M. J., Juez, C. and De Cesare, G. (2016), *Reservoir sedimentation*, Journal of Hydraulic Research, 54 (6), 595–614.

Shammaa, Y., Zhu, D. Z. and Rajaratnam, N. (2005), *Flow Upstream of Orifices and Sluice Gates*, Journal of Hydraulic Engineering, 131 (2), 127-133.

Shen, H. W. (1999), *Flushing sediment through reservoirs*, Journal of Hydraulic Research, 37 (6), 743–757.

White, W. R. and Bettess, R. (1984), *The feasibility of flushing sediments through reservoirs*, in Walling, D. E., Foster, S. S. D. and Wurzel, P. (Eds) *Challenges in African hydrology and water resources*, Walingford, 1984, pp. 577-587.

8th International Junior Researcher and Engineer
Workshop on Hydraulic Structures
ISBN: 978-0-578-37416-1
https://doi.org/10.26077/8af6-6aaf

Galway, Ireland,
5th - 8th June 2021

Approach flow depth influence on nonlinear weir discharge capacity

Benane Redha[1], Sebastien Erpicum[2] and Michel Pirotton[2]

[1] Faculty of civil engineering,
University of Sciences and Technology of Houari Boumediene,
ALGERIA

[2] Urban and Environmental Engineering Research Unit - HECE Research Group,
Liege University
BELGIUM
E-mail: redhabenane@gmail.com

Abstract: *The high hydraulic efficiency and the compactness of nonlinear weirs favor their use in several rehabilitation or new dams projects. Main types of nonlinear weirs are labyrinth and piano key weirs. The purpose of this paper is to provide indications on the influence of the approach flow depth on the discharge capacity of these nonlinear weirs. To do so, a series of experimental tests have been carried out in the laboratory of Engineering Hydraulics of the Liege University. A labyrinth and a piano key weir have been tested in channel configuration (upstream flow width equal to the weir width) considering various dimensionless dam heights. A large range of discharge has been tested for each case. The results show that the dimensionless dam height increase may decrease up to 8% of the labyrinth weir discharge capacity while it has only very limited but opposite effects for the piano key weir.*

Keywords: *Physical modelling, labyrinth weir, PK weir, head-discharge curve.*

1. INTRODUCTION

The weir is an essential element of dam spillways. It controls the upstream reservoir level rise by releasing excess water, in particular during floods. When placed across a natural or artificial watercourse, a weir can also be used for measuring discharge or controlling the water depth.Replacing a linear weir with a nonlinear weir can be an effective way to increase discharge efficiency (increase discharge released for a given upstream head) for a constant width on a dam crest or in a channel. Nonlinear weirs are linear weirs folded in plan to increase the crest length. Since the discharge capacity of a free surface weir is proportional to its crest length, nonlinear weirs exhibit higher discharge capacity than linear weirs for the same width (Tullis et al., 1995). Different geometric configurations for nonlinear weirs have been developed in order to increase this length while limiting the weir footprint area, such as labyrinth weirs (Hay and Taylor, 1970; Tullis et al., 1995; Crookston, 2010), skewed or oblique weirs (Kabiri-Samani, 2010; Noori and Chilmeran, 2005), duck-bill weirs (Khatsuria et al.,1988), piano key weirs (Leite Ribeiro et al., 2007; Laugier, 2007; Lempérière and Ouamane, 2003) and fuse gates (Falvey and Treille, 1995). In the present study, we are interested in two specific types of nonlinear weirs: the labyrinth weir and the piano key weir (PK weir).

1.1. Labyrinth weir

Labyrinth weirs are nonlinear weirs with vertical walls. The first study reported on the labyrinth weir was carried out by Gentilini (1941); although, the first prototype labyrinth weir documented in the literature was on the East Park Dam (1910) on Little Stony Creek, California, USA (Crookston et al., 2019). Depending on the geometry in plan view of the so called alveoli, there are several forms of labyrinth weir, i.e. trapezoidal, triangular or rectangular (Crookston, 2010). According to Falvey (2003), the symmetrical trapezoidal shape is the most used because of the ease of construction and its hydraulic performance. Alveoli may be aligned along a straight line or a curve (Crookston and Tullis, 2012 a).

Crookston (2010) defines the main parameters generally used to detail the geometry of a labyrinth weir with a linear arrangement (Figure 1). The alveoli geometry is defined by the length of side wall l_c, the width of a cycle w, the wall thickness t_w, the side walls angle α, the alveoli apex width A and the height of the vertical walls P. The total width of the weir W, the number of cycles N and the developed length L ($L=N\ (2l_c+2A)$) are parameters describing the full weir geometry.

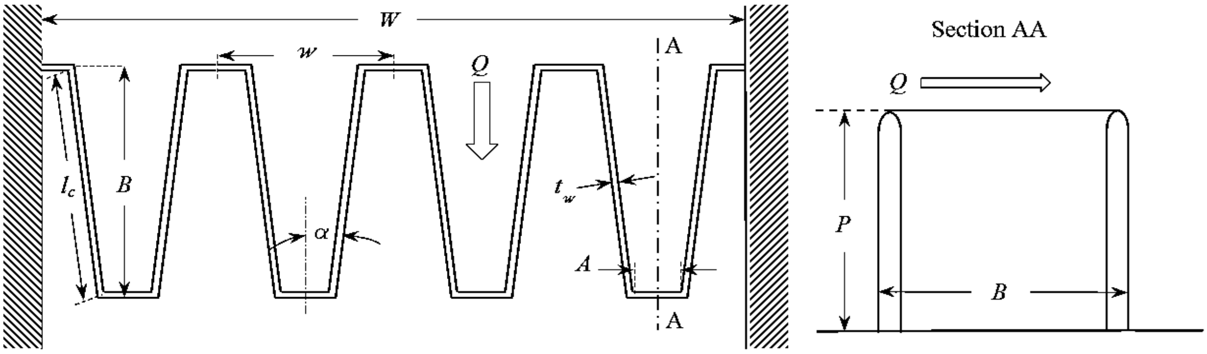

Figure 1 - Fundamental parameters of the labyrinth weir. Plan view (left) and typical cross-section (right).

1.2. Piano key weir

A PK weir is a rectangular labyrinth weir with ramped floor and cantilevered apexes. This arrangement enables a decrease in the basement length and then the area needed to ground the weir. It is then possible to place PK weirs on a very limited area, such as on the top of gravity dams. This specific geometry exhibits high discharge capacity, greater than a labyrinth weir with the same crest (Anderson and Tullis, 2012 and 2013). The PK weir was firstly described by Lempérière and Ouamane (2003). The use of the PK weir as a solution for the rehabilitation of spillways in operation started in 2006 at Goulours dam in France with a project by the EDF company (Laugier, 2007).

Similar to labyrinth weirs, the PK weir geometry (Figure 2) is characterized by (Pralong et al., 2011) the upstream and downstream heights P_o and P_i, denoted simply P when both values are equal, the width of the upstream and downstream alveoli W_i and W_o, the lengths of the upstream and downstream overhang B_i and B_o, the length of the base B_b, the length of the lateral wall B ($B = B_i + B_o + B_b$), the slopes of the upstream and downstream alveoli S_i and S_o and the wall thickness T_s. The total width of the weir W_t, the cycle width W_u, the number of cycles N and the developed length L ($L=N(2B+W_i+W_o+T_s)$) describe the global weir geometry.

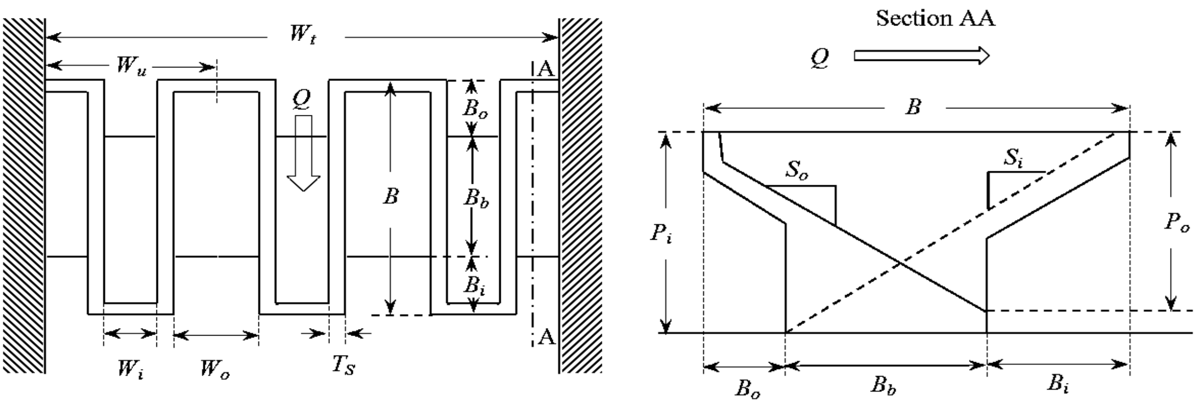

Figure 2 - Fundamental parameters of the PK Weir. Plan view (left) and typical cross-section (right).

1.3. Previous Studies

PK and labyrinth weirs have been extensively studied over the years using physical and numerical models. Both structures are free surface weirs. Their discharge capacity follows then an equation similar to (Tullis et al., 1995; Machiels et al., 2011a):

$$Q = C_d\, W\sqrt{2gH_T^3} \qquad (1)$$

with Q the discharge, C_d the dimensionless discharge coefficient, W the weir width, g is the gravity acceleration and H_T the total upstream head.

The various research works carried out to date showed that discharge coefficient is higher for small upstream head and decreases with increasing upstream head. The weir geometry affects significantly its discharge capacity. For instance, for labyrinth weirs, Hay and Taylor, 1970; Lux and Hinchliff, 1985; Tullis et al., 1995; Crookston and Tullis, 2012 a, b, 2013 a, b., showed that the main parameters influencing hydraulic performance are the head water ratio H_T/P, the sidewall angle α, and the cycle width ratio w/P. With regards to the PK weir, since the proposal of a first design by Hydrocoop in collaboration with Biskra University (Algeria), the Hydraulic Laboratory of Electricité de France (France) and Roorkee University (India) (Lempérière and Ouamane, 2003), numerous works and publications have been carried out (Ouamane and Lempérière, 2006; Machiels et al., 2011 and 2014; Leite Ribeiro et al., 2012 a, b; Machiels, 2012; Anderson and Tullis, 2012, 2013) and showed that the main parameters influencing hydraulic performance of the PK Weir are the headwater ratio H_T/P, the developed crest length L/W ratio and the unit width ratio W_u/P.

The available literature indicates that all the studies conducted to date have never analyzed the effect of the dam height on the discharge capacity of a nonlinear weir. Since this might be an important parameter when considering the construction of a nonlinear weir on the top of a dam, the objective of the present study is to experimentally study this parameter considering a labyrinth weir and a PK weir.

2. EXPERIMENTAL SETUP

2.1. Test facility

Tests are carried out in a 1.2 m wide, 1.2 m high and 7.2 m long horizontal flume in the laboratory of Engineering Hydraulics of the Liege University. The flume is supplied through an upstream tank 1.8 m long, 1.2 m wide and 2.1 m deep and by two pipes connected to centrifugal pumps. A baffle wall is located at the connection between the tank and the flume. At the downstream extremity of the flume, the water freely falls down a 0.9 m high chute and goes back to a 400 m³ underground reservoir supplying the pumps (closed system).

The weirs were placed 3.6 m downstream of the baffle wall on a 0.76 m high support (Figure 4) with a vertical upstream face. A plywood plate has been used to modify the reservoir bottom level and then the dam height P_d (Figure 4) along the whole upstream section of the flume.

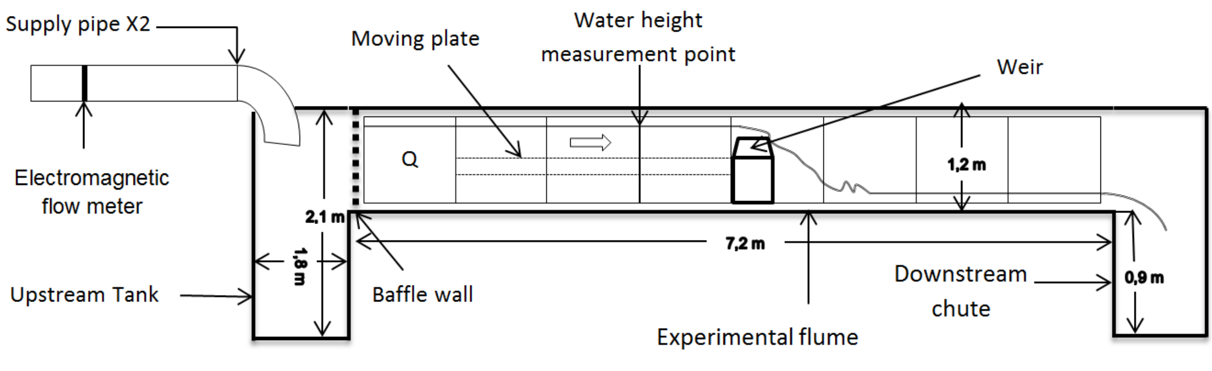

Figure 3 - Testing flume side view.

The discharge supplied to the flume was measured using an electromagnetic flow meter (accuracy of 0.5%) on upstream pipes. A point gauge with a vernier (accuracy of 0.1 mm on free surface at rest) and an ultrasonic sensor (accuracy of 1%) enabled the measurement of water levels upstream of the weirs. The ultrasonic sensor was calibrated on the model. The point gauge was used to check the ultrasonic sensor result. A drawing of the flume is shown in Figure 3 and hydraulic parameters are detailed in Figure 4.

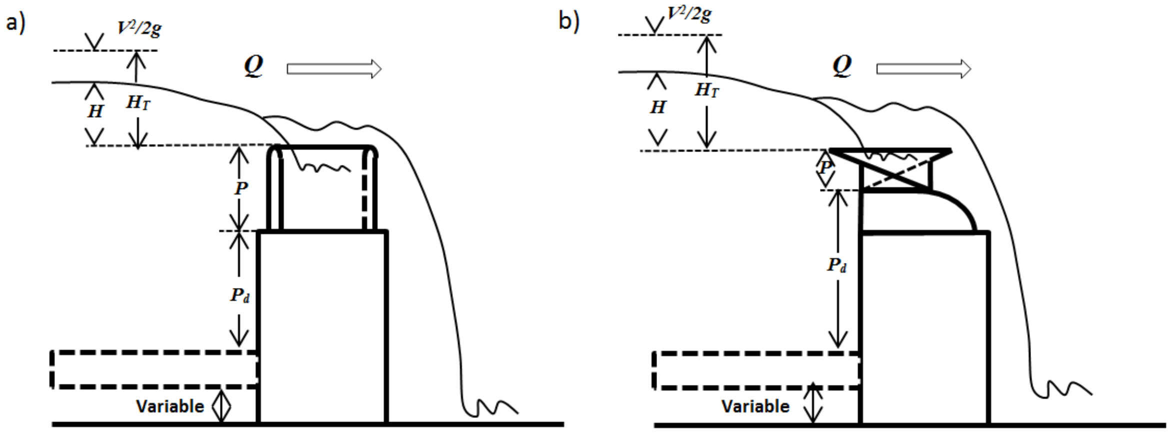

Figure 4 - Hydraulic parameters of flow over the labyrinth weir (a) and the PK weir (b).

2.2. Weirs characteristics

Both nonlinear weir models considered in this study (Figure 5) were fabricated with PVC by the laboratory staff. Their geometric characteristics are summarized in table 1 and table 2. The labyrinth weir had a half rounded crest. The PK weir had a flat topped crest. The labyrinth weir was placed 0.05 m downstream of the support vertical upstream face, while the PK weir was aligned with the support upstream face. The labyrinth weir width was equal to the flume width (1.2 m). Since the PK weir width was 0.8 m, vertical plywood plates were used to narrow the channel along the whole section upstream of the weir. Consequently, both weirs have been tested in channel configuration, i.e. with an upstream chanel width equal to the weir width.

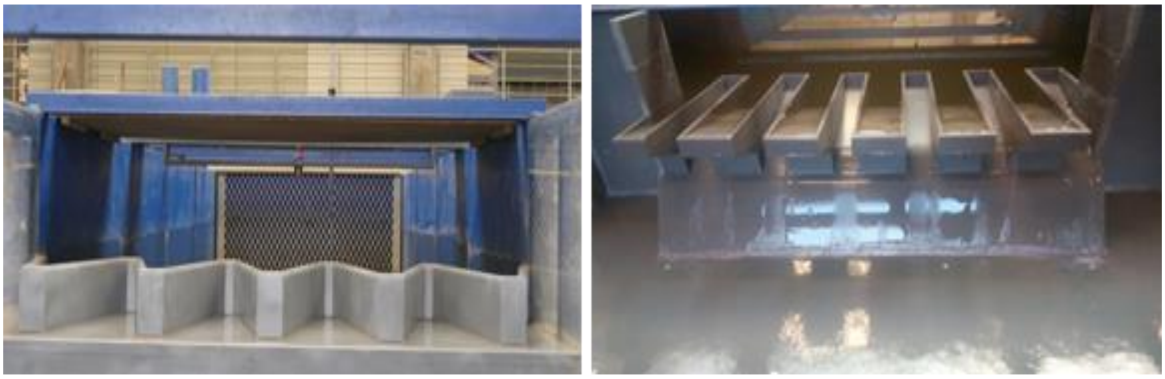

Figure 5 - Downstream view of labyrinth weir model (left) and PK weir model (right).

Table 1 - Geometric characteristics of the labyrinth weir.

Parameter	P	B	L	w	α	A	D	t_w	N	Crest type
Value (cm)	12.00	38.00	425.11	24.00	12.50°	2.50	5.30	2.00	5.00	Half rounded

Table 2 - Geometric characteristics of the PK weir.

Parameter	P	B	L	W_i	W_0	S_i	S_0	T_s	N	Crest type
Value (cm)	13.30	37.80	537.10	6.90	4.90	2.08	3.73	0.60	6.00	Flat topped

2.3. Testing procedure

Each weir was tested separately with different dam heights P_d ranging from 0 to 0.76 m for the labyrinth (7 configurations) and equal to 0 or 0.897 m for the PK weir (2 configurations) and with discharges varying from 0.01 to 0.15 m³/s. For each weir configuration, two series of tests were conducted. The upstream water level was measured first with increasing discharges from the smallest value to the maximum value and then with decreasing discharges from the maximum value to the smallest value. Two water level measurements are then available for each discharge and each weir. The discharge variation step was 0.02 m³/s for the labyrinth and 0.01 m³/s for the PK weir. For each discharge, the water level was measured during 5 minutes at a 1 Hz frequency with the ultrasonic sensor and the mean value was computed.

The total upstream head H_T on the weir crest is calculated from water depth measurements as:

$$H_T = H + {V^2}/{2g} \tag{2}$$

The mean cross sectional flow velocity V is calculated as:

$$V = {Q}/{W(H + P + P_d)} \tag{3}$$

The discharge coefficient C_d is evaluated using equation 1.

3. EXPERIMENTAL RESULTS AND DISCUSSION

Figure 6 shows the variation of the total upstream head H_T with respect to the discharge for different values of the relative dam height P_d/P. The almost linear trends of head-discharge curves of the labyrinth weir and the PK weir are clearly visible and the difference between the tests with different dam heights P_d/P is limited.

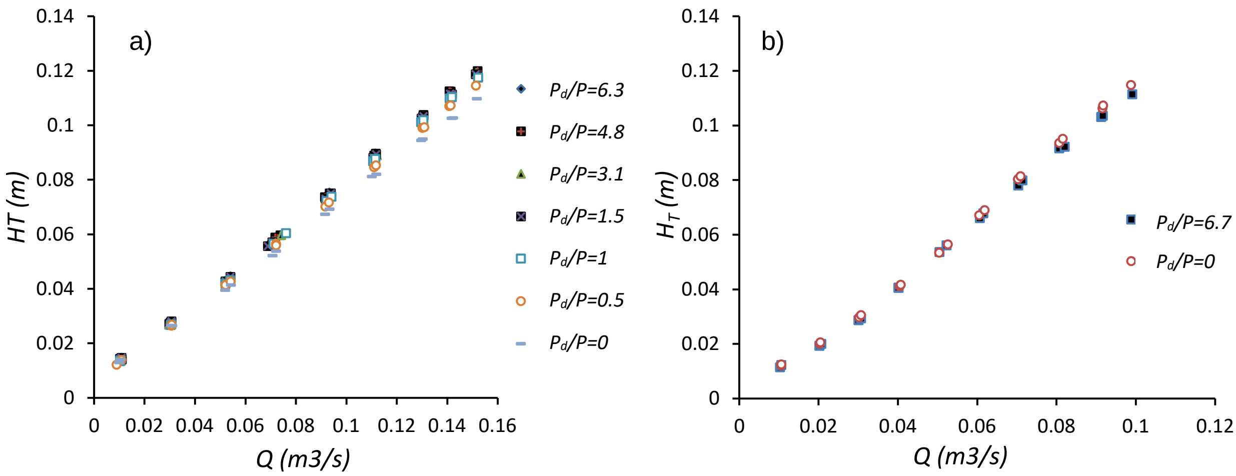

Figure 6 - Head-discharge curves of the labyrinth weir (a) and the PK weir (b).

Looking at the results in terms of discharge coefficient and dimensionless upstream head makes the differences more visible (Figure 7 and 8). On these figures, the dotted line represents the limit of experimental results affected by scale effects according to the 3 cm criterion on upstream water level proposed by Erpicum et al. (2016) for PK weirs. It can be seen that below this limit, results gained with the two series of tests with the same discharge are different.

For the PK weir, the discharge coefficient is slightly affected by the dam height while the labyrinth weir efficiency significantly decreases with increasing dam height.

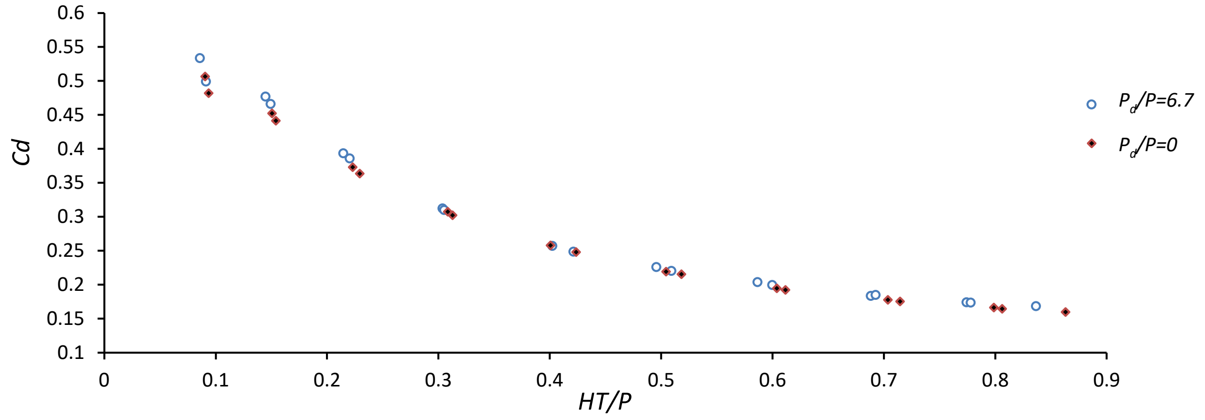

Figure 7 - Dimensionless discharge capacity the PK weir.

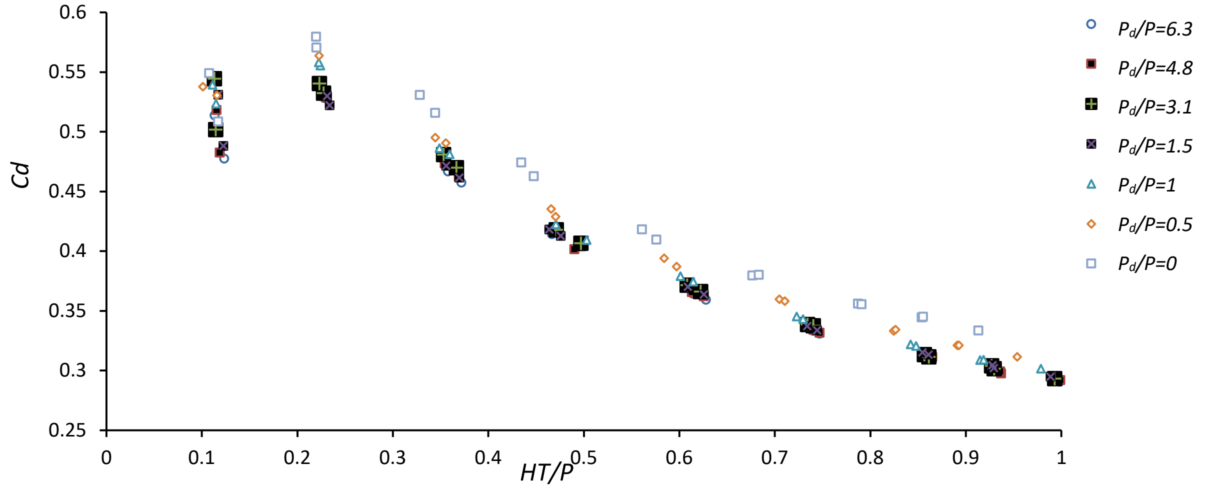

Figure 8 - Dimensionless discharge capacity of the labyrinth weir.

The labyrinth has a design similar to the one considered by Crookston et al. (2010) except where the wall thickness is larger in the present study (*P/6* compared to *P/8*). Interpolation of the analytical curves from Crookston et al. (2010) for α equal to 12.5° provides a reference for comparison when P_d/P=0 (figure 9). Both data sets merge well for H_T/P > 0.4. For smaller heads, the reference curve exhibits higher efficiency. This could be explained, at least partly, by the broader crest considered in this study.

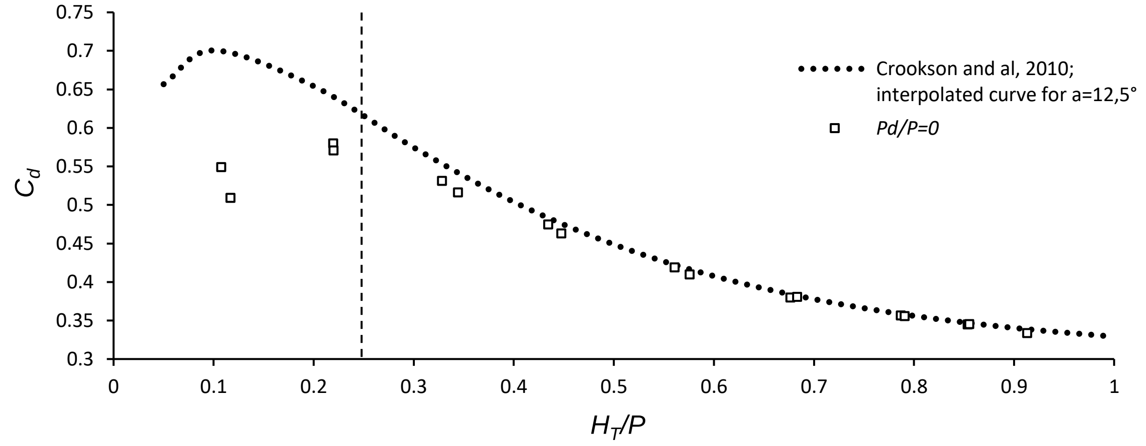

Figure 9 – Comparison of the experimental results with the interpolated relation from Crookston et al. (2010).

Figure 10 shows the ratio between the discharge coefficient with a non-zero relative dam height ratio (C_{di}) to the reference one (C_{d0}) gained with P_d/P = 0. To compare values at identical upstream head ratios, the data for each weir have been approximated with a polynomial of degree 6 where the polynomial equation has been used to calculated discharge coefficient value at various upstream heads. Table 3 and 4 present the averaged discharge coefficient ratio C_{di}/C_{d0} for the labyrinth weir and for the PK weir.

It appears that the efficiency of the labyrinth weir decreases fast with limited increase of dam height and then stabilizes at around a 8% decrease for a deep approach flow. In the case of the PK weir, the trend is of smaller amplitude and opposite: figure 11 shows that the efficiency increases slightly, around 2%, for the higher dam. Despite more investigation is needed to understand these different behaviors, the explanation might, at least partly, be linked to the direction of the flow velocity approaching the inlet key in relation to the inlet bottom slope. In the case of a labyrinth weir, the mainly horizontal incoming flow velocity is more affected by a deeper upstream water flow than in the case of a PK weir, where the ramped inlet key bottom induces incoming flow velocity with a stronger vertical component.

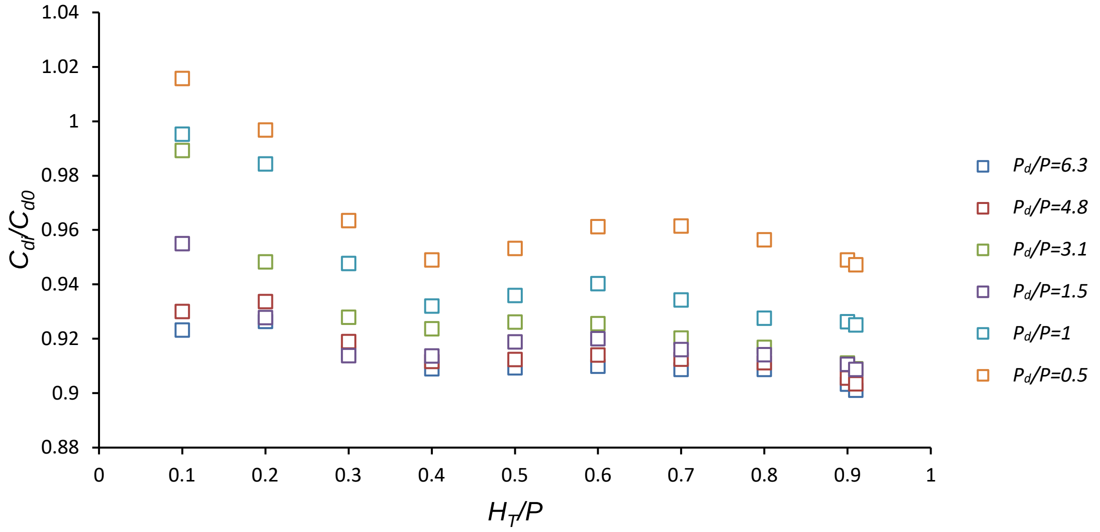

Figure 10 - Theoretical C_{di}/C_{d0} ratio as a function of H_T/P for the labyrinth weir.

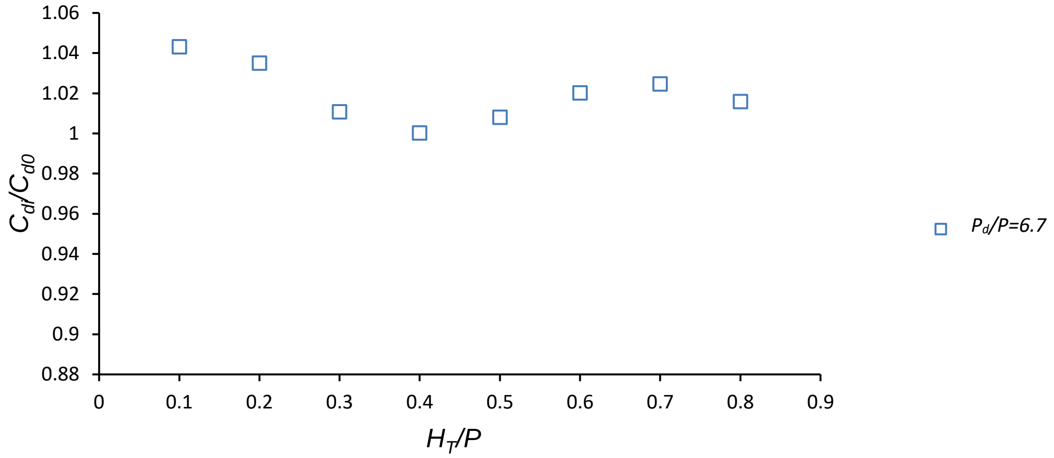

Figure 11 - Theoretical C_{di}/C_{d0} ratio as a function of H_T/P for the PK weir.

Table 3 - Averaged C_{di}/C_{d0} for the labyrinth weir

P_d/P	6.3	4.8	3.1	1.5	1	0.5
C_{di}/C_{d0}	0.91	0.92	0.93	0.92	0.94	0.97

Table 4 - Average C_{di}/C_{d0} for the PK weir

P_d/P	6.7
C_{di}/C_{d0}	1.02

4. CONCLUSION

In an effort to provide indications on the influence of the approach flow depth on the discharge capacity of nonlinear weirs, a series of experimental tests have been carried out considering a labyrinth and a PK weir scale model operated in channel configuration in a flume with a movable upstream bed level.

The results show that a dimensionless dam height in the range 0 to 1.5 significantly affects the labyrinth weir discharge capacity. In particular, the reference discharge capacity observed with an upstream bed elevation equal to the labyrinth weir bottom elevation (P_d/P=0) is reduced by 8% in average when P_d/P is equal to or higher than 1.5.

On the contrary, for the PK weir, the influence of dam height was found to be negligible despite showing opposing results: discharge capacity increases slightly, around 2%, with increasing dam height compared to the reference situation where the upstream channel bed elevation is equal to the elevation of the PK weir inlet entrance.

As shown in this study, the dam height might be an essential parameter to take into consideration when designing nonlinear weirs placed on the top of dams. Additional research is required to confirm the findings of this paper, considering other labyrinth and PK weir geometries in addition to providing a better understanding of the reason for the varied effects observed between different weir types.

5. ACKNOWLEDGMENTS

The Authors acknowledge the help of the technicians of the Engineering Hydraulics laboratory of the Liege University in building and operating the models. They also acknowledge ISL Ingénierie and Groupement GBN-CCN for their permission to use the labyrinth weir model in the framework of this research.

REFERENCES

Anderson, R.M. and Tullis, B.P. (2012). *Comparison of Piano Key and Rectangular Labyrinth Weir Hydraulics*, J. Hydraulic Eng. 138(4): 358-361.

Anderson, R.M. and Tullis, B.P. (2013). *Piano Key Weir Hydraulics and Labyrinth Weir comparison*. J. Irrig. Drain. Eng. 139(3): 246-253.

Crookston, B.M, Erpicum, S., Tullis, B.P., Laugier, F. (2019). *Hydraulics of Labyrinth and Piano Key Weirs: 100 Years of Prototype Structures*, Advancements, and Future Research Needs, J. Hydraulic Eng. 145(12): 02519004

Crookston, B.M and Tullis, B.P. (2012a). *Arced Labyrinth Weirs.* J. Hydraulic Eng. 138(6): 555-562.

Crookston, B.M and Tullis, B.P. (2012b). *Discharge Efficiency of Reservoir-Application Specific Labyrinth Weirs*. J. Irrig. Drain. Eng. 138(6): 564-568.

Crookston, B.M and Tullis, B.P. (2013a). *Hydraulic Design and Analysis of Labyrinth Weirs. I: Discharge Relationships*. J. Irrig. Drain. Eng. 139(5): 363-370.

Crookston, B.M and Tullis, B.P. (2013b). *Hydraulic design and analysis of labyrinth weirs. II: Nappe aeration, instability, and vibration*. J. Irrig. Drain. Eng. 139(5): 371-377.

Crookston, B.M., (2010). *Labyrinth Weirs*. Ph.D. dissertation, Utah state Univ. Logan, UT.

Erpicum, S., Tullis, B.P., Lodomez, M., Archambeau, P., Dewals, B. and Pirotton, M. (2016). *Scale effects in physical piano key weirs models*. J. Hydraulic Res. 54(6): 692–698.

Falvey, H. (2003). *Hydraulic design of labyrinth weirs*. ASCE, Reston, Va.

Falvey, H., and Treille. P., (1995). *Hydraulics and design of fusegates*. J. Hydraulic Eng. 121(7): 512-518.

Gentilini, B. (1941). Stramazzi con cresta a pianta obliqua e a zig-zag. Memorie e studi dell'Instituto di Idraulicae Costruzioni Idrauliche del Regio Politecnico di Milano. No. 48. (In Italian).

Hay, N., and Taylor, G. (1970). *Performance and design of labyrinth weirs*. J. Hydraulic Eng. 96(11): 2337-2357.

Kabiri-Samani, A. (2010). *Analytical approach for flow over an oblique weir*. Transaction A: Civil Engineering. 17(2): 107-117.

Khatsuria, R., Deolalikar, P., and Bhosekar, V. (1988). *Design of duckbill spillway and reversed sloping curved stilling basin*. Salauli Project, 54th R&D Session, CBI&P, Ranchi, India.

Laugier, F. (2007). *Design and construction of the first Piano Key Weir (PKW) spillway at the Goulours dam*. Hydropower and Dams. 14 (5): 94-101.

Leite Ribeiro, M., Pfister, M., Schleiss, A.J. and Boillat, J.-L. (2012a). *Hydraulic design of A-type Piano Key Weirs*. J. Hydraulic Res. 50(4): 400–408.

Leite Ribeiro, M., Bieri, M., Boillat, J.-L., Schleiss, A.J., Singhal, G. and Sharma, N. (2012b). *Discharge capacity of Piano Key Weirs*. J. Hydraulic Eng. 138(2): 199–203.

Leite Ribeiro, M., Boillat, J., Schleiss, A., Laugier, F., and Albalat, C. (2007). *Rehabilitation of St-Marc dam. Experimental optimization of a piano key weir*. Proc. of the 32nd Congress of IAHR, Venice, Italy.

Lempérière, F. and Ouamane, A. (2003). *The piano keys weir: a new cost-effective solution for spillways*, Hydropower & Dams. 10(5): 144–149.

Lux, F. and Hinchliff, D. (1985). *Design and construction of labyrinth spillways*. 15th Congress ICOLD, Vol. IV, Q59-R15, Lausanne, Switzerland, 249-274.

Machiels, O. (2012). *Experimental study of the hydraulic behaviour of Piano Key Weirs*. PhD thesis. HECE research unit, University of Liège, Belgium. http://hdl.handle.net/2268/128006.

Machiels, O., Erpicum, S., Dewals, B., Archambeau, P. and Pirotton, M. (2011). *Experimental observation of flow characteristics over a Piano Key Weir*. J. Hydraulic Res. 49(3): 359–366.

Machiels, O., Pirotton, M., Archambeau, P., Dewals, B.J. and Erpicum, S. (2014). *Experimental parametric study and design of Piano Key Weirs*. J. Hydraulic Res. 52(3): 326–335

Noori, B. and Chilmeran, T. (2005). *Characteristics of flow over normal and oblique weirs with semicircular crest*. Al Rafidain Eng. J., 13(1): 49-61.

Ouamane, A. and Lempérière, F. (2006). *Design of a new economic shape of weir*. In Berga et al. (eds), Dams and Reservoirs, Societies and Environment in the 21st Century: 463–470. Taylor and Francis: London.

Pralong, J., Vermeulen, J., Blancher, B., Laugier, F., Erpicum, S., Machiels, O., Pirotton, M., Boillat, J.L., Lite Ribeiro, M. and Schleiss, A.J. (2011). *A naming convention for the Piano Key Weirs geometrical parameters*. Proc. Intl Workshop on Labyrinths and Piano Key Weirs PKW 2011, CRC Press, 271-278.

Tullis, P., Amanian, N., and Waldron, D. (1995). *Design of labyrinth weir spillways*. J. Hydraulic Eng. 121(3): 247-255.

8th International Junior Researcher and Engineer
Workshop on Hydraulic Structures
ISBN 978-0-578-37416-1
https://doi.org/10.26077/bec3-52cb
Galway, Ireland,
5th - 8th June 2021

Modelling velocity profiles of aerated flows down grassed spillways

H. Cui[1,2], S. Felder[2] and M. Kramer[1]
[1] School of Engineering and Information Technology (SEIT)
UNSW Canberra
Canberra ACT 2610, AUSTRALIA
[2] Water Research Laboratory, School of Civil and Environmental Engineering
UNSW Sydney
AUSTRALIA
E-mail: hanwen.cui@adfa.edu.au

Abstract: *The ecological and environmental benefits of grassed spillways present a green solution to the construction of low head conveyance structures. On a grassed spillway, the aggregate of the grass canopy and root structure may alter flow resistance, velocity distribution and other flow properties. While subcritical flows in vegetated open channels have been extensively researched, only little is known about flow properties in supercritical high-velocity flows, which are typically characterized by self-aeration. The current study explores the application of a velocity superposition to supercritical aerated flows on a spillway with artificial grass. Velocity measurements were conducted with a Pitot tube and a phase-detection conductivity probe, allowing for the extraction of shear velocities at the canopy top which revealed an additional free-stream velocity layer. A comparison of the mixing layer length scale with the shear length scale (of the mixing layer) demonstrated a good correlation. Overall, this study provided new insights into the flow resistance of supercritical flows on grassed spillways.*

Keywords: *artificial grass, eco-friendly structures, flow resistance, high-velocity air-water flows, water sensitive urban design.*

1. INTRODUCTION

Grass linings on spillways and waterways with mild to moderate slopes provide ecological and environmental benefits such as ground water replenishment, vegetation growth (Mossa et al., 2017) and water quality improvement (Van Hemert et al., 2013). These advantages have promoted the use of grassed spillways for embankment protection (Wilcock et al., 1999), as agricultural floodway or small-scale drainage floodway (Van Hemert et al., 2013). The grass canopies act as roughness elements and enhance flow resistance, while the grass root structure provides additional support to the soil ground (Chen et al, 2012). In the past, flow resistance of grassed spillways was often investigated from a soil mechanics perspective, where the aggregate of soil and grass patches undergoes constant erosion and scouring damage (Ralston and Brevard, 1988). From a hydraulics point of view, subcritical flow conditions have been extensively researched with experimental and analytical modelling in both submerged and emergent conditions (Nepf, 2012) for various density (Guillén-Ludeña et al., 2020), expanding research of canopy flows into broader aspects of river floodplains (Crosato and Saleh, 2011) and tidal and coastal environments (Tinoco et al., 2020). Flow properties of grassed spillways under high-velocity supercritical flow conditions have received less attention.

In supercritical flows, the Froude number exceeds unity and turbulent energy obtained by the flows generates strong eddy motions, deforming the coherent free-surface that is maintained by surface tension and gravity (Brocchini and Peregrine, 2001). As turbulent forces dominate over surface tension and gravity, entrained air pockets break up into smaller air bubbles, a process termed self-aeration. Self-aeration on smooth spillways and the role of entrapped and entrained air was systematically described in Wilhelms and Gulliver (2005). Valero and Bung (2018) described the importance of free-surface instabilities on self-aeration in smooth and stepped spillways. However, self-aeration in flows down grassed spillways was only considered recently (Scheres et al. 2020). On grass-lined waterways, the supercritical flows can lead to erosion of the soil structure and engineering design guidelines must account for this as well as flow aeration. To provide a more controlled environment, the current study deployed a dense cover of artificial grass, allowing a detailed investigation into mean velocity profiles and flow resistance of grassed spillways.

Nikora et al. (2013) developed a model to characterize velocity profiles of flat grassed waterways in subcritical flows, which uses a linear superposition of several conventional concepts. In the present study, the application of the velocity superposition of Nikora et al. (2013) was applied to supercritical flows on a spillway with artificial grass. The results revealed an additional free-surface layer, which led to an expansion of Nikora's et al. (2013) subcritical flow model. In addition, shear velocities at the canopy top were extracted through log-law fitting, demonstrating a good agreement with shear velocities evaluated from the friction slope, providing new information on the local flow resistance.

2. METHODOLOGY

2.1. Velocity superposition

The current study investigated the superposition of streamwise velocity profiles in supercritical free-surface flows down grassed spillways. The velocities in the water phase were superposed using conventional concepts after Nikora et al. (2013), including (i) a uniform velocity distribution inside the canopy layer, (ii) the mixing layer region, (iii) the logarithmic layer and (iv) the wake function; the current study proposes an additional (v) free-surface layer to reflect the interfacial velocity of free-surface waves.

The velocity distribution within the canopy is governed by the vegetational drag (with drag coefficient $C_d = 1.0$), further depending on the frontal area of grass per unit volume ($a = 281$ 1/m) and the channel slope ($S_0 = 0.19$). Herein, the single-phase model of Nikora et al. (2013) was applied up to the characteristic flow depth Y_1 where the void fraction is first measured ($C(Y_1) \approx 0.01$):

$$\bar{u}_{UD} = \begin{cases} \left(\dfrac{gS_0}{0.5\, C_d\, a}\right)^{0.5} & \text{if } 0 < y < Y_1 \\ \text{else } 0 \end{cases} \tag{1}$$

where $\bar{u}_{UD}$ is a quasi-constant velocity (Nikora et al.,2004; Nepf, 2012; Nikora et al., 2013) and y is the bed-normal coordinate. The mixing layer includes the appearance of an inflection point and the velocity distribution $\bar{u}_{ML}$ is governed by a Kelvin-Helmholtz instability, generating mixing layer eddies (Raupach et al., 1996; Nepf, 2012; Nikora et al., 2013):

$$\bar{u}_{ML} = \begin{cases} (\bar{u}_i - \bar{u}_{UD})\left(1 + \tanh\frac{y-y_i}{L_e}\right) & \text{if } 0 < y < Y_1 \\ \text{else } 0 \end{cases} \tag{2}$$

where $\bar{u}_i$ stands for the velocity at the inflection point, y_i is the location of the inflection point and L_e is a characteristic length scale of the mixing layer. The logarithmic layer follows a classical logarithmic velocity profile $\bar{u}_{LL}$, expressed as (Nikora et al. (2013):

$$\bar{u}_{LL} = \begin{cases} u_{*c}\,\frac{1}{\kappa}\ln\frac{y-y_i-d_i}{y_0} & \text{if } y_i + y_0 + d_i < y < Y_1 \\ \text{else } 0 \end{cases} \tag{3}$$

where u_{*c} represents the shear velocity at the top of the canopy as a momentum transport scale, κ is the von Karman constant ($\kappa = 0.41$), d_i is the distance between the log layer and the inflection point and y_0 is the hydraulic roughness height, respectively. The wake function $\bar{u}_{WF}$ can be approximated as (Monin and Yaglom, 1971):

$$\bar{u}_{WF} = \begin{cases} u_{*c}\,\frac{2\Pi}{\kappa}\sin^2\frac{\pi y}{2Y_1} & \text{if } y_i + y_0 + d_i < y < Y_1 \\ \text{else } 0 \end{cases} \tag{4}$$

where $\bar{u}_{WF}$ is the velocity of the wake and Π is the Coles wake parameter (Coles, 1956). The combination of these components provides a semi-analytical description of the velocity profile on grassed channels, as defined by for subcritical flow conditions:

$$\bar{u} = \bar{u}_{UD} + \bar{u}_{ML} + \bar{u}_{LL} + \bar{u}_{WF} \tag{5}$$

Supercritical flows on chutes are characterized by high velocities and shallow flow depths. In these flows, turbulence is generated at the bed boundary and leads to free-surface roughness, deformation and breakup once turbulence overcomes the two stabilizing factors, i.e., gravity and surface tension (Brocchini and Peregrine, 2001). In the present experiments, an additional layer of constant velocity ($\bar{u}_{FS}$) was observed, which was superposed to Nikora's et al. (2013) velocity superposition model, describing the near-surface region of the water column where free-surface instabilities and waves were observed:

$$\bar{u}_{FS} = \begin{cases} \bar{u}_{UD} + (\bar{u}_i - \bar{u}_{UD})\left(1 + \tanh\frac{Y_1 - y_i}{L_e}\right) + \frac{u_{*c,LL}}{\kappa}\left(\ln\frac{Y_1 - y_i - d_i}{y_0} + 2\Pi\right) & \text{if } Y_1 < y < Y_{90} \\ \text{else } 0 \end{cases} \tag{6}$$

where Y_{90} is the characteristic bed-normal depth where $C = 0.90$. A conceptual drawing of the velocity superposition from the bed to the free-surface is shown in Figure 1, and the complete velocity profile is defined as:

$$\bar{u} = \bar{u}_{UD} + \bar{u}_{ML} + \bar{u}_{LL} + \bar{u}_{WF} + \bar{u}_{FS} \tag{7}$$

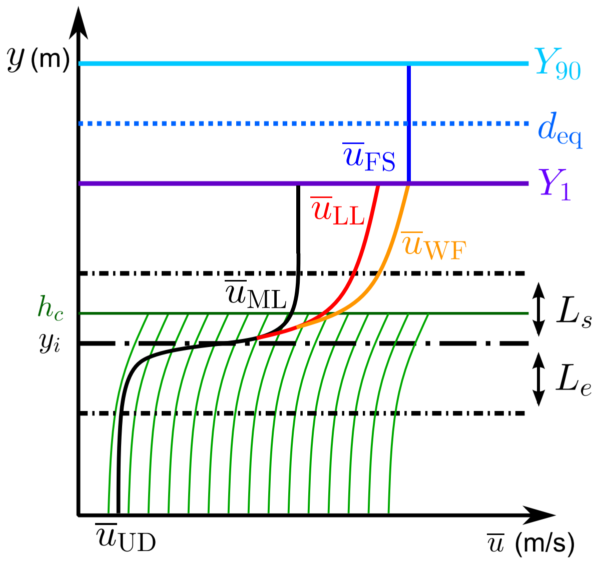

Figure 1 – Conceptual drawing of the velocity profile; additional parameters are the equivalent clear water depth (d_{eq}), the deflected grass height (h_c), the shear length scale of the mixing layer (L_s), and the mixing layer length scale (L_e)

2.2. Experimental facility and instrumentation

Experiments were performed in a laboratory chute at the UNSW Water Research Laboratory (WRL), which was 8 m long, 0.8 m wide and had a slope of 10.8 degrees. As shown in Figure 2a, the surface of the chute was equipped with a dense layer of artificial grass whose stems were uniformly attached to an underlying mesh. Herein, a specific flow rate of q = 0.188 m²/s was used, leading to a deflected grass height h_c = 20 mm. The flow rate was monitored with an ABB electromagnetic flow meter with uncertainty of $\pm$ 0.4%. The flow conditions corresponded to a Reynolds number $Re = q/\nu$ = 1.88 × 10⁵,a Froude number $Fr = \langle\bar{u}\rangle/(g\ d_{eq})^{1/2}$ 2.63 which was measured in the uniform flow region, i.e. at x = 7.5 m, with d_{eq} = 0.153 m being the equivalent clear water flow depth (Eq. 8). Note that parts of this dataset have been presented by Cui et al. (2020).

The flows just downstream of the weir crest were non-aerated and the free-surface was smooth, which was because surface tension was able to maintain the cohesion of the water phase (see Brocchini and Peregrine 2001). As the turbulence builds up, free-surface perturbations were observed at x = 2.1 m, leading to surface aeration at x = 3.8 m. In the non-aerated part of the spillway, the flow depth was measured with a pointer gauge, while a dual-tip conductivity probe was used to estimate air concentration distributions (C) in regions with surface aeration, enabling the computation of d_{eq}:

$$d_{\mathrm{eq}} = \int_{y=0}^{y=Y_{90}} (1 - C)\,\mathrm{d}y \tag{8}$$

(a) (b)

Figure 2 – (a) Experimental chute with dense coverage of grass; (b) WRL dual-tip conductivity probe

The region above Y_{90} is commonly classified as the spray region, consisting of ejected water droplets that do not contribute significantly to the flow, and are therefore disregarded in the calculation of d_{eq} (Wood, 1983; Felder and Chanson, 2013). Water velocities were measured with a Pitot tube at 8 cross-sections, starting 0.5 m downstream of the weir crest with an interval of 1 m. In the air-water surface region, the Pitot tube data were complemented with interfacial velocities measured with a phase-detection conductivity probe. Herein, the same dual-tip conductivity probe as in Felder and Chanson (2018) was deployed, having a streamwise distance between the leading and trailing tip of Δx = 8.104 mm (Figure 2b), while the transverse distance was 1 mm. The probe was made in-house at the WRL and the inner and outer electrodes had diameters of 0.125 mm and 0.5 mm, respectively. Based upon a sensitivity analysis of sampling parameters, the phase-detection signals were recorded at a sampling frequency of 40 kHz for a duration of 180 s at each elevation. The signal processing for extracting velocities followed Kramer et al. (2019, 2020).

3. RESULTS

3.1. Velocity profiles

Figure 3 shows the development of streamwise velocity distributions along the grassed spillway for $q =$ 0.188 m^2/s, comprising water velocities ($\bar{u}$) measured with the Pitot tube (hollow symbols) and interfacial velocities ($\bar{u}_{aw}$) measured with the dual-tip conductivity probe (solid symbols). The Pitot tube provided detailed velocity profiles in monophase flow regions, while the conductivity probe was able to measure the travel speed of surface deformations, waves and water droplets close to the free-surface, which had almost constant interfacial velocities (Figure 3). The velocity distributions evolved along the chute and approached uniform profiles towards the downstream end of the spillway. The equivalent clear water flow depth was calculated based upon the air-water flow data and the results are added in Figure 3, showing a small decline in d_{eq} towards the downstream end approaching uniform flow conditions. In the flow region where both instruments were able to measure velocities, the interfacial velocities agreed with the water velocities. Considering this close agreement, it can be assumed that $\bar{u}_{aw} \approx \bar{u}$.

The velocity profiles of three exemplary cross-sections at the end of the chute were compared against the model of Nikora et al. (2013) (Eq. 5) and the expanded model with the additional free-surface layer (Eq. 7) (Figure 4a). All velocities were normalized with the shear velocity at the channel bed u_* to highlight the universal agreement of the model with the velocity data. While the model of Nikora et al. (2013) fitted the experimental data well from the channel bed up to the wake region, the velocities deviated in the free-surface region (Figure 4a). In contrast, the expanded model (Eq. 7) fitted the experimental data well across the full flow column.

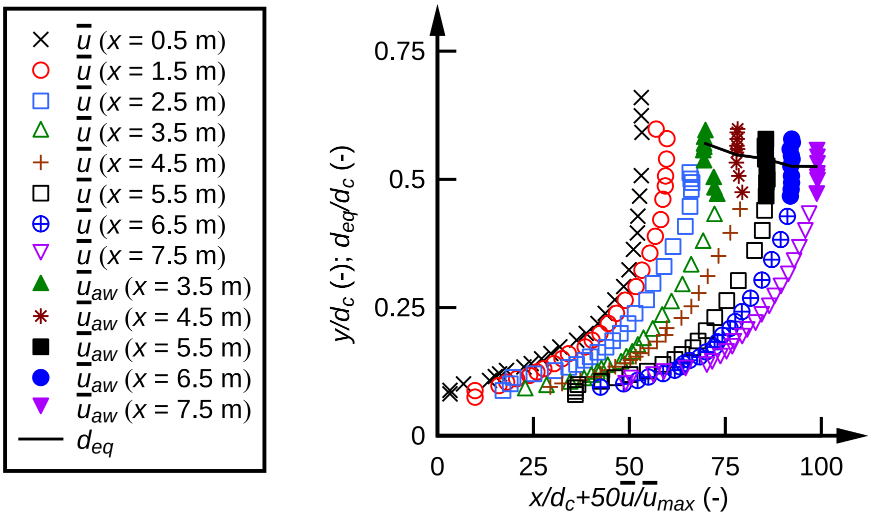

Figure 3 – Velocity profiles along the grassed spillway for q = 0.188 m²/s. Hollow symbols = Pitot tube data; solid symbols = dual-tip conductivity probe data

Figure 4b illustrates the corresponding dimensionless void fraction (C) and bubble count rate ($F/F_{\max}$) distributions, where $F_{\max}$ is the maximum bubble count rate in a cross section; both C and F were measured with the leading tip of the conductivity probe. Comparing the velocity data with the air-water flow properties shows that the presence of air-water interfaces in the form of entrapped air, free-surface roughness and waves in the upper part of the flows is represented by the constant interfacial velocity component (Eq. 6). The expanded model (Eq. 7) accounts for the air-water flow interactions and it is believed that this model is also applicable to grass-lined spillway flows with stronger aeration.

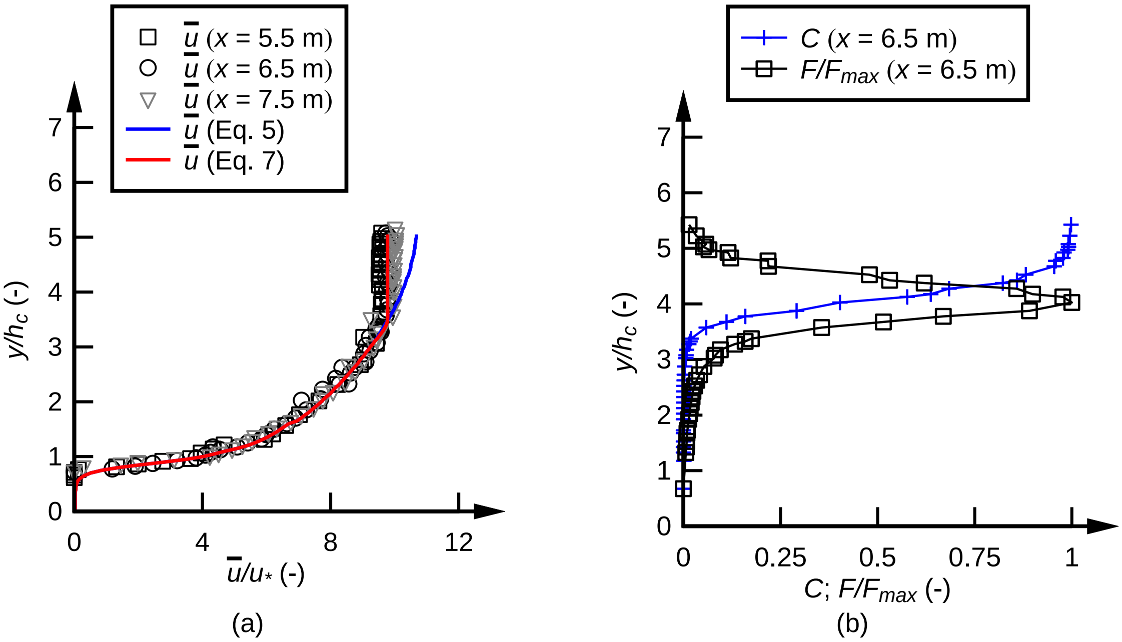

Figure 4 – (a) Comparison of supercritical velocity data at the downstream end with the model of Nikora et al. (2013) (Eq. 5) and the expanded model (Eq. 7) for q = 0.188 m²/st; (b) Corresponding void fraction (C) and bubble count rate (F) distributions.

3.2. Shear velocity

The shear velocity is commonly used to represent the bed shear stress of a flow, indicating the flow resistance. It has the same units as a velocity and is therefore often used for the normalization of velocity distributions (Figure 4a). The shear stress can be obtained by fitting the log law to the velocity profile which was conducted for the velocity distributions in the present study. The velocity profiles in the mixing and log layers agreed well with the model of Nikora et al. (2013) (Figure 4a). Using the dimensionless expression of u^+ and y^+, the measured velocities above $(y_i + d_i + y_0)$ and below the upper limit $((d - y_i - d_i) * 0.3 + y_i + d_i)$ were fitted to the log-law (Eq. 3), providing the shear velocities at the canopy top $u_{*,LL}$ (the subscript LL stands for log-law). The shear velocities at the canopy top ranged between 0.30 m/s $< u_{*c,LL} <$ 0.35 m/s, which was comparable to a micro-rough spillway with assorted grains (Severi, 2018).

Towards the downstream end of the spillway, the shear velocity from log law fitting ($u_{*c,LL}$) was compared with the shear velocity u_{*c}, derived from the channel slope assuming uniform flow conditions:

$$u_{*c} = \sqrt{\tau/\rho} = \sqrt{gS_0(d_{\text{eq}} - h_c)} \tag{10}$$

where τ is the shear stress at the canopy top and ρ is the density of water. Figure 5b shows this comparison, indicating good agreement between the two shear velocity estimates. Therefore, it appears that the log law fitting can be applied to grass-lined spillways. Future research must test if this is also valid for a wider range of flow conditions and for more strongly aerated flows on vegetated spillways.

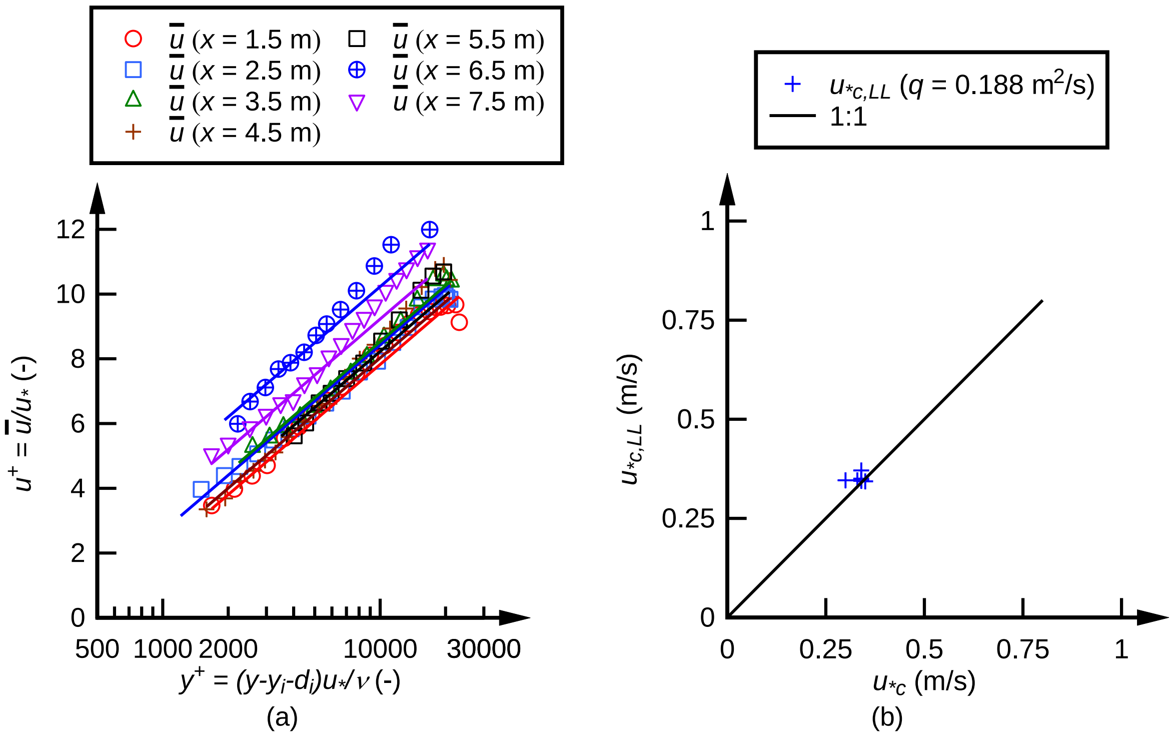

Figure 5 – (a) Comparison of the velocity data with the log law; (b) Comparison of shear velocities extracted from the log layer fitting $u_{*,LL}$ with shear velocities u_{*c} calculated with Eq. (10).

4. DISCUSSION: MIXING LAYER LENGTH SCALE

The mixing layer represents the coflowing zone of inside- and outside-canopy flows which generate vortex motions as Kelvin-Helmholtz waves (Raupach et al., 1996). It depicts an inflectional velocity profile featuring the transition between the uniform velocity profile (inside-canopy) to the log law velocity profile (outside-canopy). The mixing layer of a grassed channel was modeled with a hyperbolic function

(Eq. 2) by Nikora et al. (2013), where the mixing layer velocity becomes constant at $y > y_i + L_s$ (Figure 1). L_s is defined as the shear length scale of the mixing layer (Raupach et al., 1996; Nikora et al., 2013), indicating the region where the inflectional mixing layer applies (Figure 1). According to Raupach et al. (1996) and Nikora et al. (2013), the shear length scale of the mixing layer can be determined via:

$$L_s = \bar{u}_i / \left(\frac{\Delta \bar{u}}{\Delta y}\right)_{y_i} \tag{11}$$

Computed by a forward differences method, the shear length scale of the mixing layer L_s reflects the above-canopy section of the canopy-scale vortices (Figure 1). Whereas the mixing layer length scale L_e in Eq. (2) resembles the penetration of canopy-scale vortices into the grass canopy (Ghisalberti and Nepf, 2002). Under the assumptions that (i) the inflection point is in the middle of the mixing layer, and (ii) that the uniform velocity $\bar{u}_{UD}$ is much smaller than $\bar{u}_i$, both length scales should be identical, implying that the thickness of the mixing layer is $\delta_m = L_e + L_s = 2 * L_e = 2 * L_s$ (Raupach et al., 1996; Nikora et al. (2013)).

Herein, the velocities measured with the Pitot tube were used to calculate L_e and L_s applying Eqns. (2) and (11) respectively, and the calculated values are compared in Figure 6. Previous data of L_e and L_s of Nikora et al. (2013) for subcritical flows were added as well as the suggested relationship between L_e and L_s (Nikora et al., 2013) (Figure 6). The present length scales compared similarly to the observations of Nikora et al. (2013) (Figure 6). The close agreement between L_e and L_s confirms the statement from Raupach et al. (1996) and Nikora et al. (2013) that the shear length scale of mixing layer is also representative of the mixing layer thickness and the equivalency of L_e and L_s in the current configuration. The present supercritical flows were much shallower compared to subcritical flow conditions. Irrespective of this, the close agreement between sub- and supercritical flow observations of L_e and L_s extended the mixing layer concept to high-velocity flows on grassed spillways.

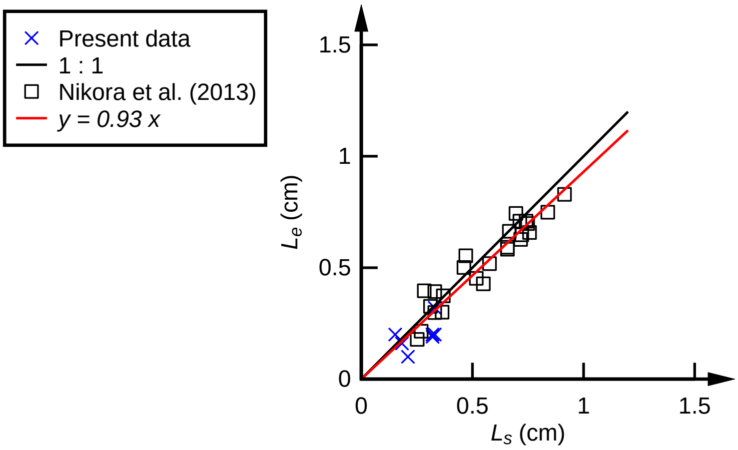

Figure 6 – Comparison of mixing layer length scales L_e (Eq. 2) and shear length scale of mixing layer L_s (Eq. 11) of the present study together with previous results from Nikora et al. (2013).

5. CONCLUSION

Detailed experiments of flows down a grass-lined spillway were conducted, providing new insights into the velocity distributions and shear velocities. The velocity profiles were obtained through measurements with a Pitot tube and a dual-tip conductivity probe, comprising a data set of both non-aerated flows close to the channel bed and aerated flows close to the free-surface. Both velocity measurement methods complemented each other and provided reliable velocity profiles across the full flow column. The present data were compared with the predicted velocity profile by Nikora et al. (2013). While the present data were well fitted from the bed to the wake layer, the model was expanded to the free-surface region characterized by free-surface roughness, entrained air and free-surface waves. Fitting the velocity profile to the log law provided the shear velocity estimate for grass-lined spillways, which was similar to spillway flows with a micro-rough bed. The mixing layer length scale was compared with the shear length scale indicating close agreement of the two in supercritical flows. Overall, the present study provided novel insights into the flow resistance of grassed spillways through a detailed assessment of velocity distributions, which will be expanded to a wider range of flow conditions including real vegetation in future research.

6. ACKNOWLEDGMENTS

The authors would like to thank Rob Jenkins and Larry Paice (WRL, UNSW Sydney) for their technical assistance.

REFERENCES

Brocchini, M., Peregrine D.H. (2001). The dynamics of strong turbulence at free surfaces. Part 1. Description. Journal of Fluid Mechanics, 449, 225-254.

Chen, S.C., Kuo, Y.M., Yen, H.C. (2012). Effect of submerged flexible vegetation and solid structure bars on channel bed scour. International Journal of Sediment Research, 27, 323–336.

Crosato, A., Saleh, M.S. (2011). Numerical study on the effects of floodplain vegetation on river planform style. Earth Surface Processes and Landforms, 36, 711-720.

Cui, H., Kramer, M., Felder, S. (2020). Velocity profiles on a grass-lined spillway in supercritical flow, Proc. 1st IAHR YPN Congress 2020, Spain Water and IWHR, China.

Felder, S., Chanson, H. (2013). Aeration, flow instabilities, and residual energy on pooled stepped spillways of embankment dams. Journal of Irrigation and Drainage Engineering, 139, 880–887.

Felder, S., Chanson, H. (2018). Air–water flow patterns of hydraulic jumps on uniform beds macroroughness. Journal of Hydraulic Engineering, 144(3), 04017068.

Ghisalberti, M., Nepf, H. M. (2002). Mixing layers and coherent structures in vegetated aquatic flows. Journal of Geophysical Research, 107(C2).

Guillén-Ludeña, S., Lopez, D., Mignot, E., Riviere, N. (2020). Flow resistance for a varying density of obstacles on smooth and rough beds. Journal of Hydraulic Engineering, 146(2), 4019059.

Kramer, M., Valero, D., Chanson, H., Bung, D.B. (2019). Towards reliable turbulence estimations with phase-detection probes: an adaptive window cross-correlation technique. Experiments in Fluids, 60(2).

Kramer, M., Hohermuth, B., Valero, D., Felder, S. (2020). Best practices for velocity estimations in highly aerated flows with dual-tip phase-detection probes, International Journal of Multiphase Flow, 126, 103228.

Monin, A.S., Yaglom, A.M. (1975). Statistical Fluid Mechanics: Mechanics of Turbulence. Volume 1. MIT Press, Boston.

Mossa, M., Ben Meftah, M., De Serio, F., Nepf, H.M. (2017). How vegetation in flows modifies the turbulent mixing and spreading of jets. Nature Scientific Reports, 7, 1–14.

Nepf, H.M. (2012). Flow and transport in regions with aquatic vegetation. Annual Review of Fluid Mechanics 44, 123–142.

Nikora, V., Koll, K., McEwan, I., McLean, S., Dittrich, A. (2004). Velocity distribution in the roughness layer of rough-bed flows. Journal of Hydraulic Engineering, 130, 1036–1042.

Nikora, N., Nikora, V., O'Donoghue, T. (2013). Velocity profiles in vegetated open-channel flows: combined effects of multiple mechanisms. Journal of Hydraulic Engineering, 139(10), 1021–1032.

Ralston, D.C., Brevard, J.A. (1988). Design and performance of earth spillways, Proc. The ASCE Hydraulics Division, Special Conference, 871–876.

Raupach, M., Finnigan, J., Brunei, Y. (1996). Coherent eddies and turbulence in vegetation canopies: The mixing-layer analogy. Boundary-Layer Meteorology, 78, 351–382.

Severi, A. (2018). Aeration Performance and Flow Resistance in High-Velocity Flows over Moderately Sloped Spillways with micro-rough bed. Ph.D. Thesis, School of Civil and Environmental Engineering, UNSW Sydney, Australia.

Scheres, B., Schuettrumpf, H., Felder, S. (2020). Flow resistance and energy dissipation in supercritical air-water flows down vegetated chutes. Water Resources Research, 56, 1–18.

Tinoco, R.O., San Juan, J.E., Mullarney, J.C. (2020). Simplification bias: lessons from laboratory and field experiments on flow through aquatic vegetation. Earth Surface Processes and Landforms, 45, 121–143.

Valero, D., Bung, D.B. (2018). Reformulating self-aeration in hydraulic structures: turbulent growth of free surface perturbations leading to air entrainment. International Journal of Multiphase Flow, 100, 127–142.

Van Hemert, H., Igigabel, M., Pohl, R., Sharp, M., Simm, J., Tourment, R., Wallis, M. (2013). The International Levee Handbook. Ciria C731.

Wilcock, R.J., Champion, P.D., Nagels, J.W., Croker, G.F. (1999). The influence of aquatic macrophytes on the hydraulic and physico-chemical properties of a New Zealand lowland stream. Hydrobiologia, 416, 203–214.

Wilhelms, S.C., Gulliver, J.S. (2005). Bubbles and waves description of self-aerated spillway flow. Journal of Hydraulic Research, 43(5), 522–531.

Wood, I.R. (1983). Uniform region of self-aerated flow. Journal of Hydraulic Engineering, 109(3), 447-461.

Wood, I.R., Ackers, P., Loveless, J. (1983). General method for critical point on spillways. Journal of Hydraulic Engineering, 109, 308–312.

8th International Junior Researcher and Engineer Workshop on Hydraulic Structures
ISBN: 978-0-578-37416-1
https://doi.org/10.26077/d58d-6bcc

Galway, Ireland,
5th - 8th June 2021

Numerical Simulation of Fish Passage Over a Weir

L. Kaminski[1], C. Thorenz[1] and R. Weichert[1]
[1]Federal Waterways Engineering and Research Institute
76187 Karlsruhe
GERMANY
E-mail: linus.kaminski@baw.de

Abstract: *Downstream migration over weir structures has been a mostly neglected element of ecological continuity in the last decades. The guidelines currently applied in Germany to prevent damage to fish do not sufficiently consider the conditions present at weirs. To improve knowledge of the risks of fish passage over a weir due to physical strike, pressure changes and shear stress, a numerical method using the three-dimensional computational fluid dynamics package OpenFOAM® was developed to simulate fish passage over a weir by tracking passively transported particles. In this study, the method is tested on an overshot and an undershot weir and the results are compared to known critical parameters to assess the hazard potential of these weirs. As expected, pressure changes are much more relevant in the undershot scenario, physical strike and shear stress are dominant in the overshot scenario. Altogether both situations result in only collisions with low impact velocities and relatively low shear stress and pressure changes, assuming little threat to fish due to the relatively low drop height and absence of baffle blocks or an end sill. To improve the methods reliability, additional enhancements are necessary.*

Keywords: *numerical modelling, OpenFOAM, weir, fish, migration*

1. INTRODUCTION

By implementing the European Water Framework Directive in 2000 the member states of the European Union have set the good ecological status of surface water bodies as an objective. To achieve this goal, one important measure is to establish ecological continuity by providing adequate fishways at barrages for upstream and downstream migration. Whereas upstream migration as well as downstream migration through turbines or over spillways has been a focus of research in the last decades, downstream migration over weirs with low and medium heads (approx. 5 m) has been mostly neglected.

To prevent significant effect on fish, a German guideline (DWA 2005) recommends, that the plunge pool depth should be equal to a quarter of the drop height but at least 0,9 m and the impact velocity should not exceed 13 m/s. These currently applied design criteria refer to uncited design guidelines mentioned in Odeh and Orvis (1998), lack advanced scientific proof and can only be understood as documented recommendations by experts. Thorenz et al. (2018) showed that the currently applied guidelines aren't sufficient to judge on the safety of fish passage in many cases. Using the three-dimensional simulation package OpenFOAM® they modelled a weir passage adhering and not adhering to the DWA guidelines. As it can be seen in Figure 1, in some situations the far-field tailwater level has a negligible effect due to its displacement by the nappe. According to the DWA guideline, the situation on the right is acceptable, the far-field tailwater level is sufficient, the situation on the left is not acceptable. In this case, adhering to the DWAs tailwater guideline has only a marginal effect, whereas the thickness of the nappe seems to be of much more importance (Thorenz et al. 2018).

With several weir structures in federal waterways that need to be replaced in the near future, a thorough assessment of downstream fish passage over weir structures is needed (Thorenz et al. 2018). To evaluate the risk for migratory fish, a method has been developed to model the downstream passage for different weir structures by tracking passively transported particles in 3D-CFD simulations. By tracking the particles path, collisions, surrounding pressure and shear forces the risk of injury for different weir structures is estimated.

In this paper sources of risk for fish during downstream passage over a weir and threshold values for fish injuries from literature are discussed and compared with first results of the described 3D-CFD method for an exemplary weir.

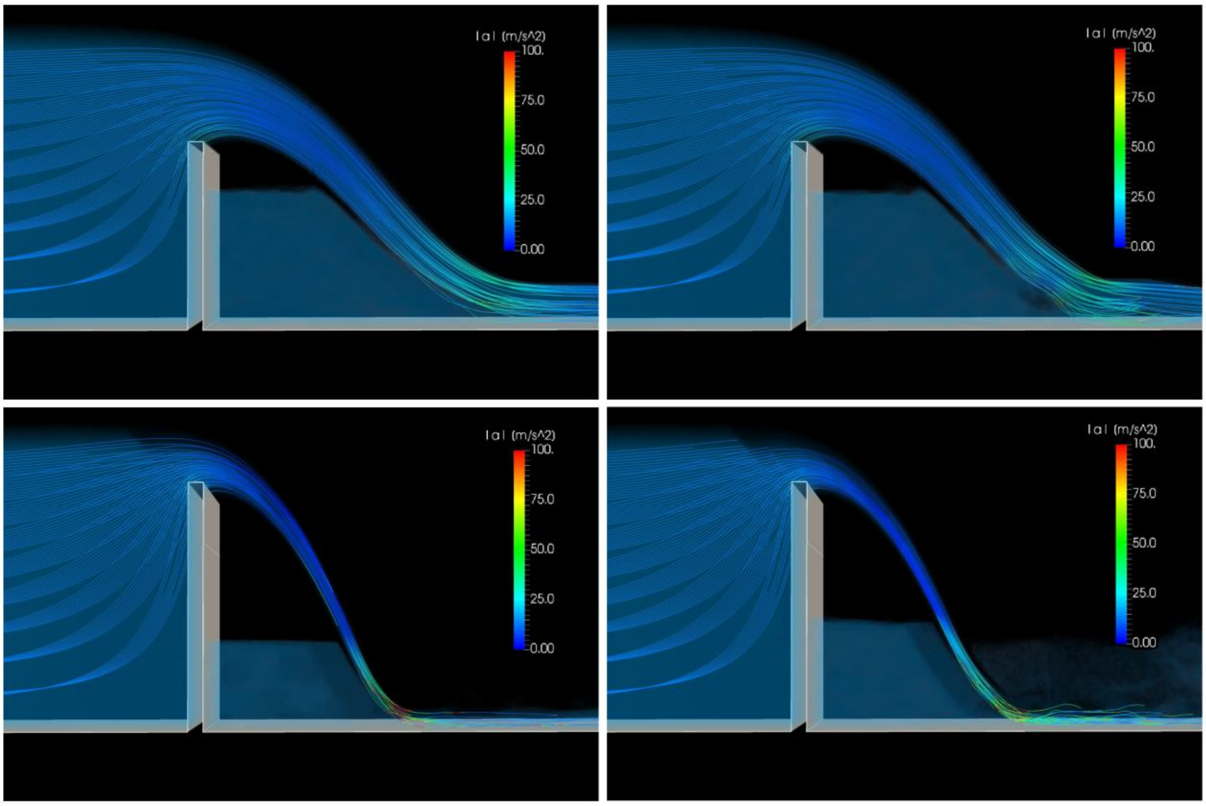

Figure 1 – Comparison of different weir heights and tailwater levels. Convective acceleration plotted in streamtubes for weir heights of 3 m (top figures) and 4 m (bottom figures) and different far-field tailwater levels of 0 m (left figures) and 2 m (right figures) over the weir sill (Thorenz et al. 2018).

2. HYDRAULIC STRESSORS DURING DOWNSTREAM PASSAGE

Fish moving downstream over or under a weir structure can be exposed to a variety of stressors. Studies on downstream migration of fish have found three major sources of injury and mortality that are most relevant for the majority of low-head weirs. These are rapid pressure changes, physical strike and excessive shear stress. In certain situations, other stressors can also have substantial impact on fish like gas supersaturation or higher vulnerability to predation due to disorientation, often a complex series of interacting stressors can facilitate injuries which makes it hard to isolate the impact of a single hydraulic characteristic. (Baumgartner et al. 2014)

2.1. Physical strike

Especially at low-head weirs, physical strike can be the most severe stressor (Pflugrath et al. 2019). Physical strike occurs when a fish collides with an object such as a baffle block, stilling basin end sill, flow splitter or other hard structure, but also with the water surface when the fish is not embedded in the nappe. The probability of sustaining an injury depends on many factors. Generally, the chance of contact with an object is higher if the fish loses mobility control due to high velocities and turbulence. When a physical strike occurs factors like the impact velocity but also the objects shape, material or the condition of the surface influences the likelihood of injury or mortality. Sharp edges and rough surfaces lead to a higher hazard potential.

Physical strike is generally associated with both overshot and undershot weirs. The weir design, but also how it is operated, plays a role regarding its danger for fish. Situations that lead to injuries are for example discharge into low tailwater environments or high velocity and turbulence in the stilling basin (Baumgartner et al. 2013).

For the downstream passage through hydropower turbines, blade strike injuries have been studied extensively. The strike chance depends on several factors like blade rotation speed, fish length and blade spacing, which makes it possible to use mathematical modelling to predict the probability of strike (Deng et al. 2007). In contrast to fish passage through hydropower turbines, few data on injuries or mortality due to physical strike during the passage over or under low-head weirs is available. In the formerly mentioned DWA guideline (2005), an impact velocity of 13 m/s on a water surface is associated with small fish damage. Other threshold values are listed in the following Table 1.

Regarding impact velocities it is import to mention free fall acceleration. Depending on their size varying heights are necessary to reach critical velocities falling through air, small fish of around 10 cm - 15 cm have a terminal velocity of less than 15 m/s free falling through air, even smaller fish might not reach critical speed at all (Schwevers and Adam 2020).

Altogether, knowledge regarding injury or mortality of physical strike during downstream passage is inadequate especially if considered that the effect on fish depends on not only the impact velocity but also many additional factors as previously stated.

Table 1 – Effect on fish for collision with water or solid objects for different velocities from literature.

Collision with	Velocity [m/s]	Effect on fish	Reference
Water surface	13	Small damage	(DWA 2005)
Water surface	15	3 % mortality	(Odeh and Orvis 1998)
Water surface	20	0 % mortality	(USACE 1991)
Water surface	28	35 % mortality	(USACE 1991)
Water surface	45	100 % mortality	(USACE 1991)
Water surface	15-16	Critical value	(Schwevers and Adam 2020)
Solid object	5	0 % mortality	(USACE 1991)
Solid object	18	60 % mortality	(USACE 1991)
Solid object	26	90 % mortality	(USACE 1991)
Solid object embedded in water	11	Critical value	(Schwevers and Adam 2020)

2.2. Shear stress

Shear stress occurs when two water masses of different velocities intersect or are adjacent to each other. Due to the viscosity of water, an object caught between two intersecting masses experiences a force, depending on the objects size and the water velocity and mass. Throughout the world, shear stress naturally occurs in rivers and streams. Fish are adapted to it even partially rely on it to move and prevent displacement (Cada et al. 1999). Only when shear stress exceeds tolerable levels, it becomes a substantial problem for fish (Guensch et al. 2002).

High shear levels occur at hydroelectric turbines, spillways, fish bypass systems or downstream of undershot weirs but also in natural environments like waterfalls or rapids. Due to the natural occurrence, some fish are well adapted to shear stress, other species who avoid fast flowing water are not. But the threshold fish can withstand does not only differ among species but also within species. Fish size also plays a role and some life stages, especially fish eggs, are particularly sensitive to shear stress. A fish could therefore have different thresholds for shear stress over its life, which makes it difficult to evaluate the impact over a range of species and sizes (Baumgartner et al. 2013). Another factor concerning fish tolerance to shear stress is the fish’s orientation (Neitzel et al. 2000).

Areas with high shear stress are characterized by intersecting water bodies with high velocities. At weirs high shear forces can be expected for instance downstream of undershot weirs, especially close to the gate. Generally, high shear stress often occurs in small locally constrained areas. Susceptibility to injury for downstream migrants would be largely determined by the proximity of passage to these critical areas (Baumgartner et al. 2013). Therefore, it is important to not only know the general occurrence of shear stress near weir structures but also the fish’s path.

As previously stated, tolerance to shear stress highly differs among and within fish species. For some sizes and species experiments with shear stress created by jets have been performed. The results of some of these studies have been summarized in the following table 2. Knowledge of tolerance to shear stress of European freshwater fish is still low.

Table 2 – Observed effect of shear stress on fish, based on a spatial resolution of Δy = 1.8 cm.

Species, life stage	**Strain rate [m/(s*m)]**	**Effect on fish**	**Reference**
Oncorhynchus mykiss, juvenile	517	No signif. injuries	(Neitzel et al. 2000)
Alosa sapidissima, juvenile	688	No signif. injuries	(Neitzel et al. 2000)
Balantiocheilos melanopterus	600	Threshold mortality	(Thorncraft et al. 2013)
Balantiocheilos melanopterus	1200	20 % mortality	(Thorncraft et al. 2013)
Oncorhynchus tshawytscha, juvenile	677	10 % injury	(Deng et al. 2005)
Oncorhynchus tshawytscha, juvenile	933	10 % mortality	(Deng et al. 2005)
Bidyanus bidyanus, egg	148	100 % mortality	(Navarro et al. 2019)
Bidyanus bidyanus, larva	600	No signif. injuries	(Navarro et al. 2019)
Trichopodus trichopterus, adult	688	> 50 % injury	(Colotelo et al. 2018)
Pangasionodon hypophtalmus, juv.	1008	> 50 % injury	(Colotelo et al. 2018)

2.3. Pressure changes

The most important factors concerning pressure change is the structure height and operation mode (overshot or undershot). Because fish usually acclimate to their surrounding pressure and pressure linearly increases with depth, undershot weirs with large heights pose great risks for fish. During downstream passage through an undershot weir, the pressure changes rapidly from high pressure due to deep water to low pressure after the weir passage. Due to high velocity the static pressure can even fall under the atmospheric pressure, in extreme cases even below the vapor pressure, leading to cavitation which can pose another risk for fish. Fish exposed to a rapid pressure change may experience barotrauma which is caused by the rapid and unregulated expansion of gas and fluid filled structures within the fish. In extreme cases of barotrauma fatal injuries like swim bladder rupture or hemorrhaging can occur. (Baumgartner et al. 2013)

Pressure changes are commonly given in the ratio of pressure change (RPC). The RPC is the change of pressure that a fish experiences between the pressure it is acclimated to (neutrally buoyant) before passage, and the lowest pressure it is exposed to during weir passage (Boys et al. 2014). As for the other stressors, knowledge of effects of pressure changes in general and especially on European freshwater fish is still low. To minimize these shortcomings and give recommendations for species that were not studied yet, Boys et. al (2016a) followed a precautionary principle. Table 3 shows their multispecies recommendation of an RPC of 0.7 and other literature values.

Table 3 – Observed effect of rapid pressure change on fish given in the ratio of pressure change RPC. No effect on eggs at any RPC was found.

Species, life stage	**RPC [-]**	**Effect on fish**	**Reference**
Maccullochella peelii, egg	-	No effect on eggs	(Boys et al. 2014)
Maccullochella peelii, larva	0.4	No injury	(Boys et al. 2014)
Maccullochella peelii, juvenile	0.6	No injury	(Boys et al. 2014)
Oncorhynchus tshawytscha, juvenile	0.5	6 % mortality	(Carlson et al. 2010)
Bidyanus bidyanus, egg	-	No effect on eggs	(Boys et al. 2016b)
Bidyanus bidyanus, larva	0.4	No injury	(Boys et al. 2016b)
Multispecies precautionary principle	0.7	No injury	(Boys et al. 2016a)
Most fish species and life stages	0.6	No injury	(Cada and Charles 1997)

Not all fish are in the same way susceptible to pressure change. Bony fish (teleosts) can be largely divided into physostomes and physoclists (Schreer et al. 2009). Physostomes have a pneumatic duct connecting the swim bladder and the intestinal tract. They can actively vent excessive swim bladder gas and therefore quickly adapt to pressure changes. Adult physoclists do not have this pneumatic duct and consequently lack the ability to rapidly adapt to pressure changes (Baumgartner et al. 2013). Therefore, physoclists like the European perch (perca fluviatilis) are much more susceptible to pressure changes than physostomes like the Antlantic salmon (Salmo salar). Fish’s tolerance to pressure changes also differs between life stages. Eggs are not affected by pressure changes and also the larvae of many fish are much more tolerant because they have not actively filled their swim bladder yet (Boys et al. 2014).

3. NUMERICAL SIMULATION

To get a better understanding of the hazard potential for downstream migrating fish and evaluate if and where fish are exposed to the described potentially harmful situations, numerical models were used to simulate the fish's passage over a weir. The simulations were performed with the three-dimensional simulation package OpenFOAM®, using the two-phase solver interFoam (Weller et al. 1998). In the model, fishes were replaced by particles, which represent passively transported fish. These are calculated in a Langrangian approach. To achieve this, the particle phase basicKinematicParticle was added to the interFoam solver. The extended Eulerian/Lagrangian-solver models the fluids as continuous phases while the positions of particles, which represent passively transported fish, are calculated discretely. As the volume fraction of the solid material "fish" of up to 10^{-4} is rather small and as the fish have the same density as the surrounding water, not a two-way coupling, but a one-way coupling mechanism was chosen. This means that the flow of the carrier fluid influences the particle trajectories but the particles have no effect on the carrier fluid (Greifzu et al. 2016). Using a one-way coupling mechanism and also ignoring collisions between particles creates a situation where every particle can be examined autonomously, without being influenced by other particles.

Two different scenarios were simulated, an overshot and an undershot situation at the same radial gate with an additional flap gate. Both numerical models had a width of 4 m and a length of 40 m. The computational grids had approximately 11 million cells and 8 million cells respectively and was iteratively refined around the gate and in the vicinity of the nappe from a base cell edge length of 20 cm down to 2.5 cm. The cell size was determined by previous independence studies and the particle size. The particle diameter had to be substantially smaller than the cells. The downstream boundary conditions were defined as outlet with fixed water level at 1.7 m while the upstream boundary conditions were defined as inlet with constant inflow and free water level. A water level of approximately 5.4 m was achieved by a flow rate of 7.2 m³/s and 11.6 m³/s respectively. In the overshot scenario 784 and in the undershot scenario 948 spherical particles with a diameter of 1 cm and a density of 1000 kg/m³ were added. The initial situation of the simulations is depicted in Figure 2. The particles are added without any velocity in an area with a surrounding water velocity between 1.2 m/s and 3.5 m/s, the typical top speed of European freshwater fish with a length between 10 cm and 30 cm (Ebel 2014). After the addition, the particles quickly adapt to the surrounding velocity, simulating a passively drifting fish. These simulations were used to evaluate the hazard potential of this weir on fish during downstream passage due to physical strike, pressure changes and shear stress.

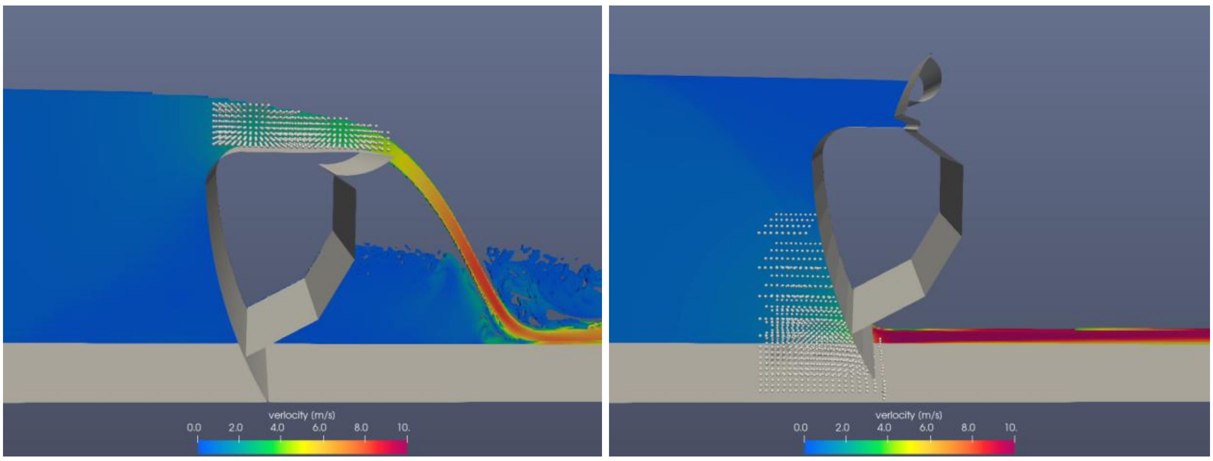

Figure 2 – Initial situation of the overshot scenario (left) with particles over the weir and the undershot scenario with particles in front of the outlet. The fluid velocity is plotted on a vertical slice in the background.

3.1. Physical Strike

The utilized method is able to detect collisions of particles with selected patches. In addition to the impacts time, also the particles velocity and the location of the collision is tracked. However, it currently was not possible to assign collisions to a certain particle due to limitations in the postprocessing procedure. Explicit identification was not possible due to the used parallel computation, which works on decomposed computational grids. This leads to particles with the same identification number in the different decomposed domain areas. Therefore, it was not possible to track which particle was responsible for a collision and consequently multiple collisions by a single particle could not be detected properly. This skews the average number of collisions by particle because an overwhelming amount of collisions go back to a few particles that got dragged along the river bed. But because of the low impact velocity, these collisions are mostly negligible.

In the undershot scenario a total number of 796 collisions were detected, in the overshot scenario 2448. Figure 3 shows the collisions divided according to impact velocity. Whereas all impact velocities at the undershot scenario are below 3 m/s, at the overshot scenario the highest impact velocity is at 7.5 m/s.

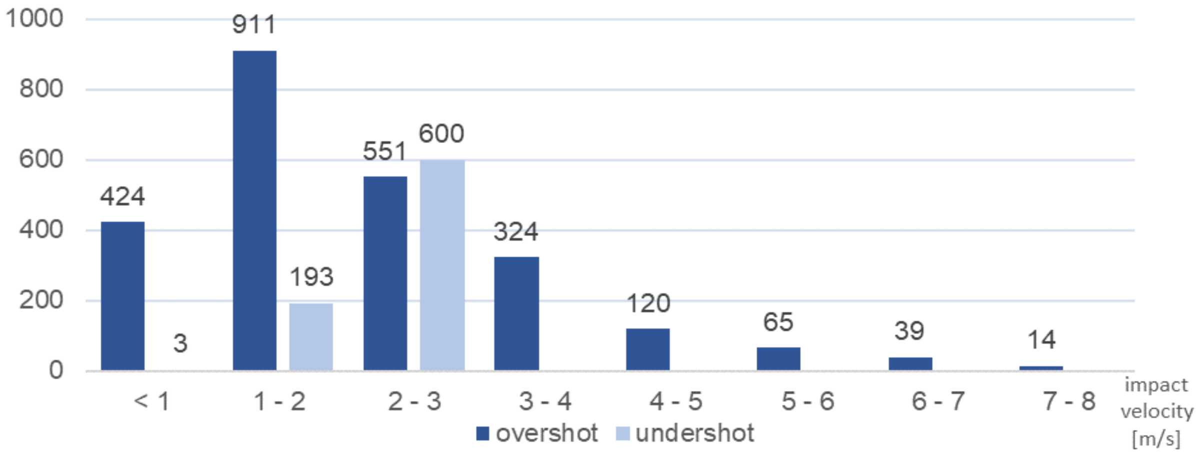

Figure 3 – The numbers of collisions for both the overshot and the undershot scenario divided according to impact velocity.

3.2. Shear stress

To evaluate if shear stress is a hazard potential in the observed situations it was analysed if potential harmful areas exist in the undershot or overshot scenario. To detect shear stress, the velocity in all cells in areas with potentially high velocity gradients was tracked and the velocity difference between adjacent cells calculated. Because of the cell edge length of 2.5 cm, the calculated shear stress is based on a spatial resolution of Δy = 2.5 cm. The highest detected shear stress in the undershot scenario was 154 m/(m*s). To allow comparison with laboratory trials which used a spatial resolution of Δy = 1.8 cm, the same change of velocity over a distance of only 1.8 cm would give a shear rate of 214 m/(m*s). Again, the hazard potential seems to be higher at the overshot scenario with shear stress of up to 232 m/(m*s) or 322 m/(m*s) based on a theoretical spatial resolution of Δy = 1.8 cm. In laboratory trials with fish that seem to be susceptible to shear stress, the lowest values that injured fish have been found to be at 339 m/(m*s) for the blue gourami (Trichopodus trichopterus, Colotelo et al. 2018) and 444 m/(m*s) for the silver shark (Balantiocheilos melanopterus, Thorncraft et al. 2013). Some minor injuries to very susceptible fish species might be possible here, but significant impairment seems unlikely.

3.3. Pressure changes

Tracking the pressure of every single particle was not feasible at this stage. To evaluate the danger of sudden pressure changes on fish, selected particles where tracked. Due to the greater depth, the particles in the undershot scenario are subjected to a higher pressure which decreases rapidly when passing under the gate. The particles in the overshot scenario, on the other hand, are subjected to a

much lower starting pressure.
Relevant to evaluate the danger of pressure changes is the ratio between the starting pressure, which a fish would be acclimated to, and the lowest pressure during the downstream passage, given in the RPC. As expected, the RPCs of the overshot scenario seem unproblematic with the lowest being 0.84 (95% CI: 0.85 – 0.87). During the undershot situation, the pressure change is much higher and therefore the RPCs smaller, with the smallest detected RPC of 0.67 (95% CI: 0.68 – 0.70). Also in this situation, severe injuries seem unlikely with Cada and Charles (1997) seeing a RPC of 0.6 as unproblematic for most fish species and life stages and Boys (2016a), applying a multispecies precautionary principle, considering a RPC of 0.7 as safe for fish.

4. CONCLUSION

Summarized, both the overshot and the undershot scenario seem unlikely to have significant impact on fish due to physical strike, high shear stress or rapid pressure changes. Further information on tolerable levels of these stressors are necessary to improve reliability. As expected, the undershot scenarios most relevant stressor is the change of pressure, unlike the overshot scenario, in which elevated shear levels and collisions with higher impact velocities pose the greatest threat.

The method of tracking particles in a numerical simulation has proven to be promising to evaluate the potential hazards on fish during downstream passage over a weir. Consequences of using small particles to simulate passively transported fish need to be evaluated to further improve this methods reliability, as well as additional enhancements to the method itself. To calculate a particles probability of collision and not only the average number of collisions per particle, it is necessary to detect multiple collisions by a single particle and to track each particles collisions during the weir passage. In this case, evaluating the highest shear values present was sufficient. Even those were not high enough to pose significant threat. In other cases, with higher shear levels, it is necessary to track if and how many particles come in contact with these dangerous shear stress areas. Tracking the pressure changes worked fine, to improve the results conclusiveness, the utilized method has to be performant enough to track each individual particle and not only a few selected ones. Integrating those improvements can make this method a valuable tool to evaluate weir passage hazards.

5. REFERENCES

Baumgartner, Lee; McPherson, Bronson; Doyle, Jonathon; Cory, Frances; Cinotti, Nestor; Hutchison, Jamie (2013): *Quantifying and mitigating the impacts of weirs on downstream passage of native fish in the Murray-Darling Basin*. In Fisheries Final Report Series (Nr. 136).

Baumgartner, Lee J.; Daniel Deng, Z.; Thorncraft, Garry; Boys, Craig A.; Brown, Richard S.; Singhanouvong, Douangkham; Phonekhampeng, Oudom (2014): *Perspective towards environmentally acceptable criteria for downstream fish passage through mini hydro and irrigation infrastructure in the Lower Mekong River Basin*. In Journal of Renewable and Sustainable Energy 6

Boys, C. A.; Robinson, W.; Miller, B.; Pflugrath, B.; Baumgartner, L. J.; Navarro, A. et al. (2016a): *A piecewise regression approach for determining biologically relevant hydraulic thresholds for the protection of fishes at river infrastructure*. In Journal of fish biology 88 (5), pp. 1677–1692.

Boys, Craig; Navarro, Anna; Robinson, Wayne; Fowler, Anthony; Chilcott, Stephen; Pflugrath, Brett et al. (2014): *Downstream fish passage criteria for hydropower and irrigation infrastructure in the Murray–Darling Basin*. In Fisheries Final Report Series (Nr. 141).

Boys, Craig A.; Robinson, Wayne; Miller, Brett; Pflugrath, Brett; Baumgartner, Lee J.; Navarro, Anna et al. (2016b): *How low can they go when going with the flow? Tolerance of egg and larval fishes to rapid decompression*. In Biology open 5 (6), pp. 786–793.

Cada, Glenn; Carlson, Thomas; Ferguson, John; Richmond, Marshall; Sale, Michael (1999): *Exploring the Role of Shear Stress and Severe Turbulence in Downstream Fish Passage*. In Peggy A. Brookshier (Ed.): Hydro's future. Technology markets and policy. Waterpower Conference 1999. Las Vegas, Nevada, United States.

Cada, Glenn; Charles, Coutant (1997): *Development of Biological Criteria for the Design of Advanced Hydropower Turbines*. Oak Ridge National Laboratory. U. S. Department of Energy. Oak Ridge, USA.

Carlson, T J; Brown, R S; Stephensons, J R; Gingerich, A J; Pflugrath, B D; Colotelo, A H et al. (2010): *Assessment of Barotrauma in Untagged and Tagged Juvenile Chinook Salmon Exposed to Simulated Hydro Turbine Passage*. Pacific Northwest Laboratory. Richland, Washington, USA.

Colotelo, A. H.; Mueller, R. P.; Harnish, R. A.; Martinez, J. J.; Phommavong, T.; Phommachanh, K. et al. (2018): *Injury and mortality of two Mekong River species exposed to turbulent shear forces*. In Marine and Freshwater Research 69 (12), p. 1945.

Deng, Zhiqun; Carlson, Thomas J.; Ploskey, Gene R.; Richmond, Marshall C.; Dauble, Dennis D. (2007): *Evaluation of blade-strike models for estimating the biological performance of Kaplan turbines*. In Ecological Modelling 208 (2-4), pp. 165–176.

Deng, Zhiqun; Guensch, Gregory R.; McKinstry, Craig A.; Mueller, Robert P.; Dauble, Dennis D.; Richmond, Marshall C. (2005): *Evaluation of fish-injury mechanisms during exposure to turbulent shear flow*. In Can. J. Fish. Aquat. Sci. 62 (7), pp. 1513–1522.

DWA (2005): *Fischschutz- und Fischabstiegsanlagen. Bemessung, Gestaltung, Funktionskontrolle. 2. korr. Aufl*. Hennef: DWA Dt. Vereinigung für Wasserwirtschaft Abwasser und Abfall (DWA-Themen).

Ebel, Guntram (2014): *Modellierung der Schwimmfähigkeit europäischer Fischarten — Zielgrößen für die hydraulische Bemessung von Fischschutzsystemen*. In Wasserwirtschaft 104 (7-8), pp. 40–47.

Greifzu, Franziska; Kratzsch, Christoph; Forgber, Thomas; Lindner, Friederike; Schwarze, Rüdiger (2016): *Assessment of particle-tracking models for dispersed particle-laden flows implemented in OpenFOAM and ANSYS FLUENT*. In Engineering Applications of Computational Fluid Mechanics 10

Guensch, Greg R.; Mueller, Robert P.; McKinstry, Craig A.; Dauble, Dennis D. (2002): *Evaluation of Fish-Injury Mechanisms During Exposure to a High-Velocity Jet*. Pacific Northwest Laboratory. Richland, Washington, USA.

Navarro, Anna; Boys, Craig A.; Robinson, Wayne; Baumgartner, Lee J.; Miller, Brett; Deng, Zhiqun D.; Finlayson, C. Max (2019): *Tolerable ranges of fluid shear for early life-stage fishes. Implications for safe fish passage at hydropower and irrigation infrastructure*. In Mar. Freshwater Res. 70 (11), p. 1503.

Neitzel, Duane A.; Richmond, Marshall C.; Dauble, Dennis D.; Mueller, Robert P.; Moursund, Russell A.; Abernethy, Cary S.; Guensch, Greg R. (2000): *Laboratory Studies on the Effects of Shear on Fish*. Pacific Northwest Laboratory. Richland, Washington, USA.

Odeh, M; Orvis, C (1998): *Downstream Fish Passage Design Considerations and Developments at Hydroelectric Projects in the North-east USA*. In Matthias Jungwirth (Ed.): Fish migration and fish bypasses. Oxford: Fishing News Books, pp. 267–280.

Pflugrath, Brett D.; Boys, Craig A.; Cathers, Bruce; Deng, Zhiqun Daniel (2019): *Over or under? Autonomous sensor fish reveals why overshot weirs may be safer than undershot weirs for fish passage*. In Ecological Engineering 132, pp. 41–48.

Schreer, Jason F.; Gokey, Jason; DeGhett, Victor J. (2009): *The Incidence and Consequences of Barotrauma in Fish in the St. Lawrence River*. In North American Journal of Fisheries Management 29

Schwevers, Ulrich; Adam, Beate (2020): *Fish protection technologies and fish ways for downstream migration*. Cham, Switzerland: Springer.

Thorenz, Carsten; Gebhardt, Michael; Weichert, Roman (2018): *Numerical Study on the hydraulic Conditions for Species Migrating Downstream over a Weir*. In International Association for Hydro-Environment Engineering and Research (Ed.): 7th International Symposium on Hydraulic Structures. Aachen, 15-18 May.

Thorncraft, Garry; Phonekhampheng, Oudom; Baumgartner, Lee; Martin, Kate; Pflugrath, Brett D.; Brown, Richard S. et al. (2013): *Optimising fish-friendly criteria for incorporation into the design of mini-hydro schemes in the Lower Mekong Basin*. National University of Laos.

USACE (1991): *Fisheries Handbook of Engineering Requirements and Biological Criteria*. With assistance of Milo C. Bell: US Army Corps of Engineers, North Pacific Division.

Weller, H. G.; Tabor, G.; Jasak, H.; Fureby, C. (1998): *A tensorial approach to computational continuum mechanics using object-oriented techniques*. In Comput. Phys. 12 (6), p. 620.

8th International Junior Researcher and Engineer
Workshop on Hydraulic Structures
ISBN: 978-0-578-37416-1
https://doi.org/10.26077/35a9-e8e8

Galway, Ireland,
5th - 8th July 2021

Probability of Woody Debris Passage at Rock Weirs

K.A. Margetts[1] and B.M. Crookston, Ph.D., P.E.[1]
[1]Civil & Environmental Engineering Dept., Utah Water Research Laboratory
Utah State University
Logan UT 84321
UNITED STATES
E-mail: kathryn.margetts@usu.edu

Abstract: *Often, large woody debris (LWD) at hydraulic structures is considered hazardous from a performance and public safety perspective. However, the sustainable management of rivers requires the consideration of ecological impacts of LWD such as cover for aquatics and the natural movement of LWD through a catchment. Therefore, this study explores the interaction of natural (nonuniform) LWD with rock weirs through field observations in the Blacksmith Fork River in Utah, USA and laboratory testing at the Utah Water Research Laboratory. The passage probability of individual LWD at rock weirs is observed and tested in an effort to describe the balance between hydraulic structure performance and river ecology via the natural transport of LWD by the river at rock weirs. Results demonstrate that LWD entrapment is a function of rock weir geometry, hydraulic conditions at the weir, and LWD element length and representative diameter. Orientation of LWD elements approaching the rock weir also contributes to entrapment probability. For lesser flow depths, minor accumulations of LWD at rock weirs do not negatively impact the hydraulic performance as evidenced by the head-discharge rating curve.*

Keywords: *rock weir, large woody debris, natural debris elements, physical modelling.*

1. INTRODUCTION

The natural transport and accumulation of driftwood or large woody debris (LWD) in a river reach is beneficial for watersheds as it helps to maintain or restore natural river functions that promote self-sustaining river ecology and river processes (Aadland, 2010; Reclamation, 2016). As a result, the physical benefits of LWD in streams has been of high interest in the river science community over the past decade (Gurnell *et al*., 1995; Wohl *et al*., 2016, 2019). In fact, manual placement of LWD and engineered woody structures are now common mitigation or restoration strategies used to address habitat loss due to extensive wood removal, channel dredging, etc. (Cramer, 2012; Roni *et al*., 2015; Rosgen, 2001; Wohl *et al*., 2016, 2019).

However, it is not uncommon for streams and rivers to include hydraulic structures for management efforts. It is common for LWD to accumulate at various structure types such as spillway crests (Crookston *et al.*, 2015; Furlan *et al.*, 2018; Pfister *et al.*, 2013), gates (Bénet *et al.*, 2021), bridge piers (Schalko *et al.*, 2020) or culverts (Larinier, 2002). Often, transport of debris is linked to catchment geomorphology, landcover, and hydrology; for example, increased river flows resulting from precipitation events or seasonal cycles (e.g., snow melt). As a result, LWD may be an engineering safety concern as accumulation on a structure may inhibit hydraulic performance, such as performance of a fish ladder, passage of a large storm event through a spillway, or overtopping and failure of a road crossing.

Natural functions associated with LWD accumulation include provision of habitat for aquatic species, particularly cover for fish, increased habitat complexity, and increased nutrient and sediment storage in the watershed (Gurnell *et al.,* 1995, 2002). Juvenile and rearing trout in particular seek cover in pools near boulders and LWD (Andonaegui, 2000). Natural processes also include large-scale fluxes in LWD, via transfer processes of input and output along a stream reach. Although improvement of natural processes is not typically the primary project objective for implementing hydraulic structures such as rock weirs, those weirs where LWD has accumulated have proven to be ecologically beneficial (Andonaegui, 2000; Rosgen, 2001). Rock weirs are intended to mimic nature in design (i.e., grade control structures, diversions, fish passage), and it is becoming a common practice in the USA to design rock weirs to include large, woody elements (Rosgen, 2001; Reclamation, 2016).

Alternatively, structures may cause LWD to accumulate, which can potentially block the entire crest or channel. This poses a risk both hydraulically and ecologically as significant debris blockage can inhibit existing river processes, reduce the hydraulic efficiency of a structure, and for rock weirs, potentially cause structural instability of the stones (Larinier, 2002; USFWS, 2019). The effects of LWD accumulation have been studied for large concrete structures such as spillways (Furlan *et al.,* 2018; Vaughn, 2020; Crookston *et al.,* 2015) and bridge piers (Schmocker & Hager, 2011, 2013; Schalko *et al.,* 2020). However, to the authors' knowledge no studies pertaining to LWD affecting the hydraulic performance of rock weirs has been conducted. Thus, a key remaining research challenge for rock weirs is to assess the relative benefits and potential concerns of LWD accumulation (Wohl *et al.,* 2016) and to provide design guidance that promotes balance between conveyance/hydraulic performance objectives, river morphology, and environmental objectives for more sustainable rock weir designs.

1.1 Rock Weirs

Rock weirs consist of a row of boulders or stones placed in a channel and thus have an uneven crest elevation (Figure 1a). They are built for a variety of purposes such as stream rehabilitation, fish passage, channel alignment or grade control, and improved sediment processes (Rosgen, 2001). These weirs have a variety of geometries (Kupferschmidt & Zhu, 2017) and weirs may be placed in series to form a rock ramp (i.e., block ramp) as a natural passage for fish (Figure 1b). Rosgen (2001) has cataloged a selection of generally accepted methods used in the design of rock weirs. Furthermore, there are multiple USA government-issued design manuals on rock weir and natural fish passage design (e.g., Aadland, 2010; Reclamation, 2016; USFWS, 2019).

a) b)

Figure 1 – Examples of rock weirs including a) a V-Notch rock weir located in Blacksmith Fork River, Hyrum, Utah, USA (photo courtesy of K. Margetts) and b) a rock ramp acting as a natural fish ladder in Rock Creek, Montana, USA (photo courtesy G. Jordan). https://www.flickr.com/photos/usfwsmtnprairie/8960106516

The design of a rock weir considers hydraulic performance, rock element stability, foundation scour, and sedimentation. Examples of hydraulic studies on individual stone stability and foundation scour include Pagliara and Palermo (2013a,b), which provide improved methods for the design and construction of rock weirs. Guidelines for predicting sedimentation and incipient bedload motion at rock weirs have also been standardized by Reclamation (2016). However, as with many in-stream hydraulic structures, the successful implementation of a rock weir not only requires proper field installation but also requires a detailed understanding of the river reach, river morphology, and corresponding catchment while anticipating future growth and change in the system. This includes river ecology and biological processes supported by the natural transport of woody debris (Gurnell *et al*., 1995; Wohl *et al*., 2016, 2019).

Although literature includes numerous noteworthy studies on large woody debris (LWD) at other in-stream structures (Pfister *et al*., 2013; Ruiz-Villanueva *et al*., 2014; Schalko *et al*., 2020; Schmocker & Hager, 2011, 2013), rock weir design guidance provides limited information regarding passage or blockage probabilities of debris elements and consideration for debris accumulation and corresponding hydraulic effects (e.g., Reclamation, 2016; USFWS, 2019; Aadland, 2010; Rosgen, 2001). Indeed, as with the aforementioned considerations the accumulation of LWD should also be anticipated in design and to achieve sustainability goals, which support natural processes such as the creation of habitat cover and storage of organic material and sediment (Wohl *et al.,* 2019). Overlooking LWD accumulation at rock weirs may result in failure to achieve hydraulic performance goals, unforeseen maintenance such as debris removal or relocating boulders after a storm event, or unsatisfactory river connectivity and channel response. Therefore, there is a clear need to understand first the blockage or passage probabilities for natural debris elements and additionally, the effects of LWD accumulation at rock weirs for appropriate design consideration.

2. RESEARCH METHODS

In this study, investigating the interaction of LWD at rock weirs included two components: field observations along the Blacksmith Fork (BSF) River located in Hyrum, Utah, USA and large-scale laboratory testing at the Utah Water Research Laboratory at Utah State University in Logan, Utah, USA. In the Blacksmith River, field observations provided insights as to construction and behavior of typical rock weirs in a mountainous catchment. In the laboratory, LWD was modeled using non-uniform branches collected at the Logan River and classified by geometries including average element diameter and total length. A model rock weir (see section 2.2) was constructed in a large flume to assess the passage probability of natural woody debris elements. Additional testing will include debris accumulation scenarios, modeled on actual stream debris loadings (Roni *et al.,* 2015).

2.1 Large Woody Debris

LWD has been modeled using both uniform and nonuniform elements. Vaughn (2020) and Schmocker and Hager (2013)) used smooth dowels or sticks to represent trees stripped of branches as transported to and by the river. The focus of this study, however, is on modeling LWD using more complex debris elements with twists, knots, and branches similar to those found in nature and what was observed in the Blacksmith Fork River. This approach expands upon prior studies which have utilized trunks with multiple branches or root wads (trunks with branches at one end) (Bénet *et al.,* 2021; Pfister *et al.,* 2013; Schmocker & Hager, 2011). LWD elements are defined herein as singular trunks with up to one branch (extending >2 cm) along with natural variations (knots, etc.). Branches were sourced locally and divided into size classes based on length and diameter for flume testing (see Table 1 and Figure 2). For example, class D4 represents 100 cm ≤ L ≤ 149 cm and an average element diameter D =4 cm.

Table 1 – Length and Diameter classes with corresponding flow rates tested for individual debris element passage probability.

		Experimental Discharge Q		
Length Class, L (cm)		**Diameter Class, D (cm)**		
		2	**4**	**6**
B	50-74	20, 30 l/s		
C	75-99	20, 30, 40, 50 l/s	20, 30, 40, 50 l/s	
D	100-149	20, 30, 40, 50 l/s	20, 30, 40, 50 l/s	30, 40, 50 l/s
E	150-169	20, 30, 40, 50 l/s	20, 30, 40, 50 l/s	40, 50 l/s
F	170-185	30, 40, 50 l/s	30, 40, 50 l/s	50 l/s
			40, 50 l/s	50 l/s

Figure 2 – Selection of LWD size classes pictured with a 45.7 cm (18 in.) ruler.

2.2 Laboratory Testing: Passage Probability

The laboratory study was conducted in a large (trapezoidal) flume with a base of 1 m, length of 6 m, and 2H:1V side slopes. Rough-cut flat-topped rocks obtained with permission from the Blacksmith River were placed at the downstream end of the channel to form a cross-vane rock weir (i.e., an I-weir; see Rosgen (2001), Figure 3) with a width of 0.25 m, length of 2.53 m, and height of 0.21 m. Mortar was used to ensure rock stability and eliminate seepage between rocks and between the weir and channel. The top of the rock weir was specifically designed with a nonuniform crest elevation, including several lower areas such as might be seen in typical rock weirs.

Instrumentation in the flume included a piezometer connected to a stilling well and point gage (±0.15 mm) for measurement of water elevation upstream of weir. Total head above the weir (*H*) was calculated from point gage elevation and a survey of the flume bottom (0.0016 m accuracy). Discharge was measured with a magnetic flow meter (±0.25%) calibrated per ASTM standards. Debris characteristic diameters and lengths were measured within ±1 mm.

Passage probability tests were patterned after Vaughn (2020), who studied the probability of individual LWD entrapment at labyrinth weirs. Testing was carried out by introducing individual woody debris elements approximately 3 meters upstream of the laboratory rock weir at discharges of: 20 l/s, 30 l/s, 40 l/s, and 50 l/s (see Table 1). Passing probabilities Π were recorded along with individual element characteristics, approach orientation of the woody element to the rock weir (stream-wise or channel-spanning) and the element location in the channel (center, right, left looking downstream). Passage probability tests for each size class of LWD were repeated at least 30 times to ensure 90% confidence passage probability (Furlan *et al.,* 2018).

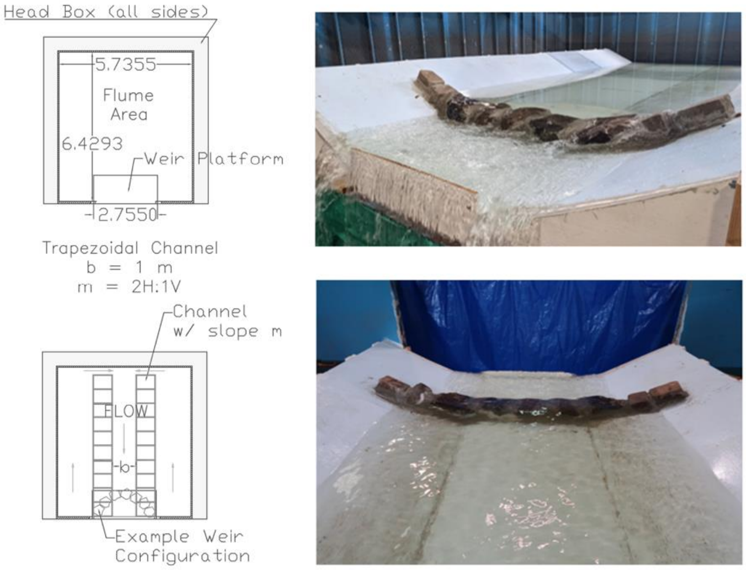

Figure 3 – Flume plans (lengths in m) and laboratory setup with flows of 30 L/s (top right) and 50 L/s (bottom right), photos courtesy K. Margetts.

3. RESULTS

Passing probability Π tests were conducted at four flow rates, *Q* (see Table 1). Each class of LWD was categorized by *L* and *D*, and initial results show that these dimensions are the most influential in determining element passage or entrapment at the rock weir. Despite LWD orientation or the presence of some small branching, the overall controlling factors for entrapment remained the characteristic *L* and *D* of the given element. In general, passage probabilty, the inverse of entrapment probability, increased with flow rate, particularly as class size decreased.

This is evident in results of passing probability as a function of the dimensionless diameter-to-total head ratio (*D/H*) and dimensionless length-to-total head ratio (*L/H*) shown in Figure 4b. Of these parameters, *D/H* appears to play a slightly larger role than *L/H* in passage probability, as evidenced by a slightly steeper downward trend in passing probability (Figure 4a). Note that the variability in Π is in part due to the twists, knots, and branches of the elements and the irregular surface of the rock weir. Another controlling factor in the variability of Π is the flow rate Q. As Q increases, the probability LWD will pass also increases. Higher flow rates (40, 50 L/s) and corresponding greater flow depths have more ability to pass debris than lower flow rates (20,30 L/s), particularly for the more natural debris shapes. As shown in Figure 4, higher discharges also have a greater Π to pass the same size of debris.

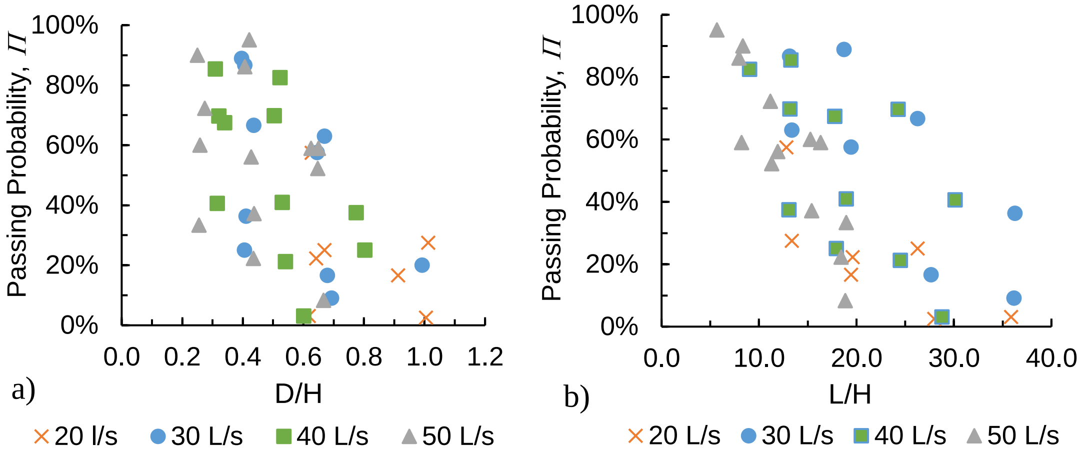

Figure 4 – Passing Probability versus (a) *D/H*) and (b) *L/H* at *Q*= 20 L/s, 30 L/s, 40 L/s, and 50 L/s.

Laboratory tests also showed evidence that LWD elements aligned perpendicular to the channel (channel-spanning) were slightly more likely to become entrapped than those oriented parallel to the channel (stream-wise). The probability of LWD entrapment was higher for channel-spanning elements than for streamwise LWD that approached the weir.

4. FIELD OBSERVATIONS: BLACKSMITH FORK RIVER

Field observations also indicated the likelihood of LWD entrapment at rock weirs. Rock weirs in the Blacksmith Fork River (BSF River) were investigated regarding general conditions between date of installation or construction and current conditions, with a focus on LWD accumulation. The rock weirs shown in Figure 1a are a v-shaped rock weir and are part of a series of 14 rock weirs implemented along a 2 km reach of the BSF River in 2013 to aid in flood protection (NRCS, 2013). Construction of the weirs included significant dredging and removal of sediments in this river reach (personal communication B. Neilson, Nov. 3, 2020). By 2017, the river's response had compromised the majority of the rock weirs, which had become filled with sediment, single rock toppling, etc. Figure 5 shows how the channel meandered to the north (right if looking downstream) and scoured the rock weir abutment or channel tie-in. It is unsurprising to see the large sediment deposit on the left bank.

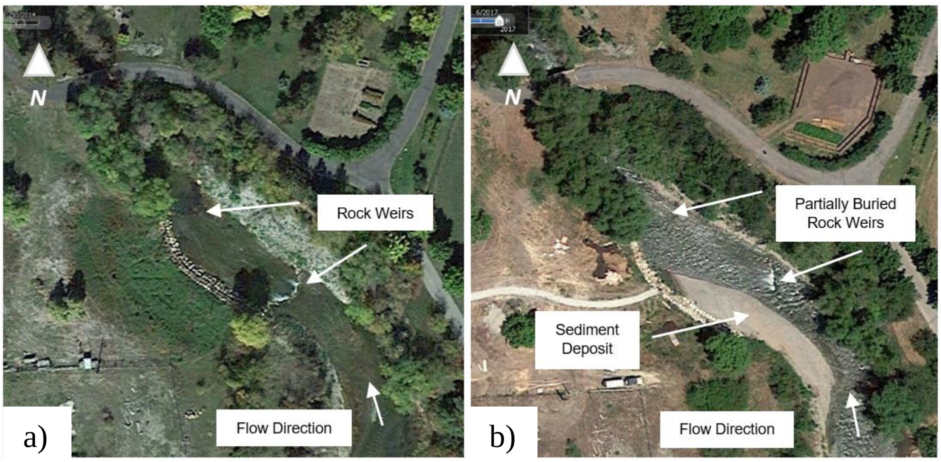

Figure 5 – Blacksmith Fork River Rock Weirs in (a) 2014 and (b) 2017 (Google, n.d.).

During field observations conducted on November 3, 2020, researchers observed current conditions at 7 V-notch rock weirs in the BSF River. At the time of observation, USGS stream gage 10113500 (9 km upstream of the weirs) gave a discharge of 2100 l/s (USGS, 2020). The active channel was 9 to 15 m in width and approximately 0.5 to 1 m in depth with some deeper pools.

It was observed that areas of sedimentation at several weirs had become heavily vegetated with riparian grasses and small shrubs. Weirs located farther downstream displayed toppled or mis-aligned rocks, likely due to insufficient stone foundation preparation (stones not well seated for seasonal flow fluctuations), excessive loading from sedimentation, and/or the passage of woody debris through the channel. Two of the observed weirs had accumulated a very small amount of woody debris (<25% m^3 LWD/m^2 channel area).

Additional field observations were carried out on October 29, 2021 under similar conditions. Figure 6 shows accumulations of LWD at a rock weir, which was entirely buried with non-cohesive gravels and sands on the left portion. LWD covered approximately 25% of the weir, oriented both parallel and perpendicular to the weir.

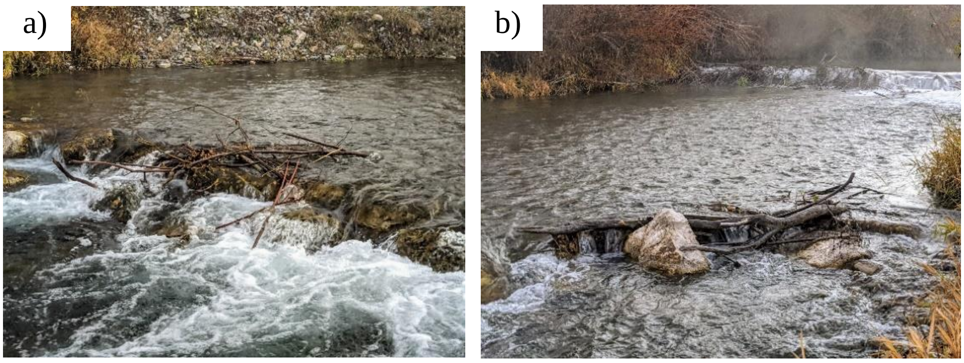

Figure 6 – Stream-wise and channel-spanning LWD entrapped at a BSF River rock weir October 29, 2021 (photo courtesy of K. Margetts).

It was concluded that sediment buildup at the BSF rock weirs led to a decrease in channel slope, altering river morphology. Such changes in river morphology and corresponding habitat may have undesirable ecological impacts such as temperature changes, higher flow velocities, insufficient flow depths, etc. In contrast, the presence of small LWD accumulations caught at the rock weirs provided some cover (Figure 5). Based on the amount of LWD observed, it is unlikely that LWD accumulation was the primary cause of a structural failure to the weirs (i.e., stone displacement).

Although this study does not focus on rock weirs and sedimentation, field observations indicate that the river in only 2 years had a significant response to the weirs in terms of sedimentation. It is unknown if this response was intended, but likely the design of the rock weirs and dredging the river of gravels and sands did not sufficiently consider river morphology and annual bedload cycles and sediment sources in the BSF upstream of the rock weirs. It is also unknown if any future maintenance will be performed on the rock weirs.

5. CONCLUSION

Healthy incorporation of large woody debris (LWD) at rock weirs includes understanding the balance between hydraulic and ecologic performances necessary for a sustainable river system. Field observations and laboratory testing provided useful insights on the interaction of LWD with straight and v-shaped rock weirs.

V-shaped rock weirs observed at the BSF River demonstrated the potential negative impacts of a rock weir channel stabilization project. Heavy sedimentation and toppled rocks due to high flows resulted in poor performance of the weirs. Ecologically, the river response and change in habitat raise concerns for local aquatics including trout. The BSF River is an example of how the objectives of channel stabilization projects do not always align with habitat improvement (Ball *et al.,* 2007) and the challenges of considering river morphology and catchment hydrology in the design of rock weirs.

Although the BSF rock weirs were not functioning properly, LWD accumulations were representative of the likelihood for organic material to become caught at this type of in-stream structure. LWD trapped at the rock weirs provided a minimal amount of cover and organic matter to the channel, while not appearing to disrupt the structure or hydraulics of the weir.

Laboratory testing provided further evidence of the potential for LWD to become entrapped at rock weirs. Element length L and diameter D were the most significant factors in the probability of LWD passage. The D/H ratio had more of an impact on passage probability than the length-head ratio. LWD elements aligned perpendicular to the channel were slightly more likely to become entrapped at the rock weir than those oriented streamwise (parallel).

Due to the potential for LWD to become entrapped at rock weirs, further testing of entrapment probability is necessary for identifying the hydraulic thresholds that balance LWD conveyance objectives with natural benefits. Data collected on the impacts of LWD passage, entrapment and accumulation will help improve future design of rock weirs. Data from the physical model may be used in future research or CFD modeling of rock weirs. Rock weirs may be the perfect in-stream structure for accumulating LWD in moderate, environmentally beneficial amounts while not putting critical infrastructure at risk.

ACKNOWLEDGMENTS

This work was conducted in collaboration with the Utah State University and the Utah Water Research Laboratory with special thanks to Dr. Bethany Neilson and Dr. Belize Lane. Funding for this research was provided by the State of Utah and a generous donation from D. B. Campbell.

REFERENCES

Aadland, L. P. (2010). *Reconnecting Rivers: Natural Channel Design in Dam Removals and Fish Passage*. Minnesota Department of Natural Resources.

Andonaegui, C. (2000). *Salmon, Steelhead and Bull Trout Habitat Limiting Factors*. Washington State Conservation Commission.

Ball, D., Maendly, R., & Poindexter, C. (2007). *Rock Weirs as Tools for Stabilization in Restoration Projects: An appraisal and comparison of two stream restoration projects in Northern California* (Restoration of Rivers and Streams). UC Berkeley: Water Resources Collections and Archives. https://escholarship.org/uc/item/50g0x121

Bénet, L., De Cesare, G., & Pfister, M. (2021). Reservoir Level Rise under Extreme Driftwood Blockage at Ogee Crest. *Journal of Hydraulic Engineering*, *147*(1), 04020086. https://doi.org/10.1061/(ASCE)HY.1943-7900.0001818

Cramer, M. L. (2012). *Stream Habitat Restoration Guidelines*. Co-published by the Washington Departments of Fish and Wildlife, Natural Resources, Transportation and Ecology, Washington State Recreation and Conservation Office, Puget Sound Partnership, and U.S. Fish and Wildlife Service.

Crookston, B. M., Mortensen, D., Stanard, T., Tullis, B. P., & Vasquez, V. M. (2015). *Debris and Maintenance of Labyrinth Spillways*. 22.

Furlan, P., Pfister, M., Matos, J., & Schleiss, A. J. (2018). Influence of density of large stems on the blocking probability at spillways. *International Symposium on Hydraulic Structures*, 3.

Google. (n.d.). [Google Earth Imagery of Rock Weirs at Blacksmith Fork River]. Retrieved May 1, 2021.

Gurnell, A. (2007). *Wood in world rivers*. Earth Surface Processes and Landforms, 32(8), 1129–1130. https://doi.org/10.1002/esp.1546

Gurnell, A. M., Gregory, K. J., & Petts, G. E. (1995). The role of coarse woody debris in forest aquatic habitats: Implications for management. *Aquatic Conservation: Marine and Freshwater Ecosystems*, *5*(2), 143–166. https://doi.org/10.1002/aqc.3270050206

Gurnell, A. M., Piégay, H., Swanson, F. J., & Gregory, S. V. (2002). Large Wood and Fluvial Processes. *Freshwater Biology*, *47*(4), 601–619. https://doi.org/10.1046/j.1365-2427.2002.00916.x

Kupferschmidt, C., & Zhu, D. Z. (2017). Physical modelling of pool and weir fishways with rock weirs. *River Research and Applications*, *33*(7), 1130–1142. https://doi.org/10.1002/rra.3157

Larinier, M. (2002). *Fish Passage through Culverts, Rock Weirs and Estuarine Obstructions*. *Bulletin Français de La Pêche et de La Pisciculture*, *364 supplément*, 119–134. https://doi.org/10.1051/kmae/2002097

NRCS. (2013). *Emergency Watershed Protection: Blacksmith Fork River Floodplain Restoration*. NRCS, Cache County, Logan City. https://www.nrcs.usda.gov/wps/portal/nrcs/detail/ut/programs/planning/ewpp/?cid=nrcs141p2_034036

Pagliara, S., & Palermo, M. (2013a). *Block Ramp For Torrent Control and Stream Restoration*. In *Check Dams, Morphological Adjustments and Erosion Control in Torrential Streams*. Nova Publishers.

Pagliara, S., & Palermo, M. (2013b). Rock grade control structures and stepped gabion weirs: Scour analysis and flow features. *Acta Geophysica*, *61*(1), 126–150. https://doi.org/10.2478/s11600-012-0066-0

Pfister, M., Capobianco, D., Tullis, B., & Schleiss, A. J. (2013). Debris-Blocking Sensitivity of Piano Key Weirs under Reservoir-Type Approach Flow. *Journal of Hydraulic Engineering*, *139*(11), 1134–1141. https://doi.org/10.1061/(ASCE)HY.1943-7900.0000780

Roni, P., Beechie, T., Pess, G., & Hanson, K. (2015). Wood placement in river restoration: Fact, fiction, and future direction. *Canadian Journal of Fisheries and Aquatic Sciences*, *72*(3), 466–478. https://doi.org/10.1139/cjfas-2014-0344

Rosgen, D. L. (2001). The Cross-Vane, W-Weir and J-Hook Vane Structures...Their Description, Design and Application for Stream Stabilization and River Restoration. *Wetlands Engineering & River Restoration 2001*, 1–22. https://doi.org/10.1061/40581(2001)72

Ruiz-Villanueva, V., Bodoque, J. M., Díez-Herrero, A., & Bladé, E. (2014). Large wood transport as significant influence on flood risk in a mountain village. *Natural Hazards*, *74*(2), 967–987. https://doi.org/10.1007/s11069-014-1222-4

Schalko, I., Schmocker, L., Weitbrecht, V., & Boes, R. M. (2020). Laboratory study on wood accumulation probability at bridge piers. *Journal of Hydraulic Research*, *58*(4), 566–581. https://doi.org/10.1080/00221686.2019.1625820

Schmocker, L., & Hager, W. H. (2011). Probability of Drift Blockage at Bridge Decks. *Journal of Hydraulic Engineering*, *137*(4), 470–479. https://doi.org/10.1061/(ASCE)HY.1943-7900.0000319

Schmocker, L., & Hager, W. H. (2013). Scale Modeling of Wooden Debris Accumulation at a Debris Rack. *Journal of Hydraulic Engineering*, *139*(8), 827–836. https://doi.org/10.1061/(ASCE)HY.1943-7900.0000714

U.S. Bureau of Reclamation (Reclamation), Gordon, E. H., Collins, K., Holmquist-Johnson, C., & Scurlock, M. (2016). *Rock Weir Design Guidance*. 197.

U.S. Fish and Wildlife Service (USFWS). (2019). *Fish Passage Engineering Design Criteria*. USFWS, Northeast Region R5, Hadley, Massachusetts.

USGS. (2020). *USGS Current Conditions for USGS 10113500* Blacksmith Fork. Hyrum, UT. *Blacksmith Fork AB Up and l Co.'s Dam nr Hyrum, UT*. https://waterdata.usgs.gov/nwis/dv?cb_00045=on&cb_00060=on&cb_00065=on&cb_72192=on&format=html&site_no=10113500&referred_module=sw&period=&begin_date=2020-10-18&end_date=2020-11-05

Vaughn, Taylor, "Submerged and Floating Woody Debris-Blocking Sensitivity of Labyrinth Weirs" (2020). All Graduate Theses and Dissertations. 7844. https://digitalcommons.usu.edu/etd/7844.

Wohl, E., Bledsoe, B. P., Fausch, K. D., Kramer, N., Bestgen, K. R., & Gooseff, M. N. (2016). Management of Large Wood in Streams: An Overview and Proposed Framework for Hazard Evaluation. *JAWRA Journal of the American Water Resources Association*, *52*(2), 315–335. https://doi.org/10.1111/1752-1688.12388

Wohl, E., Kramer, N., Ruiz-Villanueva, V., Scott, D. N., Comiti, F., Gurnell, A. M., Piegay, H., Lininger, K. B., Jaeger, K. L., Walters, D. M., & Fausch, K. D. (2019). The Natural Wood Regime in Rivers. *BioScience*, *69*(4), 259–273. https://doi.org/10.1093/biosci/biz013

8th International Junior Researcher and Engineer
Workshop on Hydraulic Structures
ISBN: 978-0-578-37416-1
https://doi.org/10.26077/1aca-bbb5

Galway, Ireland,
5th - 8th June 2021

Experimental and Numerical Analysis of the Hydraulic Jump Stilling Basin and the Downstream Scour Depth

L.J. Miranda[1] and R. Sánchez[2]
[1]School of Civil Engineering, Universidad Nacional de Ingeniería
Lima, Túpac Amaru 210
E-mail: lmirandam@uni.pe
[2]School of Civil Engineering, Universidad Andina del Cusco
Cusco, El Sol 3107
E-mail: redysanchez20@gmail.com
PERÚ

Abstract: *This paper presents a study of a tridimensional low-head hydraulic jump stilling basin by using both physical and numerical models. Laboratory tests up to 15 hours in duration were carried out in a 1.9 m wide and 14 m long flume. Four gates produced a jet with a submerged hydraulic jump in a positive-step stilling basin, after which scour developed in a nearly uniform sand bed. Acoustic Doppler Velocimeter, piezometers and image processing were used to collect the hydrodynamic data, and Reynolds Averaged Navier-Stokes simulations developed in OpenFOAM were tested for validation purposes. Then, the study focused on (1) the temporal evolution of the experimental scour depth downstream the stilling basin and (2) the efficiency of the numerical models to reproduce the interior fields. Regarding the first point, it was found that temporal scour evolution agrees with empirical dimensionless formulation, but differences in magnitude were found, indicating that some variables should be further investigated. The validation of numerical models has shown that the K-Epsilon Standard model is much better than the K-Omega SST counterpart in reproducing velocity fields but similar values were found for turbulent kinetic energy. Pressure fluctuations numerical coefficient also showed values similar to those found by other authors, however lateral flow and Reynolds stress issues appeared because of the tridimensional nature of the case study.*

Keywords: *Hydraulic jump, stilling basin, scour, numerical model, OpenFOAM.*

1. INTRODUCTION

Energy dissipators serve to protect the riverbed and banks from erosion as well as guarantee that the hydraulic structure (dams and intakes) and other elements do not have damage because of the high turbulence flow (Khatsuria, 2004). The stilling basin is the most common dissipation structure, which uses the hydraulic jump to reduce the energy head. However, studying the flow in these stilling basins is still complex and difficult to analyse because this is an unsteady and highly turbulent flow subjected to random fluctuations (Lopardo and Romagnoli, 2009).

Understanding this phenomenon, in which macro pressure and velocity fluctuations, flow separation, eddies, and phases-mixture can be combined, is of vital importance, since they can generate vibration, fatigue and cavitation in structures (Lopardo, 1985). Likewise, the remaining energy at the outlet of the structures can scour the river bed and endanger their stability (Adduce and Sciortino, 2006).

Since the first known study of turbulence in hydraulic jumps (Rouse et al., 1959), quite a lot of studies have been carried out. In this sense, Peterka (1984) and Hager (1992) managed to compile several experiments and present a characterization and analysis of different types of hydraulic jump in energy dissipation structures. Particularly, other authors have focused on interior hydrodynamics and the air concentration in the jump (Rajaratnam, 1967) and pressure fluctuations (Lopardo, 1985; Steinke et al., 2021), among other aspects.

On the other hand, in order to obtain empirical formulas that make it possible to predict erosion downstream of hydraulic structures, researchers have conducted experiments on moving bed models with non-cohesive sand. Among these, Chatterjee et al. (1994), Hassan and Narayanan (1985) and Breusers (1967) analysed the effect of a jet that is directed from a rigid bed towards a sand bed. Subsequent investigations inquired about the downstream effect of stilling basin, and found that a positive step affects the magnitude of the erosion depth (Oliveto and Comuniello, 2009) and this effect is highly dependent on the particle Froude number (Aminpour and Farhoudi, 2017).

Although experimentation provides real values that improve the understanding of hydrodynamics and sediment transport to propose solutions for the operation of hydraulic structures (Chanson, 2015), it has a limited scope in data collection. To address these shortcomings, Computational Fluid Dynamics (CFD) has been applied using numerical models (Bayón, 2017). In this line, turbulence modelling is not only a key aspect of CFD applications, but indispensable to study the performance in a stilling basin (Macián, 2019).

In recent years, the k-epsilon turbulence model is one of the most studied models to reproduce hydraulic jumps, and promising results have been obtained when evaluating its effectiveness in terms of water levels and velocity range, among other parameters. The numerical approach has also been used to evaluate design alternatives in terms of energy dissipation, such as the effect of converging walls (Babaali et al., 2015) or composite dissipative pools (Zhou and Wang, 2019). However, accuracy issues have been found in the estimation of the bed shear stresses (Carvalho et al., 2008) and the aeration within the hydraulic jump (Macián, 2019).

The objective of this paper is to describe the scour depth downstream the stilling basin and compare two numerical models' efficiency to predict the hydrodynamic fields. To achieve this goal, a battery of tests similar to those performed by Oliveto and Comuniello (2009) were carried out on a physical scaled model of a mobile barrage of a diversion dam. In order to complement these studies, numerical simulations with RANS approach were accomplished using the k-epsilon Standard and k-omega SST turbulence models already applied by Bayón and López (2015) for hydraulic jump stilling basin in OpenFOAM. However, the case presented here is a completely three dimensional layout, regarding water depth, velocity field, pressure, and Reynolds stresses.

2. MATERIALS AND METHODS

2.1. Experimental setup

Figure 1 shows a diagram of the flume where 5 tests were carried out under gate operating conditions (extreme flows were not studied). The mobile barrage was made up of 4 gates, two gates of 0.50 m in the middle and two gates of 0.25 m on both sides of the flume. The energy dissipator was 2.51 m long and B = 1.90 m wide. The discharge (m^3/s) was measured in a calibrated rectangular weir where a Neyrpic point gauge was installed with a precision of ± 0.2 l/s. The gate openings were established in such a way that the inlet flow depth y_0 = 0.32 m was set constant for water harvesting purposes, while the downstream levels h_{tw} (see Table 1) were controlled by an adjustable gate according to the normal depth of the river. Downstream the structure, mobile horizontal sand bed (d_{50} = 0.24 mm, d_{90} = 0.58 mm) was uniformly compacted and saturated for each test. Kinematic viscosity ν changed according the measured temperature in the day of the tests.

Table 1. Summary of the main parameters

Parameter		**Test 1**	**Test 2**	**Test 3**	**Test 4**	**Test 5**
Gate opening	a (m)	0.0259	0.0454	0.0682	0.0948	0.1289
Discharge	Q (m^3/s)	0.0634	0.1053	0.1482	0.1896	0.2327
Kinematic viscosity	ν (10^{-6} m^2/s)	1.0	0.99	0.977	0.868	0.886
Inlet velocity	U_0 (m/s)	0.1043	0.1735	0.2427	0.3111	0.3891
Shear velocity*	u* (m/s)		0.01	0.01224	0.01414	
Froude (after gate)	Fr (-)	3.84	4.18	3.47	3.00	2.66
Particle Froude number	F_d (-)	5.46	7.39	7.63	8.21	9.67
Outlet depth	h_{tw} (m)	0.0926	0.1232	0.1478	0.1865	0.211
Characteristic erosion time	t_* (h)	4.37	3	1.67	1.15	0.77

**Characteristic shear velocity u* came from numerical model simulated only for tests 2, 3 and 4.*

Vectrino Acoustic Doppler Velocimeter (ADV) allowed measuring instantaneous velocity, using a sampling frequency of 50 Hz (as high as possible to allow acoustic signals to travel between bubbles that may exist in the flow) and 30 mm of sampling height to capture the smallest possible turbulent eddies flowing through the volume in intervals of 12 s. Signal to Noise Ratio (SNR) was above 30 dB, and turbulence quantities were obtained by data processing. The maximum scour was determined by taking pictures every 10 min (ranging from 8 to 15 hours) using a camera with 4160x3120 pixels located on the left side where there were three acrylic window whereas mean pressures were measure with 28 piezometers conveniently distributed throughout the stilling basin.

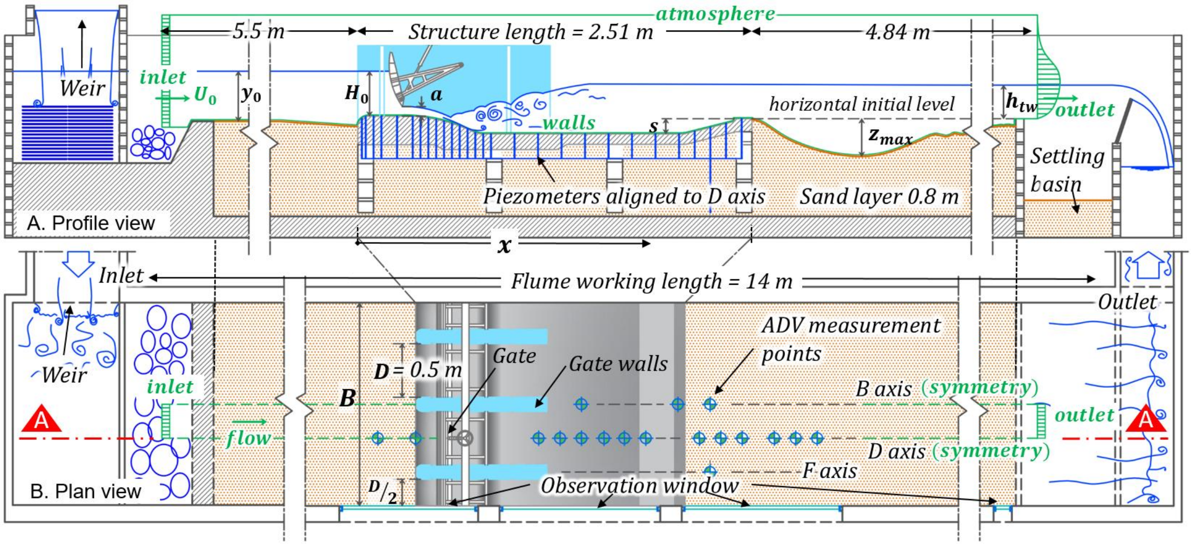

Figure 1 – Profile (A) and Plan (B) view of the physical model on experimental flume in National Laboratory of Hydraulics and numerical model boundaries (green lines).

2.2. Modelling equations

Reynolds-averaged Navier Stokes' (RANS) three-dimensional equations were used as implemented in OpenFOAM. In RANS momentum equation (1), *U,p,u',ρ* and F_b stand for velocity (m/s), pressure (Pa), velocity fluctuation (m/s), fluid density (Kg/m^3) and the force over the cell (m/s^2) respectively, and the symbols <> represent the time averaging operator.

$$\frac{\partial \langle \vec{U} \rangle}{\partial t} + \overrightarrow{\langle U \rangle} \nabla \cdot \overrightarrow{\langle U \rangle} = \frac{-1}{\rho} \nabla \langle p \rangle + \nu \nabla^2 \overrightarrow{\langle U \rangle} + \frac{1}{\rho} \nabla \langle -\rho u' u' \rangle + \overrightarrow{F_b} \quad (1)$$

The surface was tracked by the Volume of Fluid (VOF) method, which introduces a fluid fraction variable α_w (dimensionless) that lies between 0 and 1, calculated with the continuity flow equation (2).

$$\frac{\partial \alpha_w}{\partial t} + \nabla \cdot \left(\overrightarrow{\langle U \rangle} \alpha_w \right) = 0 \quad (2)$$

In high turbulent flows, turbulent kinetic energy (TKE, m^2/s^2) is an important analysed variable, which is defined from velocity fluctuations in the three directions u', v' y w':

$$k = \frac{\langle u'^2 \rangle + \langle v'^2 \rangle + \langle w'^2 \rangle}{2} \quad (3)$$

In order to estimate the TKE and model the nonlinear terms <-*ρu'u'*> in equation (1) that result from averaging the variables, turbulence models were used. Although some authors have used the K-Epsilon RNG model to study hydraulic jumps, Bayón (2017) found slight advantages in time consumption for the Standard version. At this stage, the K-Epsilon Standard (Launder and Spalding, 1974) and K-Omega SST (Menter et al., 2003) models were used, regarding the standard coefficients implemented in OpenFOAM 2.4. To do so, laboratory test 1 was discarded due to differences in the opening of the gates, and also test 5 was, due to lack of bathymetry of the bed. In this way, simulations were made for three conditions, which will be called N2, N3 and N4 onwards. The PISO algorithm, created for transient flows, was used, and a Courant limit of 2 was maintained (Courant decreases from gate to jump body).

2.3. Mesh

A structured mesh comprising the inlet bed domains, gate, stilling basin, and eroded bed was constructed with the help of OpenFOAM's SnappyHexMesh application. To reproduce the high air mixture that occurs into the hydraulic jump, a higher refinement was generated in this area guaranteeing the quality of the mesh, with limits of orthogonality less than 70° and obliquity less than 4. Each mesh reached around 6 million cells.

Dimensionless cell size $\Delta x^{+} = \Delta x \cdot u^{*}/\nu$ and time interval $\Delta t^{+} = \Delta t \cdot u^{*2}/\nu$ were calculated in terms of the characteristic shear velocity *u** and the kinematic viscosity ν. The cell size was distributed over a wide range $10 < \Delta x^{+} < 570$, and average time interval reached $\Delta t^{+} = 0.37$. Dimensionless wall distance $y^{+} = u_t \cdot y/\nu$, calculated in function of the wall shear stress u_t and the cell distance to the wall y, reached $30 < y^{+} < 220$ for the stilling basin; however, for the sand bed it was $5 < y^{+} < 50$.

2.4. Boundary conditions

Boundary conditions were established as suggested by Bayón (2017), considering the air and water inlets, atmosphere and walls; except for the outlet condition, for which a mixed condition (Dirichlet and Von Newman) was used, using an OpenFOAM application. *D* and *B* axis (see Figure 1) were set up as symmetry planes to simplify the study. Wall functions were assigned according to the logarithmic-law of the wall, which includes a correction for rough wall cases. A nutkRoughWallFunction was used, where the total roughness parameter *Ks* = 0.00024 (m) was assigned for the sand bed and *Ks* = 0.0001 for the concrete wall, whereas nutkWallFunction was assigned to plexiglass gate and smooth wood walls.

3. SCOUR ANALYSIS

Breusers (1967) proposed equation (4) for the maximum erosion Z_{max} at a specific time *t*.

$$\frac{z_{max}}{z_{*}} = \left(\frac{t}{t_{*}}\right)^{0.38} \qquad (4)$$

where Z_{*} is the characteristic length and t_{*} is characteristic time (see Table 1) when $Z_{max} = Z_{*}$. However, Oliveto and Comuniello (2009) found a better fit using an exponent of 0.19. The aforementioned authors defined Z_{*} based on the geometric layout of their models; but, in the present study $Z_{*} = H_0/2$ is used because it represents better the energy load with a potential to generate erosion in the channel. In this study, temporal evolution of the scour hole was monitored through the observation window as it is shown in Figure 2, where the maximum scour hole present quasi-homothetic evolution, similar to what was found by Bombardelli et al (2018). However, the scour depth grew faster than its location in x direction.

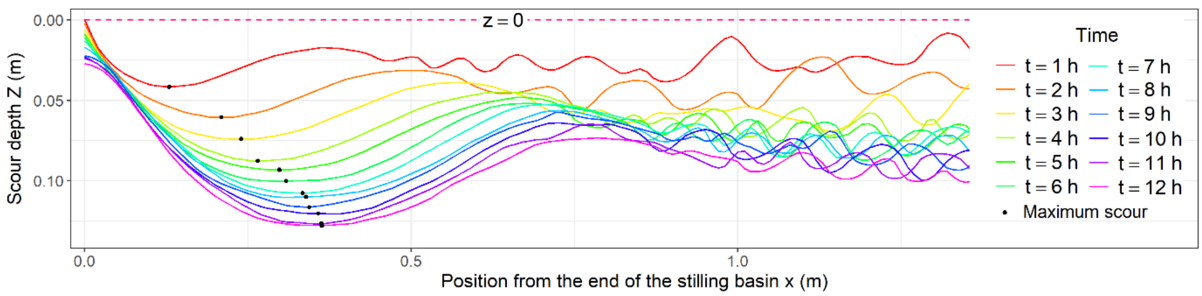

Figure 2 – Evolution of longitudinal profile for test N°2 from the observation window.

A comparison was made between the results obtained in the laboratory and the erosion calculated with equation (5) proposed by Oliveto and Comuniello (2009), where s is end-sill height, h_{tw} is the tail water depth, $F_d = V/(g' \cdot d_{50})^{1/2}$, is the particle Froude number, $g' = g(\rho_s - \rho)/\rho$ is the modified gravity acceleration, g = gravity acceleration and ρ = density of water, ρ_s = density of sand grain, and dimensionless time $T = (g' \cdot d_{50})^{1/2} \cdot t/s$.

$$\frac{z_{max}}{s} = 3.4\left(\frac{h_{tw}}{s}\right)^{3/4}\left(\frac{d_{50}}{s}\right)^{6/5}(F_d - 1)^{6/5}T^{1/4} \quad (5)$$

In Figure 3a, three exponential adjustments between erosion and the time scales are represented for values of $Z_{max}/Z_* < 1.5$. Figure 3a shows that the best fitting corresponds to the exponent 0.38 (Eq. 4). Figure 3b shows that experimental results were about 380% (on average) of those calculated with equation (5) at times *t = 6, 9 and 12 hours*. It could be mentioned here that the quantity z_{max}/s might not be the best way to define the non-dimensional scour since z_{max} and s are not physically related. It also should be noted that the slope of the end-sill of the physical model was 1v:4h, in contrast to the 1v:1h used by Oliveto and Comuniello (2009). As this parameter influences the scour depth (Farhoudi and Shayan, 2014), and it is not considered in the above equation, it could be another cause of difference and should be further investigated.

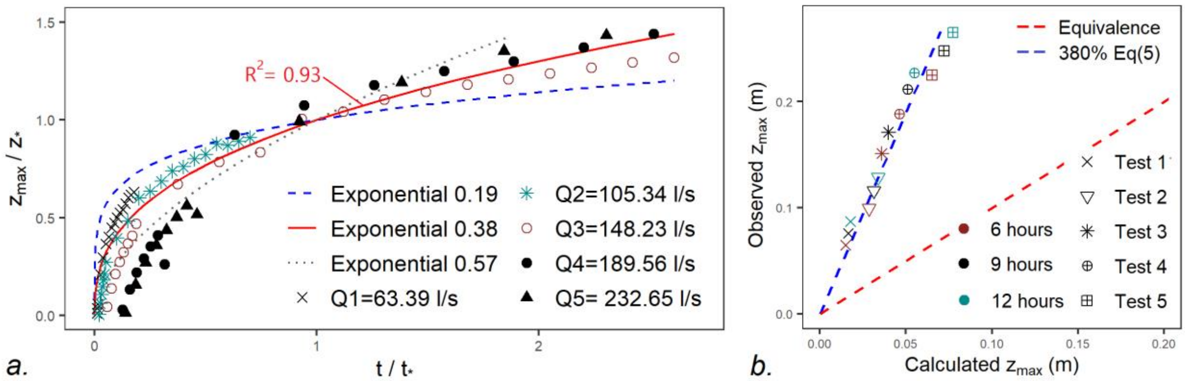

Figure 3 - (a) Dimensionless scour depth vs time and (b) observed vs calculated scour from Eq. 5.

4. VALIDATION OF RANS SIMULATIONS

Nash-Sutcliffe efficiency indicator (NSE) was used as defined by Nash and Sutcliffe (1970), where very good values from 0.75 are considered, whereas negative ones indicate that error is greater than the standard deviation. In order to determine the accuracy of the numerical model in relation to the experimental data, NSE was calculated for different quantities (Table 2).

Table 2. NSE between numerical and experimental values for different variables

Model	Case	Pressure	Water depth	TKE	Velocity profiles U_x		
					Upstream	Basin	Scour hole
k-ε	N2	0.876	-0.1868	0.889	0.801	-2.109	0.940
k-ε	N3	0.925	0.7748	0.884	0.733	-0.309	0.946
k-ε	N4	0.936	0.7948	0.978	0.769	-0.135	0.915
k-ω	N2	0.728	0.3698	0.744	0.787	-8.241	-1.839
k-ω	N3	0.915	0.7999	0.822	0.365	-3.991	-0.441
k-ω	N4	0.897	-0.2486	0.972	0.667	-1.637	-0.294

4.1. Water depth and pressure in stilling basin

During the simulation it was observed that the jump was slightly submerged in the gate, while in experiments, submergence occurs after the gate. This causes the numerical water depths to differ from experiments at the beginning of the jump. The k-ε Standard and k-ω SST models showed good accuracy for mean pressures inside the stilling basin and, although the water depths are qualitatively similar to the observed ones (Figure 4a), the longitudinal range of measurement was small due to the limitation of the observation window, causing the NSE to reach negative values (Table 2).

The pressure fluctuations coefficient *C'p*, an important parameter to study cavitation risk (Lopardo, 1985), is calculated from numerical model and plotted in Figure 4b against the dimensionless distance x/h_1, where h_1 is the critical depth at the jump toe and *x* is the distance from this point. *C'p* values at the beginning of the jump are of the same order of magnitude as those presented by other authors, and it can be seen particularly that the estimations of *C'p* are higher in the k-ε model than in the k-ω model, except for *Fr* = 3.0. As expected for RANS type models, *C'p* drastically decreases towards the jump body, where the fluid fraction variations are minimum.

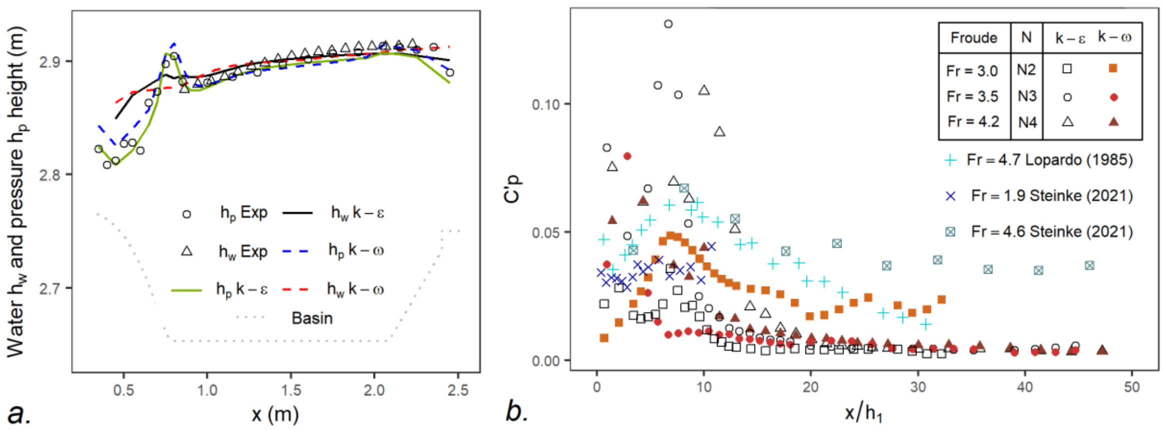

Figure 4 - (a) Water and pressure height for the test N3, and (b) numerical pressure fluctuation coefficient C'p compared with experimental results from Steinke et al. (1990) and Lopardo (1985).

4.2. Velocity, Reynolds stresses and turbulent kinetic energy

Figure 5a,b shows the velocity (u and w) before the gate (1,2), into the stilling basin (*3,4*), and the scour hole (*5,6*) for the test N3. It is observed that both Standard k-ε and k-ω SST did reproduce the velocity in the region before the gate, but problems arise later. At *x* = 1.55, the k-ε model shows positive and negative estimation errors in the *D* and *B* axis respectively, which implies a little overestimation of the lateral flow at the end of the gate wall (*x* = 1.23) or before (ADV does not capture well this region), although this error dissipates in the scour hole. On the other hand, the k-ω SST model increases this error from the hydraulic jump towards the sand bed, which may be due to a wrong reproduction of the vortices in the *xy* direction generated at the end of the gate wall. These problems could be sorted out by using other turbulence models. Constantinescu et al (2010) found, for instance, that DES models were "significantly more successful" in predicting the velocity distribution in the river channel.

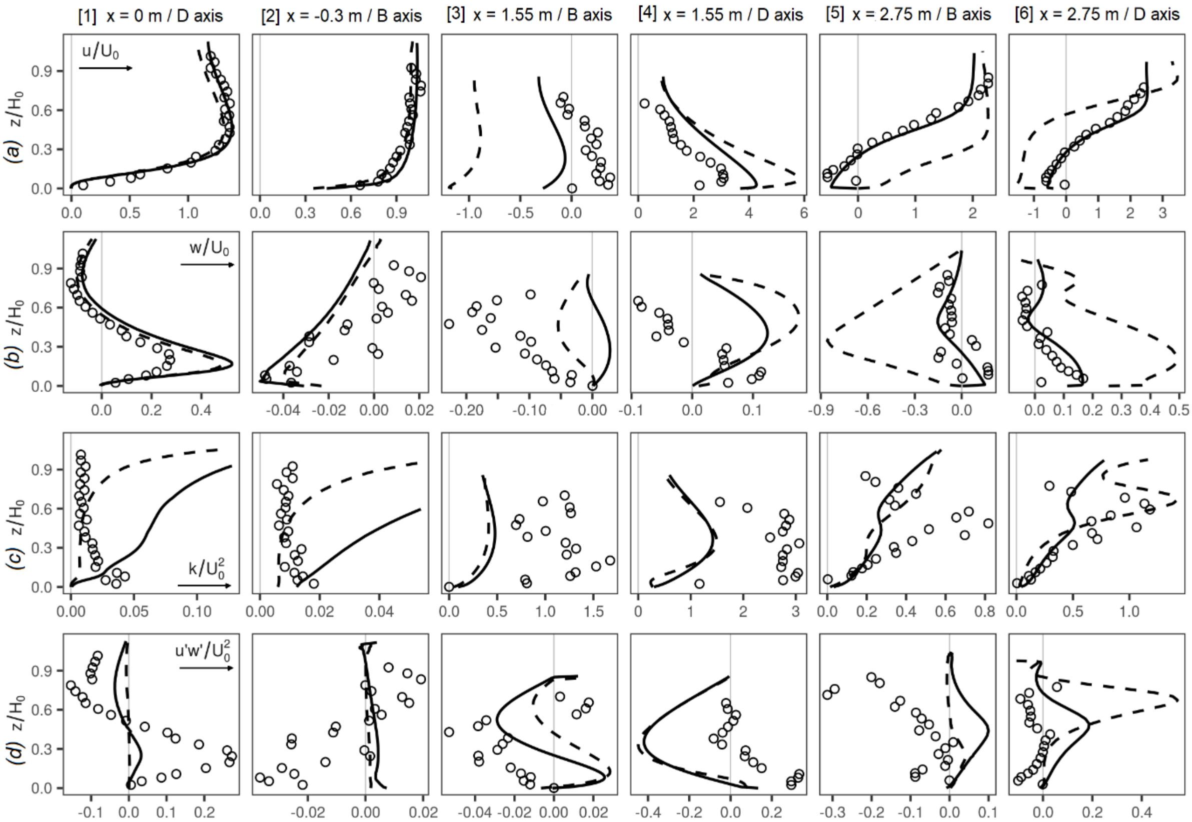

Figure 5 - Experimental (dots) and numerical k-ε (continuous) and k-ω (dashed) data for test N3.

Observed Reynolds stresses <*u'w'*> were compared using Boussinesq's approximation for numerical results without good correspondence (Figure 5d). This is possibly due to high turbulent anisotropy (in the jump region) or that sediment load (in the scour region) was not considered in the numerical model. Figure 5c also shows that numerical models overestimate the value of TKE before the gate, however underestimate that value in the interior of the hydraulic jump. This accuracy issue may be due to the jump submergence that affects the TKE production. In any case, the experimental data shows high values of TKE gradient at the stilling basin walls, so the wall functions must be further analysed. Despite these differences, the dissipation of energy was reproduced, with TKE reduction of the order of 80% from the hydraulic jump to sand bed, and the NSE taken with the logarithms of the numerical values from stilling basin to scour hole is high (Table 2).

5. CONCLUSIONS

Based on laboratory experiments and numerical simulations, it can be concluded that:

1. Unlike experiments carried out by Oliveto and Comuniello (2009), where equilibrium was reached in approximately 70 hours, the scour process was faster in the present study. Although complete equilibrium was not reached, very low scour rates were observed up to 15 hours (end of the tests) reasonably because of the difference in sand size and particle Froude number.
2. The temporal variation of the maximum erosion depth Z_{max} was measured in laboratory tests. Eq. (4) suggested by Breusers (1967) was tested and the results revealed a similarity. Then, equation (5) was compared with observed Z_{max} at the generic time t. It shows that the results obtained with equation (5) differ from those observed in experiments. The slope-height parameters should be further analysed to re-evaluate this formulation.
3. Standard k-ε and k-ω SST models were assessed and it was found that the first one reproduces the hydrodynamic fields better, having a good fit in the prediction of water levels, field velocities and kinetic energy. However, there was an error of lateral flow that generated velocity underestimation along the gate wall axis. This could be improved using a wider domain with cyclic lateral boundary condition or testing other turbulence models such as DES models.

4. It is promising that, although RANS models only capture the main characteristics, the models produced a pressure fluctuations coefficient *C'p* comparable to those obtained from other researchers, at least, in the regions with high fluid fraction variation. It can be suggested to continue studying this parameter with similar approaches.
5. Both Standard k-ε and k-ω SST models fail to correctly reproduce Reynolds stresses, but this could be due to the simplifications (isotropy, Boussinesq assumption) taken in the RANS models. Therefore, RSM (Reynolds Stress Model) could improve this shortcomings. Similarly, TKE shows larger gradients in the inlet bed and the stilling basin walls. Anyhow, both models reproduce the dissipation from the hydraulic jump to the sand bed.

6. ACKNOWLEDGMENTS

Authors thanks to all researchers and staff at National Laboratory Hydraulics for the facilities in the laboratory and the support for numerical modelling.

7. REFERENCES

Adduce, C. and Sciortino G. (2006), *Scour due to a horizontal turbulent jet, Numerical and experimental investigation*, Journal of Hydraulic Research, 44 (5), 663-673.

Aminpour, Y. and Farhoudi, J. (2017), *Similarity of local scour profiles downstream of stepped spillways,* International Journal of Civil Engineering, 15 (5), 763-774.

Babaali, H., Shamsai, A. and Vosoughifar, H. (2015), *Computational Modeling of the Hydraulic Jump in the Stilling Basin with Convergence Walls Using CFD Codes*, Arab Journal for Science and Engineering, 40, 381–395.

Bayón, A. and López, P.A. (2015), *Numerical Analysis of Hydraulic Jumps Using OpenFOAM*, J. Hydroinformatics, 17(4), 662–678.

Bayón, A. (2017), *Numerical Analysis of Air-water Flows in Hydraulic Structures Using Computational Fluid Dynamics (CFD)*. PhD Program in Water and Environmental Engineering, Polytechnic University of València, València.

Bombardelli, F.A., Palermo, M., and Pagliara, S. (2018), *Temporal evolution of jet induced scour depth in cohesionless granular beds and the phenomenological theory of turbulence*, Physics of Fluids, 30, 085109.

Breusers, H. N. C. (1967), *Time scale of two-dimensional local scour: in Nicht V. (Ed) Proceedings of the 12th IAHR Congress*, Vol. 3, Fort Collins,1967, pp. 275–282.

Carvalho, R.F., Lemos, C.M. and Ramos, C.M. (2008), *Numerical Computation of the Flow in Hydraulic Jump Stilling Basin*, Journal of Hydraulic Research, 46 (6), 739–752.

Chanson, H. (Ed.). (2015). *Energy dissipation in hydraulic structures*, CRC Press.

Chatterjee, S. S., Ghosh, S. N., and Chatterjee, M. (1994), *Local scour due to submerged horizontal jet*, Journal of Hydraulic Engineering, 1208, 973–992.

Constantinescu, G.; Koken, M.; Zeng, J. (2010), *Simulation of flow in an open channel bend of strong curvature using Detached Eddy Simulation*, River Flow 2010, 1527–1534.

Farhoudi, J., and Shayan, H. K. (2014). *Investigation on local scour downstream of adverse stilling basins,* Ain Shams Engineering Journal, 5 (2), 361-375.

Hager, W. H. (1992), *Energy dissipators and hydraulic jump*, Springer Science + Business Media B. V., Kluwer, Dordrecht, The Netherlands.

Hassan, N. M. K. and Narayanan, R. (1985), *Local scour downstream of an apron*, Journal of Hydraulic Engineering, ASCE, 111 (11), 1371-1385.

Khatsuria, R. M. (2004), *Hydraulics of spillways and energy dissipators*, CRC Press

Launder, B.E. and Spalding, D.B. (1974), The Numerical Computation of Turbulent Flows, Computer Methods in Applied Mechanics and Engineering, 3, 269-289.

Lopardo R. A. (1985), Metodología de estimación de presiones instantáneas en cuencos amortiguadores, Anales de la Universidad de Chile, 8 (5), 437–455.

Lopardo R. A. and Romagnoli M. (2009), *Pressure and velocity fluctuations in stilling basin: Proc.16th IAHR-APD Congress and 3rd Symposium of IAHR-ISHS*, Nanjing, October 20-23, 2009, pp. 2093–2098.

Macián, J.F., García, R., Huber, B., Bayón, A. and Vallés, F.J. (2019), *Approach to the Void Fraction Distribution within a Hydraulic Jump in a Typified USBR-II Stilling Basin, E-proceedings of the 38th IAHR World Congress, Water: Connecting the World*, Panama City, September 1-6, 2019, pp. 3627-3634.

Menter, F.R., Kuntz, M. and Langtry, R. (2003), *Ten Years of Industrial Experience with the SST Turbulence Model: Turbulence,* in Hanjalic, K., Nagano, Y. and Tummers, M. *(Eds) Proceedings of the 4th International Symposium on Heat and Mass Transfer*, West Redding, 2003, pp. 625-632.

Nash, J.E., and Sutcliffe, J.V. (1970), *River flow forecasting through conceptual models: Part I. A discussion of principles*. Journal of Hydrology, 119 (3), 429-442.

Oliveto, G. and Comuniello, V. (2009), *Local Scour Downstream of Positive-Step Stilling Basins*, Journal of Hydraulic Engineering, 135 (10), 846-851.

Peterka, A. J. (1984), *Hydraulic design of stilling basins and energy dissipators*, Engineering Monograph no. 25, US Bureau of Reclamation.

Rajaratnam, N. (1967), *Hydraulic Jumps*, Department of Civil Engineering, University of Alberta, Canadá.

Rouse, H., Siao, T.T. and Nagaratnam, S. (1959), *Turbulence Characteristics of the Hydraulic Jumps*, Transactions of the American Society of Civil Engineers, ASCE, 124 (1), 926-966.

Steinke, R., Dai Prá, M., Lopardo, R.A., Marques, M.G., de Melo, J.F., Priebe, P.S., and Teixeira, E.D. (2021), *Low Froude Number Stilling Basins–Hydrodynamic Characterization*, Journal of Hydraulic Engineering, 147 (4), s.p.

Zhou, Z. and Wang, J. (2019), *Energy dissipation due to the compound stilling basin: E-proceedings of the 38th IAHR World Congress, Water: Connecting the World*. Panama City, September 1-6, 2019, pp. 3515-3524.

8th International Junior Researcher and Engineer Workshop on Hydraulic Structures
ISBN: 978-0-578-37416-1
https://doi.org/10.26077/1e5d-bd83

Galway, Ireland,
5th - 8th July 2021

Discharge Capacity of a Piano Key Weir with Curvilinear Keys

R.K. Mishra and Z. Ahmad
Department of Civil Engineering
Indian Institute of Technology Roorkee
Roorkee - 247667
INDIA
E-mail: ravimishra059@gmail.com

Abstract: *The Piano Key Weir (PKW) has emerged as a cost effective and viable solution for dam rehabilitation and new projects with high level of space constraints. The geometrical dimensions of PKW are main factors affecting their discharging capacity. Since, it is a relatively new type of weir that has only been developed in recent years, the description of the effect of its geometrical parameters is still immature. The geometric designs of these weirs presented in the literatures incorporate only linear floor slope of the keys. For better understanding of the influence of curvilinear shapes of outlet key slopes on discharge capacity, an experimental study was conducted. In general, the results showed that PKW with ogee shaped outlet key is more efficient than the linear shaped counterpart for heads higher than its design head. The maximum increase in coefficient of discharge of weir model with curvilinear outlet key in comparison to model with linear outlet key was 5.2%.*

Keywords: *Piano key weir, Hydraulic design, Weir discharge efficiency.*

1. INTRODUCTION

The ability to control water through structures like dams has facilitated the development of human societies throughout history. The spillway or weir is the safety component of the dam that releases flood in a controlled manner. It consists of a passage constructed in the dam body or in the reservoir bank to allow the evacuation of extreme floods. The reports on incidents of dam failures in recent past have shown that inadequate capacity of the spillway was the cause for a third of these accidents (Schleiss, 2011). The strong motivation to maximize the discharging capacity of spillway have resulted in development of various non-linear crest geometries. The Piano Key Weir (PKW) is a modified labyrinth-type weir that makes use of inclined apexes in order to maximize the allowable weir length that can fit in a given channel width. The PKWs have emerged as an innovative and viable solutions for both dam rehabilitation and new projects with space constraints.

The concept of PKW was presented more than 20 years ago by Hydrocoop (Blanc & Lempérière, 2001; Lempérière & Ouamane, 2003). After a few years of elaborate conceptualization, the first PKW was built by Electricité de France (EDF) in 2006 at Goulours dam in France (Laugier, 2007). Many other PKWs are currently under different stages of design, construction and operation around the world: France, Vietnam, India, and South Africa (Singhal & Sharma, 2011; Khanh, 2013; and Erpicum, et al 2017).

The geometry of PKW is complex as it is governed by large sets of parameters. A naming convention was specifically developed in some laboratories to amalgamate the notations (Pralong, et al 2011). The chief geometric parameters are the width of the inlet and outlet keys, denoted W_i and W_o respectively, the height of weir P, depth below inlet key P' the width of one cycle or PKW unit W_u, the total number of PKW units N_u, the total stream wise crest length B, the lengths B_o and B_i of the up- and downstream overhangs, the base length B_b and the thickness of wall T. Most of these defining parameters for PKW with three cycles are depicted in Figure 1. The width of a PKW unit W_u is equal to $W_i + W_o + 2T$ and the total width W of the weir is equal to $N_u \times W_u$. The developed crest length L_u of a PKW unit is equal to $W_u + 2B$ and the total developed crest length L of the weir is calculated as $N_u \times L_u$ (Erpicum, et al 2017).

A series of both experimental and numerical studies have been conducted by various investigators to enumerate the discharge capacity of the PKW. Leite Ribeiro et al (2012) conducted a set of experiments on several PKWs with overhangs on both upstream and downstream (Type-A) and identified the primary and secondary parameters affecting the flow. They formulated a head–discharge relation for PKW by providing an expression for increased discharge ratio of PKW with respect to a rectangular sharp-crested weir. Similarly, other comprehensive and systematic model tests have resulted in more complex design equations with a rather good accuracy within the limits of the parameter range specified by the researchers (Cicero & Delisle, 2013; Crookston, et al 2018 and Kumar, et al 2019). A parametric study to investigate thirty-one different models of this weir with different height, keys widths and overhangs lengths of the PKW with *L/W* equal to 5 was conducted at University of Liege, Belgium (Machiels, et al 2014). Mahabadi & Sanayei (2020) evaluated the implementation of bilateral side slopes in the outlet key and its impact on efficiency through numerical simulations.

The available literatures indicate that all the studies conducted to date have only incorporated PKWs with linear slopes of the inlet and outlet keys. Therefore, the influence of curvilinear shapes of key slopes on its discharge capacity is not known. This study presents the experimental results for the discharge efficiency of PKW with linear and curvilinear slopes in the outlet key.

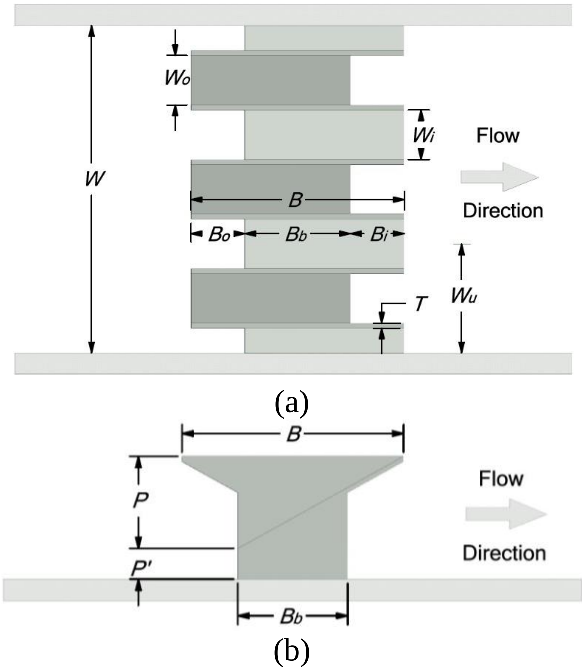

Figure 1 - Typical geometry of PKW: (a) plan; (b) side-elevation.

2. METHODOLOGY

2.1. Geometry of Models

In this study, two laboratory-scale models of Type-A PKW with varying profiles of slope in the outlet key have been tested. The first PKW model with three cycles and standard linear slopes in both inlet and outlet keys is identified as PKW-L. All the parameters of this model are similar to the one used by Kumar, et al (2019) and are as follows: B = 0.254m, $B_i = B_o$ = 0.064m, $W_i = W_o$ = 0.059m, P = 0.105m, P' = 0.035m and W = 0.39m. Another model with all geometric parameters consistent with the PKW-L except for the slope profiles of outlet keys is referred to as PKW-CL. An overview of both these models are depicted in Figure 2 (a and b).

The curvilinear profile of the outlet key slopes selected for PKW-CL weir was the downstream ogee profile based on Waterways Experiment Station (WES) standard spillway shape given the following equation.

$$X^n = K \times H_d^{(n-1)} \times Y \tag{1}$$

Where, X and Y are coordinates of profile with the origin at the highest point of the outlet key crest. H_d is the selected design head for the profile. K and n are parameters which depend on the slope of upstream face and were taken corresponding to vertical slope as K = 2 and n = 1.85. For reverse curve, the radius r was taken as half of H_d and the angle of 60° was provided (see Figure 2c).

This shape is derived from lower surface of a free-falling nappe and is known for its ability to pass flows efficiently and safely (Savage & Johnson, 2001). A reverse curve was provided at the lower end of the key slope to smoothly guide the falling jet towards downstream. The schematic diagram with details of the curvilinear profile has been depicted in Figure 2 (c). The design head over the crest (H_d) had to be fixed to derive the profile of the slope for the model with curvilinear outlet keys. Since, PKWs are highly efficient at lower heads, majority of these weirs developed till date have total design head to weir height ratio (H_d/P) of less than one (Crookston, et al 2019). Accordingly, the profile of the outlet slopes of this model was assumed for H_d/P value of 0.5.

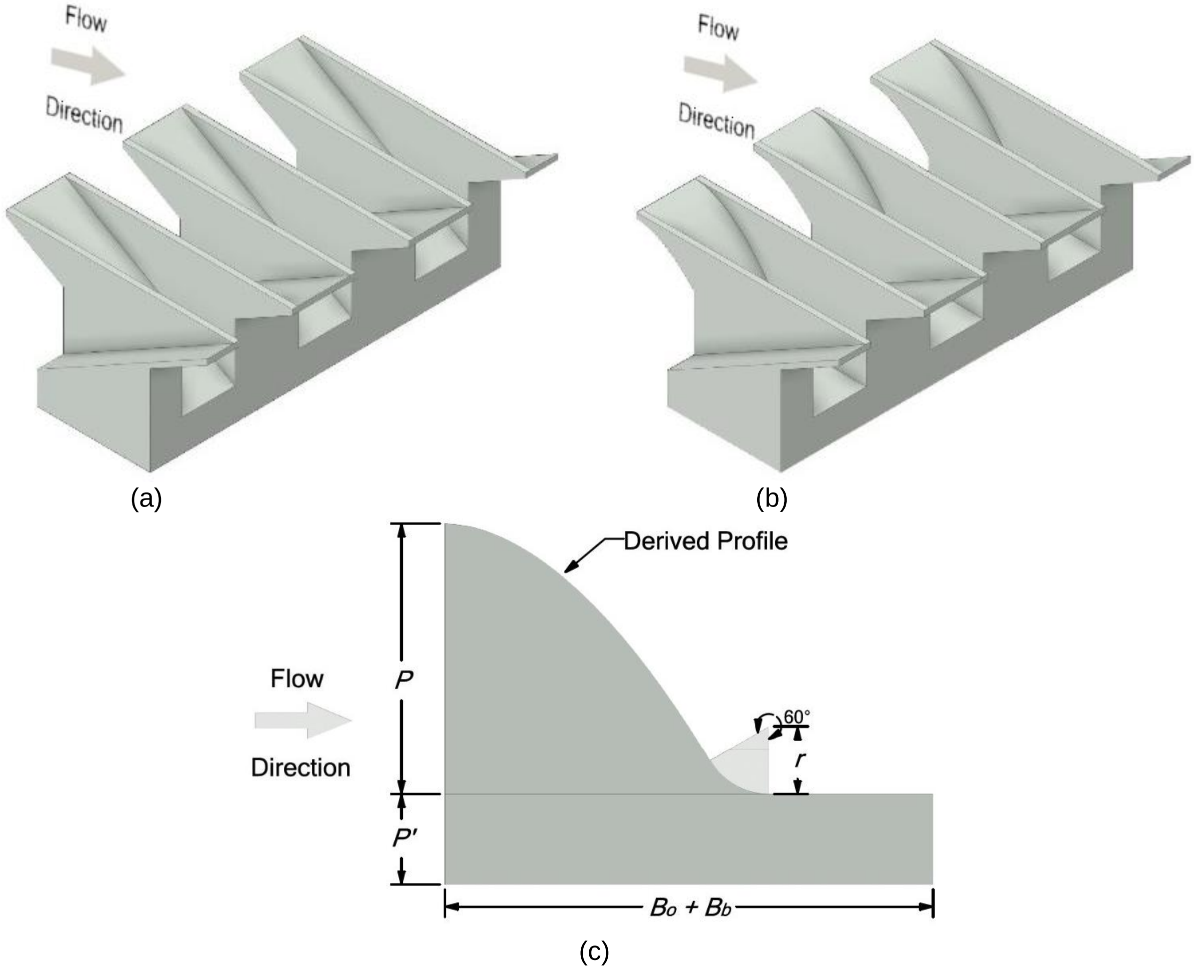

Figure 2 - (a) Overview of PKW-L weir model; (b) overview of PKW-CL weir model; (c) profile of outlet key for PKW-CL weir model.

2.2. Experimental Setup

The experiments were conducted in a rectangular flume of length 15m, width 0.39m and height 0.52m. A major section of flume consisted of glass side walls which allowed for visualization of flow over the weir. A recirculating tank was provided at the end of the flume for the storage of water and re-circulation of flow. A pump was installed to supply water through an inlet pipe having inner diameter of

0.1m. The discharge was regulated using a control valve fitted in this inlet pipe. An ultrasonic flow meter with an accuracy of 1% was used to measure the discharge flowing in the pipe. The entrance of the flume was equipped with honeycomb grid walls to minimize the disturbances in the flow as shown in Figure 3. Also, flow straighteners and wave suppressor were provided near the entrance to suppress cross currents and surface disturbances, respectively. A point gauge system having a least count of 0.1mm was used to measure the water level.

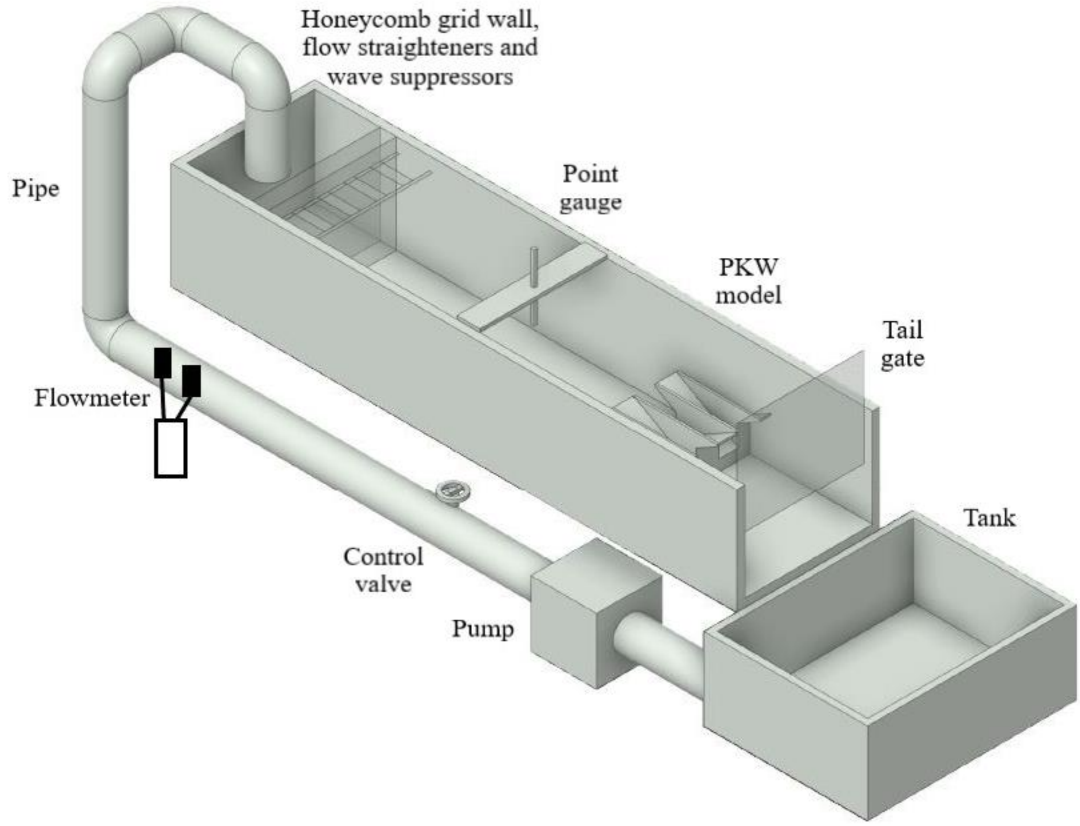

Figure 3 - Schematic of the experimental setup.

The models of the PKW were fabricated using plastic sheets of 6mm in thickness as per geometric dimensions mentioned earlier. For curvilinear slopes, the plastic sheets were heated and then pressed into the desired profile. These weirs were then attached to the base of the flume using sealant to ensure water-tight joints. The point gauge system was positioned at 2×*P* (i.e. 0.21m) upstream from outlet crest to measure the water level. The tests on each PKW model were performed for flows ranging from 5×10^{-3} m^3/s to 35×10^{-3} m^3/s. The point gauge was used to measure the water level for each discharge after the flow had stabilized for a minimum of 15 minutes. At least three readings were taken for the water level consecutively to ensure that steady state had been achieved, given that all the readings were in agreement.

3. RESULTS

The discharge capacity of the PKW can be described by the common weir formulation as given below (Kumar, et al 2019)

$$Q_{PKW} = \frac{2}{3} C_{PKW} W \sqrt{2gH^3} \qquad (2)$$

Where, Q_{PKW} is discharge over the weir, C_{PKW} is coefficient of discharge, g is acceleration of gravity, W is total width of the weir and H is total upstream head.

The coefficient of discharge (C_{PKW}) lumps the effect of geometric parameters on the discharge efficiency of the weir. The variation of this coefficient for PKW-L and PKW-CL models with the normalized total head given by the ratio *H/P* is shown in Figure 4. According to the data observed, the discharge efficiency of PKW-L was higher for the lower head values of $H/P < 0.46$. As the head increased, PKW-CL became more efficient than the former for $H/P > 0.46$. Nevertheless, both of these weirs showed similar trends of significant loss of efficiency with increasing head.

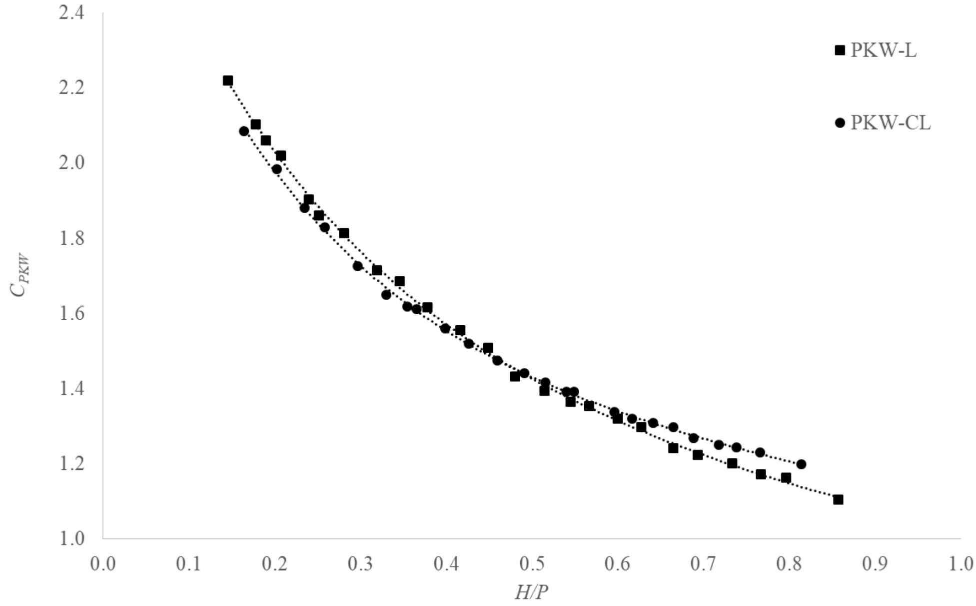

Figure 4 - C_{PKW} versus *H/P* data for PKW-L and PKW-CL weirs.

The comparisons of discharge efficiencies as the ratio of C_{PKW} value of PKW-CL with respect to that of PKW-L weir are presented in Figure 5. These results suggest that the discharge efficiency of PKW-CL is relatively enhanced as the head over the weir becomes equal to or greater than the design head of the outlet key slopes. PKW-CL shows a maximum increase in efficiency by 5.2% for $H/P = 0.81$. However, ogee profile provided in the outlet keys has a negative impact on the discharge capacity for hydraulic heads below its design head for the tested model.

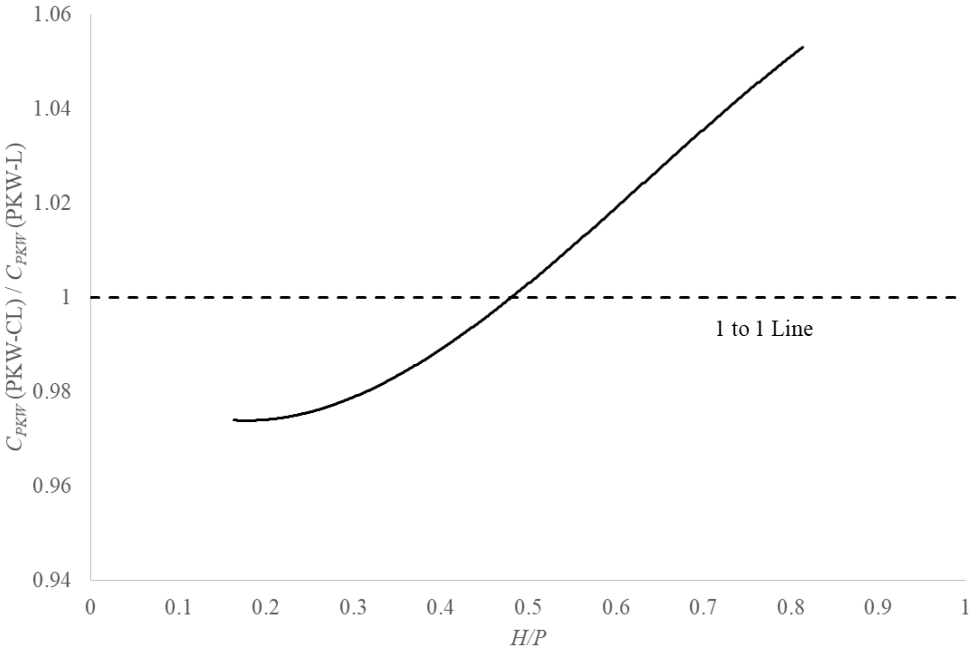

Figure 5 – C_{PKW} (PKW-CL) / C_{PKW} (PKW-L) versus *H/P* data.

4. DISCUSSION

The flow passing over a PKW is three-dimensional and comprises of following portions: a normal jet flow over the up- and downstream crests and a lateral jet flow over the sidewalls. At low upstream heads, the normal and lateral jets flowing into the outlet key are close to the walls. As the head increases, these jets spring and collide with each other in the downstream region of the outlet key. This interference of jets in the downstream of outlet crest reduces the discharging ability of the outlet portion. Thus, the significant loss in the efficiency of both PKW models with increasing head can be attributed to the nappe interference.

The influence of curvilinear outlet key profiles on the discharge efficiency of the PKW can, in part, be explained as follows. The shape of the ogee profile is derived from the lower surface of an aerated nappe flowing over sharp crest for a single upstream head. So, for the heads lower than this design head, the efficiency is reduced due to the bed surface resistance. At higher heads, this resistance to the flow over the key slope diminishes and its ability to evacuate the flow without separation is improved. Furthermore, the slopes of the curvilinear profiles are steeper than the linear profile for major portion of the outlet key and hence allows for rapid exit of flowing stream. Consequently, the limits of nappe interference for PKW-CL were observed to have moved less towards the downstream than for PKW-L under similar high flow conditions as shown in Figure 6 (a and b).

(a) (b)

Figure 6 - Limit of nappe interference for $Q_{PKW} \approx 3\times10^{-2}$ m³/s (a) PKW-L at H/P= 0.76; (b) PKW-CL at H/P = 0.73.

5. CONCLUSION

To study the effect of shape of outlet key slope on the discharge capacity of PKW, two experimental models with linear slope (PKW-L) and curvilinear slope (PKW-CL) were tested. The conclusions based on the results from this study are as follows:

- For flow conditions resulting in hydraulic head (H) higher than the design head (H_d), the discharge efficiency of PKW-CL became moderately higher than PKW-L. The maximum increase in coefficient of discharge (C_{PKW}) of PKW-CL in comparison to PKW-L was 5.2% for 0.16< H/P <0.81.
- The ogee profile of PKW-CL had negative influence on its discharge efficiency for flows with $H < H_d$ due to bed surface resistance at outlet. Thus, its C_{PKW} value was less than that of PKW-L for these low flow conditions.
- Both weirs showed considerable decrease in their discharge capacity with increase in H because of interference of normal and lateral jets flowing into the outlet keys. However, the limit of nappe interference in case of PKW-L was observed to be further downstream than in PKW-CL for high flows leading to better performance of the latter.

This paper presents results for a single PKW model with an ogee shaped outlet keys. Tests on more curvilinear profiles will help to reinforce the findings of the present study. Further, additional research to investigate modifications of the general PKW elements is deemed necessary to further enhance its hydraulic behaviour. More detailed evaluations of these variations will provide greater comprehension towards the optimal geometric design of these weirs.

6. REFERENCES

Blanc, P. and Lempérière, F. (2001). Labyrinth spillways have a promising future. *Int. J. Hydro. Dams,* 8(4), pp. 129-131.

Cicero, G. M. and Delisle, J. R. (2013). Discharge characteristics of piano key weirs under submerged flow. In: *Labyrinth and Piano Key Weirs II – PKW 2013.* Leiden: CRC Press, p. 101–109.

Crookston, B. M., Anderson, R. M. and Tullis, B. P. (2018). Free-flow discharge estimation method for Piano Key weir geometries. *J. Hydro Environ. Res.,* Volume 19, p. 160–167.

Crookston, B. M., Erpicum, S., Tullis, B. P. and Laugier, F. (2019). Hydraulics of Labyrinth and Piano Key Weirs: 100 Years of Prototype Structures, Advancements, and Future Research Needs. *J. Hyd. Eng.,* 145(12), p. 02519004.

Erpicum, S., Archambeau, P., Dewals, B. and Pirotton, M. (2017). *Hydraulics of Piano KeyWeirs: A review.* In: *Labyrinth and Piano Key Weirs III – PKW 2017.* London, CRC Press, p. 27-36.

Khanh, M. H. T. (2013). The Piano KeyWeirs: 15 years of Research & Development – Prospect. In: *Labyrinth and piano key weirs II – PKW 2013.* London: CRC Press, p. 3–14.

Kumar, B., Kadia, S. and Ahmad, Z. (2019). Evaluation of discharge equations of the piano key weirs. *Flow Measurement and Instrumentation,* Volume 68, p. 101577.

Laugier, F. (2007). Design and construction of the first Piano Key Weir (PKW) spillway at the Goulours dam. *Int. J. Hydro. Dams,* 14(5), pp. 94-101.

Leite Ribeiro, M., Pfister, M., Schleiss, A. J. and Boillat, J. L. (2012). Hydraulic design of a-type piano key weirs. *J. Hydraul. Res.,* 50(4), p. 400–408.

Lempérière, F. and Ouamane, A., (2003). The piano keys weir: a new cost-effective solution for spillways. *Int. J. Hydro. Dams,* 10(5), pp. 144-149.

Machiels, O., Erpicum, S., Dewals, B., and Pirotton, M. (2014). Experimental observation of flow characteristics over a piano key weir. *J. Hydraul. Res.,* 49(3), p. 359–366.

Mahabadi, N. A. and Sanayei, H. R. Z.(2020). Performance evaluation of bilateral side slopes in piano key weirs by numerical simulation. *Modeling Earth Systems and Environment,* Volume 6, p. 1477–1486.

Pralong, J., Vermeulen, J., Blancher, B., Laguer, F., Erpicum, S., Machiels, O., Pirotton, M., Boillat, J., Ribeiro, M.L., and Schleiss, A. (2011). A naming convention for the Piano Key Weirs geometrical parameters. In: *Labyrinth and piano key weirs – PKW 2011.* London: CRC press, p. 271–278.

Savage, B. M. and Johnson, M. C. (2001). Flow over ogee spillway: Physical and numerical model case study. *J. Hyd. Eng.,* 127(8), p. 22378.

Schleiss, A. J., (2011). From Labyrinth to Piano KeyWeirs – A historical review. In: *Labyrinth and piano key weirs – PKW 2011.* London: CRC Press, p. 3–15.

Singhal, G. and Sharma, N. (2011). Rehabilitation of Sawara Kuddu Hydroelectric Project – Model studies of Piano KeyWeir in India. In: *Labyrinth and piano key weirs – PKW 2011.* London: CRC Press, p. 241–250.

8th International Junior Researcher and Engineer
Workshop on Hydraulic Structures
ISBN: 978-0-578-37416-1
https://doi.org/10.26077/f0a0-2bf7

Large-Scale Morphodynamic Impact of Groups of Piers on Low-Land Rivers

Abdelrahman Abdou[1,2], Daniel Valero[1,3] and Alessandra Crosato[1,4]
[1]Water Resources and Ecosystems Department,
IHE Delft Institute for Water Education,
the Netherlands
[2]Channel Maintenance Research Institute
National Water Research Center
Egypt
[3]Institute for Water and River Basin Development (IWG),
Karlsruhe Institute of Technology (KIT),
Germany
[4]Faculty of Civil Engineering and Geosciences,
Delft University of Technology,
the Netherlands
E-mail: abdouhosny1991@gmail.com

Abstract: *This study explores the morphodynamic impact of groups of piers with different configurations (i.e., span characteristics, number of piers, and different reach locations) in a river cross section. It focuses on sandy low-land rivers presenting steady alternate bars and low Froude numbers. A 2DH (vertically integrated) numerical physics-based model (Delft3D) is used to simulate a straight channel, which is inspired from a Nile River reach in Egypt, downstream of the High Aswan Dam. The results show the formation of a forced bar upstream and downstream of the piers and increased deposition over the existing steady bars with different intensities. The nearest bars to the structures are the most affected ones. Large spans between bridge piers and more uniform pier distribution are found to decrease the deposition and its extension, hence reducing dredging investments for navigability.*

Keywords: *Bars, Bridge Piers, Delft3D, River Engineering.*

1. INTRODUCTION

Hydraulic structures, such as bridge piers, weirs, and groynes, induce changes in bed topography that can lead to erosion and, as a consequence, also the bank alignment of rivers. These changes are caused by erosion and sedimentation in different zones of the river. Some of them are local, like the scouring in the vicinity of bridge piers, whereas others present larger-scale features arising from bed erosion, sedimentation, bank erosion, and bar formation upstream and downstream of the structure. Several works have been carried out in the past to study the local hydrodynamic and morphodynamic impact of bridge piers (Melville, 1975, Breusers et al., 1977, Melville and Chiew, 1999, Oliveto and Hager, 2002, Hager and Unger, 2010, Khosronejad et al., 2012) with different approaches, including numerical models, physical models, and field studies.

Most studies focus on local hydraulic and morphological effects of bridge piers and only a few assess the larger-scale impact of these structures. Mosselman and Sloff (2002) demonstrate that indeed local scour can affect the large-scale morphology of rivers where the flow tends to concentrate in local scour holes causing upstream erosion and a forced bar further downstream. Azhar (2018) shows that installing a single bridge pier in morphodynamically unstable rivers leads to the formation of local steady bars upstream and downstream of the structure and of migrating bars further downstream. However, in morphodynamically stable systems (Crosato and Mosselman, 2020), only the local upstream and downstream steady bars form and no bars develop further downstream, either migrating or steady. Bed protection around bridge piers only prevents local scouring around the structure but does not prevent downstream bar formation (Azhar, 2018).

In morphodynamically unstable rivers (Crosato and Mosselman, 2020), bridge piers alter the flow structure in their vicinity, with morphological effects which are noticeable also further downstream. When the flow meets a bridge pier, a stagnation point occurs, with subsequent increase in axial velocity. This impinges the bed creating a scour hole. The scour hole generates a horseshoe vortex, which entrains the sediment near the pier, transporting it downstream. Flow separation occurs around the pier and, as a result, wake vortices are formed at its downstream face, which entrain sediment further downstream (Melville, 1975, Melville and Coleman, 2000).

There is a research gap that requires further investigation on the large-scale impact of multiple bridge piers in realistic sandy low-land rivers with steady bars. Using a physics-based numerical model, this research studies how different engineering situations related to bridge piers installation (span, number of piers, and location) affect the large-scale morphodynamics of sandy low-land rivers. This research builds on a virtual flume, with characteristics inspired by a real river reach assumed as representative of low-land sandy rivers.

2. METHODOLOGY

The main investigation tool used in this study is a 2DH physics-based numerical model developed using the open-source Delft3D software (www.deltares.nl). A virtual straight channel, here referred to as the "numerical flume", is set up for the investigation using a Nile River reach downstream of the High Aswan Dam (HAD) as a reference. All physical variables (average reach-scale width, sediment size, slope, among others) of the numerical flume are based on available data from the selected river reach. Calibration coefficients and numerical parameters like the values of roughness coefficient, transverse bed slope, sediment transport formula, and the spiral flow coefficient are selected based on a morphodynamic calibration with the aim to reproduce the measured 2D river bed topography of the selected reach. Further details on the calibration procedure can be found in the work of Abdou (2021). The so-developed numerical flume is then used as an experimental facility to study a number of scenarios with the aim to infer the role of several factors, such as different bridge pier configurations, varying numbers of piers and spans between piers, and different pier locations with respect to existing steady bars.

2.1. Reference low-land river

The reference Nile River reach extends from 14 km to 22 km downstream of HAD, for a total length of 8 km. The upstream boundary of the reach is located at 24° 9' 1.54" N latitude and 32° 52' 43.60" E longitude, while the downstream boundary is located at 24° 13' 4.20" N latitude and 32° 51' 55.29" E longitude. The river reach is almost straight, with a sinuosity index (ratio between the actual river length and the straight length) of 1.004, with a variable channel width, ranging from 558 m to 844 m. Due to the presence of the large reservoir, the current discharge regime is strongly regulated. Considering 2004 as a typical hydrological year and given that there is available data for that year, the maximum daily averaged discharge (2,893 m^3/s) and the minimum discharge (868 m^3/s) are considered as references. Information on bed sediment characteristics were obtained from Abdel-Fattah et al. (2004) who describe the results of field measurements carried out in 1997, 15 km downstream of HAD (within the selected reach). According to them, the average median diameter of the river bed sediment is 0.378 mm, which corresponds to medium sand, based on (ISO 14688-1, 2002) classification. The average longitudinal surface water slope is 3.510^{-5}m/m. These measurements were assumed to be representative of the reach taken into consideration.

2.2. Numerical model

The Delft3D hydrodynamic model is based on the depth-averaged momentum equations [Eqs. *(1) and (2)]*, assuming the fluid is incompressible, pressure is hydrostatic and the flow is shallow ; coupled with the continuity equation *[Eq. (3)]* (Schuurman et al., 2013, Duró et al., 2016):

$$\frac{\partial u}{\partial t}+u\frac{\partial u}{\partial x}+v\frac{\partial u}{\partial y}+g\frac{\partial z_w}{\partial x}-\nu_H\left(\frac{\partial^2 u}{\partial x^2}+\frac{\partial^2 u}{\partial y^2}\right)+\frac{gu\sqrt{u^2+v^2}}{C^2h}+F_x=0 \qquad (1)$$

$$\frac{\partial v}{\partial t}+u\frac{\partial v}{\partial x}+v\frac{\partial v}{\partial y}+g\frac{\partial z_w}{\partial y}-\nu_H\left(\frac{\partial^2 v}{\partial x^2}+\frac{\partial^2 v}{\partial y^2}\right)+\frac{gv\sqrt{u^2+v^2}}{C^2 h}+F_y=0 \tag{2}$$

$$\frac{\partial h}{\partial t}+\frac{\partial hu}{\partial x}+\frac{\partial hv}{\partial y}=0 \tag{3}$$

Where u is the depth-averaged flow velocity (m/s) in x-direction (longitudinal), v is the depth-averaged flow velocity (m/s) in y-direction (transverse), z_w is the water level in the vertical direction (m), ν_H is the horizontal eddy viscosity (m^2/s), g is the gravitational acceleration (m/s^2), h is the water depth (m), F_x and F_y are the acceleration terms resulting from non-uniform horizontal velocity in the perpendicular direction (m/s^2).

In this research, Engelund and Hansen's (1967) formula is used for sediment transport calculations. This formula was selected among others after a calibration stage.

$$q_s=\frac{0.05\propto u^5}{\sqrt{g}C^3\Delta^2 D_{50}} \tag{4}$$

Where q_s is the sediment transport rate per unit width (m^2/s), $\propto$ is a calibration factor (-), C is the Chézy friction coefficient (m$^{0.5}$/s), Δ is the relative sediment density (-) and D_{50} is the median grain size (m).

2.3. Numerical flume setup

The virtual straight channel is set up to investigate different research scenarios focusing on selected variables, thus under well-defined flow conditions and allowing changing one parameter at a time (Table 1). The numerical flume length is 16 km, which is assumed to be long enough to capture the large-scale impact of bridge piers upstream and downstream, including the steady bars developing in the river. The width is 650 m, obtained by taking the average river width of several cross sections generated every kilometre on the selected Nile River reach. The grain size is assumed uniform and the river banks are assumed to be fixed. Horizontal eddy viscosity and horizontal eddy diffusivity are assumed to be constant. Given the scope of this study, these are reasonable assumptions, commonly embraced in morphodynamic studies (Schuurman et al., 2013, Duró et al., 2016, Azhar, 2018).

2.3.1. Computational grid

The size of the considered bridge piers is small compared to the river size and hence the model requires relatively high resolution. To avoid excessively long computational times, a rectangular grid is set with three domains (Figure 1) connected using the *domain decomposition* option, which is a tool in Delft3D that connects domains with different cell sizes (Figure 1). The coarse domain covers the majority of the reach, except from the part of the reach around the bridge piers that is covered by the transitional and fine domains. Cell dimensions of the coarsest domain are 59 m and 29.55 m in x and y directions, respectively. This means that the transverse section is simulated with 22 cells in y direction. The transitional domain is created to connect between the coarse and the fine domains. Its cells are refined with a factor of 3 in both directions, the grid cell dimensions being 19.67 m and 9.85 m in x and y directions, respectively. The fine grid provides finer resolution around the bridge piers, with cell dimensions of 6.56 m and 3.28 m in x and y directions, respectively. The fine grid domain, where the bridge piers are installed, is 354 m long, while the transitional domain is 590 m long upstream and 590 m long downstream of the fine domain. The coarse domain length upstream and downstream of the bridge piers depends on the location of the bridge piers, which is different for different scenarios (Section 2.4). The computational grid size falls within the range of the recommended values regarding orthogonality, aspect ratio, and smoothness, with values 0.0, 2.0, and 1.0, correspondingly (Deltares, 2014).

2.3.2. Morphological computations

The “morphological factor” is introduced in Delft3D to speed-up the computation of bed level changes (morphological changes) (Ranasinghe et al., 2011, Carraro et al., 2018). For instance, using a factor equal to 5 means computing the morphological changes with a 5 times faster rate. In practice, the morphological changes that pertain to a certain hydrodynamic time step are multiplied by 5. In this way running a typical hydrological year corresponds to simulating the morphological changes of 5 typical years. This is based on the assumption that the bed level changes are much slower than the changes in water flow which is true only at low Froude numbers. The morphological factor is especially applicable to regulated rivers, with little hydrodynamic variations, like the Nile River in Egypt. From a sensitivity analysis, negligible differences in results were observed for morphological factors of 40, compared to a value of 1 (no morphological acceleration), after carrying out two simulations for 20 morphological years. Consequently, a value of 40 is used herein.

Starting from a flat bed, the average morphological time (scaled-up time after using the morphological factor) that is needed by the model to obtain steady bars, similar to those observed in the real river reach, was estimated over at least 150 years. To avoid re-computing this morphological development for every scenario that was run, the initial river bed with alternate bars was obtained once for all scenarios using a coarser model (only coarse domain, Figure 1), here named “initial bed model”. By running 40 typical years with a morphological factor of 40, the simulation covered 160 “morphological years”. A waving bed with hybrid bars (steady and periodic bars, as defined by Duró et al., 2016) was obtained by adding a groyne 1 km downstream of the upstream boundary. This triggers the formation of hybrid alternate bars that are characteristic of most large low-land rivers (Crosato and Mosselman, 2020). The time step used for this computation was 30 seconds for stability considerations. The equilibrium bed topography obtained with this model was then used as starting condition for all scenario computations. For these, due to the presence of finer grid cells, the time step assigned to the “numerical flume” (with the three domains) was 6 seconds.

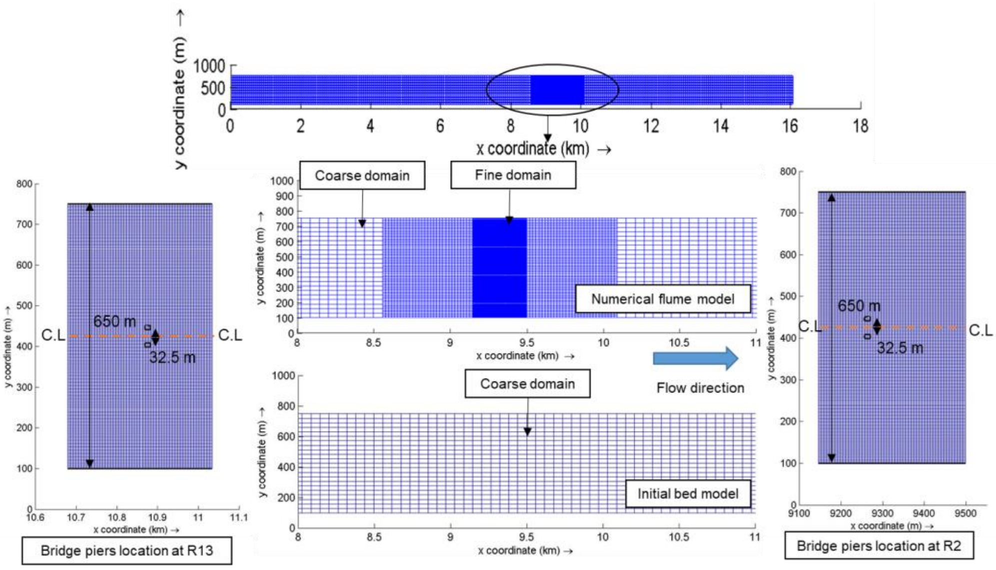

Figure 1 - Computational grid of the numerical flume, initial bed flume models, and bridge piers location at scenarios R2 AND R13 (see Table 1).

2.3.3. Boundary conditions

The total water discharge is assigned as upstream boundary condition and water levels, obtained from the computation of normal water depths, are assigned as downstream boundary condition for all scenarios. The incoming sediment, as well as the outgoing sediment transport rates, are computed at the upstream and downstream boundaries, respectively, using the Engelund and Hansen's (1967) formula. The bridge piers are simulated as thin dams. When introduced in the mesh, thin dams forbid exchange of flow between two adjacent grid cells without affecting the total wet surface and the model volume, which implies that no flow can go through them (Deltares, 2014).

2.4. Scenario definition

The numerical flume is used to study the impact of different spans (distance between bridge piers) on the river morphology and the impact of installing varying numbers of bridge piers in the river cross section, resulting in different obstruction ratios. The obstruction ratio is the ratio between the summation width of the piers in the transverse section and the total numerical flume width. The span between the bridge piers is constant (base-case span), but with a different number of bridge piers in the transverse section (Table 1). The bridge piers are installed at 9.265 km downstream of HAD for all scenarios except R13, for this the bridge piers are located at 10.875 km downstream of HAD. The installation of the piers starts at the centreline of the transverse section depending on the span and number of bridge piers in different scenarios.

All simulations start from a bed with steady and periodic alternate bars, named hybrid bars, to reproduce a realistically large river bed configuration. Table 1 lists the simulated scenarios, R2 being the base-case. For all scenarios, the initial longitudinal bed slope is 3.510^{-5} m/m and the average discharge is 1,837.5 m^3/s, corresponding to the present average discharge of the reference Nile River reach under strongly regulated conditions. The bridge piers are rectangular and their dimensions are 9.84 m for the width (y-direction) and 13.11 m for the length (x-direction).

In simulation R13, the model is used to check the differences between installing the bridge piers in the transitional zone between two successive bars and in the zone near a bar top, where one side of the cross section is occupied by a bar and the other side by a pool, here named "bar-pool zone".

Table 1 Research scenarios.

Group	Initial bed	ID	Bridge span / River width	Number of piers	Obstruction ratio (%)	Flow intensity (u/u_c)
Span sensitivity	B1(*)	R1	0.025	2	3	17.30
		R2	0.05	2	3	20.27
		R3	0.10	2	3	20.54
		R4	0.20	2	3	20.27
		R5	0.40	2	3	20.27
Obstruction (no of piers) sensitivity	B1(*)	R6	0.05	1	1.5	13.51
		R7	0.05	4	6	20.27
		R8	0.05	6	9	20.54
		R9	0.05	8	12	20.81
		R10	0.05	12	18	21.62
		R11	0.05	14	21	21.89
		R12	0.05	16	24	22.16
Zone	B1(*)	R13 (**)	0.05	2	3	17.30

B1 (*) refers to the aforementioned "initial bed" scenario where a system with no piers reaches the steady state, R13 (**) refers to the bar-pool zone scenario, u refers to average approaching velocity, and u_c refers to the average critical velocity.

Each scenario triggers a different morphological alteration of the "numerical flume" bed. The area around the bridge piers is the most affected zone and, therefore, a fixed area is selected around the bridge piers to carry out the numerical analysis for all scenarios. The study area, named "forced bar field", starts 1,500 m upstream of the bridge piers and ends 1,500 m downstream. To quantify the impact of each scenario, a MATLAB script was written to compute the maximum scour depth and the maximum deposition height, in addition to the percentage of deposition area and scour area, relative to the total area under study. Small deposition and scour amplitudes – with alterations smaller than 10 % of the base case normal water depth (0.4 m) – are neglected in the numerical analysis so as to focus on greater impacts.

3. RESULTS AND DISCUSSION

3.1. Span sensitivity scenarios

Five scenarios with different spans are simulated (Table 1), each covering 40 morphological years until the bed changes become negligible, which indicates morphological equilibrium. The model shows deposition zones upstream and downstream of the bridge piers, here named forced bars as in Duró et al. (2016). Scouring on the sides of the piers is also noticed. Deposition is observed mainly on the bar close to the bridge piers, and becomes less significant for the alternate bars that are located further downstream. In relatively small span scenarios, the flow reduces considerably between the bridge piers. Flow velocity at the upstream and downstream side of the piers is lower than around them and, as a result, less sediment is transported in this zone. This leads to larger accumulation of sediment upstream and downstream of the bridge piers (Figure 2). When the span, or distance between the bridge piers increases, the flow between the structures increases. Therefore, more sediment transport occurs with less sediment accumulation as a result.

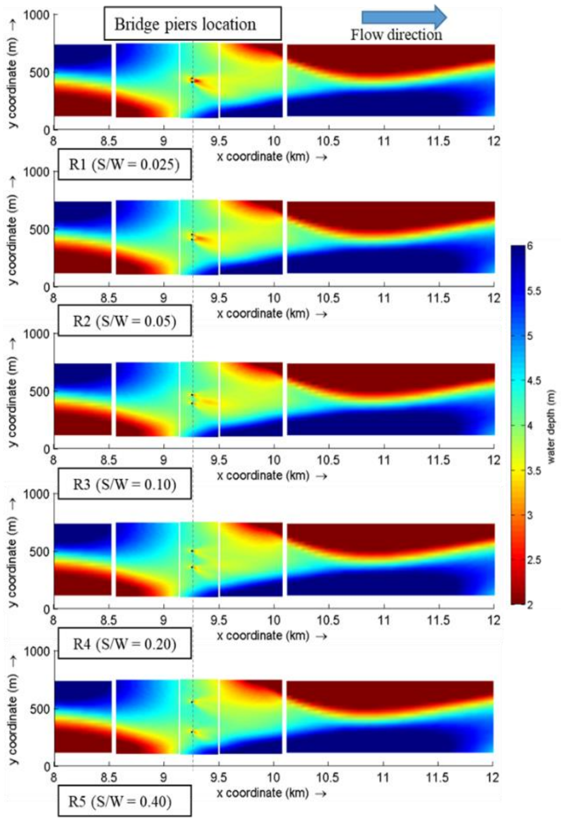

Figure 2 - Water depth of scenarios R1-R5 (“span sensitivity” analysis, see Table 1).

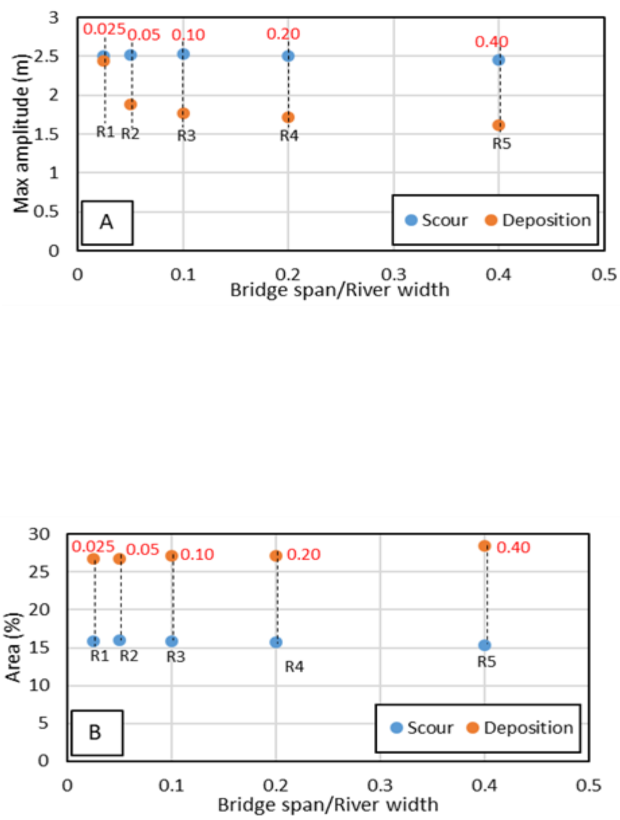

Figure 3 - Numerical analyses of scenarios R1-R5, Bridge span / River width and A) Maximum scour depth and deposition height B) Area of scour and deposition (“span sensitivity” analysis, see Table 1).

Based on the numerical analysis of the forced bar field, the maximum scour depth is larger than the maximum deposition height for all five scenarios, except for R1, for which S/W (Bridge span / River width) equals 0.025, where deposition and scour have approximately the same amplitude (Figure 3A). The maximum scour depth (roughly 2.5 m) is similar in all five scenarios while the maximum deposition height is inversely proportional to the piers span as it changes from 2.44 m at R1 (S/W = 0.025) to 1.61 m at R5 (S/W = 0.40) (Figure 3A). In the forced bars field, the deposition area is always larger than the scour area (Figure 3B). The ratio between these two values is more or less constant, regardless of the changes in bridge piers configuration. The scouring area is localized mainly on the sides of the piers, regardless of the changes in the span between the two piers. It must be noted that grid resolution is not targeted to reproduce local scouring around the piers, but the flow structures resulting from the presence of a bridge that may induce river changes downstream and upstream. The deposition area is slightly increased with increasing span between the bridge piers as it changes from 26.71 % at R1 (S/W = 0.025) to 28.41 % at R5 (S/W = 0.40) (Figure 3B). The depth-averaged velocity in the whole reach ranges between 0.21 m/s at the bar zones and 0.84 m/s at the pool zones.

3.2. Obstruction (number of piers) sensitivity scenarios

Eight scenarios (R6-R12 and R2, Table 1) consider different numbers of bridge piers in the transverse sections but the same span values. Similar to the other runs, these scenarios cover 40 morphological years until the bed topography reaches equilibrium. Increasing the number of bridge piers in the transverse section increases the flow obstruction area. Deposition is formed upstream and downstream of the bridge piers due to relatively low flow velocity, which likewise leads to less sediment transport in this zone. The flow is thus concentrated at the sides of the area occupied by the bridge piers, which leads to an increased erosive force and more sediment transport in the flow-dominated zones.

The maximum deposition height in the forced bar field at R10, R11, and R12 are less than in the other five scenarios (Figure 4A) with more bridge piers in the transverse section. The reason could be that the scenarios with a larger number of bridge piers, as in R10, R11 and R12, results in more uniformly distributed flow in the cross section, due to more uniform hydraulic resistance, so that also the flow velocity becomes more uniform in the transverse section. Thus, the flow is not concentrated on the sides of the cross sections. R12, for instance, with 16 uniformly distributed piers, has the lowest maximum deposition height among all scenarios. The deposition and scour areas increase with increasing number of piers (obstruction ratio), but up to a limit, after which further increasing the number of piers (obstruction ratio) (R12) leads to a decrease in deposition and scour areas. This may be because the flow is distributed more uniformly (Figure 4B). It must be noted that scour and deposition amplitudes below 0.40 m are neglected from this analysis. In general, the amplitude of maximum deposition is lower than the maximum scour amplitude, while the deposition area is always larger than the scour area (Figure 4).

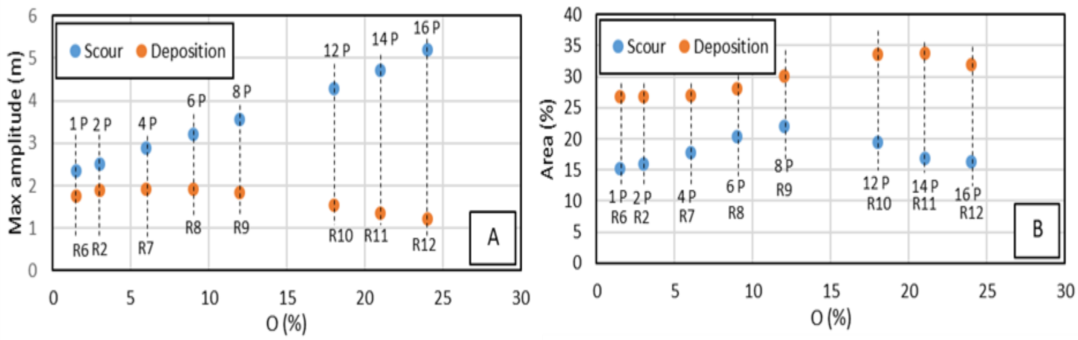

Figure 4 - Obstruction (number of piers) scenarios R6-R12, bridge span / river width and A) maximum scour depth and bed level rise, B) area of scour and deposition (“obstruction sensitivity” analysis, see Table 1). (P) refers to the number of bridge piers at each scenario.

3.3. Piers locations scenarios

In the previous simulations, the piers were installed in the transitional zone between two bars. However, in one scenario (R13, Table 1) the piers were installed near a bar top. In this zone there is a bar on one side and a pool on the other side (“bar-pool zone”, see Figure 5). Again, the simulation covers 40 years. The main effect of bridge piers located in the bar-pool zone is extra deposition over the bar near the piers. In this scenario, the bridge piers cause deposition also above the hybrid bars further downstream, although with lesser amplitude. The numerical analysis shows lower maximum scour depth in this scenario (0.83 m), while the maximum scour depth in R2 (equivalent transitional zone scenario with similar transverse pier distribution) is 2.52 m. The maximum deposition height is 2.14 m, larger than in R2 (1.88 m). Percentages of deposition and scour areas in the bar-pool zone scenario (R13) in the forced bar field are 22.18 % and 13.13 %, respectively, and thus less than in R2 in which the deposition and scour areas, occupy 26.8 % and 15.8 % of the area, respectively. Thus, locating the piers in the transitional zones between two bars increases the surface where morphological changes occur.

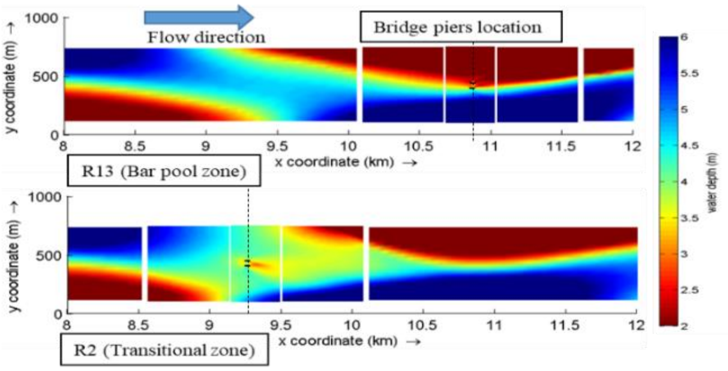

Figure 5 - Water depth for case R2 (piers in transitional zone) and R13 (piers in bar-pool zone).

4. CONCLUSIONS

This study investigates the effects of pier-span to river-width ratio and the effects of obstruction rate (by increasing the number of piers) on equilibrium river morphology. The results show that at low-land river conditions the span between bridge piers controls deposition and scour areas around the structures. Relatively small span values result in reduced flow between bridge piers compared to the flow at the side of the area occupied by the piers. This yields a higher maximum bed level rise downstream. The scour area and the maximum scour depth are minimally affected by the distance between bridge piers. Increasing their number (with constant span and dimensions) increases the extension of the deposition and scour areas, and the maximum deposition height, but up to a limit. With a further increase in pier number, the flow may become more uniform where the deposition area, bed level rise and scour area decreases.

An additional simulation considers bridge piers installed in a bar-pool zone, whereas in the other scenarios the piers were placed in a transitional zone between two successive bars. The results show that if the piers are located in a bar-pool zone, the deposition area, scour area, and maximum scour depth are smaller than if they are located in the transitional zone. The results suggest that bridge piers in the bar-pool zone may have lower impact on the river bed than bridge piers in the transitional zone.

Installation of bridge piers increases the deposition over the hybrid bar present in the river, with the nearest bars being the most affected ones. In all simulations, the deposition area is always larger than the scour area. Large spans between uniformly distributed bridge piers would decrease the deposition area and its elevation, hence reducing dredging investments for navigability. Thus, not only the diameter of piers affects the resulting river changes, but also their arrangement, as is demonstrated in this research. Installation of bridge piers in bar-pool zones can decrease the impact of the bridge piers. This study includes simplifications, for example: assuming uniform sediment size and fixed banks. Since any river has heterogeneous sediment, it is recommended to consider the different sediment sizes and include the effect of bank erosion in future studies. Besides, cell resolution may not be able to finely capture local scouring around structures but, instead, is targeted to resolve changes in bulk quantities of the flow that may lead to downstream river changes.

ACKNOWLEDGEMENTS

This research was funded by the Orange Knowledge Programme (Dutch Ministry of Foreign Affairs), and has benefited from computational resources provided by SURFsara.

REFERENCES

Abdelfattah, S., Amin, A. and Van Rijn, L. (2004). *Sand transport in Nile river, Egypt*, Journal of Hydraulic Engineering, 130, 488-500.

Abdou, A. (2021). *Large-Scale Morphodynamic Impact of Groups of Piers on Low-Land Rivers.*, Msc Thesis WSE-HERBD-21.01,IHE Delft, the Netherlands.

Azhar, F. (2018). *Morphodynamic changes around a bridge pier*, Msc Thesis WSE-HERBD-18.03,IHE Delft, the Netherlands

Breusers, H., Nicollet, G. and Shen, H. (1977). *Local scour around cylindrical piers*, Journal of Hydraulic Research, 15, 211-252.

Carraro, F., Vanzo,D., Caleffi, V., Valiani, A. and Siviglia, A. (2018). *Mathematical study of linear morphodynamic acceleration and derivation of the MASSPEED approach*. Advances in Water Resources, 117, 40-52.

Crosato, A. and Mosselman, E. (2020). *An integrated review of river bars for engineering, management and transdisciplinary research.* Water, 12, 596.https://doi.org/10.1016/j.advwatres.2018.05.002.

Deltares (2014). *Delft3D flow user manual*, Delft, The Netherlands.

Duro, G., Crosato, A. and Tassi, P. (2016). *Numerical study on river bar response to spatial variations of channel width*, Advances in Water Resources, 93, 21-38.

Engelund, F. and Hansen, E. (1967). *A monograph on sediment transport in alluvial streams*, Technical University of Denmark Ostervoldgade 10, Copenhagen K.

Hager, W.H. and Unger, J. (2010). *Bridge pier scour under flood waves*, Journal of Hydraulic Engineering, 136, 842-847.

ISO 14688-1(2002). *Geotechnical investigation and testing – Identification and classification of soil – Part 1: Identification and description*, International Organization for Standardization (ISO).

Khosronejad, A., Kang, S. and Sotiropoulos, F. (2012). *Experimental and computational investigation of local scour around bridge piers*, Advances in Water Resources, 37, 73-85.

Melville, B. (1975). *Local scour at bridge sites*, University of Auckland, Department of civil engineering.

Melville, B.W. and Chiew, Y.-M. (1999). *Time scale for local scour at bridge piers*, Journal of Hydraulic Engineering, 125, 59-65.

Melville, B. W. & Coleman, S. E. (2000). *Bridge scour*, Water Resources Publication.

Meyer-Peter, E. and Müller, R.(1948). *Formulas for bed-load transport*, IAHSR 2nd meeting, Stockholm, appendix 2, 1948. IAHR.

Mosselman, E. and Sloff, C. (2002). *Effect of local scour holes on macroscale river morphology*, River Flow, 2002. 767-772.

Oliveto, G. and Hager, W.H. (2002). *Temporal evolution of clear-water pier and abutment scour*, Journal of Hydraulic Engineering, 128, 811-820.

Ranasinghe, R., Swinkels, C., Luijijendijk, A., Bosboom, J., Roelvink, D., Stive, M. and Walstra, D. (2011). *Morphodynamic upscaling with the MORFAC approach: dependencies and sensitivities*. Coastal Eng., 58 (8), 806-811, 10.1016/j.coastaleng.2011.03.010.

Schuurman, F., Marra, W.A. and Kleinhans, M.G. (2013). *Physics-based modeling of large braided sand-bed rivers: Bar pattern formation, dynamics, and sensitivity*, Journal of geophysical research: Earth Surface, 118, 2509-2527.

8th International Junior Researcher and Engineer Workshop on Hydraulic Structures
ISBN: 978-0-578-37416-1
https://doi.org/10.26077/14a8-743d

Three-dimensional characterization of laboratory scour holes around bridge piers

Ana Margarida Bento[1,2,3,*], Teresa Viseu[1], João Pedro Pêgo[2,3] and Lúcia Couto[1]

[1]Water Resources and Hydraulic Structures Division, Hydraulics and Environment Department, National Laboratory of Civil Engineering
1700-066 Lisboa
PORTUGAL
[2]Hydraulics, Water Resources and Environmental Division, Civil Engineering Department, Faculty of Engineering of the University of Porto
4400-465 Porto
PORTUGAL
[3]Interdisciplinary Centre of Marine and Environmental Research of the University of Porto, 4450-208 Matosinhos, Portugal
*Current address: Institute for Sustainability and Innovation in Structural Engineering, University of Minho
4800-058 Guimarães
PORTUGAL
E-mail: ana.bento@fe.up.pt

Abstract: *The presence of a bridge foundation leads to the formation of a scour hole, from which entrainment and transport of sediments are controlled by the turbulent structures therein developed. Hence, once formed, these scour holes interfere significantly with the scouring process in several ways, for instance, by modifying the incoming flow patterns. Therefore, a three-dimensional survey of the scour hole and the characterization of the deposition features is essential for prevention and safety control purposes. To investigate this, scouring experiments around two oblong bridge piers were performed in a tilting flume of the Portuguese National Laboratory of Civil Engineering (LNEC), under live bed flow conditions. A comprehensive characterization of laboratory scour holes was performed using two advanced image-based measuring techniques, namely close-range photogrammetry and the Kinect V2 sensor. The produced 3D bed morphology models provided detailed measurements, with significant accuracy, with quite similar results between the characterization approaches. A database for calibration and validation of numerical models is thus provided.*

Keywords: *bridge scour, scour hole, sediment transport, image-based techniques.*

1. INTRODUCTION

The collapse of bridges may occur due to local scouring, one of the greatest threats to their stability and safety worldwide (Melville and Coleman, 2000; Proske, 2018). Local scour occurs due to the formation of vortices around piers and abutments, resulting in the change of a unidirectional approach flow into the three-dimensional flow field impacting an erodible channel, such as a riverbed. The local scouring process is intrinsically dependent on bridge geometry, river channel morphology, and hydrologic regime, which are entirely site specific. Recently, the impact of the flow on the dynamical behaviour of the riverbed and its repercussion on the structural stability of bridge foundations has been receiving greater recognition and attention from scientists and engineers (Chiew *et al.*, 2020).

The scour mechanism around a bridge foundation depends, among others, on the approach flow intensity, which can be classified as either clear water or live bed. Although there is a wide number of studies on the clear water scour condition, most of the scour-induced bridge failures occur during floods, where a significant sediment flux is transported by the river flow and where the flow intensity is high. In the live bed condition, the scour hole equilibrium depth, when the scour depth fluctuates around a mean value, is reached faster than in the clear water condition (Melville and Coleman, 2000). Since the knowledge of scour hole dimensions is imperative in determining the extent of countermeasures needed to prevent/control scour at piers, the development of different approaches and techniques for accurate characterization of its geometry is essential. It is also worth highlighting that a detailed investigation on the scour hole morphology is also required for supporting the numerical modeling of scouring (Bento *et al.*, 2018; Bento, 2021).

Therefore, the aim of the present research was to develop image-based measurements and data processing techniques in a laboratory environment for the characterization of the scour hole and deposition zones geometry caused by the presence of bridge pier models in a movable bed, under live bed conditions. Oblong bridge pier models, made of rectangular round-nose concrete columns, were considered since it is the typical shape in Portuguese bridges, from the 19^{th} and 20^{th} centuries.

2. LOCAL SCOURING EXPERIMENTS

2.1. Experimental apparatus

Two local scouring experiments, reproducing the flow at the vicinity of bridge pier models embedded in a uniform sediment bed, were performed in a 40.7 m long, 2.0 m wide and 1.0 m deep glass-sided rectangular tilting flume (Figure 1), located at the National Laboratory of Civil Engineering (LNEC), Lisboa (Portugal).

(a) View from upstream (b) View from inside

Figure 1 - Tilting flume at LNEC.

Two bridge pier models, properly characterized by a three-dimensional coordinate measuring machine, MMC 3D, were used with widths (W) of 0.11 m and 0.14 m (henceforth called *Pier 11* and *Pier 14*, respectively). Oblong bridge pier models were chosen as their geometries replicate the typical shape of bridge foundations, most common in Portugal in the 19^{th} and 20^{th} centuries. They were installed at the middle cross-section of an existing sand recess, 5.0 m long and 0.4 m deep, filled with a uniform quartz sand, characterized by a mean sediment diameter, D_{50}, of 0.86 mm, a specific gravity, s, of 2.65, and a geometrical standard deviation, σ, of 1.28. The corresponding dimensionless sediment diameter (being g the gravity acceleration and υ the kinematic viscosity coefficient) was 21.7.

The sand adopted and the position and the geometrical characteristics of the bridge pier, were chosen to avoid the sand bed gradation effect, and the flume sidewall effects on the scouring process. The non-ripple-forming sediment criterion was respected and the effect of non-uniformity of sediment on the depth of the scour hole was avoided (Lee & Sturm 2009). Sediment coarseness ratios (W/D_{50}) of 127.9 and 162.8 were obtained for *Pier 11* and *Pier 14*, respectively, which effects were not negligible according to recent studies (Lee & Sturm 2009). The influence of flume sidewall on the scour hole development was avoided since the relation W/B < 10% was verified, being W the pier width and B the flume width (Chiew & Melville 1987). At the inlet of the tilting flume, a metallic grid assured the development of a uniform approach flow distribution. At the upstream end of the recess box, a fine gravel mattress, 0.3 m thick and 0.2 m long, allowed a smooth and progressive transition, avoiding scouring at the transition between the fixed and the movable bed.

2.2. Devices, measured variables and instrumentation

This experimental study comprised the monitoring of hydraulic variables and the temporal evolution of the scour depth at piers' front during the scouring experiments with a 95% confidence interval. The approach flow discharge *Q*, was regulated by the rotational speed of the pumping system and monitored by an electromagnetic flowmeter (accuracy of ± 0.25%). A sluice gate placed at the downstream end of the flume enabled the flow depth adjustment inside the flume. Two resistive probes, suitably deployed to not interfere with the experiments, allowed the monitoring of the approach flow depth during the scouring experiments. The signals from the resistive probes and the electromagnetic flowmeter were acquired at a sampling frequency of 25 Hz.

The scour depth was registered with the aid of limnimeters at the upstream faces of the bridge pier models, with an accuracy of ± 0.05 mm. The flume was equipped with three moving carriages that moved along the longitudinal axis of the flume on two precisely levelled rails. These allowed the access to the experimental area for measuring purposes, particularly for flow and scouring parameters. A comprehensive measurement system was adopted for the three-dimensional characterization of the scour and deposition zones at the piers' vicinity. It consisted of capturing images, with a 12 MP spatial resolution camera (Action Cam NK 3056 Full HD) and on acquiring scans, at the beginning and at the end of the experiments using two advanced image-based techniques, namely close-range photogrammetry and the Kinect V2 sensor.

2.3. Experimental procedure

After the installation of the oblong bridge pier model, the recess box was filled with the sand and flattened before the flume was slowly filled with water to allow air entrapped in the sand to escape. The flow was then drained and the sand arranged once again. The pier models were protected with metallic plaques to preclude undesirable scour at the beginning of the experiments. The tilting flume was filled again by increasing the rotational speed of the pump and by gradually adjusting the level of the downstream sluice gate until reaching the desired hydraulic variables. Once the prescribed flow conditions were reached, the metallic plaques covering the sand were carefully removed to initiate the local scouring experiment. Before the beginning of experiments, a careful inspection of all instrumentation and measuring supports was undertaken. During experiments, the scour depth time evolution was measured at the piers' front in line with the development of the scouring phenomena (higher periodicity was adopted for the first instance as scour developed more rapidly). Further details can be found in Bento (2021). Scan images and photos of the bed morphology were captured at two moments of the scouring experiments: at the flat (initial) and the eroded (final) bed stages for characterizing the scouring effects and its respective ensemble. The three-dimensional characterization comprises the application of two image-based techniques, specifically the close-range photogrammetry and the Kinect V2 sensor. Both approaches required the previous emptying of the flume and control points deployed in specific locations of well-known dimensions for reliable results.

2.4. Hydraulic conditions and time duration

The scouring experiments were conducted under live bed flow conditions, hereinafter designated as *Exp_Pier 11* and *Exp_Pier14* (Table 1). Preliminary tests have shown that the sand particles start moving for conditions close to critical velocity predicted by Neill's formula (1967), which was thus used to establish the experimental hydraulic conditions. Table 1 depicts the main hydraulic variables concerning the approach flow, namely discharge (*Q*), depth (*h*), velocity (*V*), Froude number (*Fr*), flow Reynolds number ($Re = Vh/\upsilon$), and, the parameter respecting the relation with the obstacle: the pier Reynolds number ($Re_D = VW/\upsilon$). The flow discharge and the water levels within the flume of the experiments were acquired continuously. For this reason, the main hydraulic variables were estimated with a 95% confidence interval, in which the estimated error corresponded to the sample error. Further details regarding the data filtering methods tested and applied to the flow discharge time evolution can be found in Bento (2021).

The water depth, *h*, within the tilting flume was assigned as the arithmetic average of the resistive probes data. Similar analysis was performed for the assessment of the corresponding experiments' flow intensities. This uncertainty analysis has shown that the variability of the parameters of flow discharge, flow depth and flow intensity had no impact on the final results, as can be observed in Table 1. Both experiments were performed under subcritical flow conditions (Fr < 1.0), whilst the flow and pier Reynolds numbers (Re and Re_D in Table 1) ensured fully turbulent approach flows.

Table 1 - Hydraulic conditions of experiments *Exp_Pier11* and *Exp_Pier14*.

Experiment (-)	*Pier width* *(m)*	Q (m^3/s)	h (m)	V (ms^{-1})	I_f (-)	Fr (-)	Re (-)	ReD (-)
Exp_Pier11	0.11	0.1226 ± 6x10^{-7}	0.1453 ± 1x10^{-6}	0.4222 ± 3x10^{-6}	1.335 ± 1x10^{-5}	0.2964 ± 5x10^{-6}	61069 ± 0.3	46254 ± 0.4
Exp_Pier14	0.14	0.1244 ± 1x10^{-6}	0.1570 ± 2x10^{-6}	0.3964 ± 6x10^{-6}	1.2626 ± 2x10^{-5}	0.2575 ± 6x10^{-6}	61977 ± 0.6	55281 ± 0.8

The time required to reach 90% of the respective equilibrium scour depth (t_{90}), dependent of the reference time (*tr*, given in Sheppard *et al.* 2011), was used as a basis criterion for the time duration of the scouring experiments. The estimates of 2.9 days for *Exp_Pier11* and 4.1 days for *Exp_Pier14* were in line with findings of Liang *et al.* (2019). Despite the estimated values for t_{90}, the former, *Exp_Pier11,* lasted 3.1 days and the latter, *Exp_Pier14,* only 1.8 days of the scouring process (roughly 44.4% of the planned duration). Mechanical faults have been responsible for the experiment's interruption.

3. SCOUR HOLE AND DEPOSITION ZONE CHARACTERIZATION

3.1. Close-range photogrammetry

Photographs of the scour hole and the surrounding affected area were acquired at a height of 0.50 m from the initial (flat) bed level, as considered in Bento *et al.* (2018). Those photo captures were then processed in a Structured from Motion (SfM) software, particularly *Agisoft Metashape Profesional Edition*, version 64 bit 1.6.3 to reconstruct the bed's morphology models. Digital Elevation Models (DEM) were then extracted and post-processed. For a successful completion of the DEMs, a minimum photo quality of 0.70 and an image overlap of about 60% should be guaranteed (Agisoft, 2020). These features play a relevant role in the success of the different processing phases in the generation of the 3D bed morphology models, bed contour surfaces and profiles.

3.2. Kinect V2 sensor

The Kinect V2 sensor is composed by a projector and two internal cameras: one *infrared camera* and an *RGB camera*. The *infrared projector* transmits a predefined pattern of light, which is deformed based on the distance of various points of the area of interest from the sensor (at a vertical distance of 0.5 m). This deformed pattern is then captured by the *infrared camera* and is correlated against a reference speckle pattern projected on the surface at a known distance from the sensor to build a 3D map of the object. The resulting point clouds were then introduced in the 3D net processing *CloudCompare* software, version 64 bit 2.11, to build topographic 3D maps and corresponding, contour surfaces and bed profiles. The scans acquired from the Kinect V2 sensor were spatially referenced with a resulting Root Mean Square Error (RMSE) kept lower than 0.03 for obtaining a reliable model.

4. RESULTS

4.1. Scour depths at piers' front

Figure 2 illustrates the scour depth at 0.05 m from the upstream faces of the pier models, as well as with the corresponding logarithmic scales.

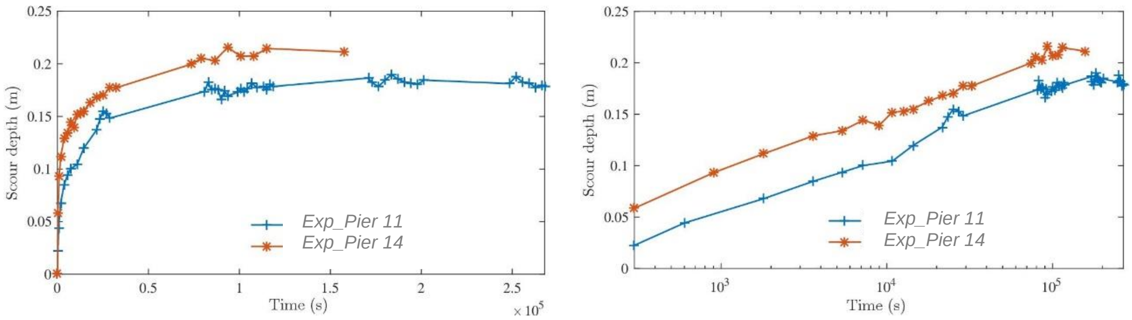

(a) Scour depth time evolution (b) Scour depth time evolution in logarithmic scale

Figure 2 - Temporal evolution of the scour depths at 0.05 m from the piers' front.

Evident differences were observed for the experiments (Figure 2). The higher width of *Pier 14* (*Exp_Pier14*) explained the temporal evolution of the scour depths towards higher scour depths than for *Exp_Pier11*. At the end of the first hour of *Exp_Pier11*, the measured scour depth attained was 0.085 m, whereas for *Exp_Pier14* such values almost reached the value of 0.13 m. The night period (of almost 11 hours, from the last measurement performed on the first day and the first one on the second day), registered an increase of the scour depth of 0.0225 m. During the second day experiments, a reduction of slope was visible. At the end of experiments, the final scour depths were 0.1790 m (*Exp_Pier11*) and 0.2114 m (*Exp_Pier14*). This latter scour depth, registered at roughly 1.8 days of *Exp_Pier14*, was higher than the corresponding scour depth of *Exp_Pier11*, as can be observed in Figures 2(a) and 2(b). These results were used for validation purposes of the image-based techniques.

4.2. Scour holes and deposition zones at piers' vicinity

Eight three-dimensional models of the bed morphology at the vicinity of the pier models were derived, either from the application of close-range photogrammetry or by using the KinectV2 sensor, at the beginning and at the end of the experiments. Figure 3 depicts the eroded bed models around *Pier 11* and *Pier 14* for the two scouring experiments (*Exp_Pier11* and *Exp_Pier14*), highlighting the control points. The origin (x,y,z) = (0; 0; 0) was taken at the center of the pier at the flume mid-plane surface. The characterization of the flat condition of experiments allowed the assessment of the initial stage of the bed elevation model. Thus, on average, the elevations were 0.230 m for *Exp_Pier11* and 0.225 m for *Exp_Pier14* below zero. The bed morphology models (Figure 3) are quite similar despite slight differences due to the quality of captures and image-based techniques' accuracy, which was assessed based on the reference points of the respective models and their absolute coordinates. The application of the close-range photogrammetry technique returned position average errors of 0.79 mm and 0.63 mm (8.1% and 26.7% lower than D_{50}) for *Exp_Pier11* and *Exp_Pier14*, respectively.

The three-dimensional bed models allowed the creation of contour surfaces, displayed in Figure 4, as a function of scour depth-to-approach flow depth (ds/h). The contour surfaces obtained for *Exp_Pier11* (Figure 4(a) and 4(b)) present quite similar results, showing the maximum scour depth at the pier's front. However, by inspection of the 3D models (Figures 3(a) and 3(b)) it is possible to infer that the characterization given by the close-range photogrammetry technique was more reliable since a maximum scour depth of 0.20 m is closer to the measurement performed with the aid of a limnimeter at the end of the experiment. According to Figure 4(b), the maximum scour depth, given by the Kinect V2 sensor, resulted in 0.242 m, which corresponds to a difference of 26%. Such differences were responsible for the distinctive color shadows of Figures 4(a) and 4(b).

The processing phases of the Kinect V2 sensor scans, for *Exp_Pier14,* did not allow a more accurate length characterization of the bed morphology, mainly at the upstream side of *Pier 14*, as it was performed by applying close-range photogrammetry. In this experiment, the close-range photogrammetric technique gave a little deeper scour depth immediately upstream of the pier model. A difference of 0.009 m between approaches was achieved. Despite slight differences, the close-range photogrammetry technique remains the more reliable approach, as can be confirmed by the eroded bed models. There are some discontinuities, even though not significantly affecting the resulting 3D bed models. The non-feeding feature of the herein live bed scour experiments explains, in part, the bed elevations, at the upstream reach of the sand box, lower than the respective flat bed stages. In both experiments, the sand was transported beyond the working section and the concrete stretch floor, appearing accumulated on the downstream recess box.

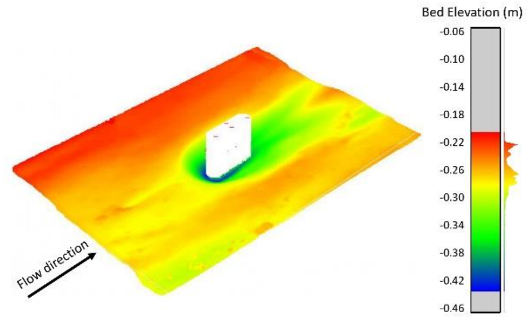

(a) *Exp_Pier11* – Photogrammetry

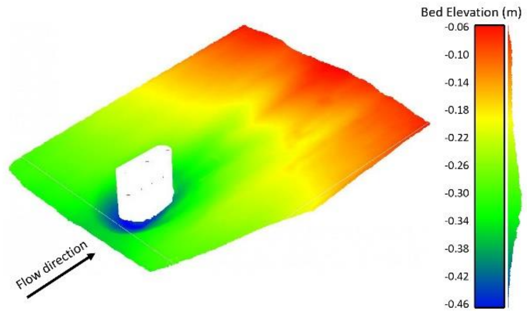

(b) *Exp_Pier11* – Kinect V2 sensor

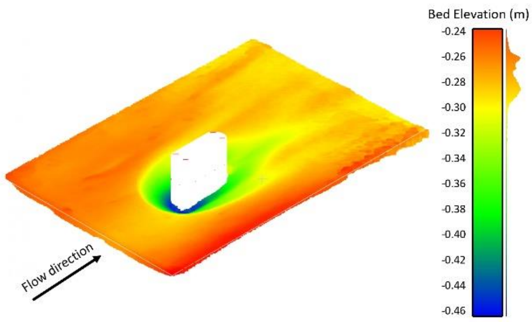

(c) *Exp_Pier14* – Photogrammetry

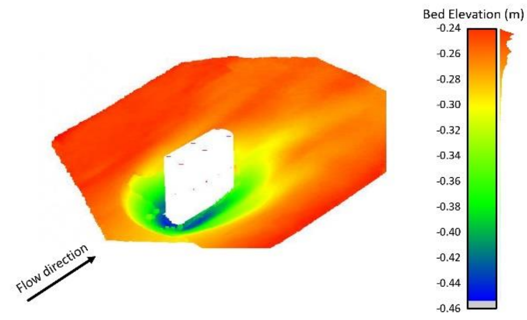

(d) *Exp_Pier14* – Kinect V2 sensor

Figure 3 - Three-dimensional eroded bed models from close-range photogrammetry (left panel) and Kinect V2 sensor (right panel).

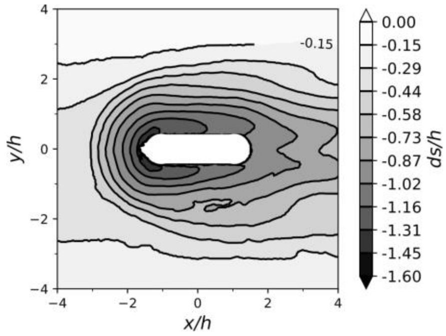
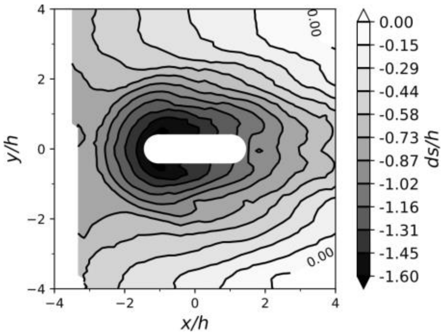

(a) *Exp_Pier11* – Photogrammetry (b) *Exp_Pier11* – Kinect V2 sensor

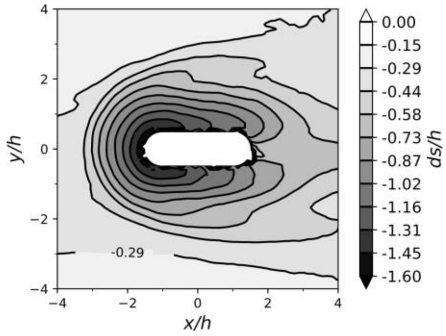
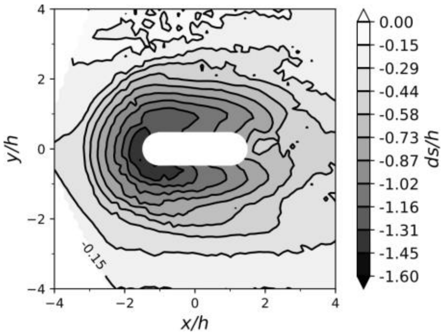

(c) *Exp_Pier14* – Photogrammetry (d) *Exp_Pier14* – Kinect V2 sensor

Figure 4 – Contours of local scour around the bridge pier models from close-range photogrammetry (left panel) and Kinect V2 sensor (right panel).

4.3. Bed profiles

Figure 5 depicts the bed profiles considered in the present analysis. These profiles, at the vicinity of the pier models, are given in Figures 6 and 7. A direct comparison between the previous techniques can thus be performed, as a function of the approach flow depth. Higher differences between the two image-based characterization techniques occurred for *Exp_Pier11* (Figure 6(a)). As stated previously, the Kinect V2 sensor was returning erroneously higher scour depth values. For that experiment, the close-range photogrammetry technique was revealed to be undoubtedly the more realistic as confirmed by the 3D model and the scour depth point-wise measurement performed at 0.05 m from the pier's front (Figure 6(a)).

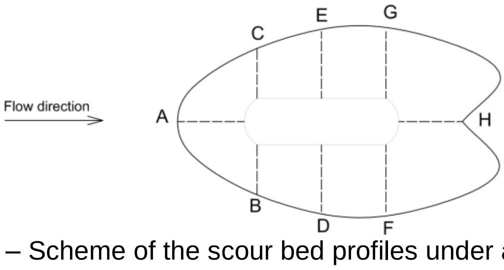

Figure 5 – Scheme of the scour bed profiles under analysis.

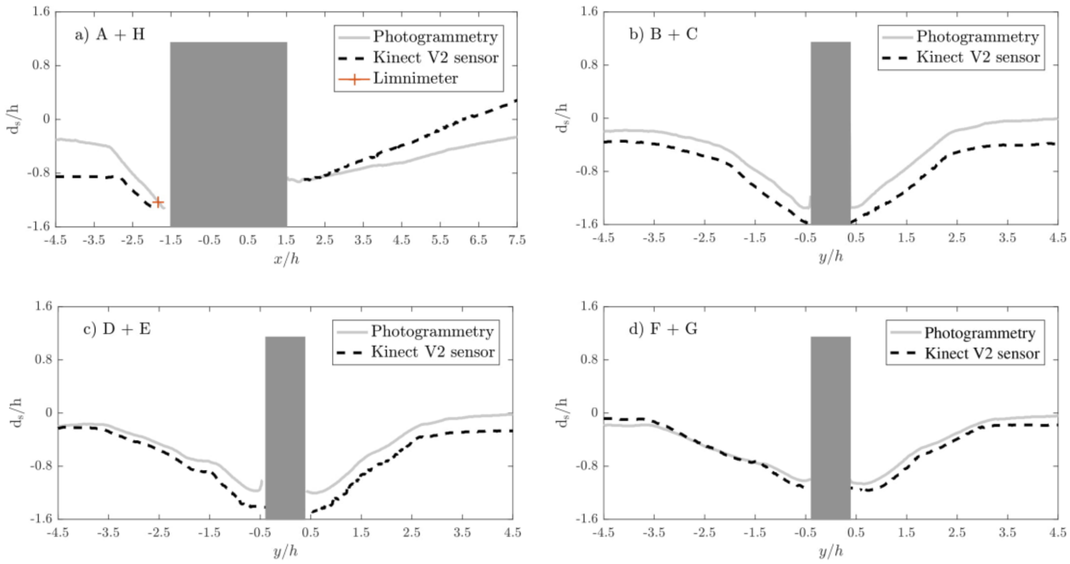

Figure 6 – Scour bed profiles from close-range photogrammetry (continuous line) and Kinect V2 sensor (dashed line) for *Exp_Pier11*.

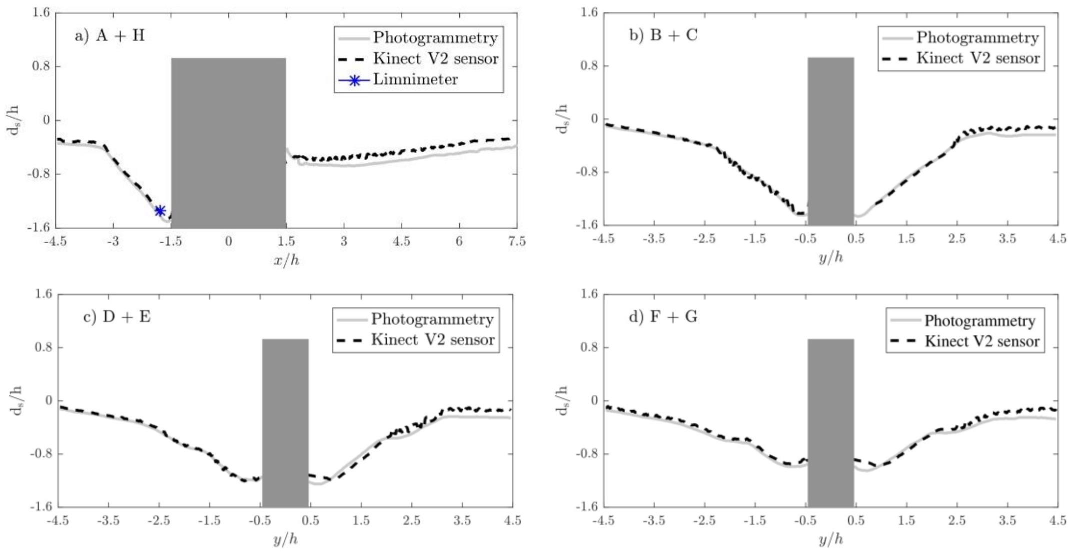

Figure 7 – Scour bed profiles from close-range photogrammetry (continuous line) and Kinect V2 sensor (dashed line) for *Exp_Pier14.*

5. CONCLUSIONS

The present paper presents scouring experiments around two oblong bridge piers, performed in a tilting flume of the Portuguese National Laboratory of Civil Engineering (LNEC), under live bed flow conditions, for the characterization of scour holes around the pier models. The study adopted advanced survey and sensor technologies with three-dimensional (3D) point clouds and digital elevation models (DEMs). Eight three-dimensional maps of bed morphology at the vicinity of the pier models were derived at the beginning and the end of experiments. The produced 3D bed morphology models provided detailed measurements with quite similar results between the image-based techniques. In addition, both transverse and longitudinal bed contour levels and 2D bed profiles are presented. Furthermore, the obtained results indicate that the two image-based techniques, Kinect V2 sensor and close-range photogrammetry, could accurately monitor (once properly validated) the scouring process and replace the traditional point-wise measurement approaches for the full characterization of the scour hole and deposition zones around a bridge pier.

6. ACKNOWLEDGMENTS

The first author thanks the financial support of the Portuguese Foundation for Science and Technology through the PhD scholarship PD/BD/127798/2016, in the framework of InfraRisk Doctoral Program. This work was conducted in collaboration with the departments of Hydraulics and Environment and the Center of Scientific Instrumentation of the National Laboratory of Civil Engineering. This research was also co-supported by the strategical funding from FCT UIDB/04423/2020 and UIDP/04423/2020.

7. REFERENCES

Agisoft, L. (2020). *Agisoft Metashape User Manual - Professional Edition, version 1.6*. Agisoft LLC.

Bento, A. M., Couto, L., Pêgo, J. P. and Viseu, T. (2018), *Advanced characterization techniques of the scour hole around a bridge pier model*, E3S Web of Conferences, vol. 40. EDP Sciences.

Bento, A. M. (2021), *Risk-based analysis of bridge scour prediction*, Ph.D. thesis, Faculty of Engineering of the University of Porto, Porto, Portugal.

Chiew, Y. M. and Melville, B. W. (1987), *Local scour around bridge piers,* Journal of Hydraulic Research 25(1), 15–26.

Chiew, Y.-M., Lai, J.-S., and Link, O. (2020), *Experimental, numerical and field approaches to scour research*, Water, 12(6), 1749.

Melville, B. W. and Coleman, S. E. (2000). Bridge scour. Highlands Ranch, Colorado: Water Resources Publications, LLC.

Lee, S. O. and Sturm, T. W. (2009), *Effect of sediment size scaling on physical modelling of bridge pier scour*, Journal of Hydraulic Engineering 135(10), 793–802.

Liang, B., Du, S., Pan, X., and Zhang, L. (2019), *Local scour for vertical piles in steady currents: Review of mechanisms, influencing factors and empirical equations*, J. Mar. Sci. Eng., 8(1), 4.

Neill, C. R. (1967), *Mean-velocity criterion for scour of coarse uniform bed-material*, 12th Proceedings Congress, vol. 3. Fort Collins, Colorado, USA.

Proske, D. (2018). Bridge Collapse Frequencies versus Failure Probabilities. Springer International Publishing

Sheppard, D. M., Demir, H. & Melville, B. W. (2011), *Scour at Wide Piers and Long Skewed Piers*, vol. 682. Transportation Research Board.

8th International Junior Researcher and Engineer
Workshop on Hydraulic Structures
ISBN: 978-0-578-37416-1
https://doi.org/10.26077/e6e8-b586

Galway, Ireland,
5th - 8th June 2021

A critical analysis of jet-induced scour formulas

J. Di Nardi[1], M. Palermo[1] and S. Pagliara[1]
[1]Department of Energy, Systems, Territory and Construction Engineering
University of Pisa
Pisa
ITALY
E-mail: jessica.dinardi@phd.unipi.it

Abstract: *Many studies investigate erosive processes occurring in non-cohesive granular materials downstream of grade-control structures, dam spillways, headcuts, and other hydraulic structures. Because of the complexity of the scour mechanism, the analysis of the scour phenomenon caused by plunging jets is generally conducted by using physical models and particularly for specific structure geometries. In this regard, many researchers proposed empirical approaches to estimate the main scour lengths, but their contributions are limited to tested conditions and cannot be generalized. This lack of generality has been (partially) overcome by other, more recent, approaches, that are either semi-theoretical or fully theoretical. Previous works assessed the predictive capability of the most well-known empirical relationships but did not present a comparative analysis between empirical and (semi-)theoretical relationships. The aim of this paper is to contribute to fill this gap of knowledge. Namely, we present an experimental validation of the most popular relationships using a large database. In addition, we compare the predictive capability of some (semi-)theoretical relationships with that of the best known empirical formulas. In doing so, we provide interesting insights into the different approaches, highlighting their limits in assessing the main scour features. Overall, this paper provides a critical and updated analysis of different approaches for scour problems caused by plunging jets.*

Keywords: *hydraulic structures, jet scour, non-cohesive sediment, scour mechanism.*

1. INTRODUCTION

Erosive processes occurring downstream of hydraulic structures may represent a threat to their stability. Consequently, many studies investigated scour processes in granular and rocky beds, providing tools to estimate the main features of the scour hole. Because of the three-phasic nature of the scour mechanism, the analysis of the phenomenon caused by plunging jets is generally conducted by using physical models and is limited to specific structural configurations and geometries. To this end, for scour in non-cohesive granular beds, many empirical equations were developed. Among others, Kotoulas (1967) proposed an empirical formula for scour depth downstream of a free overfall jet. Mason and Arumugam (1985) and Mason (1989) developed an equation to predict the scour depth associated with a variety of structures ranging from free overfalls to tunnel outlets, whereas D'Agostino (1994) analyzed the scour downstream of a sharp-crested weir. Nevertheless, these formulas are often dimensionally not correct and only valid in the tested range of parameters. Moreover, their range of application is frequently not defined (Pagliara et al. 2004). This lack of generality has been (partially) overcome by other, more recent approaches, that are either semi-theoretical or fully theoretical. In particular, the former are generally based on the jet diffusion theory in the turbulent cauldron, whereas the latter are based on first principles.

Previous works examined the predictive capability of the most well-known empirical relationships. Among others, Whittaker and Schleiss (1984) presented a compilation of the existing methods to estimate the features of jet-induced scour and compared their accuracy with prototype data. Pagliara et al. (2004) assessed the performance of the main empirical approaches by contrasting their predicting capability with a large experimental database derived from different authors. More recently, Castillo and Carrillo (2017) compared the performance of several methods to predict the scour downstream of a ski jump, including (semi-)empirical formulas and CFD simulations. Nevertheless, none of the mentioned studies presents a comparative analysis of empirical and (semi)theoretical relationships pertaining to 3D jet-induced scour processes.

Therefore, the aim of this paper is to contribute to fill this gap of knowledge. To this end, we tested the predictive capability of well-known (semi-)empirical formulas and compare their performance with that of the theoretical approach proposed by Bombardelli et al. (2018), based on the phenomenological theory of turbulence (PTT). The paper is organized as follows. We first describe the experimental setups adopted by Pagliara et al. (2008a) and (2008b) and Bombardelli et al. (2018), as we employed experimental datasets derived from these studies. Then, we critically discuss the approaches proposed by Mason and Arumugam (1985), Mason (1989), Bormann and Julien (1991), Hoffmans (2009), and Bombardelli et al. (2018). Finally, we provide interesting observations on the predicting capability of the mentioned methods, by highlighting differences and similitudes.

2. EXPERIMENTAL SETUP

Datasets used in this investigation comprise more than 100 experimental tests conducted at the Hydraulics Laboratory of the University of Pisa in collaboration with ETH Zurich (Switzerland). Experiments were conducted in two different rectangular channels, with a width B_c. Figure 1 shows a diagram of the experimental apparatus, along with the main hydraulic and geometric parameters involved, i.e., water discharge Q, water depth above the original bed D, diameter of the jet D_{jet}, inclination of the jet α, maximum scour depth Δ and length L of the scour hole, longitudinal and vertical coordinates x_i and z_i. Table 1 summarizes the range of hydraulic and geometric parameters pertaining to the selected datasets. Tests involved different types of uniform granular materials, with d_{50} indicating the median diameter of the sediment bed. The jet was generated by a circular pipe which could be placed either at the center of the channel (*full-model* arrangement) or close to the channel glassed wall (*half-model* arrangement, see Pagliara et al. 2008b for details). Pagliara et al. (2008a) adopted a *full-model* configuration; conversely, tests of Pagliara et al. (2008b) and Bombardelli et al. (2018) were conducted with a *half-model* configuration. All tests considered herein relate to the 3D scour configuration as defined by Pagliara et al. (2008a), i.e., $B_m/B_c < 3$, with B_m as the maximum width of the scour hole.

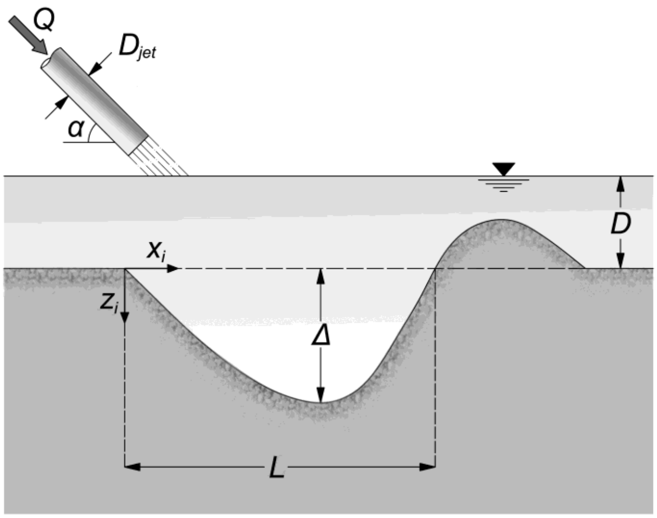

Figure 1 - Definition sketch of jet-induced scour along with the main geometric and hydraulic parameters.

It is worth mentioning that, under constant discharge, the scour hole evolves until reaching the *dynamic* equilibrium configuration. When the jet action ceases, the amount of material kept in suspension/rotation deposits in the scour hole resulting in the *static* equilibrium configuration. Therefore, the maximum *static* scour depth Δ_s might considerably differ from its *dynamic* counterpart (i.e., $\Delta_s < \Delta$).

Table 1 Summary of employed datasets

Reference	B_c (m)	Q (l/s)	D_{jet} (mm)	D (m)	d_{50} (mm)	α (deg)
Pagliara et al. (2008a)	0.80	0.51-8.89	27.0	0.015-0.289	10.3-11.5	45°, 60°
Pagliara et al. (2008b)	0.50	0.70-5.50	21.7-35.0	0.155-0.315	1.2	45°, 60°
Bombardelli et al. (2018)	0.80	2.38-3.45	16.0-51.0	0.027-0.189	7.45	90°

3. SELECTED APPROACHES

In the following, we report and discuss the methodologies listed in Table 2. In Table 3, we provide a summary of the scour formulas considered in this paper, along with the values of the parameters and the range of hydraulic and geometric conditions for which they were calibrated/validated. Note that the variables listed in Table 3 are defined in the next section.

Table 2 Scour formulas considered in the present paper.

Author(s)	Approach	Analyzed structure(s)
Mason and Arumugam (1985)	empirical	free overfalls, low level outlets, tunnel outlets, flip buckets
Mason (1989)	empirical	rectangular jet
Bormann and Julien (1991)	semi-theoretical	rectangular grade control structure
Hoffmans (2009)	semi-theoretical	rectangular jet
Bombardelli et al. (2018)	theoretical	plunging jet

Table 3 Scour formulas by different authors.

Author(s) and formula		Parameters	Tested conditions
Mason and Arumugam (1985) $D+\Delta_s = K_1 q^x h^y D^{0.15} g^{-0.30} d^{-0.10}$	model	$K_1 = 3.27$ $x = 0.60$ $y = 0.05$	$0.07<D+\Delta_s<1.18$ m $0.325<h<2.150$ m $0.015<q<0.420$ m^2/s $0.001<d_{50}<0.028$ m $25°<\alpha<85°$
	prototype	$K_1 = (6.42\text{-}3.10h^{0.10})$ $x = (0.60\text{-}300^{-1}h)$ $y = (0.15+200^{-1}h)$	$6.70<D+\Delta_s<90.0$ m $15.82<h<109.0$ m $2.36<q<220.0$ m^2/s $d_{50}=0.25$ m $20°<\alpha<72°$
Mason (1989) $D+\Delta_s = 3.39q^{0.60}(1+\beta)^{0.30}D^{0.16}g^{-0.30}d^{-0.06}$		β (Ervine, 1976)	$0.33<h<2.00$ m $\alpha=45°$
Bormann and Julien (1991) $D_p+\Delta = K_2 q^{0.6} U g^{-0.8} {d_{90}}^{-0.4} \sin\beta'$		$K_2 = C_d^2\left[\frac{\gamma\sin\varphi}{\sin(\varphi+\theta)B(\gamma_s-\gamma)}\right]^{0.8}$ B (Neill, 1968) C_d (Beltaos and Rajaratnam, 1973) $q = UY_0$	$0.10<\Delta<1.4$ m $0.05<D_p<0.38$ m $0.3<q<2.5$ m^2/s $1.58<d_{90}<1.71$ mm $18°<\lambda<90°$
Hoffmans (2009) $D+\Delta = c_{2V} q^{1/2} U^{1/2} (\sin\alpha)^{1/2} g^{-1/2}$	$d_{90}<0.0125$ m	$c_{2V} = 20d_{90}^{-1/3}g^{-1/9}\nu^{2/9}\left(\frac{\rho_s-\rho}{\rho}\right)^{-1/9}$	$0.03<h<40$ m $0.004<q<275$ m^2/s $0.1<d_{90}<100$ mm
	$d_{90}\geq 0.0125$ m	$c_{2V} = 2.9$	
Bombardelli et al. (2018) $D+\Delta = K_3\left(\frac{\rho}{\rho_s-\rho}\right)^{3/5}(Qh)^{2/5}d_{50}^{-2/5}g^{-1/5}$		$K_3 = 0.50$	$0.04<D+\Delta_s<0.67$ m $1.2<d_{50}<11.5$ mm $45°<\alpha<90°$

3.1. Mason and Arumugam (1985) and Mason (1989)

Mason and Arumugam (1985) considered a set of model and prototype scour data pertaining to different structures, including free overfalls, low level outlets, spillway flip buckets, and tunnel outlets. Their datasets included 47 model tests, for which both cohesive and non-cohesive substrates were adopted. The prototype datasets consisted of 26 scour data. The range of hydraulic and geometric conditions adopted in model and prototype tests, respectively, is summarized in Table 3, where h indicates the head drop, and q is the unit discharge. Mason and Arumugam (1985) validated a wide number of existing scour formulas against their datasets, allowing them to present the following expression to estimate the *static* scour depth:

$$D + \Delta_s = K_1 q^x h^y D^{0.15} g^{-0.30} d^{-0.10} \tag{1}$$

where g is the gravitational acceleration, and the coefficient K_1 and exponents x and y were calibrated using experimental data. Different values of K_1, x and y were proposed for model data and prototype data, as indicated in Table 3. It is worth noting that in both cases the expression is dimensionally incorrect and K_1 is not a coefficient and depends on data used for calibration.

Mason (1989) further extended Mason and Arumugam's work by examining the effect of air entrainment on scour features. In so doing, he conducted experiments with a rectangular jet for α = 45°, under a controlled air/water ratio β. Air was provided by means of a low-pressure fan and was injected under the water outlet through a control valve (see Mason,1989 for further details). This methodology allowed the air to be entrained in the water jet in small bubbles, leading to the following empirical equation:

$$D + \Delta_s = 3.39 q^{0.60} (1+\beta)^{0.30} D^{0.16} g^{-0.30} d^{-0.06} \tag{2}$$

In Eq. (2), β was calculated according to Ervine (1976). Overall, Eq. (2) has the same analytical structure of Eq. (1), with the air entrainment term replacing h. Mason (1989) suggested that Eq. (2) is valid for both models and prototypes.

3.2. Bormann and Julien (1991)

Bormann and Julien (1991) adopted a semi-theoretical approach to predict the scour downstream of a grade control structure. They considered a grade control structure with a sloping downstream face (inclination λ with respect to the horizontal) and drop height D_p. Their approach is based on jet diffusion theory (Beltaos and Rajaratnam, 1973). They assumed that the equilibrium condition is achieved when the shear stress acting on the granular bed equals the critical shear stress. In doing so, they adopted some empirically validated assumptions. Therefore, the proposed approach cannot be considered fully theoretical. Bormann and Julien (1991) derived the following equation to estimate the equilibrium scour depth:

$$D_p + \Delta = K_2 q^{0.6} U g^{-0.8} {d_{90}}^{-0.4} \sin\beta' \tag{3}$$

where the unit discharge q is calculated as $q = UY_0$, with Y_0 indicating the jet thickness and U the average velocity of the jet, d_{90} is the material size for which 90% is finer, β' is the inclination of the diffused jet with respect to the horizontal, depending on Y_0, λ, D_p, g, U, Y_t (downstream water level). The expression of K_2 is reported in Table 3, with C_d indicating the jet diffusion coefficient that depends on the inlet conditions (Beltaos and Rajaratnam, 1973), γ_s and γ the specific weights of sediment and water, respectively, φ is the submerged angle of repose of the sediment, θ is the inclination of the downstream face of the scour hole, and B is a local friction coefficient (Neill, 1968). Bormann and Julien (1991) validated their formula using large-scale experiments carried out in an outdoor channel 0.91m-wide, 27.4m-long, and 3.5m-deep. Ranges of hydraulic and geometric conditions of tests are summarized in Table 3.

3.3. Hoffmans (2009)

Hoffmans (2009) applied the linear momentum equation to a selected control volume, by assuming that the horizontal component of the resultant can be expressed using the equation of Forcheimer. Namely, he proposed the following equation:

$$D + \Delta = c_{2V} q^{1/2} U^{1/2} (\sin \alpha)^{1/2} g^{-1/2} \tag{4}$$

where the value of c_{2V} is reported in Table 3, with v indicating the kinematic viscosity of the fluid. Note that the value of c_{2V} was calibrated using a large set of plunging jet data collected by various researchers. The dataset encompassed a wide range of hydraulic conditions and different geometrical configurations, including overfalls and grade control structures (see Table 3). Based on dimensional arguments and experimental data, Hoffmans (2009) argued that the coefficient c_{2V} is almost constant for $d_{90} \geq 0.0125$m; conversely, for $d_{90} < 0.0125$m, c_{2V} is a function of the densimetric particle number and granulometric characteristics of the bed and an ad-hoc empirical expression is proposed to estimate it.

3.4. Bombardelli et al. (2018)

Following the methodologies developed by Gioia and Bombardelli (2005) and Bombardelli and Gioia (2006), Bombardelli et al. (2018) analyzed the jet-induced scour process for the 3D case. In so doing, they considered a jet of water entering a pool of depth D from a height h. By applying the phenomenological theory of turbulence and energetic considerations to the resulting turbulent cauldron, they derived a fully theoretical equation to estimate $D+\Delta$:

$$D + \Delta = K_3 \left(\frac{\rho}{\rho_s - \rho}\right)^{3/5} (Qh)^{2/5} d_{50}^{-2/5} g^{-1/5} \tag{5}$$

where K_3 is a multiplicative constant set equal to 0.50. The exponents of each variable were theoretically derived. Therefore, this formula is dimensionally correct. Note that the theoretical values of the exponents were compared with those of the best-known empirical formulas, revealing a considerable agreement. Most importantly, the approach of Bombardelli et al. (2018) provides unprecedented insight into the physics of the interaction between sediment and turbulent flow. It is worth mentioning that Bombardelli et al. (2018) also proposed an equation for the 2D case [with the same structure as Eq. (5)] for which specific exponents and the multiplicative constant were determined.

4. RESULTS AND DISCUSSION

All the empirical and semi-theoretical equations adopted herein involve the unit discharge q. This variable can be easily defined (and computed) for jets originating from drop structures. But what does q represent for circular jet-driven scour processes? To answer this question, we tested the previous approaches assuming $q = Q^*/B_c$ and $q = Q^*/D^*$, with $Q^* = Q$ and $D^* = D_{jet}$ for tests conducted in *full-model* configuration, whereas $Q^* = 2Q$ and $D^* = 2^{0.5}D_{jet}$ for tests conducted with the *half-model* configuration. Note that D^* is the equivalent jet diameter, allowing to obtain the same jet velocity U for *full* and *half-model* arrangements.

In the formula of Mason and Arumugam (1985) we assumed $h = U^2/(2g)$. Note that Eq. (1) provides similar results regardless of the coefficients adopted. Therefore, the following estimations were done using the coefficients calibrated for models. Figure 2 contrasts measured (subscript *meas*) and calculated (subscript *calc*) values obtained assuming $q = Q^*/B_c$ (Fig. 2a) and $q = Q^*/D^*$ (Fig. 2b). In both cases, the estimations provided by Mason and Arumugam's formula exhibit a similar deviation from the perfect agreement line. However, for $q = Q^*/B_c$ experimental values are significantly underestimated, whereas the opposite occurs for $q = Q^*/D^*$ and results are in agreement with the findings of Pagliara et al. (2004) (see Figures 2a and 3a of that study). From a practical point of view, the second approach is preferable, as it can be assumed to include a safety coefficient. Overall, such differences could depend on the geometrical configuration of the tests analyzed by Mason and Arumugam (1985), involving different structures like flip buckets and tunnel outlets. However, as the resulting equilibrium morphology is essentially 3D, it is believed that the assumption $q = Q^*/D^*$ is more consistent with the physics of the jet-scour processes.

It is worth remarking that Mason and Arumugam (1985) and Mason (1989) formulas were calibrated using *static* scour data, whereas data of Pagliara et al. (2008a) and (2008b) and Bombardelli et al. (2018) refer to the *dynamic* equilibrium configuration. Consequently, an underestimation of the data should be expected. Nevertheless, Pagliara et al. (2004) argued that the performance of Eq. (1) does not vary considerably considering the *static* and *dynamic* scenarios. The inclusion of the air entrainment effect does not alter the overall predicting capability of the approach proposed by Mason (1989). In fact, the average deviation of predicted values of $D+\Delta$ using Eqs. (1) and (2) is less than 10% for $q = Q^*/B_c$, and less than 2% for $q = Q^*/D^*$. This slight difference may be due to the fact that experimental tests adopted herein were conducted under black water conditions.

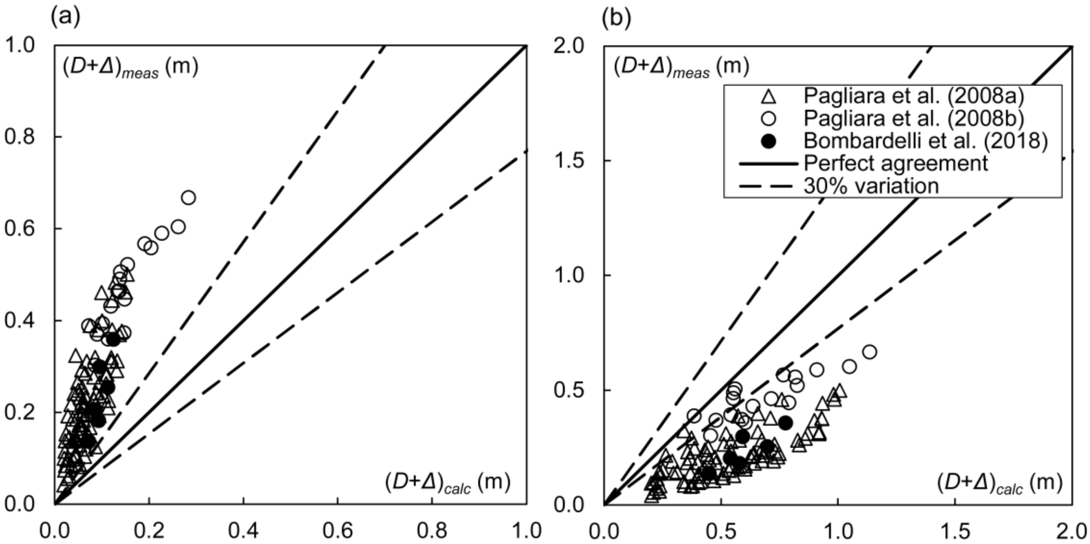

Figure 2 – Comparison of measured and calculated (using Eq. 1) values of the variable $D+\Delta$ for (a) $q=Q^*/B_c$ and (b) $q=Q^*/D^*$.

Likewise, Eq. (3) was tested assuming $D_p = D$; $U = (2gh)^{0.5}$, $\beta' = \alpha$, $\varphi = 25°$, $C_d = 1.8$, $\theta = \alpha$, and $B = 2.0$. Figures 3a and b show the results obtained for $q = Q^*/B_c$ and $q = Q^*/D^*$, respectively. It is worth mentioning that we also tested the performance of Eq. (3) assuming $q = UY_0$ (as suggested by the authors for grade-control structures), with $Y_0 = D^*$. In this case, we obtain $q = 4Q/(\pi D^*) = 1.27Q/D^*$. But considering that the exponent of q is equal to 0.6 in Eq. (3), the calculated values of $D+\Delta$ (not reported herein) are consistent with those shown in Fig. 3b. Figure 3 indicates that the predicting capability of Eq. (3) improves for Q^*/B_c, providing reasonable results (36% of data are within a ±30% deviation from the perfect agreement line). Overall, this approach tends to underestimate the diffusion length for jet-driven scour processes. Conversely, Eq. (3) systematically overestimates experimental data for $q = Q^*/D^*$. This occurrence should not be a surprise, as Bormann and Julien (1991) considered 2D structures and, consequently, assumed that the flow features in the downstream pool are essentially two-dimensional. This is in stark contrast with the physics of an impinging jet originating from a dam spillway. However, when the resulting equilibrium morphology becomes less three-dimensional, scour processes may exhibit some similitudes. Therefore, in such cases, B_c appears to be a more adequate reference length. Finally, the agreement between data and predictions (with $q = Q^*/B_c$) seems to improve with $D+\Delta$, i.e., with the increase of the diffusion length, for which, generally, scour features are more two-dimensional.

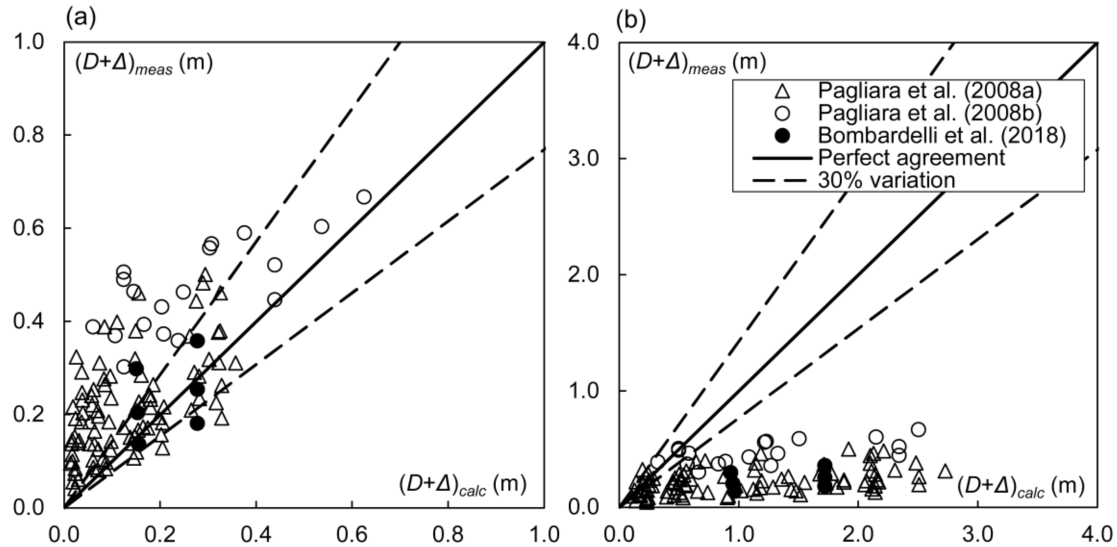

Figure 3 – Comparison of measured and calculated (using Eq. 3) values of the variable $D+\Delta$ for (a) $q=Q^*/B_c$ and (b) $q=Q^*/D^*$.

As regards the approach of Hoffmans (2008), we assumed $U = (2gh)^{0.5}$ and $v = 10^{-6}$ m^2/s. Figures 4a and b show the comparison between measured and predicted values of $D+\Delta$ using $q = Q^*/B_c$ and $q = Q^*/D^*$, respectively. Results are consistent with those obtained using Eq. (3) although, overall, Eq. (4) performs better for both cases. Once again, this occurrence should be expected provided that Hoffmans (2008) applied the linear momentum equation to a control volume per unit width. More specifically, the performance of Eq. (4) is reasonably acceptable for $q = Q^*/B_c$ (the deviation of 42% of predicted data is less than 30%), although data are underestimated by 40% on average. Therefore, considerations similar to the previous case apply also to this approach.

Finally, we contrasted measured values of the variable $D+\Delta$ against those computed by using Eq. (5), for which we assumed $h = U^2/(2g)$ (Fig. 5). The PTT-based approach does not account for the effect of the jet inclination. Nevertheless, it should be mentioned that Pagliara et al. (2008a) and Hoffmans (1998) argued that it is not prominent for oblique jets with $\alpha > 60°$. Overall, it was found that the theoretical approach performs better than any of those analyzed in this paper. Regardless of the simplifications adopted to develop Eq. (5), the PTT-based approach has the advantage to be independent of the tested conditions and, in principle, is not affected by scale effects.

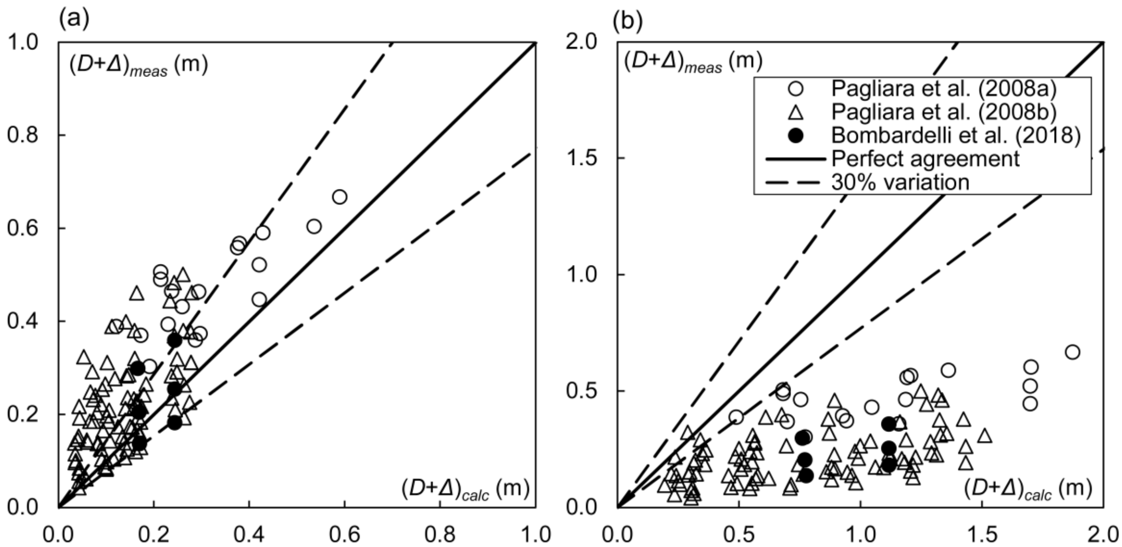

Figure 4 – Comparison of measured and calculated (using Eq. 4) values of the variable $D+\Delta$ for (a) $q=Q^*/B_c$ and (b) $q=Q^*/D^*$.

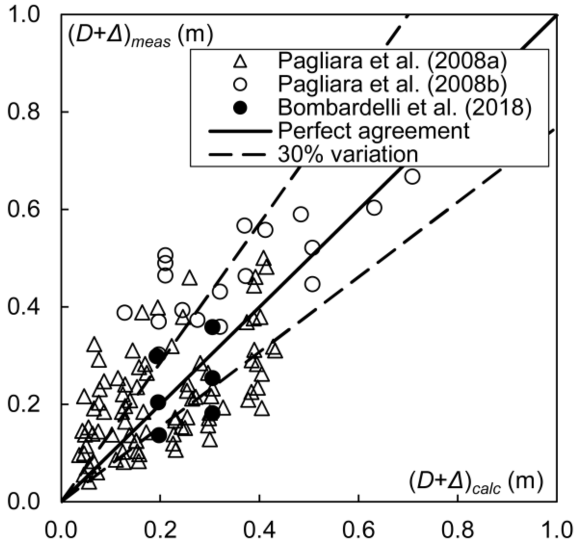

Figure 5 – Comparison of measured and calculated (using Eq. 5) values of the variable D+Δ.

5. CONCLUSION

In this paper, we analyzed the performance of different approaches to estimate the scour depth caused by circular plunging jets. We presented a selection of empirical, semi-theoretical, and theoretical formulas and discussed their applicability to the case of a 3D equilibrium configuration. To this end, interesting observations were provided pertaining to the estimation of the unit discharge present in most of the analyzed approaches. In particular, we pointed out that different estimations of the unit discharge may lead to discordant results, and we indicated the most reasonable estimation method for each formula. In doing so, we highlighted differences and similarities characterizing the selected equations. By using a large dataset pertaining to the 3D equilibrium scour depth, we also corroborated the limits of applicability of both empirical and semi-empirical formulas. Conversely, we showed that the fully theoretical approach proposed by Bombardelli et al. (2018) provides reliable results regardless of the tested range of parameters.

6. ACKNOWLEDGMENTS

This research did not receive any specific grant from funding agencies in the public, commercial, or not-for-profit sectors.

7. REFERENCES

Beltaos, S., and Rajaratnam, N. (1973). *Plane turbulent impinging jets*. Journal of Hydraulic Research, 11(1), 29-59.

Bombardelli, F. A. and Gioia, G. (2006). *Scouring of granular beds by jet-driven axisymmetric turbulent cauldrons.* Physics of Fluids 18, 088101.

Bombardelli, F.A., Palermo, M., and Pagliara, S. (2018). *Temporal evolution of jet induced scour depth in cohesionless granular beds and the phenomenological theory of turbulence.* Physics of Fluids, 30(8), 085109.

Bormann, N. E. and Julien, P. Y. (1991). *Scour downstream of grade-control structures*. Journal of Hydraulic Engineering 117(5), 579–594.

Castillo, L.G. and Carrillo, J.M. (2017). *Comparison of methods to estimate the scour downstream of a ski jump.* International Journal of Multiphase Flow, 92, 171–180.

D'Agostino, V. (1994). *Indagine sullo scavo a valle di opere trasversali mediante modello fisico a fondo mobile*. L'Energia Elettrica, 71(2), 37–51 (in Italian).

Ervine, D. A. (1976). *The entrainment of air in water*. International Water Power and Dam Construction, 28(12), 27-30.

Gioia, G. and Bombardelli, F. A., (2005). *Localized turbulent flows on scouring granular beds.* Physical Review Letters 95, 014501.

Hoffmans, G. J. C. M. (1998). *Jet scour in equilibrium phase*. Journal of Hydraulic Engineering. 124(4), 430-437.

Hoffmans, G. J. C. M. (2009). *Closure problem to jet scour*. Journal of Hydraulic Research. 47(1), 100-109.

Kotoulas, D. (1967). *Das Kolkproblem unter besonderer Berücksichtigung der Faktoren "Zeit" und "Geschiebemischung" im Rahmen der Wildbachverbauung*. Schweizerische Anstalt für das Forstliche Versuchswesen, 43(1). Beer: Zürich (in German).

Mason, P. J. and Arumugam, K. (1985). *Free jet scour below dams and flip buckets*. Journal of Hydraulic Engineering. 111(2), 220-235; 113(9), 1192-1205.

Mason, P. J. (1989). *Effects of air entrainment on plunge pool scour*. Journal of Hydraulic Engineering 115(3), 385-399; 117(2), 256-265.

Neill, C. R. (1968). *Note on initial movement of coarse uniform bed material.* Journal of Hydraulic Research, 6(2), 173-176.

Pagliara, S., Amidei, M., and Hager, W. H. (2008a). *Hydraulics of 3D plunge pool scour*. Journal of Hydraulic Engineering. 134(9), 1275–1284.

Pagliara, S., Hager, W.H., and Minor, H.-E. (2004). *Plunge pool scour formulae - An experimental verification.* 29° Convegno di Idraulica e Costruzioni Idrauliche, Trento, Italy, Bios Cosenza, 1, 1131–1138.

Pagliara, S., Hager, W. H., and Unger, J. (2008b). *Temporal evolution of plunge pool scour*. Journal of Hydraulic Eng 134(11), 1630 (2008b).

Whittaker J.G., and Schleiss A. (1984) *Scour related to energy dissipaters for high head structures.* Mitteilung 73 (D. Vischer, ed.). Versuchsanstalt für Wasserbau, Hydrologie und Glaziologie, ETH Zürich, Switzerland.

8th International Junior Researcher and Engineer Workshop
on Hydraulic Structures
ISBN: 978-0-578-37416-1
https://doi.org/10.26077/e5fd-df7a

CFD Simulation of Supercritical Flow in Narrow Channels Including Sediment Bypass Tunnels

Subhojit Kadia[1], Elena Pummer[1] and Nils Rüther[1]
[1]Department of Civil and Environmental Engineering
Norwegian University of Science and Technology
7491 Trondheim, NORWAY
E-mail: subhojit.kadia@ntnu.no (corresponding author)

Abstract: *Secondary currents, turbulence characteristics and bed shear stress distribution are the crucial parameters for specifying sediment transport. Hence, to understand the sediment transport in sediment bypass tunnels (SBTs), we performed computational fluid dynamics (CFD) simulation of supercritical flow in a narrow straight channel. The results of the steady state simulation (Froude number ≈ 1.8) were compared with experimental results. The commonly used two-equations linear eddy-viscosity models are limited to isotropic turbulence closure and hence could not replicate the desired secondary currents. Therefore, the LRR Reynolds Stress Model was used, and predicted the flow features and the secondary currents (three kinds in total) effectively. The secondary currents affected the longitudinal velocity and caused velocity dip. The existing atmEpsilonWallFunction was used to represent the dissipation of turbulent kinetic energy on the free surface. The obtained mean bed shear stress was 9.265 N/m² which is lower than the measured value of 10.225 N/m². This initial study contributes to the existing knowledge on the applications of CFD modelling in supercritical flow and SBTs. However, a comprehensive study considering different flow scenarios in narrow channels using improved LRR model and boundary conditions, over the used ones, is aimed to improve the accuracy in the estimation of flow field and bed shear stress.*

Keywords: *supercritical flow, secondary currents, CFD simulation, LRR.*

1. INTRODUCTION

Sediment bypass tunnels (SBTs), as "active sediment management" strategy, are increasingly used mainly in small and medium sized reservoirs for sediment management. SBTs are generally operated in supercritical open channel flow conditions and can be found around the world, but mostly in Switzerland and Japan (Auel & Boes, 2011). In some Japanese reservoirs, SBTs have accomplished more than 80% bypass efficiency and protracted the remaining reservoir lifespan by some hundreds of years (Auel *et al.*, 2016). Until now, the designs of existing SBTs are mainly based on model studies and some recommendations for selection of tunnel cross-section, bends, bed slope, regime of particle motion were proposed by Boes *et al.* (2014). We aim to develop numerical models which can estimate the flow characteristics, bed shear stress and sediment movement in narrow channels and SBTs. Thus, the time and cost involvements in the model studies can be reduced.

SBTs are designed for aspect ratio $b/h < 5$; where b = channel width and h = flow depth and perform like narrow open channels. Turbulence driven secondary currents in these channels can significantly influence the mean flow, turbulence structures, bed shear stress distribution (Kang and Choi, 2006) and thus the flow-sediment interactions. Auel *et al.* (2014); Jing *et al.* (2019) and Demiral *et al.* (2020) carried out physical model tests in supercritical flow conditions and observed secondary currents (Prandtl's second type) and velocity dips below the free surface as shown in Figure 1(a). Auel *et al.* (2014); Demiral *et al.* (2020) used the flow equilibrium parameter $\beta = \left(dR_h/dx - S_e\right)gR_h/U_{*l}^2$ to check the flow uniformity; where R_h is the hydraulic radius; S_e is the energy line slope; U_{*l} is the shear velocity calculated using the log-law; x is the distance along the longitudinal direction. Auel *et al.* (2014); Demiral *et al.* (2020) studied decelerating supercritical flow (β > -1) in flumes with 1% bed slope. Still, in a few cases at comparatively low Froude numbers (Fr) they achieved flow conditions very close to the uniform condition (β close to -1). And one of such cases is simulated in this study. Numerically, different approaches to model the turbulence driven secondary currents were carried out for subcritical flow conditions (Cokljat, 1993; Kang & Choi, 2006). The preferred two-equation turbulence models in hydraulics are based on eddy-viscosity concept, limited to isotropic turbulence closure, and thus incapable to reproduce the secondary currents and their effect on the flow field

(Cokljat, 1993; Cokljat & Younis, 1995; Kang & Choi, 2006). Cokljat (1993); Cokljat & Younis (1995); Kang & Choi (2006) used the Reynolds Stress Model (RSM) to represent such flow features for subcritical uniform flow conditions. Recently, Nasif *et al.* (2020) used the *k-ω* SST turbulence model in a detached-eddy simulation (computationally expensive) to model the supercritical flow in smooth channels. They observed stronger secondary vortices with a reduction in the aspect ratio. However, they did not observe velocity dips in their simulations for aspect ratios between 2 and 12.

To find a computationally cost-effective method, we test how far the supercritical flow observed by Auel *et al.* (2014) can be simulated using different closure models for the Reynolds-Averaged Navier-Stokes equations. The LRR Reynolds stress model performed acceptably. We simulated the test run TR1 from Auel *et al.* (2014) which was almost a uniform flow because β was close to -1.0 and compared the results with the experimental findings. The simulation was performed in OpenFOAM (v2012), an open-access computational fluid dynamics (CFD) tool based on the finite volume method, using *simpleFoam* solver which is a steady state solver based on SIMPLE algorithm (Talebpour, 2016; Talebpour & Liu, 2019).

2. NUMERICAL MODELLING

In CFD, one of the most popular approaches for solving the flow variables is the solution of the Reynolds-averaged Navier-Stokes equations. The Reynolds-averaged Navier-Stokes equations for incompressible fluid can be represented in cartesian coordinate system using the Einstein summation convention as (Wilcox, 2006; Alfonsi, 2009; Dey, 2014):

$$\frac{\partial U_i}{\partial x_i} = 0 \tag{1}$$

$$\rho \frac{\partial U_i}{\partial t} + \rho U_j \frac{\partial U_i}{\partial x_j} = -\frac{\partial P}{\partial x_i} + \mu \frac{\partial^2 U_i}{\partial x_j \partial x_j} - \rho \frac{\partial \overline{u_i' u_j'}}{\partial x_j} \tag{2}$$

where U = mean velocity, P = mean pressure, ρ = fluid density, μ = dynamic viscosity of the fluid, u' = velocity fluctuations and $R_{ij} = \overline{u_i' u_j'} =$ specific Reynolds stress tensor. The commonly used Reynolds-averaged Navier-Stokes equations turbulence closure models are based on the following “Boussinesq model” (Wilcox, 2006) and are called linear eddy-viscosity models

$$-\overline{u_i' u_j'} = \underbrace{2\nu_t S_{ij}}_{deviatoric} \underbrace{- \frac{2}{3} k \delta_{ij}}_{isotropic} \tag{3}$$

where ν_t = eddy-viscosity, $S_{ij} = 0.5\,(\partial U_i / \partial x_j + \partial U_j / \partial x_i) =$ mean strain-rate tensor, $k = 0.5\,\overline{u_i' u_i'} =$ turbulent kinetic energy and δ_{ij} = Kronecker’s delta. However, because the Reynolds stress tensor is approximated by a scalar quantity ν_t and assumed to vary linearly with the mean strain-rate, the approximation is unable to properly represent the complex flow phenomenon caused by sudden change in strain, curved surface, secondary currents, rotating fluid and 3D flows (Wilcox, 2006). The present study models the secondary currents in straight channels (Prandtl’s second type). The initial simulations were performed using the commonly used two-equations linear eddy-viscosity models: standard *k-ε*, Renormalization *k-ε*, *k-ω* shear stress transport, but they could not simulate the desired secondary currents. The turbulence driven secondary currents were mostly modelled previously using non-linear two-equation models, algebraic stress models (ASMs) and Reynolds stress models (RSMs) in several studies as described in Cokljat (1993); Kang & Choi (2006). The RSMs were found to be more accurate than others. The similar RSMs simulations performed earlier were also based on steady state simulation.

In RSMs, all six components of the Reynolds stress tensor are solved directly using transport equations. The transport equation is expressed as (Hanjalic & Launder, 1972; Launder *et al.*, 1975; Speziale *et al.*, 1991; Wilcox, 2006; Alfonsi, 2009):

$$\frac{D\overline{u_i'u_j'}}{Dt} = \frac{\partial \overline{u_i'u_j'}}{\partial t} + U_k \frac{\partial \overline{u_i'u_j'}}{\partial x_k} = \underbrace{-\left(\overline{u_i'u_k'}\frac{\partial U_j}{\partial x_k} + \overline{u_j'u_k'}\frac{\partial U_i}{\partial x_k}\right)}_{\text{Production}} \underbrace{- 2\nu \overline{\frac{\partial u_i'}{\partial x_k}\frac{\partial u_j'}{\partial x_k}}}_{\text{Dissipation}} + \underbrace{\overline{\frac{p'}{\rho}\left(\frac{\partial u_i'}{\partial x_j} + \frac{\partial u_j'}{\partial x_i}\right)}}_{\text{Pressure strain}}$$
$$-\frac{\partial}{\partial x_k}\underbrace{\left(\overline{u_i'u_j'u_k'} + \frac{1}{\rho}\left\{\overline{p'u_i'}\delta_{jk} + \overline{p'u_j'}\delta_{ik}\right\} - \nu\frac{\partial \overline{u_i'u_j'}}{\partial x_k}\right)}_{\text{Diffusion}} \tag{4}$$

The dissipation rate tensor basically consists of isotropic and deviatoric components. For high Reynolds number, the deviatoric part is considered as zero based on the "Kolmogorov hypothesis of local isotropy" (Wilcox, 2006; Alfonsi, 2009) and the dissipation rate tensor becomes a function of the dissipation rate of the turbulent kinetic energy ε and kinematic viscosity ν. The scalar quantity ε is basically obtained by solving its transport equation (Hanjalic & Launder, 1972; Launder *et al.*, 1975; Wilcox, 2006). The second and third terms in diffusion are basically ignored as detailed in Wilcox (2006). The tensor formed by the triple product of the velocity fluctuations is modelled in OpenFOAM using the simple gradient-transport or gradient-diffusion hypothesis proposed by Daly & Harlow (1970) (OpenCFD, 2021). Alternate gradient-diffusion models were proposed later by Hanjalic & Launder (1972); Launder *et al.* (1975) which satisfied the rotational symmetry. However, in various flows researchers found better overall results using Daly & Harlow (1970) (Cokljat, 1993). The pressure-strain correlation has been one of the main focusing points for turbulence modelers. The commonly used models are LRR or Launder, Reece and Rodi (Launder *et al.*, 1975) and SSG or Speziale, Sarkar and Gatski (Speziale *et al.*, 1991). The LRR model approximates the slow pressure-strain part or return-to-isotropy term using the method proposed by Rotta (1951) (Launder *et al.*, 1975; Cokljat, 1993; Cokljat & Younis, 1995; Wilcox, 2006). Continuing from the initial analysis of Rotta (1951), Launder *et al.* (1975) expressed the rapid pressure-strain (forth-order tensor) as a linear function of the Reynolds stress. Considering the dominant role of one term, Launder *et al.* (1975) also proposed the following simplified approach for the rapid pressure-strain:

$$\Pi_{ij,r} = -C\left(P_{ij} - \frac{2}{3}P_k\delta_{ij}\right) \tag{5}$$

where $$P_{ij} = -\left(\overline{u_i'u_k'}\frac{\partial U_j}{\partial x_k} + \overline{u_j'u_k'}\frac{\partial U_i}{\partial x_k}\right)$$

Where C = 0.6; P_k is the production of turbulent kinetic energy = ½ P_{kk} (Wilcox, 2006). The existing LRR model in OpenFOAM uses this simplified approach (from LRR.C file). The solid boundary or wall modifies the pressure field and influences the turbulence close to it and thus affects the energy transfer from the streamwise direction to its normal directions (Gibson & Launder, 1978; Cokljat, 1993). The most commonly used approach is the near-wall addition models proposed by Shir (1973) and Gibson & Launder (1978) for the slow and rapid pressure-strain terms, respectively. The corrections are function of L_t/n_ir_i; where n_i = unit vector normal to the surface; r = position vector and L_t = characteristics turbulence length scale (Gibson & Launder, 1978). OpenFOAM uses this method for the near-wall correction (OpenCFD, 2021). Further, OpenFOAM uses a linear variation of L_t/n_d to represent the above function and $L_t = C_\mu^{0.75}k^{3/2}/\kappa\varepsilon$, C_μ = 0.09, $\kappa = 0.41$ (from LRR.C file); n_d = wall distance. Later, Speziale *et al.* (1991) represented the pressure-strain tensor as a nonlinear function of the nondimensional Reynolds stress anisotropic tensor (Wilcox, 2006). Kang & Choi (2006) added the damping effect of the free surface in the existing SSG pressure-strain model. They used the model proposed by Shir (1973) and Gibson & Launder (1978) and the approach calibrated earlier by Cokljat (1993).

3. METHODOLOGY

The test TR1 from Auel *et al.* (2014) was modelled in this study. The test was conducted at Reynolds number Re ≈ 4.7 × 10^5, Fr ≈ 1.8 and flow depth h = 0.106 m. Auel *et al.* (2014) performed experiments in a 13.5 m long, 0.3 m wide and 0.5 m deep tilting flume with a concrete lined bed, glass right wall and PVC left wall. The measured section was located 6.4 m downstream, and the flow was gradually decelerating. In the LRR Reynolds stress modelling, the domain was 0.3 m wide and 0.106 m high. The aspect ratio for test TR1 was about 2.8. Along the longitudinal direction one cell was considered. The simulation was performed for steady state condition using *simpleFoam.* A total of 78020 hexahedral grid cells were created using *blockMesh*. The size of the smallest cell near the walls was 10 mm × 0.1 mm × 0.1 mm and the size of the cells increased towards the channel centre and free surface upto 10 mm × 2 mm × 2 mm. The increment was gradual using the *simpleGrading* function in *blockMesh* dictionary. The z^+ value for the first cell was close to 5 and it was calculated using the experimental shear velocity U_{*l}. A nonuniform grid, using comparatively smaller cells towards the walls, eliminated oscillations or checkerboarding in the distributions of pressure and secondary velocities which were observed when a uniform grid size (conforming to log-law, i.e., for $30 < z^+ < 200$) was used. The inlet and outlet boundary conditions were considered as *cyclic* or periodic. To drive the flow, a momentum source was introduced for the whole domain by mean velocity force (1.87, 0, 0) using the *fvOptions* utility in OpenFOAM (Talebpour, 2016). The applied force produces a corresponding pressure gradient. During the iterations, the pressure gradient and velocity field are updated consequently to maintain the volumetric mean velocity. Standard wall functions were used for k, ε, R and v_t parameters at the transitional rough bed and smooth sidewalls (OpenCFD, 2021). The uniform roughness on the channel bed was represented by equivalent sand grain roughness k_s = 0.28 mm (Auel *et al.*, 2014). The top surface was considered as a wall patch for the mesh generation to extract the boundary distance data. They were required to calculate the near boundary pressure strain correction imposed by the free surface. However, to make the top surface act like a free surface, the used boundary condition for velocity was *slip*; for P, k, and R were *zeroGradient;* and for ε *and* v_t were *atmEpsilonWallFunction* and *atmNutWallFunction*, respectively. Although, the last two boundary conditions were basically proposed for atmospheric boundary layer modelling, but they performed reasonably well in the current case and also in similar cases from Demiral *et al.*, (2020). The turbulence parameters were initialised using the following commonly used expressions

$$T_i = \mathrm{Re}^{-1/8}, k = \frac{3}{2}\left(uT_i\right)^2, \varepsilon = 0.09^{3/4}\frac{k^{3/2}}{L_c}, R_{ii} = \frac{2}{3}k \tag{6}$$

where T_i = turbulence intensity; u = mean velocity on inlet; L_c = characteristics length at inlet = 0.07 D_h; D_h = hydraulic diameter. A second order divergent scheme (*divScheme)* was used for velocity. Parallel processing was performed using *Scotch* method and 22 cores. In *simpleFoam*, the iterations were performed at 1 s intervals. The convergence criteria (residual control) were 0.0001 for all parameters. The solution converged after 6084 iterations. Once the simulation was converged, it was further run upto 10000 iterations to get average field values and it provided better result. The post-processing data extraction was performed in ParaView software and the data analysis was done using the Turbulucid package based on Python software (Mukha, 2018).

4. RESULTS AND DISCUSSION

4.1. Comparison between observed and simulated mean flow characteristics

The simulated normalised longitudinal velocity U/U_{max} distributions (where U_{max} is the maximum longitudinal velocity), velocity dip, upward & downward flows and normalised vertical velocity W/U_{max} distributions are comparable to the experimental results as found in Figure 1(a-b) and Figure 1(c-d). Figure 2(a-b) show a comparison between observed and simulated absolute and normalised longitudinal velocities at the channel centre, i.e., at y/h = 0 and at different sections along the channel width, respectively. The simulated position of U_{max} at y/h = 0 is located at about z/h = 0.5 which is very close to the experimental results as shown in Figure 2(a-b). The results indicate a good estimation of U and velocity dip throughout the channel width. The observed and simulated U_{max} values were 2.25 and 2.17 m/s (see Table 1), respectively. However, while inspecting Figure 1(c) and Figure 2(a-b) carefully, a rise in U was observed near the flume centre towards the free surface beyond $z/h \approx 0.95$ which is possibly caused by the interaction of two counter rotating large free surface vortices or secondary currents located just below the free surface as shown in Figure 1(g). Such observation could not be compared with the observed data because measurement of velocity just below the free surface is a tough task and is not available for the current case from Auel *et al.*, (2014) too. Thus, those results were not considered in the comparative study. A total of three kinds of secondary currents or vortices were observed: (i) large vortex below the free surface, (ii) smaller bottom vortex near the bed and sidewall and (iii) very small inner secondary vortex at the junction of free surface and sidewall (visible when the grid resolution was increased) as shown in Figure 1(d-e and g). Previously, Kang & Choi (2006) observed similar secondary current patterns for subcritical flow. The observed secondary flow pattern is comparable to the previous studies like: Cokljat (1993); Cokljat & Younis (1995); Kang & Choi (2006). As shown in Figure 1(d-f), the magnitude of the vertical velocity *W*, lateral velocity *V* and resultant secondary flow velocity U_{WV} were within 3-4% of U_{max} in most of the cells except the cells close to the free surface.

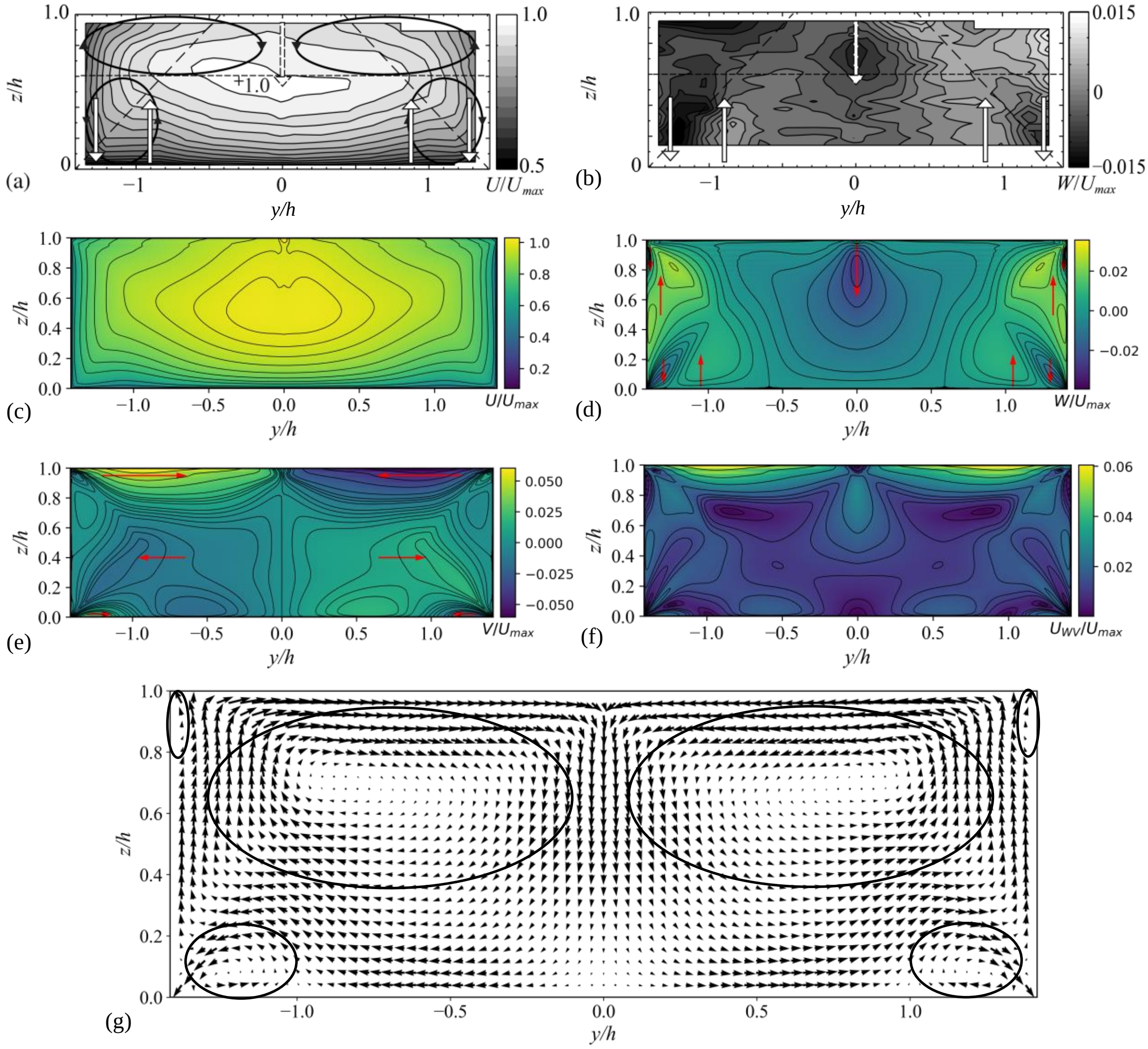

Figure 1(a-g) – Contour plots of the velocity field for test TR1 (Fr ≈ 1.8, h = 0.106 m) from Auel *et al.* (2014) (a) U/U_{max} distribution – exp. (Auel *et al.* 2014: with permission from ASCE), (b) W/U_{max} distribution – exp. (Auel *et al.* 2014: with permission from ASCE), (c) U/U_{max} distribution – CFD, (d) W/U_{max} distribution – CFD, (e) V/U_{max} distribution – CFD, (f) U_{WV}/U_{max} distribution – CFD, (g) Vector plot of secondary currents U_{WV} – CFD (z = distance from bed, h = flow depth, y = lateral distance).

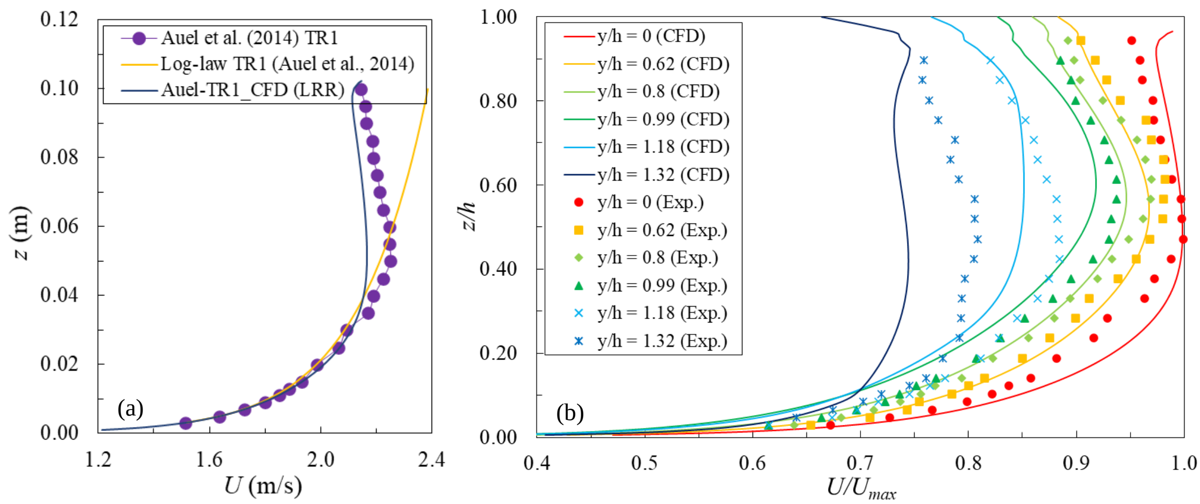

Figure 2(a-b) – Longitudinal velocity distribution (a) Absolute velocity at channel centre, (b) Normalised velocity at different lateral sections along the channel width.

4.2. Comparison of turbulence characteristics and shear stress

The turbulence intensity values for the longitudinal and vertical velocity components were calculated from the simulated specific Reynolds stress components as: $u_{rms} = \sqrt{R_{uu}}$ and $w_{rms} = \sqrt{R_{ww}}$. The shear velocity at the channel centre was calculated from the maximum specific Reynolds stress value near the bed (found at about 1 mm above the bed) as $u_{*r} = \sqrt{-R_{uw,bed}}$ and the cross-sectional averaged shear velocity U_{*r} was obtained from the R_{uw} distribution at 1 mm above the bed. The calculated results are compared with the experimental U_{*r} and U_{*l} in Table 1. Both experimental and simulated turbulence intensities, shown in Figure 3(a-d), indicate a low intensity at high U zone, i.e., around the centroid of the flow area and high intensity at low U zone, i.e., near the bed and sidewalls where the boundaries resist the longitudinal flow and affect the flow fluctuations. The simulated flow shown in Figure 3(c-d) alike the flow observed by Auel *et al.* (2014) (see Figure 3(a-b)) indicates same order of u_{rms} towards the bed and sidewalls, but greater w_{rms} towards the sidewalls than the bed. This observation is analogous to previous findings (Kang & Choi, 2006). Figure 3(e-f) display similar trend of Reynolds stress distribution for both observed and simulated flows. The Reynolds stress decreased towards the free surface from the bed and the negative minimum value was observed near the free surface and sidewall junctions where $\partial U / \partial z < 0$ due to free surface vortex. Figure 3(e-f) also indicate the upward shifting of the Reynolds stress contour lines at y/h around ± 1.0 caused by the upward flow component of the bottom vortex.

Figure 4(a-b) show the comparison between the simulated normalised turbulence intensity and normalised Reynolds stress profiles at the channel centre with those obtained from the experimental results from Auel *et al.* (2014) and Nezu (data collected from Auel *et al.* (2014)) and obtained from the universal empirical equation available for smooth uniform 2D open channel flow (Nezu & Nakagawa, 1993). The simulated profiles hold good agreement with the experimental results (except very close to the free surface in case of u_{rms}/u_{*r}) but deviated from the universal expressions due to the presence of secondary currents and velocity dip. Figure 5(a-b) show that the simulated bed shear stress decreased towards the sidewall upto the location of the bottom vortex ($y/h \approx \pm 1.0$), but increased towards the sidewalls as also observed by Auel *et al.* (2014). The simulated mean bed shear stress was 9.265 N/m^2 which is lower than the observed value of 10.225 N/m^2. But still, it is a good estimation for the purpose of flow and sediment transport in sediment bypass tunnels.

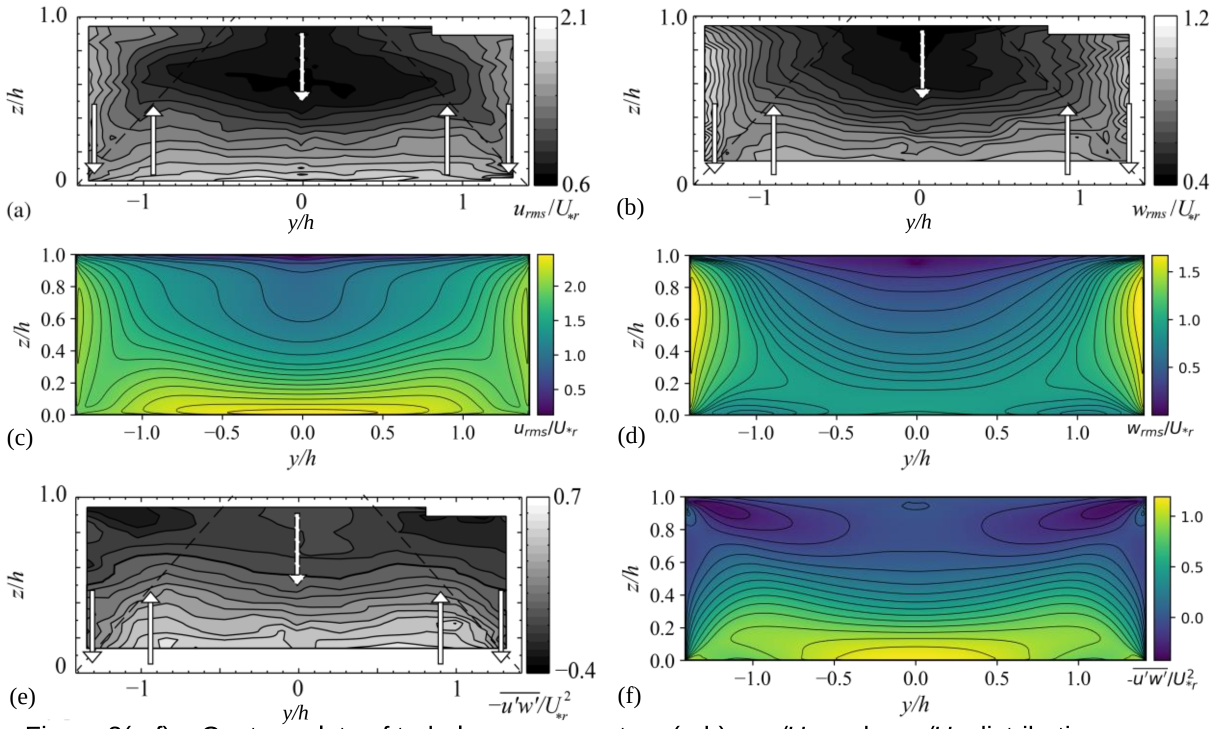

Figure 3(a-f) – Contour plots of turbulence parameters (a-b) u_{rms}/U_{*r} and w_{rms}/U_{*r} distributions – exp. (Auel *et al.*, 2014: with permission from ASCE), (c-d) u_{rms}/U_{*r} and w_{rms}/U_{*r} distributions – CFD, (e) Normalised specific Reynolds stress distribution – exp. (Auel *et al.*, 2014: with permission from ASCE) (f) Normalised specific Reynolds stress distribution – CFD.

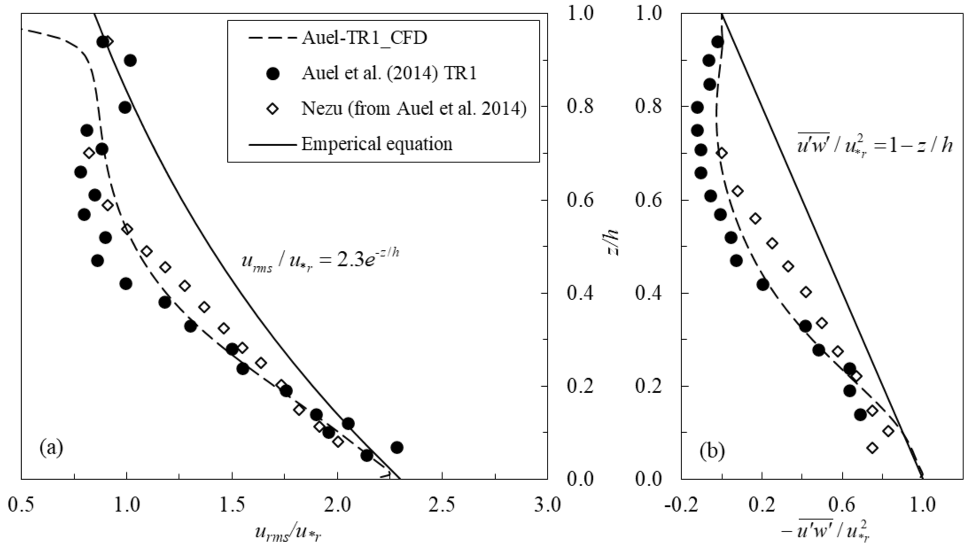

Figure 4(a-b) – Distribution of normalised turbulence parameters at the channel centre (a) Longitudinal turbulence intensity, (b) Reynolds stress.

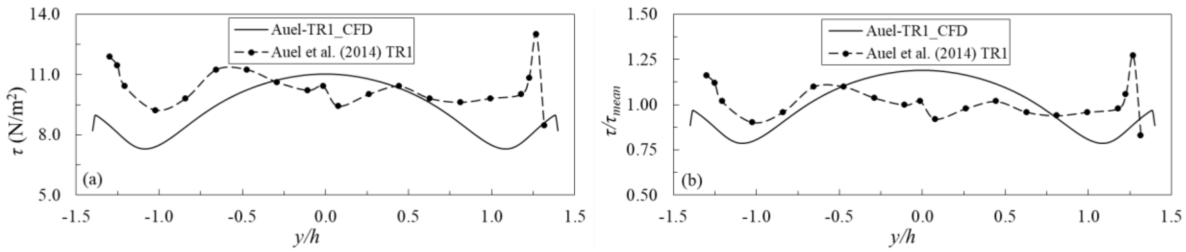

Figure 5(a-b) – Distribution of (a) Absolute bed shear stress, (b) Normalised bed shear stress.

Table 1 Comparison between exp. (Auel *et al.*, 2014) and CFD results for test TR1

Parameter	U_{max} **(m/s)**	U_{*r} **(m/s)**	U_{*l} **(m/s)**	u_{*r} **(m/s)**	u_{*l} **(m/s)**	τ_{mean} **(N/m²)**
Exp. (Auel *et al.*, 2014)	2.25	0.087	0.101	0.086	0.102	10.225
CFD	2.17	0.0963	-	0.105	$\approx u_{*r}$	9.265

5. CONCLUSIONS

The supercritical flow in an open channel flume model with aspect ratio ≈ 2.8 and Fr ≈ 1.8 was simulated in OpenFOAM using the steady state solver *simpleFoam* and the existing simplified LRR Reynolds stress model. The simulated results were compared with the experimental results for the velocity distributions, secondary currents, turbulence intensities, Reynolds stress and bed shear stress. The available *atmEpsilonWallFunction* boundary condition in OpenFOAM was used on the free surface and checked for its capability to increase the level of turbulence anisotropy and to produce the turbulence driven secondary currents. The predicted secondary currents, velocity distributions, velocity dips and turbulence parameters are comparable with the experimental results. The simulated flow showed three types of secondary currents as observed previously for subcritical flow. The model underestimated the bed shear stress within a considerable range. Overall, the simulated flow predicted most of the parameters with good precision except the near free surface lateral velocity and longitudinal turbulence intensity. However, a comprehensive study on several narrow channel flow conditions using the improved LRR model and the free surface boundary condition of ε suggested by Naot & Rodi (1982), over the used ones, is aimed to obtain the bed shear stress and the flow field characteristics with greater precision. Furthermore, measurements of lateral velocity and secondary currents in supercritical flows are challenging, and thus, CFD simulation shall be handy in such cases. This initial study adds to the existing knowledge on supercritical flow characteristics, bed shear stress distributions and CFD applications in narrow open channels including the SBTs. As the bed shear stress is crucial for sediment transport and design of SBTs, the Reynolds stress model can be utilised to estimate the bed shear stress and in the design of SBTs. The model is also expected to minimise the cost involved in the laboratory tests associated with the SBT designs.

6. ACKNOWLEDGMENTS

This study is funded by NTNU (project number 81772024). We thank Prof. Robert M. Boes (ETH Zurich), Dr. Ismail Albayrak (ETH Zurich) and Dr. Christian Auel (ILF Consulting Engineers) for their valuable contribution and for providing the experimental data. We thank to Dr. Silje K. Almeland for supporting with the Turbulucid package.

7. REFERENCES

Alfonsi, G. (2009), *Reynolds-Averaged Navier-Stokes Equations for Turbulence Modeling*, Applied Mechanics Reviews, 62(4), 1-20.

Auel, C. and Boes, R.M. (2011), *Sediment Bypass Tunnel Design - Review and Outlook*, In Schleiss, A.J. and Boes, R.M. (eds.) *Dams and Reservoirs under Changing Challenges - Proceedings of the 79 Annual Meeting of ICOLD,* Lucerne, Switzerland. London: CRC Press, pp. 403-412.

Auel, C., Albayrak, I. and Boes, R.M. (2014), *Turbulence Characteristics in Supercritical Open Channel Flows: Effects of Froude Number and Aspect Ratio*, Journal of Hydraulic Engineering, 140(4), 04014004.

Auel, C., Kantoush, S.A. and Sumi, T. (2016), *Positive Effects of Reservoir Sedimentation Management on Reservoir Life - Examples from Japan*, In *Proceedings of 84th Annual Meeting of ICOLD,* Johannesburg, South Africa, pp. 4-11-4-20.

Boes, R. M., Auel, C., Hagmann, M., and Albayrak, I. (2014), *Sediment Bypass Tunnels to Mitigate Reservoir Sedimentation and Restore Sediment Continuity*. In Schleiss, A.J. et al. (eds.) *Reservoir Sedimentation - River Flow 2014,* Lausanne, Switzerland. London: CRC Press, pp. 221-228.

Cokljat, D. and Younis, B.A. (1995), *Second-Order Closure Study of Open-Channel Flows*, Journal of Hydraulic Engineering, 121(2), 94-107.

Cokljat, D.P. (1993), *Turbulence Models for Non-Circular Ducts and Channels*, Doctoral Thesis, City University of London.

Daly, B.J. and Harlow, F.H. (1970), *Transport Equations in Turbulence,* Physics of Fluids, 13(11), 2634-2649.

Demiral, D., Boes, R.M. and Albayrak, I. (2020), *Effects of Secondary Currents on Turbulence Characteristics of Supercritical Open Channel Flows at Low Aspect Ratios*, Water, 12(11), 3233.

Dey, S. (2014), *Fluvial Hydrodynamics: Hydrodynamic and Sediment Transport Phenomena,* Springer, Berlin.

Gibson, M.M. and Launder, B.E. (1978), *Ground Effects on Pressure Fluctuations in the Atmospheric Boundary Layer*, Journal of Fluid Mechanics, 86(3), 491-511.

Hanjalic, K. and Launder, B.E. (1972), *A Reynolds Stress Model of Turbulence and Its Application to Thin Shear Flows*, Journal of Fluid Mechanics, 52(4), 609-638.

Jing, S., Yang, W. and Chen, Y. (2019), *Smooth Open Channel with Increasing Aspect Ratio: Influence on Secondary Flow*, Water, 11(9), 1872.

Kang, H. and Choi, S.U. (2006), *Reynolds Stress Modelling of Rectangular Open-Channel Flow,* International Journal for Numerical Methods in Fluids, 51(11), 1319-1334.

Launder, B.E., Reece, G.J. and Rodi, W. (1975), *Progress in the Development of a Reynolds-Stress Turbulence Closure*, Journal of Fluid Mechanics, 68(3), 537-566.

Mukha, T. (2018), *Turbulucid: A Python Package for Post-Processing of Fluid Flow Simulations,* Journal of Open Research Software, 6, 23.

Naot, D. and Rodi, W. (1982), *Calculation of Secondary Currents in Channel Flow,* Journal of the Hydraulics Division, 108(HY8), 948-968.

Nasif, G., Balachandar, R. and Barron, R. M. (2020), *Supercritical flow characteristics in smooth open channels with different aspect ratios*, Physics of Fluids, 32(10), 105102.

Nezu, I. and Nakagawa, H. (1993), *Turbulence in Open Channel Flows (IAHR Monographs)*, Balkema, Rotterdam, The Netherlands.

OpenCFD. (2021), *OpenFOAM: User Guide: V2012 OpenFOAM®: Open Source CFD : Documentation*, Available at: https://www.openfoam.com/documentation/guides/latest/doc/index.html (Accessed: 22 April 2021).

Rotta, J. (1951), *Statistische Theorie Nichthomogener Turbulenz*, Zeitschrift Für Physik, 129(6), 547-572.

Shir, C.C. (1973), *A Preliminary Numerical Study of Atmospheric Turbulent Flows in the Idealized Planetary Boundary Layer*, Journal of the Atmospheric Sciences, 30(7), 1327-1339.

Speziale, C.G., Sarkar, S. and Gatski, T.B. (1991), *Modelling the Pressure-Strain Correlation of Turbulence : An Invariant Dynamical Systems Approach*, Journal of Fluid Mechanics, 227, 245-272.

Talebpour, M. (2016), *Numerical Investigation of Turbulent-Driven Secondary Flow*, Thesis for Master of Science in Civil Engineering, The Pennsylvania State University.

Talebpour, M. and Liu, X. (2019), *Numerical Investigation on the Suitability of a Fourth-Order Nonlinear k-ω Model for Secondary Current of Second Type in Open-Channels*, Journal of Hydraulic Research, 57(1), 1-12.

Wilcox, D.C. (2006), *Turbulence Modelling for CFD*, 3rd Edition, La Canada, California: DCW Industries, Inc.

8th International Junior Researcher and Engineer Workshop on Hydraulic Structures
ISBN: 978-0-578-37416-1
https://doi.org/10.26077/bd85-0729

Galway, Ireland,
5th - 8th June 2021

Comparison of Pressure Distribution in 2D and 3D Jet-Driven Scour Processes

Simone Pagliara[1] and Deep Roy[2]
[1]Laboratory of Hydraulics, Hydrology and Glaciology (VAW)
ETH Zurich
Zürich 8093
SWITZERLAND
[2]Department of Energy, Systems, Territory and Construction Engineering
University of Pisa
Pisa 56122
ITALY
E-mail: pagliara@vaw.baug.ethz.ch

Abstract: *Water jets impacting on a non-cohesive granular bed cause a dynamic pressure distribution on the surface of the scour hole. Such distribution greatly differs from the hydrostatic one, especially in proximity of the impact zone, where the kinetic energy of the jet is dissipates due to the shear stresses acting on the scour surface. Here, the excess of shear stress causes the erosion of the bed material and can lead to the failure of hydraulic structures. Therefore, a detailed analysis of the forces acting on the scour surface is fundamental to understand the erosion mechanisms. Experimental tests were conducted under 3D and 2D conditions. Under 3D condition, the channel was wide enough to allow the full lateral development of the scour hole, whereas it was narrowed by means of vertical plates to achieve the 2D condition. Tests were conducted by monitoring the pressure distributions along the axial profile of the scour hole under both static and dynamic equilibrium conditions. The most influential parameters governing the scour process have been identified and varied, including the water discharge, the jet angle and the tailwater depth. Finally, the pressure distributions pertaining to 2D and 3D cases were compared, suggesting the dependence of the relative pressure on the tailwater and on the densimetric Froude number, and two empirical equations predicting the maximum relative pressure in case of low and high values of tailwater have been derived for design purposes. The proposed analysis represents a contribution to the development of theoretical methods for jet-driven scour processes.*

Keywords: *scour hole; plunging jets; pressure fluctuations.*

1. INTRODUCTION

The erosion phenomena due to an impacting water jet on a non-cohesive granular bed is of great interest for the design of hydraulic structures. There are multiple practical situations concerning a jet plunging into a pool of water with granular material at its bottom, such as potholes occurring downstream of dam spillways. The jet action results in a dynamic pressure distribution at the surface of the scour hole that may greatly differ from the hydrostatic one, especially in the impact region (Palermo et al 2020). During this process, the kinetic energy of the jet is dissipated due to the effects of the shear stresses which cause the movement of the granular material. If the shear stress exceeds the critical counterpart, then erosion takes place, leading to a possible failure of the hydraulic structure (Bombardelli & Gioia, 2005). The evaluation of the shear stresses due to a jet impinging on a granular bed material represents a challenging problem. A detailed knowledge of the shear stress distribution and magnitude can furnish a new insight on the dynamics of three-phase flows. Numerous studies have been conducted using laboratory models, and recently, an analytical formulation of the phenomenon has been proposed as well (see Di Nardi et al 2021). Empirical approaches have been widely used in hydraulic engineering for design purposes. Among others, significant contributions in this regard are due to Mason and Arumugam (1985), Breusers & Raudkivi (1991). In these studies, the following equation has been identified and calibrated:

$$h_0 + z_m = K\, q^{e_q}\, H^{e_H}\, g^{e_g}\, d^{e_d} \left(\frac{\rho}{\rho_s - \rho}\right)^{e_\rho} \tag{1}$$

where e_q, e_H, e_g, e_d and e_ρ are independent exponents, K is a multiplicative coefficient, ρ and ρ_s are the density of water and sediments, respectively, g is the gravitational acceleration, d is the sediment diameter, H is the falling height of the jet and q is the unit or total discharge, depending on the 2D or 3D equilibrium morphology conditions. More recently, Gioia & Bombardelli (2005) has provided the values of the abovementioned coefficients by revising equations from different authors (e.g., Schoklitsch 1932; Mueller & Eggenberger 1944; Kotoulas 1967).

An additional empirical approach was developed by Pagliara et al (2006) and then extended by Pagliara et al (2008a, b) and Pagliara & Palermo (2008). For the first time, two different equilibrium conditions have been distinguished, i.e., dynamic and static configurations, highlighting the important role played by the suspended material during the scour process. They evidenced that the scour geometry (i.e., maximum scour, length and height of the dune) mostly depends on the densimetric Froude number, the jet angle, bed sediment gradation and the air concentration in the jet. In addition, predicting relationships of the maximum scour depth for both static and dynamic equilibrium conditions have been proposed under both 2D and 3D conditions. Finally, Pagliara et al (2008a) provided a quantitative criterion to distinguish 2D and 3D cases. Namely, they introduced a three-dimensionality parameter $\lambda = b_m/B$, where B is the channel width and b_m is the extrapolated scour hole width. These authors also identified the fundamental parameters involved in the scour mechanism, i.e., the jet discharge Q, the jet velocity V_w, the jet angle α, the duration T of the jet action, the bed material characteristics (e.g., sediment density ρ_s, average diameter d_{50} and sediment non-uniformity parameter σ) and the water depth above the original sediment bed level h_0.

Likewise, semi-theoretical methods have been also developed. Among others, Stein & Julien (1993, 1994) focused on the scour evolution concluding that the equilibrium characteristics depend on the diffusion length. Hoffmans (1998) proposed an analysis based on Newton's second law, highlighting the shortcomings of empirical approaches. Finally, an attempt to use a fully theoretical approach was due to Bombardelli & Gioia (2005, 2006) who based their analysis on the phenomenological theory of turbulence.

Despite the large number of studies dealing with the topic, there are still open questions regarding the estimation of the shear stresses acting on the surface of the scour hole due to an impinging jet, such as their relationship with the pressure distribution at the bottom of the scour hole. The present study aims at highlighting the differences between the pressure distributions along the axial cross section of the scour hole under 2D and 3D conditions.

2. EXPERIMENTAL SETUP AND METHODOLOGY

2.1. Three-dimensional Plunge Pool Scour

Two different models for investigating the evolution of three-dimensional and two-dimensional scour holes due to an impinging jet have been built at the Hydraulic Laboratory of the University of Pisa, Italy. The experimental channel was 6 m long, 0.8 m wide and 0.9 m deep. The equilibrium morphology was always 3D under the tested ranges of discharge and tailwater depth.

Namely, a circular pipe with diameter D_p = 0.0215 m was used to simulate the jet. The pipe was inserted in a frame allowing for an angle variation between 0° and 90°. Two different jet inclinations were tested, i.e., α = 45° and 60°. The jet discharge Q ranged between 0.00115 and 0.00165 m^3/s and the distance between the jet pipe and the water surface was kept at a distance approximately equal to $2D_p$ (Palermo et al 2020). The experimental apparatus is schematically represented in Figure 1. One uniform granular material was adopted for the movable bed. This was characterized by a density ρ_s = 2214 kg/m^3, a mean diameter d_{50} = 0,00225 m and a nonuniformity parameter σ = 1.22. The bed material was levelled at the beginning of each test. The densimetric Froude number F_{d50} is a non-dimensional parameter that plays an important role for scour phenomena, and it is defined as $F_{d50} = V_w/(g' d_{50})^{0.5}$, where $g' = g(\rho_s-\rho)/\rho$.

Under three-dimensional scour condition, a preliminary test (termed "Test 0") was carried out to verify the consistency of half-model results with those obtained with full-model arrangement (see Pagliara et al 2008 for details). Test 0 was performed by positioning the jet along the axis of the channel, with a discharge Q = 0.003 m^3/s, water depth h_0 = 0.11 m, jet angle α = 45° and D_p = 0.028 m. After 300 seconds from the beginning of the test, the scour hole profile was surveyed under dynamic conditions by means of a special point gauge (Pagliara et al 2006). Measurements were taken in selected points. After the complete scour development (i.e., $t^* \approx 4200$ sec = 70 min) the water jet was stopped, the channel was slowly dried, and the survey of the scour hole was repeated under static condition. The full model test was repeated by locating the jet close to the glassed wall of the flume for Q = 0.0015 m^3/s and a pipe diameter D_p = 0.0215 m in order to preserve the same hydraulic conditions of the full model arrangement (i.e., same densimetric Froude number and nondimensional tailwater depth). The scour profiles and maximum scour depths obtained using the two different arrangements are consistent, thus confirming the findings of Pagliara et al (2008a). Therefore, all the other tests were conducted in the half-model setup, allowing us to monitor the scour evolution.

A total of 18 experimental tests were conducted under black-water conditions, i.e., no air was present in the water jet. A first series of 9 tests, namely "reference tests", allowed to establish the reference dynamic equilibrium configurations. At dynamic condition, the maximum scour depth z_m was measured by a point gauge at fixed time intervals. Once that the equilibrium configuration was reached, the profile of the scour hole was surveyed using a 1 mm precise point gauge. Measurements were taken along 3 longitudinal sections, with the first one located 0.02 m apart from the glass wall (i.e., axial section).

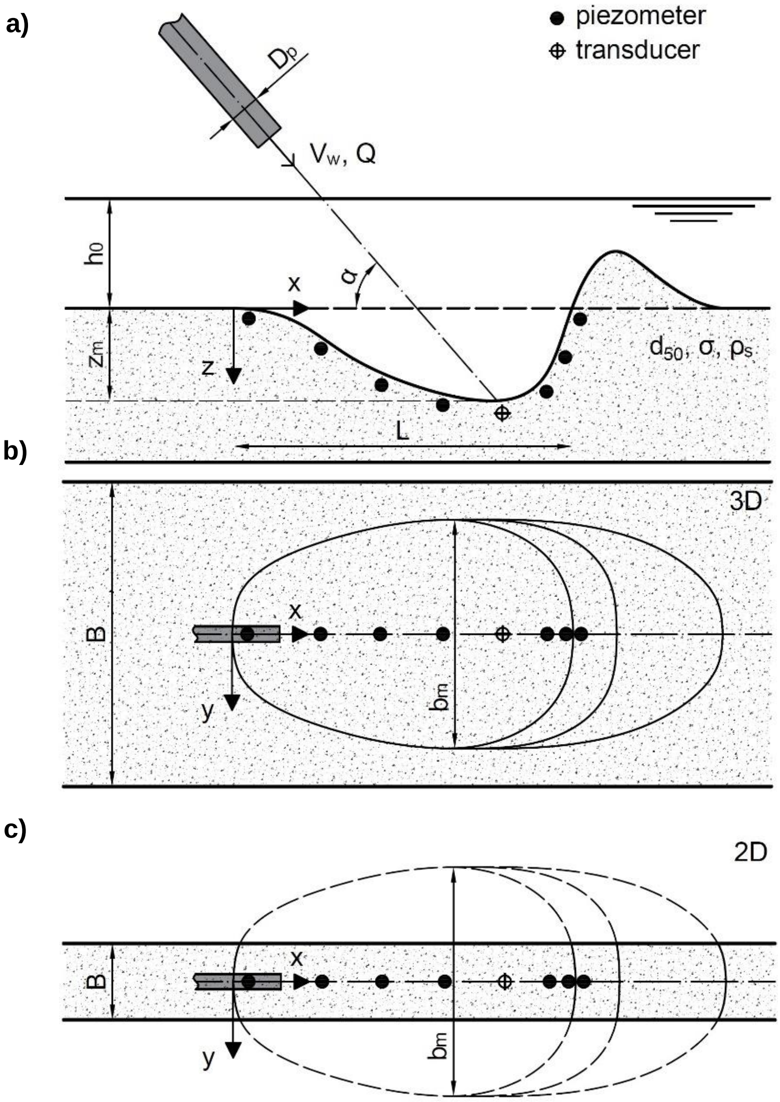

Figure 1 - Diagram sketch of the experimental setup: a) side view; b) top view and 3D condition; c) top view and 2D conditions

For the second series of experiments, the 9 tests were repeated by locating a pressure transducer and seven piezometers approximately 1 cm below the equilibrium scour surface pertaining to the corresponding reference tests. The pressure transducer was a SENSIT Type A-BIVAA-001 (Sensit, Woking, UK), characterized by a precision of ±1 % and an acquisition frequency of 10 Hz. It was located in correspondence with the jet impinging area, just below the point of maximum scour depth. Likewise, piezometers were located at other selected points below the axial equilibrium profile. The adopted instrumentation allowed to measure the distribution of the dynamic (P_d) and static (P_s) pressures along the axial profile at dynamic equilibrium condition.

Finally, the jet was stopped, resulting in the deposition of the suspended material and the complete drainage of the water inside the flume, and the static equilibrium scour profile was surveyed by means of the point gauge previously used.

2.2. Two-dimensional Plunge Pool Scour

The same experimental setup described before was adopted by Palermo et al (2020) for the investigation of the evolution of a two-dimensional scour hole due to an impinging jet. In this case, the channel width was B = 0.2 m. It is worth remarking that Pagliara et al (2008) experimentally found that a 3D scour hole occurs for λ < 1.5, while a 2D scour hole is characterized by values of λ larger than 3.0 (see Figure 1b and c; see Paragraph 1 for details about λ).

Two series of 12 experimental tests were conducted by Palermo et al (2020) and used herein for comparison. The ranges of the parameters tested under both 2D and 3D conditions are reported in Table 1, where D_{eq} indicate the equivalent jet diameter in case of 3D test condition performed with half scour and T_w is the tailwater defined as $T_w = h_0/D_{eq}$. For the 2D case, other details can be found in Palermo et al (2020).

Table 1 - Summary of test conditions for 2D (Palermo et al 2020) and 3D cases (present study).

Test #	Cond. 2D/3D	Q [m^3/s]	h_0 [m]	α [°]	D_p [m]	D_{eq} [m]	V_w [m/s]	F_{d50} [-]	T_w [-]
1	2D	0.00165	0.020	60	0.0215	0.0215	4.54	27.76	0.93
2	2D	0.00165	0.110	60	0.0215	0.0215	4.54	27.76	5.12
3	2D	0.00165	0.150	60	0.0215	0.0215	4.54	27.76	6.98
4	2D	0.00115	0.020	60	0.0215	0.0215	3.17	19.35	0.93
5	2D	0.00115	0.110	60	0.0215	0.0215	3.17	19.35	5.12
6	2D	0.00115	0.150	60	0.0215	0.0215	3.17	19.35	6.98
7	2D	0.00115	0.020	45	0.0215	0.0215	3.17	19.35	0.93
8	2D	0.00115	0.110	45	0.0215	0.0215	3.17	19.35	5.12
9	2D	0.00115	0.150	45	0.0215	0.0215	3.17	19.35	6.98
10	2D	0.00165	0.020	45	0.0215	0.0215	4.54	27.76	0.93
11	2D	0.00165	0.110	45	0.0215	0.0215	4.54	27.76	5.12
12	2D	0.00165	0.150	45	0.0215	0.0215	4.54	27.76	6.98
13	3D	0.00150	0.110	45	0.0215	0.0304	4.13	25.24	3.62
14	3D	0.00150	0.030	45	0.0215	0.0304	4.13	25.24	0.99
15	3D	0.00150	0.150	45	0.0215	0.0304	4.13	25.24	4.93
16	3D	0.00100	0.030	45	0.0215	0.0304	2.75	16.83	0.99
17	3D	0.00100	0.110	45	0.0215	0.0304	2.75	16.83	3.62
18	3D	0.00100	0.150	45	0.0215	0.0304	2.75	16.83	4.93
19	3D	0.00150	0.030	60	0.0215	0.0304	4.13	25.24	0.99
20	3D	0.00150	0.110	60	0.0215	0.0304	4.13	25.24	3.62
21	3D	0.00150	0.150	60	0.0215	0.0304	4.13	25.24	4.93

3. RESULTS AND DISCUSSIONS

3.1. Scour Hole Evolution

The scour evolution can be subdivided into two phases, i.e., developing and developed phases. The developing phase represents the initial enlargement of the scour hole and it is followed by the developed phase, when, for both 2D and 3D cases, a homothetic expansion of the scour hole occurs. The dynamic pressure increases with the scour depth until reaching an asymptotic value at equilibrium condition. In our tests, the equilibrium condition has always been reached for $t^* < 70$ minutes after the beginning of the test. In Figure 2, we show the pressure measured by the transducer as function of time t. It can be observed that in the first instants (i.e., developing phase), there is a significant increment of the pressure, followed by a quasi-stationary condition corresponding to the developed phase.

Furthermore, for both 2D and 3D conditions, the difference between dynamic and static pressure distribution is significant, because of the material rotating within the scour hole. Note that when the jet action ceases, the suspended material falls back into the scour hole, thus partially replenishing it; to this end, Figure 3 shows the non-dimensional scour depth $Z = z/z_m$ versus the non-dimensional longitudinal coordinate $X = x/L$ for the axial cross section of the scour hole of Test 14, where L is the length of the scour hole at dynamic equilibrium condition. This behaviour applies to both 2D and 3D cases. However, scour features under 3D condition are much more complex than the 2D counterpart. Namely, for the 3D case, a radial flow occurs within the scour hole; conversely, for the 2D case, the flow dynamics is characterized by a macro-vortex and a sediment transport directed only downstream. These differences reflect on the dynamic pressure distribution along the axial cross section the scour, as highlighted in the next section.

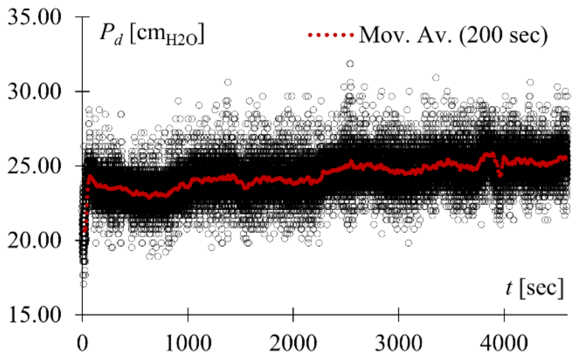

Figure 2 - Measured dynamic pressure P_d in Test 16 (Sensit pressure transducer).

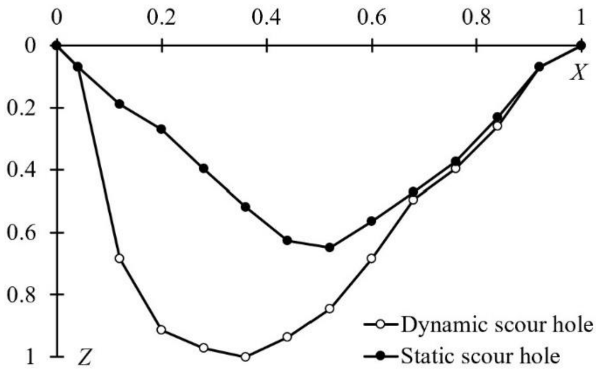

Figure 3 - Z vs X for the axial cross section of the scour hole created in Test 14.

3.2. Distribution of Pressures at Equilibrium Condition

The main objective of the present study is to investigate the differences and similitudes between the pressure distributions in correspondence with the axial cross section of the scour hole, under similar hydraulic conditions. To highlight the effects of the most influential parameters, the experimental tests have been grouped according to similar values of T_w and F_{d50}. In the following, "low tailwater" (symbol $T_w\uparrow$) indicate tests conducted for T_w = 0.93 and 0.99; whereas "high tailwater" (symbol $T_w\downarrow$) indicates tests for T_w = 5.12 and 4.93. Likewise, with "low densimetric Froude number" (symbol $F_{d50}\downarrow$) we mean those tests with F_{d50} = 19.35 and 16.83; and with "high densimetric Froude number" (symbol $F_{d50}\uparrow$), tests for which F_{d50} = 27.76 and 25.24 (see Table 1).

First, the relative pressures P_d/P_s were plotted against the non-dimensional longitudinal coordinate X in Figure 4. For α=60° and higher values of F_{d50}, the relative pressure P_d/P_s pertaining to 2D tests are always larger that the 3D counterpart, regardless of the tailwater depth T_w (Figure 4a and b, respectively). An opposite behaviour occurs for α=45° and for low values of T_w and F_{d50}, (Figure 4c). Conversely, a significant similitude of pressure distribution occurs for α=45°, low values of F_{d50} and high values of T_w.

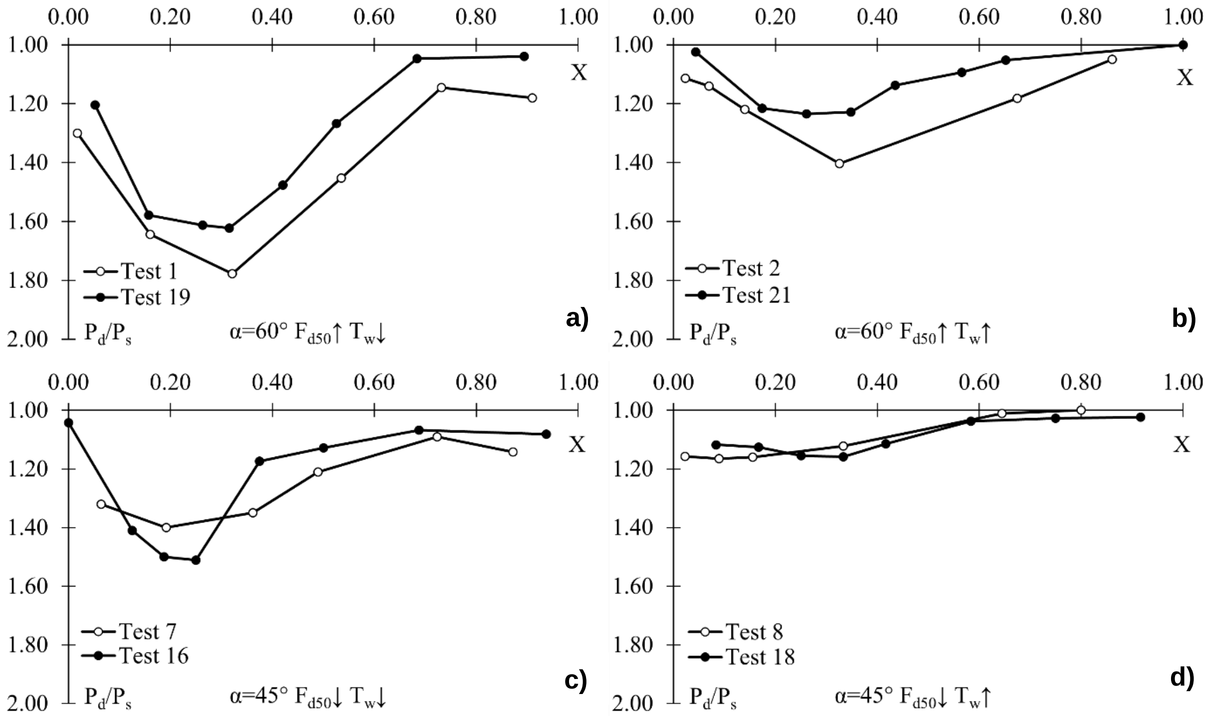

Figure 4 - P_d/P_s vs X for: a) α = 60°, high F_{d50} and low T_w; b) α = 60°, high F_{d50} and high T_w; c) α = 45°, low F_{d50} and low T_w; d) α = 45°, low F_{d50} and high T_w.

Then, the relationship between the maximum values of relative pressure $(P_d/P_s)_{\max}$ and the densimetric Froude number F_{d50} has been investigated. For low values of T_w, the behaviour of the 2D and 3D cases is consistent and $(P_d/P_s)_{\max}$ increases with α (Figure 5a) because of the increase of the vertical component of momentum flux. Conversely, if the diffusion length increases (high values of T_w), a clear distinction cannot be pointed out (Figure 5b). Furthermore, the ratio $(P_d/P_s)_{\max}$ of the two cases is consistent and it decreases with the tailwater depth (Figures 5c and d). Overall, for design purposes, the following two equation can be used to estimate the values of $(P_d/P_s)_{\max}$ (see Figure 6):

$$(P_d/P_s)_{max} = 0.0074 \cdot F_{d50} + 1.345 \quad (2)$$

valid for 16.83 ≤ F_{d50} ≤ 27.76, 0.93 ≤ T_w < 0.99, 45° ≤ α ≤ 60°, and

$$(P_d/P_s)_{max} = 0.0074 \cdot F_{d50} + 1.096 \quad (3)$$

valid for 16.83 ≤ F_{d50} ≤ 27.76, 4.93 ≤ T_w ≤ 5.12, 45° ≤ α ≤ 60°.

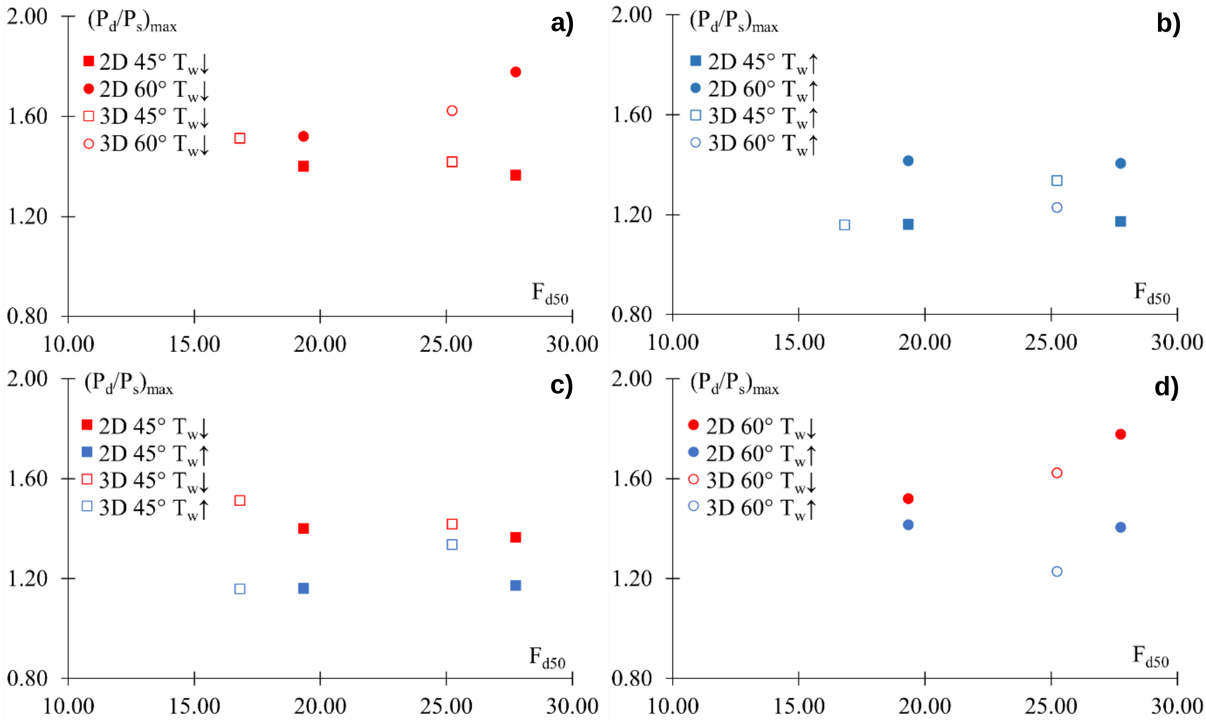

Figure 5 - $(P_d/P_s)_{max}$ vs F_{d50} for: a) low values of T_w; b) high values of T_w; c) jet angle α = 45°; d) jet angle α = 60°.

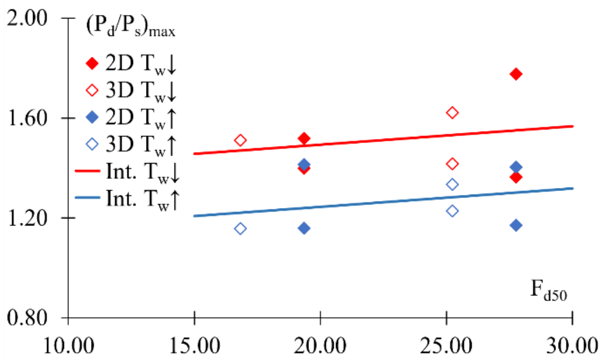

Figure 6 - $(P_d/P_s)_{max}$ vs F_{d50} for all tests, together with the predicting equations in case of low T_w (red line) and high T_w (blue line).

4. CONCLUSIONS

The scour process due to a water jet impinging on a granular bed is of great interest in hydraulic engineering since a dynamic pressure distribution greater than the hydrostatic one develops on the surface of the scour hole. Furthermore, the scour morphology and the pressure distribution differ according to the 2D or 3D condition of the scour itself. In the present study, differences between the dynamic pressure distribution along the axial section of the scour hole due to an impinging jet has been investigated for both 2D and 3D conditions. Several tests have been carried out for different hydraulic conditions: two inclinations of water jet angle α (45° and 60°), four values of water discharge Q (ranging between 0.00115 and 0.00165 m^3/s) and four values of water depth h_0 (ranging between 0.02 and 0.15 m). Qualitative differences between 2D and 3D conditions have been assessed: scour features under 3D condition are more complex since a radial flow occurs within the scour hole itself, while the 2D case is characterized by a macro-vortex causing the sediment transport to be directed in the downstream direction only. These differences reflect on the dynamic pressure distributions: for α=60° and high values of F_{d50}, P_d/P_s under 2D condition are always larger that the 3D counterpart, regardless of the T_w, while a significant similitude of the pressure distribution occurs for α=45°, suggesting a marked dependency on α. Further results show that the relative pressures P_d/P_s greatly depends on the tailwater T_w and on the densimetric Froude number F_{d50}, suggesting that P_d/P_s is larger for low values of T_w and large F_{d50}, within the tested range (i.e., 16.83 ≤ F_{d50} ≤ 27.76). Finally, the relationship between $(P_d/P_s)_{max}$ and F_{d50} was studied and two equations predicting the maximum relative pressure in case of low and high values of T_w were derived for design purposes. These may help to predict the ratio between the maximum dynamic and static pressures occurring at the point of maximum scour, and they are valid within the ranges 16.83 ≤ F_{d50} ≤ 27.76 and 45° ≤ α ≤ 60°.

REFERENCES

Bombardelli, F. A., and G. Gioia. 2005. "Towards a theoretical model for scour phenomena." In Vol. 2 of Proc., RCEM 2005, 4th IAHR Symp. On River, Coastal, and Estuarine Morphodynamics, edited by G. Parker and M. García, 931–936. London: CRC Press.

Breusers, H. N. C., and A. J. Raudkivi. 1991. Scouring: Hydraulic structures design manual series. Rotterdam, Netherlands: A.A. Balkema.

Di Nardi, J., Palermo M., Bombardelli F. A., and Pagliara S. 2021. "The Phenomenological Theory of Turbulence and the Scour Evolution Downstream of Grade-Control Structures under Steady Discharges" Water 13, no. 17: 2359. https://doi.org/10.3390/w13172359

Gioia, G., and F. A. Bombardelli. 2005. "Localized turbulent flows on scouring granular beds." Phys. Rev. Lett. 95 (1): 014501. https://doi.org/10.1103/PhysRevLett.95.014501.

Hoffmans, G. J. C. M. 1998. "Jet scour in equilibrium phase." J. Hydraul. Eng. 124 (4): 430–437. https://doi.org/10.1061/(ASCE)0733-9429(1998)124:4(430).

Mason, P. J., and K. Arumugam. 1985. "Free jet scour below dams and flip buckets." J. Hydraul. Eng. 111 (2): 220–235. https://doi.org/10.1061/(ASCE)0733-9429(1985)111:2(220).

Mueller, R., and W. Eggenberger. 1944. "Experimentelle und theoretische Untersuchungen ueber das Kolkproblem." [In German.] In Mitt. Versuchanstalt Wasserbau, No. 5. Zurich, Switzerland: ETH Zurich.

Pagliara, S., and M. Palermo. 2008. "Plane plunge pool scour with protection structures." J. Hydro-environ. Res. 2 (3): 182–191. https://doi.org/10.1016/j.jher.2008.06.002.

Pagliara, S., M. Amidei, and W. H. Hager. 2008a. "Hydraulics of 3D plunge pool scour." J. Hydraul. Eng. 134 (9): 1275–1284. https://doi.org/10.1061/(ASCE)0733-9429(2008)134:9(1275).

Pagliara, S., W. H. Hager, and H.-E. Minor. 2006. "Hydraulics of plane plunge pool scour." J. Hydraul. Eng. 132 (5): 450–461. https://doi.org/10.1061/(ASCE)0733-9429(2006)132:5(450).

Pagliara, S., W. H. Hager, and J. Unger. 2008b. "Temporal evolution of plunge pool scour." J. Hydraul. Eng. 134 (11): 1630–1638. https://doi.org/10.1061/(ASCE)0733-9429(2008)134:11(1630).

Palermo, M., Pagliara, S., & Bombardelli, F. A. 2020. Theoretical approach for shear-stress estimation at 2D equilibrium scour holes in granular material due to subvertical plunging jets. J. Hydraul. Eng. 146(4), 04020009. https://doi.org/10.1061/(ASCE)HY.1943-7900.0001703.

Schoklitsch, A. 1932. "Kolkbildung unter Ueberfallstrahlen." [In German.] Wasserwirtschaft 25 (24): 343.

Stein, O. R., and P. Y. Julien. 1990. "Sediment concentration measurements below small headcuts." In Proc., 1990 National Conf., 293–298. Reston, VA: ASCE.

Stein, O. R., and P. Y. Julien. 1993. "Criterion delineating the mode of headcut migration." J. Hydraul. Eng. 119 (1): 37–50. https://doi.org/10.1061/(ASCE)0733-9429(1993)119:1(37).

Stein, O. R., and P. Y. Julien. 1994. "Sediment concentration below free overfall." J. Hydraul. Eng. 120 (9): 1043–1059. https://doi.org/10.1061/(ASCE)0733-9429(1994)120:9(1043).

8th International Junior Researcher and Engineer Workshop on Hydraulic Structures
ISBN: 978-0-578-37416-1
https://doi.org/10.26077/6da9-2295

Galway, Ireland,
5th - 8th June 2021

Scour Downstream of Log-Frame Structures in the Presence of Rigid Vegetation

Deep Roy[1] and Simone Pagliara[2]
[1]Department of Energy, Systems, Territory and Construction Engineering
University of Pisa
Pisa 56122
ITALY
[2]Laboratory of Hydraulics, Hydrology and Glaciology (VAW)
ETH Zurich
Zürich 8093
SWITZERLAND
E-mail: d.roy1@studenti.unipi.it / 9deeproy2@gmail.com

Abstract: *Recently, various low-head environment friendly structures have been used to control the sediment transport and preserve river navigability. Among these structures, double winged log-frames are effective for concentrating the flow by decreasing channel width. Moreover, they create scour holes which can be used by fishes as resting spots. Usually, log-frames are placed in mountainous curved channels where there is natural growth of various types of in-stream vegetation in the downstream stilling basin of the structure which influences scour geometry and depth. Therefore, the current study aims to analyze the impact of rigid woody vegetation, placed downstream of double winged log-frames, on the overall equilibrium stilling basin morphology and scour depth magnitude in curved channels. The presence of rigid vegetation in different configurations and densities generally reduces the maximum scour depth with respect to the maximum scour generated in reference tests. Moreover, the vegetation considerably influences scour morphology and acts as natural protection to maintain channel bank and stilling basin stability.*

Keywords: *log-frame, rigid vegetation, scour morphology, curved channel.*

1. INTRODUCTION

To preserve and maintain the aquatic ecosystems of the world, different kinds of low-head structures like block ramps, log-frames, rock sills and others are placed in rivers. They control sediment load and enhance the natural habitat by facilitating fish migration. Double winged log-frames belong to this structure typology. Usually, the equilibrium stilling basin morphology at these structures is characterised by two distinct scour holes located upstream and downstream of the structure. These scour pools are used by fish as resting spots. There are several important studies carried out on low-head grade control structures like submerged vanes to examine the impact of the structure on flow velocity and scour pattern in straight and curved channels (Odgaard & Mosconi, 1987; Odgaard & Spoljaric, 1986; Odgaard & Wang, 1991, among others). Bhuiyan et al. (2007) conducted experiments on the characteristics of W weir in curved channels and Scurlock et al. (2012) investigated the hydraulic behaviour and scour pattern due to A-, U- and W-shaped weirs. Particularly, when the structures are placed in curved channels, secondary accelerations make the flow in the stilling basin asymmetric in nature. This leads to higher scour magnitude towards the outer bank of the channel. Therefore, the effect of channel curvature on the scour phenomena due to low-head structures was studied by some researchers (e.g., Pagliara et al., 2016). On the other hand, Pagliara et al. (2014) studied the hydraulic characteristics of log-vanes in straight channels and developed design equations to predict the main scour features. Whereas Pagliara et al. (2015) carried out a thorough investigation of the scour characteristics due to log deflectors. Finally, Pagliara et al. (2020) presented a novel scour morphology classification and proposed relationships to estimate scour geometry characteristics due to stone reinforced double winged log-frame structures in straight channels.

Usually, in field conditions, log-frames are placed in channel reaches where there is extensive growth of various kinds of vegetation in the downstream stilling basin. In some cases, the presence of in-stream vegetation in the form of large wood debris accumulation at hydraulic structures like bridge piers leads to enhanced scour and clogging effects which adversely affects the channel and structure stability. Conversely, the presence of stilling basin vegetation downstream of low-head grade control structures can have a positive effect in terms of basin stability. Some studies were made to examine the role channel vegetation has in influencing the flow characteristics (among others, Fairbanks & Diplas, 1998; Järvelä, 2005; Tsujimoto, 2000). In particular, Tanino and Nepf (2008) analyzed the drag force generated in a spatial distribution of rigid cylinders placed in the channel. Thereafter, Rominger et al. (2010) conducted a study on the impact of vegetation, located on bars at the meandering of a channel, on the overall flow properties. Chen et al. (2012) experimentally studied the role played by longitudinal solid bars and submerged vegetation to modify hydraulic characteristics of flow under clear water condition. More recently, the effect of in-stream vegetation on low-head grade control structures in curved channels was studied at the University of Pisa, Pisa (Italy). Pagliara et al. (2019) provided a preliminary analysis of the effect of downstream shrub vegetation presence on the scour morphology pattern due to double winged log-frames in channel bends. Palermo et al. (2019) showed that the presence of flexible vegetation reduces the maximum scour depth and modifies the overall scour geometry due to the same structure in curved rivers. Therefore, the current study aims to further examine the impact of rigid vegetation, placed downstream of double winged log-frames, on the equilibrium stilling basin morphology and global maximum scour magnitude in curved channels.

2. EXPERIMENTAL SET-UP

Several tests were conducted in the presence of rigid vegetation downstream of double winged log-frame structures in curved channel at the hydraulics laboratory of the Department of Energy, Systems, Territory and Construction Engineering (DESTEC) at the University of Pisa, Pisa (Italy). The curved channel used for the tests has the following characteristics: length = 6 m, width (B) = 0.5 m, depth = 0.5 m and radius of curvature (R) = 6 m (Figure 1). For a particular experiment, two different structure positions were tested, i.e., upstream position characterised by Ψ = 0.024 rad and downstream position characterised by Ψ = 0.385 rad, where Ψ is the angle subtended by the arc, extending from the beginning of the curved channel up to the position of the log-frame (Figure 1). The flow discharge is denoted by Q. Each log-frame structure consisted of two legs which were placed symmetrically in the channel. The legs were constructed from cylindrical pieces of log tied together with strings and weighted at the bottom to firmly hold the log-frame structure in position. The upstream structure is characterized by h_{st} = 0.04 m and l_{st}/B = 0.34, with h_{st} and l_{st} indicating the height and the length of a single leg of the structure, respectively. Conversely, h_{st} = 0.035 m and l_{st}/B = 0.46 for the downstream structure. Figure 2 shows the plan and cross-sectional views of a log-frame structure. In Figure 2, z_{mu} and z_{md} are maximum scour depths upstream and downstream of the structure. z_M is the maximum dune height, h_0 is the tailwater depth and α is the angle made by each leg with the direction of flow (i.e., α = 0.331 rad and 0.244 rad for upstream and downstream structure, respectively). In case of reference tests (Type 0), i.e., tests without vegetation reported in Palermo et al. (2019), the shaded dune area shown in Figure 2 is defined as A_{duneb}.

Rigid vegetation elements were placed in various spatial configurations and densities downstream of the log-frame structure. As shown in Figure 3, three different configurations of vegetation elements were tested in the downstream stilling basin, i.e., Type A, Type B and Type C. Lengths l_1, l_2, l_3 and l_4 denote the distance of a rigid vegetation element from the channel banks, downstream end of the log-frame (Figure 3) and adjacent vegetation element in the grid.

In Type B, the vegetation distribution is translated towards the inner bank as compared to Type C. Individual rigid vegetation elements were simulated using metallic cylinders of two diameters, Φ = 0.01 m and 0.008 m, which extended above the water surface and these cylinders have an average length of 0.40 m (Figure 3d). Moreover, the area of each shaded circle in Figure 3 represents the horizontal projected area of an individual rigid vegetation element. In a particular test, with a given vegetation configuration, the summation of the areas of all the circles represents the total horizontal projected area of rigid vegetation defined as A_{rv}. Tests with vegetation were conducted at identical hydraulic, granulometric and geometric conditions as that of the reference tests (Type 0) in the absence of vegetation reported in Palermo et al. (2019). A summary of experimental tests is shown in Table 1.

All tests were conducted with a uniform bed material characterised by d_{16} = 0.9 mm, d_{50} = 1 mm, d_{84} = 1.2 mm and sediment non-uniformity parameter σ = 1.15 where $\sigma = (d_{84}/d_{16})^{0.5}$ and d_{xx} is the diameter size for which xx% of material is finer. The densities of bed material and water are equal to

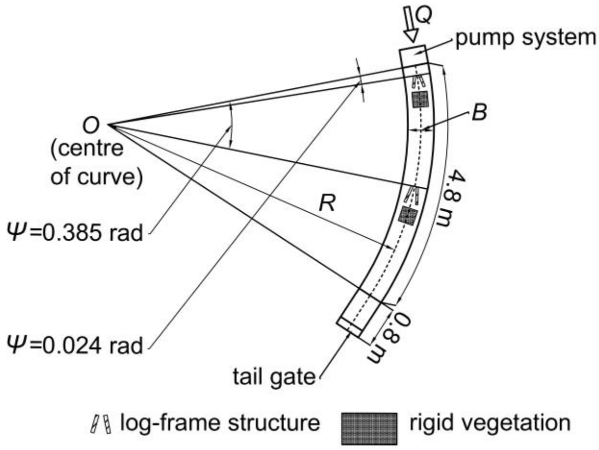

Figure 1 - Diagram of the curved channel highlighting the positions of the log-frame structure and rigid vegetation arrangement.

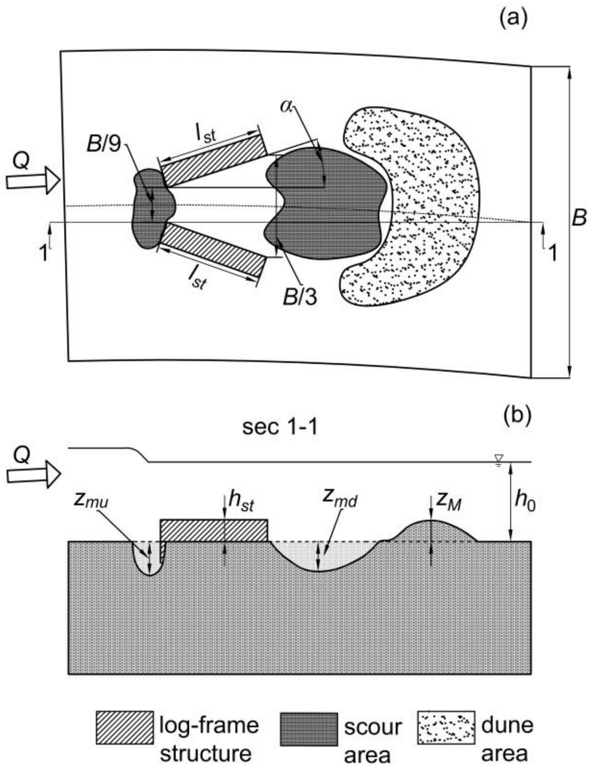

Figure 2 - a) Top view and b) cross-sectional view of a typical double winged log-frame structure used in the tests indicating important parameters.

ρ_s = 2467 kg/m^3 and ρ = 1000 kg/m^3, respectively. The bed was made horizontal before every test. The discharge and tailwater was ensured to be constant during the test duration. A sluice gate situated at the end of the channel was used to control the tailwater level. Tests were conducted under clear water and continued until an equilibrium scour condition was reached. A few supplementary tests having identical hydraulic and geometric conditions as in Table 1 were carried out to check the consistency of the scour pattern. Such tests resulted in similar scour morphology features as in the tests in Table 1. The water level and bed scour morphology were measured using a point gauge with accuracy of 0.1 mm. Points were measured in the deformed stilling basin with a spatial resolution of (1X1) cm. The precision of the scour measurements can be taken as $\pm 0.5d_{50}$ (Palermo et al., 2021).

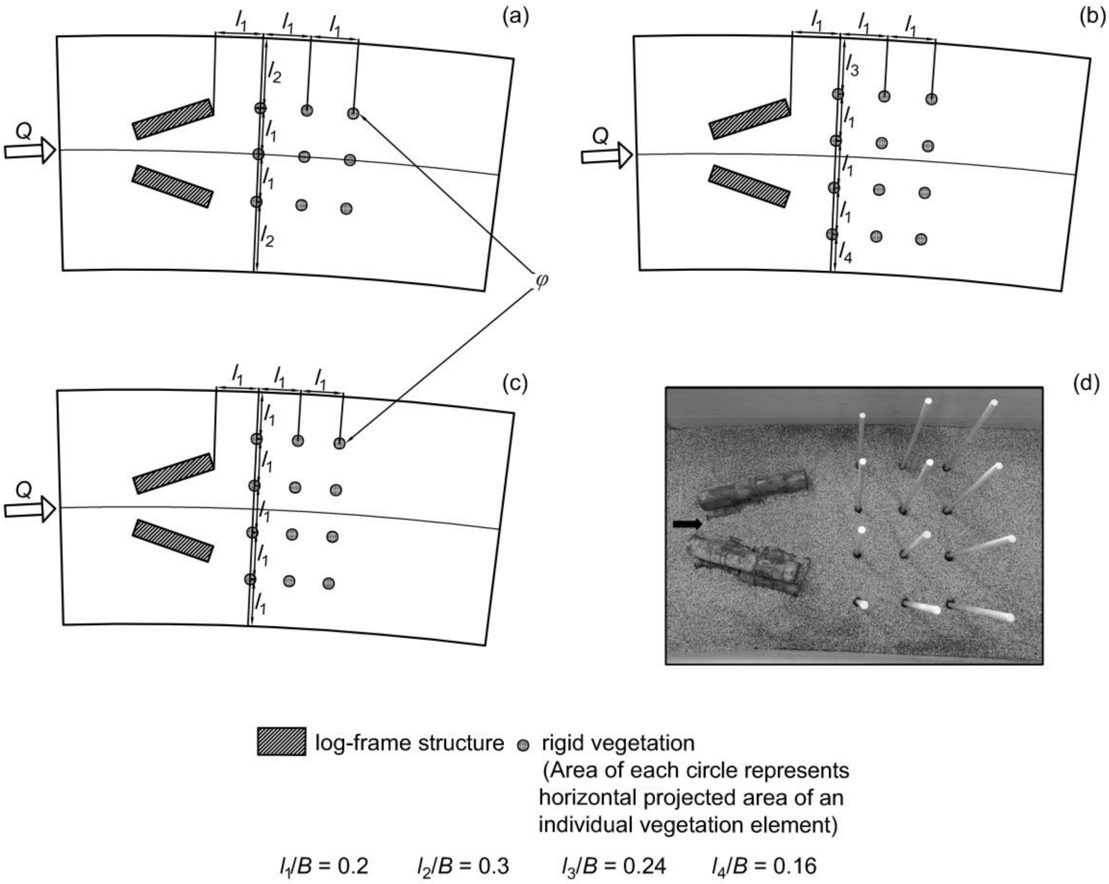

Figure 3 - Rigid vegetation spatial configurations shown as a) Type *A*, b) Type *B*, c) Type *C* and d) picture of an experimental setup during a test.

Table 1 Summary of experimental tests.

Test	***Q* (m³/s)**	***h*₀ (m)**	***Ψ* (rad)**	**Configuration**	***Φ* (m)**
1	0.0100	0.070	0.024	Type *A*	0.010
2	0.0100	0.070	0.385	Type *A*	0.008
3	0.0175	0.115	0.024	Type *A*	0.010
4	0.0175	0.115	0.385	Type *A*	0.008
5	0.0250	0.160	0.024	Type *A*	0.010
6	0.0250	0.160	0.385	Type *A*	0.008
7	0.0100	0.070	0.024	Type *A*	0.008
8	0.0100	0.070	0.385	Type *A*	0.010
9	0.0175	0.115	0.024	Type *A*	0.008
10	0.0175	0.115	0.385	Type *A*	0.010
11	0.0250	0.160	0.024	Type *A*	0.008
12	0.0250	0.160	0.385	Type *A*	0.010
13	0.0100	0.070	0.024	Type *B*	0.008
14	0.0100	0.070	0.385	Type *B*	0.010
15	0.0175	0.115	0.024	Type *B*	0.008
16	0.0175	0.115	0.385	Type *B*	0.010
17	0.0250	0.160	0.024	Type *B*	0.008
18	0.0250	0.160	0.385	Type *B*	0.010
19	0.0100	0.070	0.024	Type *B*	0.010
20	0.0100	0.070	0.385	Type *B*	0.008

21	0.0175	0.115	0.024	Type *B*	0.010
22	0.0175	0.115	0.385	Type *B*	0.008
23	0.0250	0.160	0.024	Type *B*	0.010
24	0.0250	0.160	0.385	Type *B*	0.008
25	0.0100	0.070	0.024	Type *C*	0.008
26	0.0100	0.070	0.385	Type *C*	0.010
27	0.0175	0.115	0.024	Type *C*	0.008
28	0.0175	0.115	0.385	Type *C*	0.010
29	0.0250	0.160	0.024	Type *C*	0.008
30	0.0250	0.160	0.385	Type *C*	0.010
31	0.0100	0.070	0.024	Type *C*	0.010
32	0.0100	0.070	0.385	Type *C*	0.008
33	0.0175	0.115	0.024	Type *C*	0.010
34	0.0175	0.115	0.385	Type *C*	0.008
35	0.0250	0.160	0.024	Type *C*	0.010
36	0.0250	0.160	0.385	Type *C*	0.008

3. RESULTS AND DISCUSSION

3.1. Maximum Scour Depth

From the tested results, a comparison was made between the global maximum scour depth due to log-frames in the presence of rigid vegetation and that occurring in corresponding reference tests, i.e., without vegetation. For different configurations, the non-dimensional vegetation density (η) is as follows:

$$\eta = A_{rv}/A_{duneb} \qquad (1)$$

where A_{rv} = horizontal projected area of rigid vegetation in the different tests, A_{duneb} = area of dune in corresponding reference tests. The various non-dimensional rigid vegetation densities are classified in four different groups: η_1 (for reference tests) = 0; $0 < \eta_2 \le 0.004$ (low density); $0.004 < \eta_3 \le 0.008$ (intermediate density); $0.008 < \eta_4 \le 0.026$ (high density). Moreover, as suggested by Pagliara et al. (2020), the equivalent Froude number for double winged log-frame structure (F_{deq}) is defined as follows:

$$\mathrm{F}_{deq} = Q/\{Bh_{st}[g(\Delta\rho/\rho)d_{50}]^{0.5}\} \qquad (2)$$

where g is the acceleration due to gravity and $\Delta\rho = \rho_s$-ρ is the reduced density. Note that F_{deq} accounts for the hydraulic condition of flow, structure geometry and granulometry of the channel bed. Therefore, the non-dimensional ratio between global maximum scour depths for vegetated channel (z_m) and that of corresponding reference tests (z_{mb}) are plotted against F_{deq} (Figure 4). The ratios are grouped according to structure position and non-dimensional rigid vegetation density.

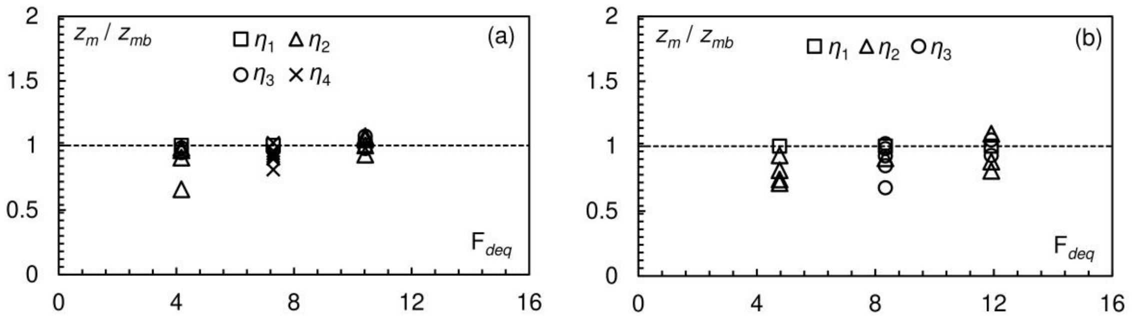

Figure 4 - Comparison of global maximum scour depth values due to various rigid vegetation densities for a) Ψ = 0.024 rad and b) Ψ = 0.385 rad.

From Figure 4, it is seen that for all structure positions and most of the vegetation densities, the ratios of the global maximum scour depth lie below the unit line. This signifies that the presence of rigid vegetation in the downstream stilling basin in curved channel usually reduces the maximum scour magnitude with respect to scour observed in reference tests. This can help to protect the structure and stilling basin against erosion. However, at high values of F_{deq}, the maximum scour depth in the presence of vegetation shows a slight increase above the unit line for some vegetation densities (Figure 4).

3.2. Scour Morphology

The equilibrium scour morphology provides interesting information for practitioners. Primarily, to analyze the effect of channel curvature on the stilling basin morphology two scour maps are considered in Figure 5. They pertain to identical hydraulic conditions, rigid vegetation diameter and configuration (Q = 0.010 m^3/s, h_0 = 0.07 m, Φ = 0.01 m, and Type *B*) but with different structure positions. For the upstream structure at Ψ = 0.024 rad (Figure 5a corresponding to Test 19), there are distinct zones of scour located in the upstream of the structure and the downstream stilling basin. The downstream scour is followed by a prominent dune region. Conversely, for the downstream structure at Ψ = 0.385 rad (Figure 5b corresponding to Test 14), the scour region is more concentrated towards the outer bank along with a prominent dune in the immediate downstream vicinity of the legs of the log-frame when compared to that of the previous case. This is because of channel curvature, that is more prominent in the downstream structure position resulting in centrifugal acceleration on the flow entering the stilling basin thereby making it asymmetric. Consequently, the scour is more pronounced in the vicinity of the outer bank of the channel. Generally speaking, for the structure positioned downstream of the curve vortex, the secondary accelerations play a major role resulting in a three-dimensional scour morphology, whereas for the structure positioned at the inlet of the curve such effects are negligible.

Figure 6 shows four scour morphology maps with similar hydraulic conditions, structure positions and vegetation diameter (Q = 0.0175 m^3/s, h_0 = 0.115 m, Ψ = 0.024 rad and Φ = 0.01 m) but with different vegetation configurations in addition to the corresponding reference test. Figure 6a shows the equilibrium morphology pertaining to the reference condition (Type 0) that is characterised by the presence of a distinct scour zone upstream of the structure and of scour and deposition zones in the downstream stilling basin. The upstream scour zone is more prominent than its downstream counterpart. Likewise, Figure 6b shows configuration Type *A* (Test 3). The equilibrium morphology is characterized by the presence of separate scour zones upstream and downstream of the log frame. The scour zone after the structure is typically double lobed and confined to the central part of channel by a dune occurring downstream. The scour and dune regions downstream of the log-frame in the presence of vegetation (Figure 6b) is deeper and larger in area than that of reference condition (Figure 6a). In Figure 6c (Test 21, Type *B*), the vegetation distribution is shifted laterally towards the inner bank resulting in an asymmetrical arrangement. However, the resulting scour morphology is quite similar to that shown in Figure 6b and is characterised by prominent scour zones upstream and downstream of structure along with a prominent dune in the stilling basin. Figure 6d (Test 33, Type *C*) exhibits similar scour morphology thereby showing that the lateral translation of the vegetation grid has negligible effect on the scour morphology.

Finally, two scour maps are shown in Figure 7 with identical hydraulic conditions, structure position and vegetation configuration (Q = 0.025 m^3/s, h_0 = 0.16 m, Ψ = 0.385 rad, and Type *C*) but having different

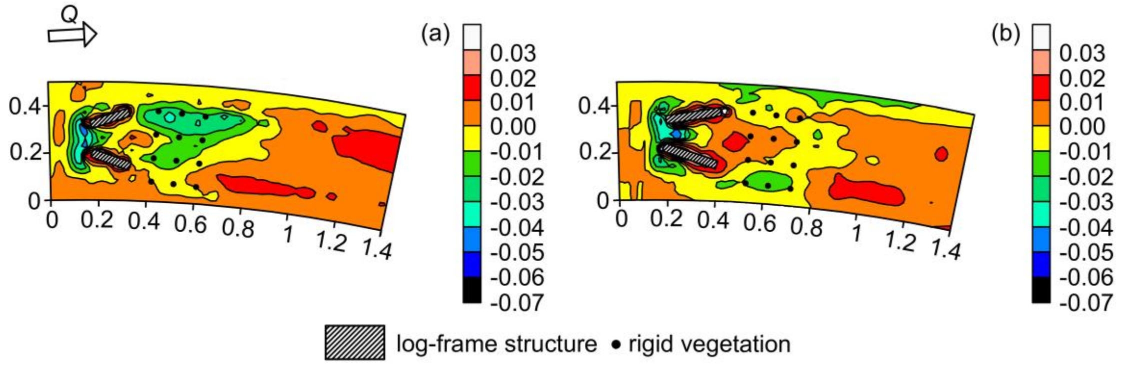

Figure 5 - Scour morphology maps for a) Test 19 (Ψ = 0.024 rad) and b) Test 14 (Ψ = 0.385 rad). All dimensions are in meter.

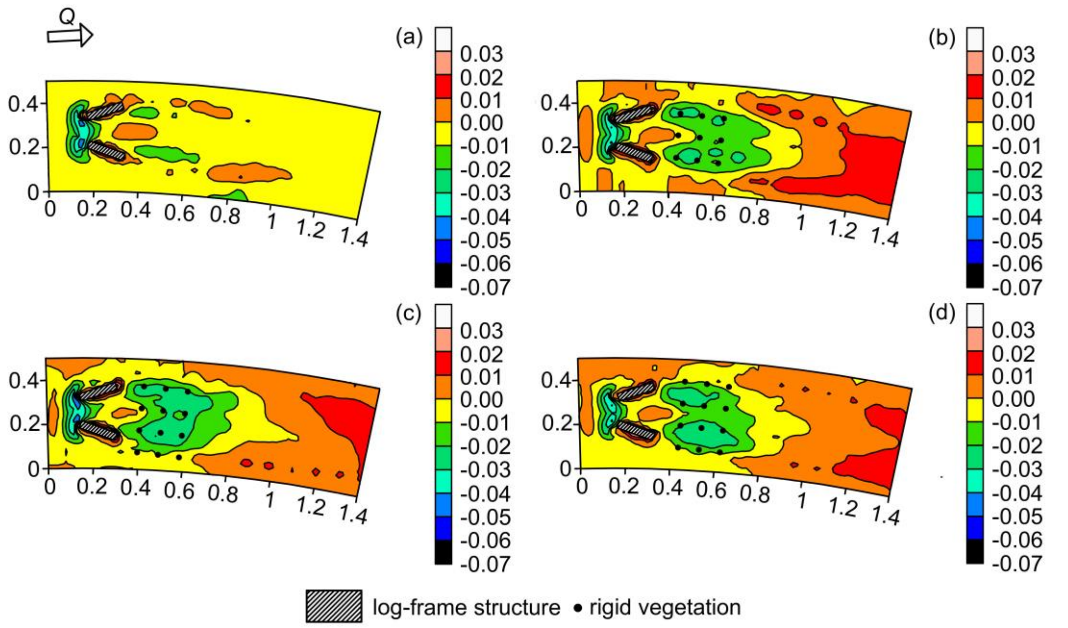

Figure 6 - Scour morphology maps for a) reference test in Palermo et al. (2019) without vegetation (Type 0), b) Test 3 (Type *A*), c) Test 21 (Type *B*) and d) Test 33 (Type *C*). All dimensions are in meter.

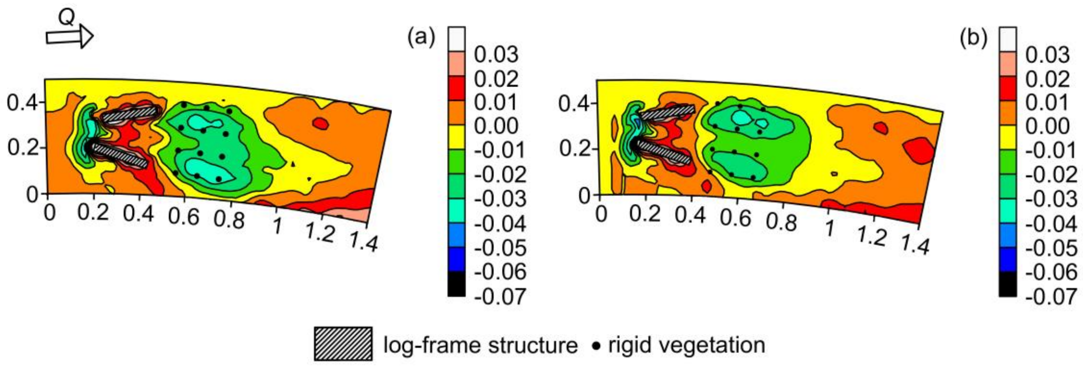

Figure 7 - Scour morphology maps for a) Test 30 (Φ = 0.01 m) and b) Test 36 (Φ = 0.008 m). All dimensions are in meter.

diameters of rigid vegetation elements. Both Figure 7a (Test 30, Φ = 0.01 m) and 7b (Test 36, Φ = 0.008 m), shows similar scour morphology characterised by scour zones both upstream and downstream of the structure. Thus, the effect of individual vegetation diameter on scour geometry is negligible.

4. CONCLUSIONS

Experiments were carried out under various hydraulic conditions to investigate the effect of downstream rigid vegetation on the maximum scour depth and equilibrium scour morphology at double winged log-frame structures in curved channels. Two different structure positions were tested in the curved channel (i.e., upstream and downstream). The diameter and spatial configuration of the rigid vegetation elements were varied. The global maximum scour depth at log-frames in the presence of rigid vegetation decreases in comparison to that for reference tests under otherwise similar conditions for both the structure positions and various vegetation densities. Consequently, the rigid vegetation can act as an eco-friendly protection measure to enhance structure and basin stability. Moreover, the rigid vegetation presence and structure position have a considerable impact on the equilibrium scour morphology due to log-frames. In case of reference tests, there are separate scour zones both upstream and downstream of the structure in the stilling basin. When rigid vegetation is introduced, the scour and dune regions downstream of the structure become more pronounced. The dune tends to confine the scour region to the central part of the channel. This is useful in curved channels where secondary accelerations cause the flow entering the stilling basin downstream of the log-frame to become asymmetric resulting in higher scour concentration towards the outer bank of the channel. In such a situation, the rigid vegetation can act as a natural stabilizer and protect the outer bank from failure due to progressive scour. Further comparison shows that the maximum scour depth in presence of both rigid and flexible vegetation generally decreases with respect to the scour depth without vegetation (Figure 4 of current paper and Figure 5 of Palermo et al., 2019). Comparing Figure 6 of this paper and Figure 7 of Palermo et al. (2019), it is seen that in the tested range, similar scour morphology can be obtained for identical configurations of rigid and flexible vegetation. For design purposes, the density and spatial configuration of the vegetation (both rigid and flexible) and structure position are important parameters for future research.

REFERENCES

Bhuiyan, F., Hey, R.D. and Wormleaton, P.R. (2007), *Hydraulic evaluation of W-weir for river restoration*, Journal of Hydraulic Engineering, 133 (6), 596-609.

Chen, S.-C., Kuo, Y.-M. and Yen, H.-C. (2012), *Effects of submerged flexible vegetation and solid structure bars on channel bed scour*, International Journal of Sediment Research, 27 (3), 323-336.

Fairbanks, J.D. and Diplas, P. (1998), *Turbulence characteristics of flows through partially and fully submerged vegetation*, in Hayes, D.F. (Ed) *Preprints of the Wetlands Engineering and River Restoration Conference: Engineering Approaches to Ecosystem Restoration*, Denver, March 22–27, 1998, pp. 865-870.

Järvelä, J. (2005), *Effect of submerged flexible vegetation on flow structure and resistance*, Journal of Hydrology, 307, 233-241.

Odgaard, A.J. and Mosconi, C.E. (1987), *Stream bank protection by submerged vanes*, Journal of Hydraulic Engineering, 113 (4), 520-536.

Odgaard, A.J. and Spoljaric, A. (1986), *Sediment control by submerged vanes*, Journal of Hydraulic Engineering, 112 (12), 1164-1181.

Odgaard, A.J. and Wang, Y. (1991), *Sediment management with submerged vanes. II: applications*, Journal of Hydraulic Engineering, 117 (3), 284-302.

Pagliara, S., Hassanabadi, L.S. and Kurdistani, S.M. (2014), *Log-vane scour in clear water condition*, River Research and Applications, 31, 1176-1182.

Pagliara, S., Hassanabadi, L. and Kurdistani, S.M. (2015), *Clear water scour downstream of log deflectors in horizontal channels*, Journal of Irrigation and Drainage Engineering, 141 (9), 1-8, 04015007.

Pagliara, S., Kurdistani, S.M., Palermo, M. and Simoni, D. (2016), *Scour due to rock sills in straight and curved horizontal channels*, Journal of Hydro-environment Research, 10, 12-20.

Pagliara, S., Palermo, M. and Roy, D. (2019), *The role of shrubs in river bed erosion: A preliminary morphological analysis*, in *Preprints of the 38th IAHR World Congress*, Panama City, September 1-6, 2019, pp. 2346-2355.

Pagliara, S., Palermo, M. and Roy, D. (2020), *Scour around double-winged log frames under clear water condition*, Journal of Irrigation and Drainage Engineering, 146 (12), 1-11, 04020038.

Palermo, M., Pagliara, S. and Roy, D. (2019), *Effect of flexible vegetation on stilling basin erosion downstream of log-frame structures*, in *Preprints of the 38th IAHR World Congress*, Panama City, September 1-6, 2019, pp. 1577-1586.

Palermo, M., Roy, D. and Pagliara, S. (2021), *Morphological characteristics of eco-friendly protected basins downstream of block ramps in river bends*, Geomorphology, 377, 107587.

Rominger, J.T., Lightbody, A.F. and Nepf, H.M. (2010), *Effects of added vegetation on sand bar stability and stream hydrodynamics*, Journal of Hydraulic Engineering, 136 (12), 994-1002.

Scurlock, S. M., Thornton, C. I. and Abt, S. R. (2012), *Equilibrium scour downstream of three-dimensional grade-control structures*, Journal of Hydraulic Engineering, 138 (2), 167-176.

Tanino, Y. and Nepf, H.M. (2008), *Laboratory investigation of mean drag in a random array of rigid, emergent cylinders*, Journal of Hydraulic Engineering, 134 (1), 34-41.

Tsujimoto, T. (2000), *Fluvial processes in streams with vegetation*, Journal of Hydraulic Research, 37 (6), 789-803.

8th International Junior Researcher and Engineer Workshop
on Hydraulic Structures
ISBN: 978-0-578-37416-1
https://doi.org/10.26077/701a-fbb2

Galway, Ireland,
5th - 8th June 2021

Particle Image Velocimetry (PIV) Investigation of Local Scour Around Emergent and Submerged Circular Cylinders

P. Williams[1], R. Balachandar[1], V. Roussinova[2] and R. Barron[3]
[1]Department of Civil and Environmental Engineering
University of Windsor
Windsor, ON N9B 3P4
CANADA
[2]Department of Mechanical, Automotive and Materials Engineering
University of Windsor
Windsor, ON N9B 3P4
CANADA
[3]Department of Mathematics and Statistics
University of Windsor
Windsor, ON N9B 3P4
CANADA
E-mail: williamq@uwindsor.ca

Abstract: *Analysis of the velocity field surrounding a circular cylinder under equilibrium of local scour has been restricted due to practical limitations of commonly used measurement techniques. This investigation summarizes select cases in the literature which have attempted to circumvent such limitations and presents flow field measurements using Particle Image Velocimetry (PIV). Scour tests were conducted in a horizontal flume fitted with a sediment recess containing erodible bed material. Tests were conducted with both emergent and submerged circular cylinders for a period of 24 hours, after which equilibrium was achieved and planar PIV measurements were obtained in the streamwise-vertical symmetry plane. Analysis of bed profiles and the distribution of the mean velocity indicated that the scour depth upstream of the cylinder was slightly (2 percent) higher for the emergent case, and separation of flow over the top of the submerged cylinder affected the formation of the dune in the wake of the cylinder.*

Keywords: *erosion, local scour, Particle Image Velocimetry (PIV), pier scour, scour modelling*

1. INTRODUCTION

Scour and erosion have been repeatedly established as the principal cause of most bridge failures in North America (Melville & Coleman, 2000, LeBeau & Wadia-Fascetti, 2007). The number of high-profile collapses spanning the past several decades are an indication of the need for improved methods of the design of foundation head with respect to local scour. While the evaluation of foundation head is predominantly achieved using empirical equations, such methods have proven inaccurate. Failure to achieve geometric similitude certainly contributes to such inaccuracy; however, it has also been determined that there are some aspects of the mechanisms that drive local scour which are not well understood. Prior work has been primarily concerned with exploring the relationship between various scour-governing parameters and the bed formation at an equilibrium condition. While this is reasonable from a design perspective, since the maximum scour depth in the vicinity of the pier is the quantity by which the foundation head is established, the examination of bed formations alone does not provide an accurate depiction of the flow field surrounding a pier under equilibrium of local scour (Williams et al., 2016).

In order to fully appreciate the mechanism of local scour and the parametric framework necessary for scour design, flow field measurements in the vicinity of the cylinder are required. Although the existence of large-scale turbulence structures (i.e., the downflow, horseshoe vortex, wake vortices) in the flow field surrounding a cylinder under equilibrium of local scour are well understood, the effect of changes in flow, sediment and cylinder characteristics on their size and strength require further consideration for design purposes. However, acquisition of such detailed flow measurements is not easily achieved. Point measurements using Acoustic Doppler Velocimetry (ADV) and Laser Doppler

Velocimetry (LDV) are time consuming, which significantly reduces the size of the region over which data can be reasonably acquired. Furthermore, the use of a downward-facing ADV probe eliminates the possibility of measurements within five centimetres of the free surface, which can amount to a significant portion of shallow flow. The use of techniques such as LDV and Particle Image Velocimetry (PIV) are also limited in scour modelling since the presence of solid features such as the pier and the bed formations reduce optical access to some areas of flow. Even so, PIV is considered preferable in order to acquire data over the cross-sectional area of flow required for the necessary analysis.

The use of planar PIV in scour experiments has been met with some difficulty, largely due to the practical need for a transparent surface through which image capture can occur. Planar capture is then realistically restricted to the *XZ* and *XY* planes. Here, *X* is the streamwise coordinate direction, *Y* is the vertical coordinate direction and *Z* is the spanwise coordinate direction. While measurements in the *XZ* plane would be possible with orientation of the laser sheet perpendicular to the flume sidewall and positioning of the camera lens in the downward vertical direction atop of the flume, the primary intention of the present experiments was to capture the flow field in the *XY* plane, in which velocity measurements using ADV are commonly presented for scour experiments. The unscoured bed material does impede image capture in the region below the original bed level in this plane; however, PIV measurements were captured in the entire flow field above this location.

Unger and Hager (2007) reported on the characteristics of the downflow and horseshoe vortex around a bridge pier. The authors assumed that the flow field around a half-cylinder placed against a transparent flume sidewall in erodible sediment would be representative of half of the flow field around a full cylinder. PIV measurements were captured in the *XY* plane for this set-up, and as such measurements within the scour hole were obtainable. Practically, however, this configuration describes abutment scour, and cannot really be viewed as intended by the authors. Kirkil et al. (2008) were able to capture streamline patterns at the free surface in the wake region of flow around a circular cylinder with scour using a large-scale Particle Image Velocimetry (LSPIV) system in the *XZ* plane. Zhang et al. (2009) explored local scour around a spur dyke placed against a transparent flume sidewall in a sediment recess. PIV measurements were made in the *XY* and *XZ* planes, and due to the location of the spur dyke, flow field measurements were once again captured within the scour hole. Guan et al. (2019) used an oblique shooting method to capture PIV measurements within the scour hole upstream of a circular cylinder. In this method, the camera was tilted at an angle and the PIV data was corrected in post-processing to account for the angle. However, in using this method, the measurements are limited to a single field-of-view in the oblique plane. Furthermore, while it was reported that there was no ‘significant’ discrepancy between measurements acquired using the oblique shooting method and a normal shooting method, there are additional potential uncertainties that could arise in using such a method. In general, the limitations of PIV use in scour experiments are well-demonstrated in the literature.

In literature, the majority of scour investigations have been carried out for emergent cylinders. However, there are many practical examples of flow past submerged cylinders in the field, including well foundations of bridge piers, piers which are submerged during flooding, structures in floodplains during flood events, structures submerged in offshore or coastal tides or currents (Dey et al., 2008), such as sub-sea caissons, platform foundations and submerged cylindrical breakwaters (Zhao et al., 2010), and submerged vegetation in natural streambeds (Dey et al., 2008). Therefore, both emergent- and submerged-type cylinders have been considered in the present investigation.

2. METHODOLOGY

2.1. Description of the laboratory facility

The experimental investigation was carried out at the Ed Lumley Centre for Engineering Innovation at the University of Windsor in Windsor, Canada. The laboratory facility contains a horizontal flume that is 10.5 m long, 0.84 m deep and 1.22 m wide. A schematic of the flume is shown in Figure 1. The flume is fitted with two flow conditioners upstream of the test section, the first of which is constructed out of 0.5-in PVC pipe sections. The second flow conditioner consists of fine polycarbonate honeycomb sections. As shown in Figure 1, a PVC ramp leads to a sediment recess of 3.68 m in length and 0.23 m in depth, encompassing the width of the flume. This test section is filled with granular material with median sediment diameter d_{50} = 0.74 mm, standard deviation of particle size σ_g = 1.34, coefficient of uniformity C_u = 1.6 and coefficient of gradation C_c = 0.96. The specific gravity of sediment was 2.65. The critical velocity of sediment (U_c) for the bed material was evaluated using standard methods, which are detailed in other works (Williams et al., 2016, 2018).

A boundary layer trip is located at the beginning of the sediment recess and the flow depth was adjusted by a gate at the downstream end of the flume. The flow is serviced by a 60-HP centrifugal pump. The flow was calibrated with v-notch weirs, using methods described in the U.S. Department of the Interior Bureau of Reclamation Water Measurement Manual (2001). The Kindsvater-Shen relationship and the 8/15 triangular weir equation were used to calculate the flow rate and develop the performance curve for the flume pump prior to installation of the test section. The orientation of the flume and experimental measurements correspond to *X* in the streamwise direction, *Y* in the vertical direction, and *Z* in the spanwise or transverse direction. The bed level was taken as zero in the *Y* direction for all experiments and the geometric centre of the cylinder was taken as the origin in the *XZ* plane. The mean velocity components *U* and *V* correspond to the velocity in the *X*- and *Y*-directions, respectively.

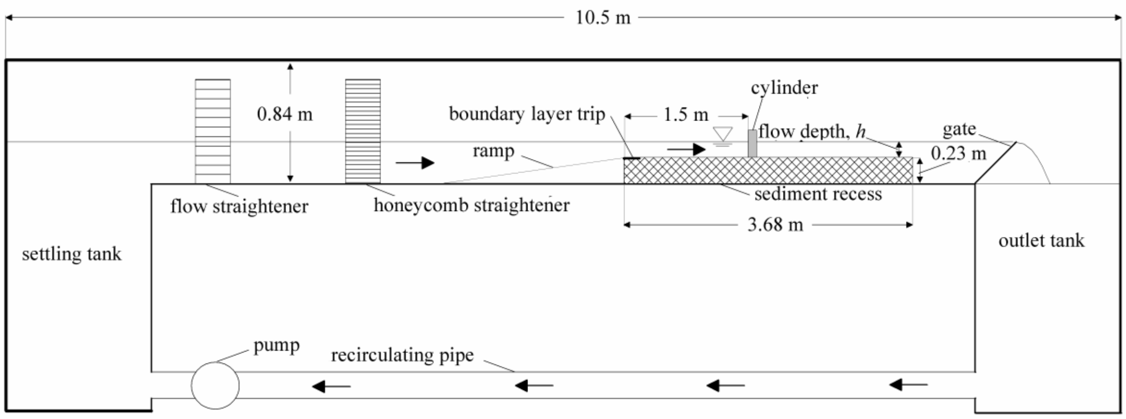

Figure 1 - Schematic of laboratory flume including test section details

2.2. Experimental program and test methodology

Prior to experimentation, PIV measurements were undertaken in the flow over the sand bed in the absence of a cylinder, in order to characterize the approach flow conditions. The depth-averaged velocity of the flow for all tests was determined to be *U* = 0.262 m/s. The flowrate *Q* for all experiments was 0.036 m^3/s. The cylinder diameter *D* for both tests was 0.056 m. The height of the submerged cylinder for test S1 was 1.88*D*. The width of the channel was adjusted using movable sidewalls to an effective width *b* = 0.40 m, corresponding to a blockage ratio *D*/*b* = 0.14. The depth of flow was held at *h* = 0.12 m for both tests in order to achieve a flow shallowness *h*/*D* of 2.14 such that the piers were classified as narrow.

Prior to testing, the sediment in the test section was carefully levelled using a trowel. For both cases, the necessary cylinder was installed in the centre of the channel. The flume was then filled with water to the desired depth. A calibration target for PIV image processing was suspended in the flume and calibration images were captured for each field-of-view. After the required calibration images were acquired, the target was removed from the flume and the pump was powered on and brought up to the required flow rate corresponding to a flow intensity (U/U_c) of approximately 0.85, to maintain clear-water conditions for local scour. The flow at the location of the cylinder was fully turbulent with a Reynolds number of 3.3 × 10^4 and subcritical with a Froude number of 0.26.

The tests were left to run for 24 hours before PIV measurements were taken. Prior analysis indicated that equilibrium of scour was reached within 24 hours, and changes in the relative scour depth d_{se}/D were minimal beyond this point in time (D'Alessandro, 2013, Williams et al., 2019). PIV measurements were then undertaken for each required field-of-view (FOV). Prior to PIV measurements, the flow was seeded with 11-μm spherical glass particles. For each scour test, four fields-of-view were taken in the streamwise-vertical symmetry plane to ensure that the flow field was captured from the upstream extent of the scour hole to the end of the primary deposit in the wake region. A thin glass plate was suspended on the free surface in the region of interest during image capture to eliminate the distortion of the laser sheet from perturbations in the free-surface region.

After the required PIV images had been acquired, the pump frequency was gradually reduced in order to avoid disturbance of the bed sediment before the pump was powered off. The flume was then drained slowly to avoid disturbance of the scour formation and a Leica laser distance meter was used to measure the bed profile in the streamwise direction along the channel centreline (Z/D = 0). The uncertainty of the acquired bed measurements due to the accuracy of the laser distance meter was determined to be ±0.05 mm from the resolution of the point measurements.

2.3. Description of the PIV setup and data acquisition

A schematic of the two-dimensional planar Particle Image Velocimetry (PIV) system is shown in Figure 2. The PIV system was supplied by TSI and is comprised of several components, including an 8 MP Illunis CCD array camera and a dual pulse Litron Nd:YAG laser generating at 532 nm wavelength with an output energy of 135 mJ/pulse and a maximum repetition rate of 15 Hz. The laser sheet was expanded through a −15-mm cylindrical lens. The 8 MP camera was used to capture images with a resolution of 3312 × 2488 pixels in dual-capture mode. The camera was fitted with a 28-105 mm Nikkor lens. The laser was mounted on a mechanical traverse system affixed to a carriage on top of the flume, and such that the laser sheet could be moved in the streamwise direction as required. The camera was mounted on a tripod slider on the flume catwalk, aligned parallel to the flume sidewall and therefore the plane of symmetry. A TSI PIV LaserPulse synchronizer was used to synchronize image capture for the specified exposure time at the corresponding maximum pulse repetition rate (i.e., the time required for exposure and readout of two images) with the timing of the laser pulses for each frame (a single pair of images).

The test section for PIV measurements in the sediment recess was located at a streamwise distance of 1.5 m downstream of the boundary layer trip. Measurements were obtained in the *XY* or vertical plane. Through prior experimentation, it was established that between 2000 and 3000 frames captured at a rate of 2 Hz were adequate for time-averaged data acquisition. The optimal pulse separation (Δt, or the time step between two concurrent laser pulses) in the sequence was evaluated for each FOV by adjusting the value of the time step such that the average length of the post-processed vectors (i.e., the displacement of particles) in the region of interest was approximately 8 pixels. The total propagated uncertainty of the velocity measurements acquired by the PIV system was estimated to be ±0.015 m/s. The uncertainty analysis was based on the methods described in Park et al. (2008), which were adapted from the Visualization Society of Japan's (2002) guidelines.

PIV measurements for individual fields-of-view were taken and stitched together for each test. Slight discontinuities and scatter in the distribution of the velocities can be attributed in part to the variability in intensity along the laser sheet in the streamwise direction as well as reflections from the laser sheet on the bed and cylinder. There is also a strong out-of-plane component in the three-dimensional flow around a cylinder which is not captured by a planar PIV and the evaluation of Δt in such areas of cross-stream flow becomes complicated. Furthermore, the flow area within the scour hole was not captured due to the physical obstruction by the sediment recess in the field-of-view of the camera. Measurements in the region very close to the free surface were also not obtainable due to the presence of the glass plate in this region.

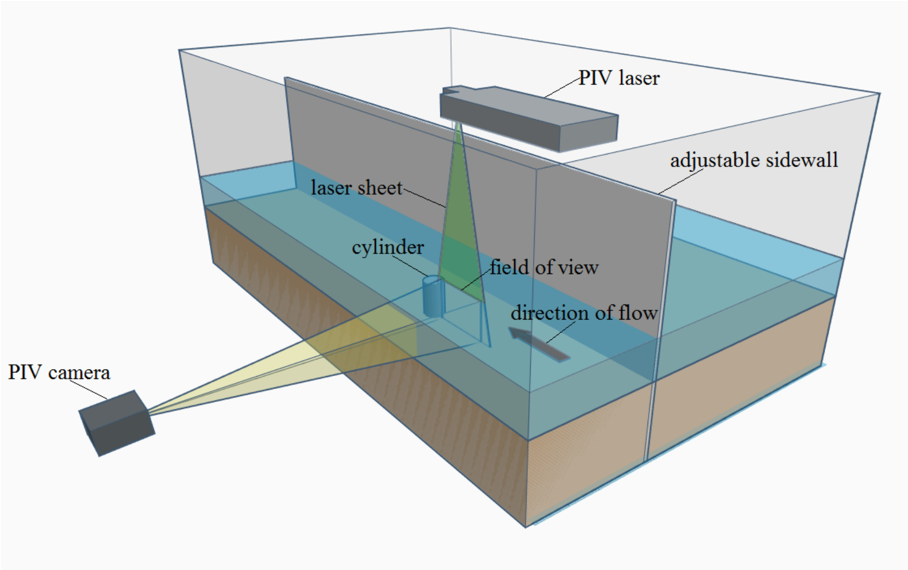

Figure 2 - Depiction of the Particle Image Velocimetry (PIV) system setup for image capture

2.4. PIV processing details

Post-processing of the PIV images was done using PIVlab, a GUI-based open-source MATLAB code (Thielicke & Stamhuis, 2019). PIVlab uses cross-correlation to determine displacement of illuminated tracer particles in the flow field. In PIVlab, a cross-correlation algorithm is used to determine vectors in the flow field by deriving the particle displacement between pairs of captured images. In this method, a "statistical pattern matching technique" is used to correlate the pattern of illuminated particles from a small interrogation area in each image of a pair, yielding a correlation matrix. The discrete cross correlation function is described by Eq. (1):

$$C(m,n) = \sum_i \sum_j A(i, j)\, B(i-m, j-n) \tag{1}$$

In Eq. (1), *A* corresponds to the interrogation area in the first image of a frame and *B* similarly corresponds to the interrogation area from the second image in the same frame. The cross-correlation technique attempts to "locate" the seeding pattern in *A* in a region with the same pattern in *B*, and the intensity peak in the generated correlation matrix *C* (based on the cross-correlation function) is deemed the "most probable" particle displacement between the interrogation areas in each image. (Thielicke & Stamhuis, 2014).

3. RESULTS AND DISCUSSION

Figure 3 shows the bed profile measurements for test E1 (emergent cylinder) and test S1 (submerged cylinder) in the *XY* symmetry plane at Z/D = 0 at an equilibrium condition, as well as a plan-view photograph of the scour formation for test S1. The profiles show that both cases result in a typical scour profile, with an inverted conical scour hole surrounding the cylinder and a dune-like primary deposit in the wake region. Upstream of the cylinder, Figure 3 shows that the scour depth is not significantly altered by the cylinder height. The scour profiles between tests E1 and S1 are very similar for X/D < -0.5. The depth of the scour hole is 2 percent deeper for test E1, which is reasonable since the downflow along the upstream face of the cylinder would be slightly stronger compared with the submerged case due to the increased projected area of the cylinder. In the wake region close to the cylinder (0.5 < X/D < 3.0), the scour depth for test S1 is very similar to that of test E1. Downstream of this point, from the leading edge of the dune onwards, the height of the scour formation is greater for test E1 and the length of the dune is greater for test E2. It appears that the dune dimensions are most affected by cylinder height.

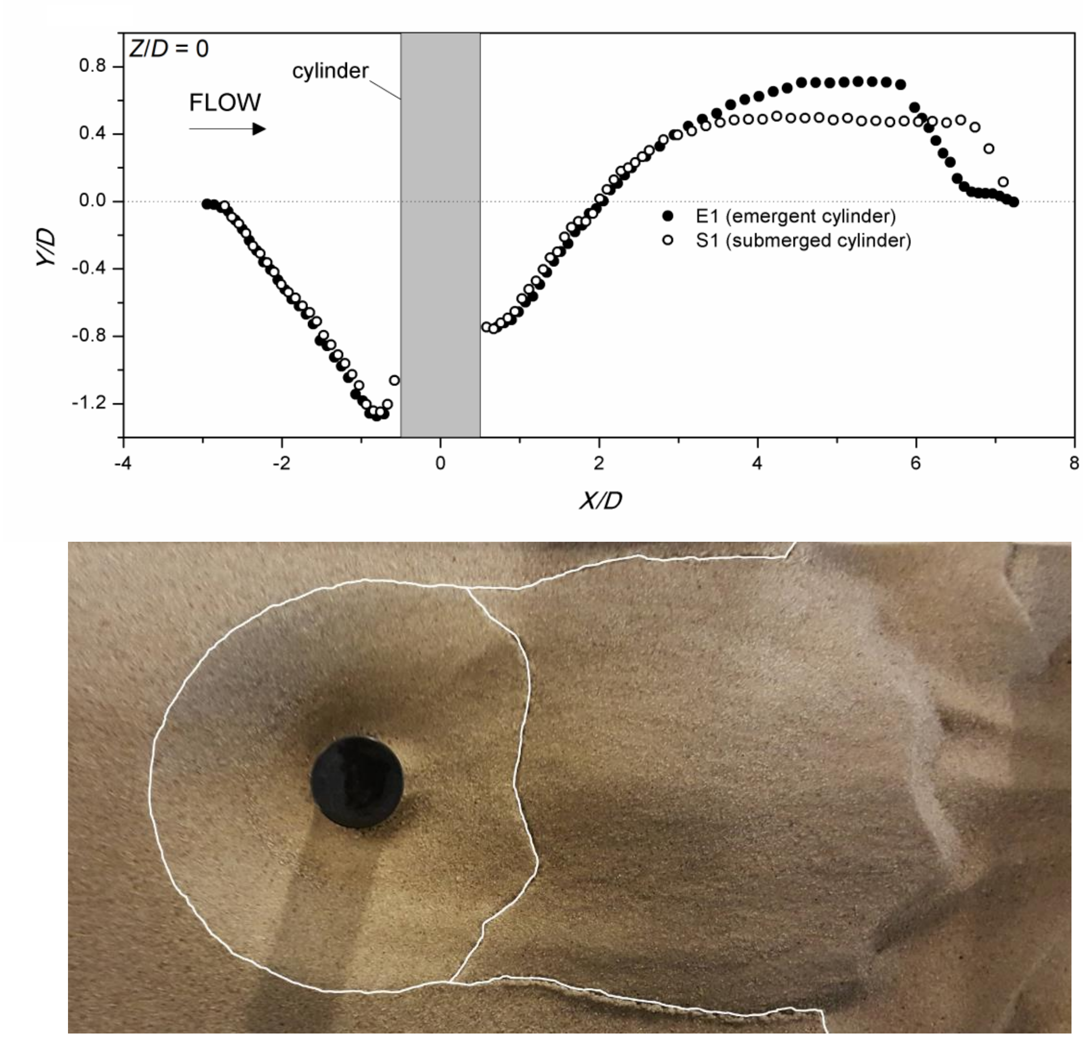

Figure 3 - Bed profile measurements for tests E1 and S1 in the XY symmetry plane at *Z/D* = 0 (top) and photograph of the scour formation for test S1 (bottom)

In Figure 4, the distribution of the mean streamwise velocity normalised by the maximum velocity of the undisturbed approach flow, U/U_e, is provided in the *XY* symmetry plane at *Z/D* = 0 for (a) test E1 and (b) test S1. The two-dimensional vector fields in the *XY* plane are also provided for (c) test E1 and (d) test S1. From the contours of U/U_e, certain features can be noted in the flow field for both tests. The adverse pressure gradient associated with the deceleration of the flow in advance of the upstream face of the cylinder is marked as feature 'A' for both tests. Feature 'C,' a region of low and negative mean streamwise velocity, is located in the immediate wake of the cylinder over the downstream portion of the scour hole. At the location of feature C, the vector fields for both tests E1 and S1 are also indicative of an upwash of flow emanating from the scour hole downstream of the cylinder. Further downstream, the acceleration of the flow up and over the primary deposit is noted as feature 'D,' and the separation of the flow from the crest of the dune is marked as feature 'E.' Each of these features is observed from the streamwise velocity contours as well as the vector fields.

A notable feature which is present in the flow field for the submerged case but not the emergent case is marked as feature 'B.' Feature 'B' is a region of flow separation emanating from the top of the submerged cylinder, characterized by an increase in the mean streamwise velocity. Although this region is located close to the free surface, it has affected the scour formation and the flow field since the flow in the submerged case is shallow. This increase in streamwise velocity near the cylinder's surface has caused an increase in erosion at the top of the primary deposit, reducing its height and increasing its length. It can also be noted that the magnitude of feature 'D' is higher in the region close to the cylinder for test S1 when compared with test E1, which is also likely to be attributable to the separation of flow and subsequent increase in *U* at the same downstream region.

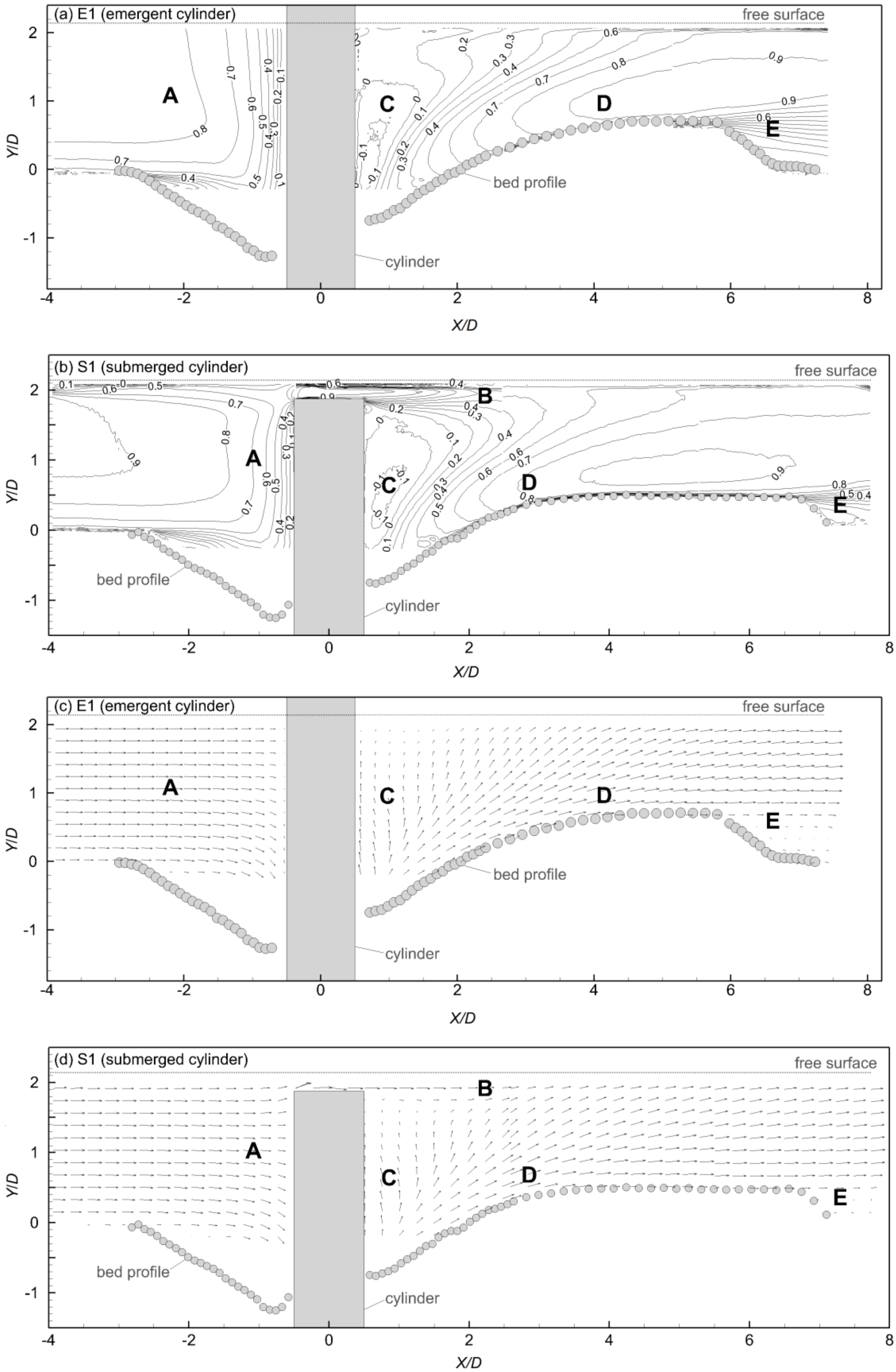

Figure 4 - (a) Distribution of U/U_e in the *XY* symmetry plane for test E1, (b) distribution of U/U_e in the *XY* symmetry plane for test S1, (c) two-dimensional vector field in the *XY* symmetry plane for test E1 and (d) two-dimensional vector field in the *XY* symmetry plane for test S1

4. CONCLUSIONS

The current investigation presents the methodology employed to acquire Particle Image Velocimetry (PIV) measurements for flume experiments involving equilibrium of local scour around circular cylinders. The results of two local scour experiments exploring the effects of cylinder height are presented. The bed profiles at equilibrium indicate that the depth of scour in the vicinity of the cylinder is not significantly affected by the cylinder submergence, but the width and length of the scour hole are greater for the emergent case. In the downstream region of the scour formation, the height and length of the dune are shown to be affected by cylinder height as well. The distribution of the mean streamwise velocity and the vector field in the streamwise vertical plane are shown to be very similar, with a region of high streamwise velocity due to the separation of the flow at the top of the cylinder visible for the submerged case and not the emergent case. This feature is shown to be responsible for the changes in the height and length of the primary deposit. In future experimental work, three-dimensional PIV measurements would be helpful in further exploration of the flow field surrounding a cylinder under equilibrium of local scour. Furthermore, although the two-dimensional PIV measurements do provide useful insight into the mechanism of local scour under varying geometry, there is a significant out-of-plane component of flow which should be captured in order to acquire a complete understanding of the flow field.

REFERENCES

D'Alessandro, C. (2013), *Effect of blockage on cylindrical bridge pier local scour* (Master's thesis). University of Windsor, Windsor, Canada.

Dey, S., Raikar, R.V., and Roy, A. (2008), *Scour at submerged cylindrical obstacles under steady flow.* J. Hydraul. Eng., 134(1), 105–109.

Guan, D., Chiew, Y.-M., Wei, M., and Hsieh, S.-C. (2019), *Characterization of horseshoe vortex in a developing scour hole at a cylindrical bridge pier*. Int. J. Sediment Res., 34(2), 118–124

Kirkil G., Constantinescu S. G., and Ettema R. (2008), *Coherent structures in the flow field around a circular cylinder with scour hole*. J. Hydraul. Eng., 134(5), 572–587.

LeBeau K. H., and Wadia-Fascetti S. J. (2007), *Fault tree analysis of Schoharie Creek bridge collapse*. J. Perform. Constr. Fac., 21(4), 320–326.

Melville, B. W., and Coleman, S. E. (2000), *Bridge Scour*. Water Resources Publication.

Park, J., Derrandji-Aouat, A., Wu, B., Nishio, S., and Jacquin, E. (2008), *Uncertainty analysis: Particle imaging velocimetry. ITTC Recommended Procedures and Guidelines*, International Towing Tank Conference (ITTC), Fukuoka, Japan, Sept, pp. 14–20.

United States Department of the Interior Bureau of Reclamation (2001), *Water Measurement Manual*. US Government Printing Office Washington, DC.

Thielicke, W., and Stamhuis, E. (2014), *PIVlab – Towards user-friendly, affordable and accurate digital particle image velocimetry in MATLAB*. J. Open Res. Softw., 2(1), e30.

Thielicke, W., and Stamhuis, E. J. (2019, September 6), PIVlab—Time-resolved digital particle image velocimetry tool for MATLAB.

Unger, J., and Hager, W. H. (2007), *Down-flow and horseshoe vortex characteristics of sediment embedded bridge piers*. Exp. Fluids, 42(1), 1–19.

Visualization Society of Japan. (2002), *Handbook of Particle Image Velocimetry*. Morikita Publishing Co. Ltd. (in Japanese).

Williams, P., Balachandar, R. and Bolisetti, T. (2019), *Examination of blockage effects on the progression of local scour around a circular cylinder*. Water, 11(12), 2631.

Williams, P., Bolisetti, T., and Balachandar, R. (2016), *Evaluation of governing parameters on pier scour geometry*. Can. J. Civ. Eng., 44(1), 48–58.

Williams, P., Bolisetti, T., and Balachandar, R. (2018), *Blockage correction for pier scour experiments*. Can. J. Civ. Eng., 45(5), 413–417.

Zhang, H., Nakagawa, H., Kawaike, K., and Baba, Y. (2009), *Experiment and simulation of turbulent flow in local scour around a spur dyke*. Int. J. Sediment Res., 24(1), 33–45.

Zhao, M., Cheng, L., & Zang, Z. (2010), *Experimental and numerical investigation of local scour around a submerged vertical circular cylinder in steady currents*. Coast. Eng., 57(8), 709–721.

8th International Junior Researcher and Engineer
Workshop on Hydraulic Structures
ISBN: 978-0-578-37416-1
https://doi.org/10.26077/1517-74d7

Galway, Ireland,
5th - 8th June 2021

Development of a 1 kW gravitational water vortex hydropower plant prototype

A. Sapkota[1], A. Gautam[1], A.B. Timilsina[1], S. Dhakal[1], S.R. Shakya[1] and T.R. Bajracharya[1]
[1]Department of Mechanical and Aerospace Engineering, Pulchowk Campus, Institute of Engineering
Tribhuvan University
NEPAL
E-mail: abtimilsina@pcampus.edu.np

Abstract: *A pilot testing of a Gravitational Water Vortex Hydropower Plant (GWVHP) has been done to evaluate the applicability in a real-world scenario and validate the results from the lab-scale model. A scaled-up model of a capacity of 1 kW was constructed for the evaluation purpose. The test provided data in good agreement with a lab-scale model and a proper visualization to install Gravitational Water Vortex in real-world scenarios. The project lasted for nearly four months and thus provided important information on the problems that might arise in scaling up the lab model to a micro-hydro system. The pilot testing shows an overall plant efficiency of 49%, validating the lab-based studies conducted beforehand. The information obtained from this pilot study shall be implemented in a micro-hydro project on a larger scale.*

Keywords: *Gravitational water vortex, Low-head hydropower, Micro-hydro, Pilot study, Similitude.*

1. INTRODUCTION

In modern society, electrical energy has become a critical commodity. Wind, solar, and small-scale water supplies can generate electricity in rural areas using renewable energy technologies. Pico/micro-hydro can be deployed at a lower cost than solar PV, grid extension, and diesel generators and thus tends to be a relatively inexpensive solution for rural electrification (Green et al. 2005; World Bank 2007). While some Pico/micro hydropower plants use small-scale replicas of commercially successful large turbine units, others use specifically designed new technologies. These new technologies are mainly “Run-of-the-River” schemes that do not necessitate heavy civil constructions and thus are less expensive and more environmentally friendly but are highly dependent on local hydrological trends (Watson et al. 2010). Gravitational Water Vortex Hydropower Plant (GWVHP) is one such technology developed by Austrian inventor Franz Zotlöterer; the prototype was installed in 2006 at the Ober-Grafendorf River, Austria. Numerous research has been done on design variation in the vortex chamber and the runner since then. The turbine system considered in this research is depicted in Figure 1 to better understand terms and terminologies that appear frequently in this article.

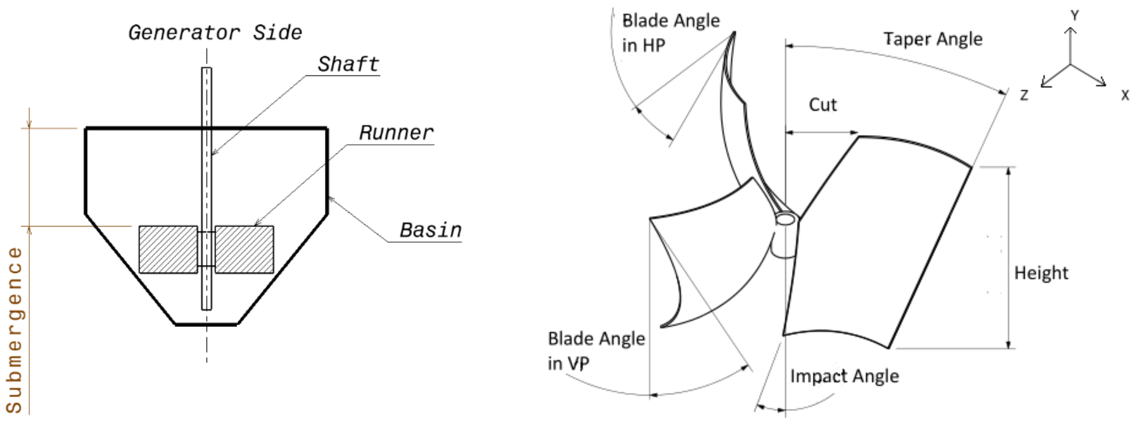

Figure 1 – On the left: basin and turbine schematics of a GWVHP (Reproduced with permission from Bajracharya et al. (2018)). On the right: a runner showing different geometric parameters (Retrieved under CC BY license from Bajracharya et al. (2020))

An experimental study (Bajracharya & Chaulagain 2012) analysing the effect of the cylindrical basin depth showed no substantial increase in power output. However, the research paved the way for modifying the basin shape into a cone (decreasing basin cross-section diameter with the depth). Later, the vortex speed and the power propulsion of the modified cylindrical and conical basins were compared by Dhakal et al. (2013). The runner was designed using the impulse turbine concept. A parametric analysis of the conical basin was conducted to determine the effect on flow velocity measured in the impeller's midplane (Dhakal et al. 2014). The optimal range for different parameters was defined; the most sensitive parameter was basin opening. Dhakal et al. (2015) showed the superiority of conical basin (Figure 2) and identified the optimal submergence with impulse type runner 65 – 75% of the basin height. To further investigate runner design, seven different geometrical parameters and their optimal range were identified by Bajracharya et al. (2020). The most efficient runner (Figure 2) had a system efficiency of 47.85%. After the study of 22 different runners, Bajracharya et al. (2020) recommended that the turbine runner respects the 5 rules below to get an efficient GWVHP design:

(i) Runner height to basin height ratio of 0.31 - 0.32,
(ii) Taper angle conforming to the basin cone angle,
(iii) Blade impact angle of 20 degrees,
(iv) Blades curved when viewed from the top only with blade angles 50º - 60º,
(v) Cut ratio less than 15%.

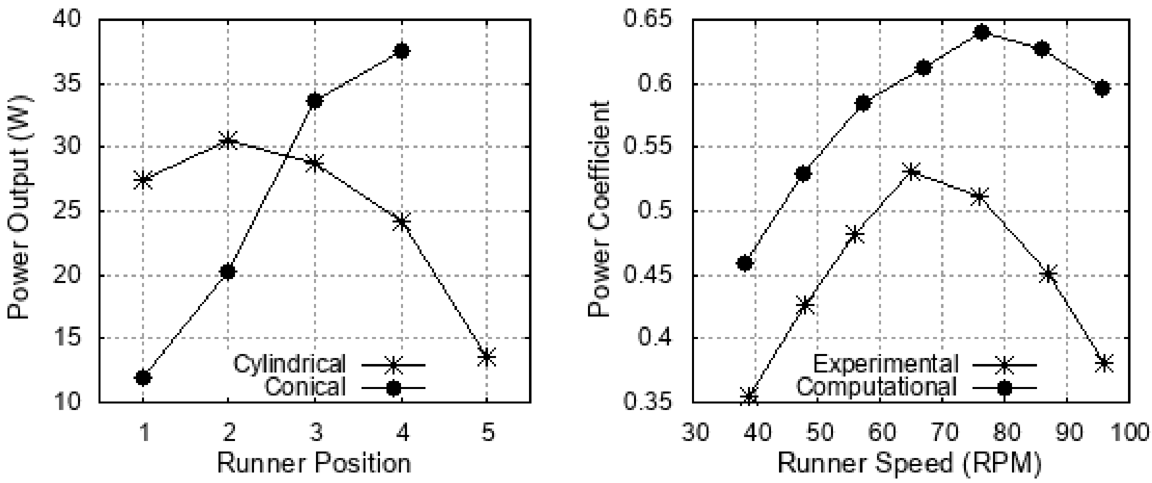

Figure 2 – On the left: Cylindrical basin vs. Conical basin (Reproduced with permission from Bajracharya et al. (2018)). On the right: Performance curve of the most efficient runner with conical basin (Retrieved under CC BY license from Bajracharya et al. (2020))

Gravitational Water Vortex (GWV) is an emerging technology with many variations for vortex chamber proposed to date. However, the vortex flow phenomenon and harnessing power from this technology is not yet fully understood. Research is being conducted on this topic to understand the flow regime in each type of basin with numerical simulation or experimental modelling or both and harness the mechanical power from the swirling flow efficiently with an appropriate turbine system. This study develops a 1 kW pilot project of GWV with a conical basin from experience gained from different lab-scale studies. The system is developed at premises of Centre for Energy Studies, Institute of Engineering. This pilot study has been done to provide a steppingstone for a handful of yearlong research done within the institute. The authors hope this study would provide ample information for routing this technology towards power production in real-world scenarios, predominantly rural and/or grid-isolated areas.

2. SIMILITUDE: MATERIALS AND METHODS

Similarity requires confirmation of geometries (shape), kinematics (motion), and dynamics (forces) between two different models. In practice, the dynamic similarity is satisfied implied that this also satisfies the other two mechanical similarities. The flow in GWVPP is an open channel flow, a fluid flow with a free surface subjected to atmospheric pressure. The dimensionless numbers to be considered in open channel flow in GWVPP are Reynolds number and Froude number. Achieving both similarities simultaneously is not possible in this study, and this gives rise to scale effects between model and prototype (Heller 2012). Due to the nature of gravity dominant flow, only Froude similitude is considered. The calculated Froude number is used to evaluate the width of the inlet canal based on the canal height. The conical basin is scaled up by a factor of 5 compared to the lab model. The basis for exit hole diameter is maintained as 18% of basin diameter, as suggested by Mulligan & Casserly (2010). Since the basin must handle the designed flow rate, the basin height was adjusted for a safety factor of 2 based on the discharge coefficient of the model. With a discharge coefficient of 0.0182, the height of the basin for the scaled-up model was calculated and rounded off to be 1.4 m. The design summary of hydraulic components is presented in Table 1:

Table 1- Hydraulic Components Sizing

Description	**Sizing**
Designed flow capacity of canal (Q_D)	0.15 m^3s^{-1}
Cross section area of canal	0.5 (*b*) * 0.6 (h_c)= 0.3 m^2 (factor of safety 2 used for height)
Diameter of cylindrical basin (D_b)	2 m
Diameter of exit hole (d_b)	0.36 m
Total height of basin (h_b)	0.5 m (cylindrical) + 0.9 m (conical) = 1.4 m
Cone angle (ϕ)	42º
Width of rectangular weir (w_w)	1 m
Capacity of one pump (Q_p)	0.009 m^3 s^{-1}
Total capacity of pumps (Q_{max})	15*(Q_p) = 0.135 m^3 s^{-1}

The runner's design is based on the lab-scale model studied by Bajracharya et al. (2020), adapted here for a large-scale model. The submergence requirement fixes the position of the runner. At this fixed position, the runner requires a clearance from the basin wall to prevent any runner blade – basin wall interaction during operation. Bajracharya et al. (2020) suggest clearance is required so that the runner placement does not stop the basin's vortex formation. The prototype runner was designed based on the computational efficiency (64%) of the model runner since the experimental efficiency of the model runner incorporates several losses starting from manufacturing precision to operating condition. For scaling up the GWV turbine, the dimensionless relationships considered are specific speed, discharge coefficient, and power coefficient whose numerical values are 58.56, 0.00181, and 2.511E-6, respectively.

The runner diameter is determined based on these dimensionless numbers as the prototype runner's top outer diameter (D_1). All other parameters are evaluated based on these calculated values and suggestions made by Bajracharya et al. (2020). The runner height ratio of 0.3 used for calculations is adjusted to 400 mm to maintain the designed head with some clearance for the flow circulation. The parameter cut (Bajracharya et al. 2020) has been adapted here slightly differently as the radial cut; defined as the ratio of the top outer diameter to top inner diameter. The runner from the lab model has a top outer diameter and the hub diameter of 360 mm and 40 mm, respectively. The radial cut equivalent to a cut of 15% is 0.245, whereas the angle of inclination obtained for the inner edge of the blade is 8.11º. The parameter cut used in the lab model study can now be replaced by inclining the inner edge runner blade (λ) against the runner's axis. From the geometry of the runner-basin system the bottom outer and diameters are given by equation (1) where X_1 and X_2 are the distance of the outer tip of the blade from runner axis at top and bottom edge of runner blade, respectively.

$$
\begin{aligned}
X_1 &= \sqrt{\left(\frac{D_1}{2}\right)^2 - \left(\frac{H\tan\gamma}{2}\right)^2} \\
X_2 &= X_1 - \frac{H\tan\psi}{\cos\gamma} \\
D_2 &= 2 * \sqrt{{X_2}^2 + \left(\frac{H\tan\gamma}{2}\right)^2} \\
d_2 &= d_1 - \frac{d_1}{D_1} * (D_1 - D_2)
\end{aligned}
\tag{1}
$$

For modelling and manufacturing, all the runner dimensions are rounded off to suitable integer values.

The dimensions are listed in Table 2. Shigley's mechanical design (Budynas & Nisbett 2011) has been followed for proper shaft selection, transmission pulleys and belts, and bearings. Table 3 shows different components and their selection sizes.

Table 2 - Turbine Runner Sizing

Description	**Sizing**
Runner height (h)	400 mm
Inlet/Outlet blade angle in HP (β)	54º
Impact angle (γ)	20º
Taper angle/Inclination of outside edge (ψ)	30º
Inclination of inside edge (λ)	8.11º
Top outer diameter (D_1)	1010 mm
Top inner diameter (d_1)	250 mm
Bottom outer diameter (D_2)	520 mm
Bottom inner diameter (d_2)	170 mm
Runner clearance with basin wall (δ)	60 mm
Number of blade (N_b)	9
Runner position (H_{max})	1050 mm (below from the top of the basin)

Table 3 - Mechanical Component Sizing

Description	**Selection and Sizing**
Shaft power rating	1 kW
Shaft speed rating	70 RPM
Factor of safety for shaft	3
Shaft diameter	30 mm
Gear ratio for single stage transmission	1400/70 = 20
Gear ratio for two stage transmission	$\sqrt{(20)} = 4.47 \approx 4.5$
Pulley belt configuration	V-belt type B, double groove
Factor for safety for pulley	1.25 (Stage 1) & 1.7 (Stage 2)
Bearing reliability	0.9 (0.97 for each)
Bearing type	Deep groove on the top and tapered roller on the bottom

Fifteen submersible pumps, each with their supply pipeline, convey water from an adjacent pond to the installed plant, then discharge back to the pond following the plant operation. The flow is varied by switching individual pumps. The drop chamber serves as a forebay for the system while both the drop chamber and the trash rack help dissipate the turbulence introduced by intake pipes and settle any unwanted debris if present. Water flows to the basin via the intake canal, forms a counter-clockwise vortex, and exits via the bottom exit hole. The turbine placed coaxially with the basin converts hydraulic energy into mechanical energy. The mechanical energy is transmitted via 2 – stage pulley system to a generator (induction motor used as a generator) which supplies power to a control panel. Several incandescent bulbs and a ballast load dissipate the power. The exit water flows back into the pond. At the end of the tailrace, a weir is used to measure the flow rate. Figure 3 shows the plant layout and runner with different components.

3. RESULTS AND DISCUSSION

The computational efficiency of the model runner studied in the lab is 64%; hence the expected power output for the given head and flow rate of the prototype is 0.659 kW. Also, the estimated operational speed of the prototype runner is 63 RPM. However, due to the spillage, seepage from concrete structures, and intake pipes, the flow into the basin is reduced and thus corrected here for calculation purposes. The data acquired from installation and operation are used to evaluate the overall system efficiency of the micro-hydro plant. The hydraulic power input to the system was:

(a)

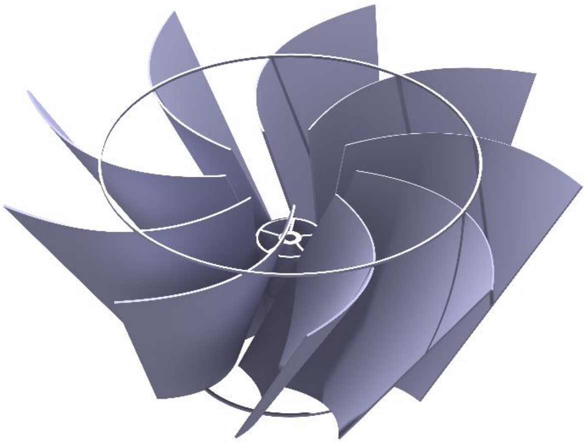

(b)

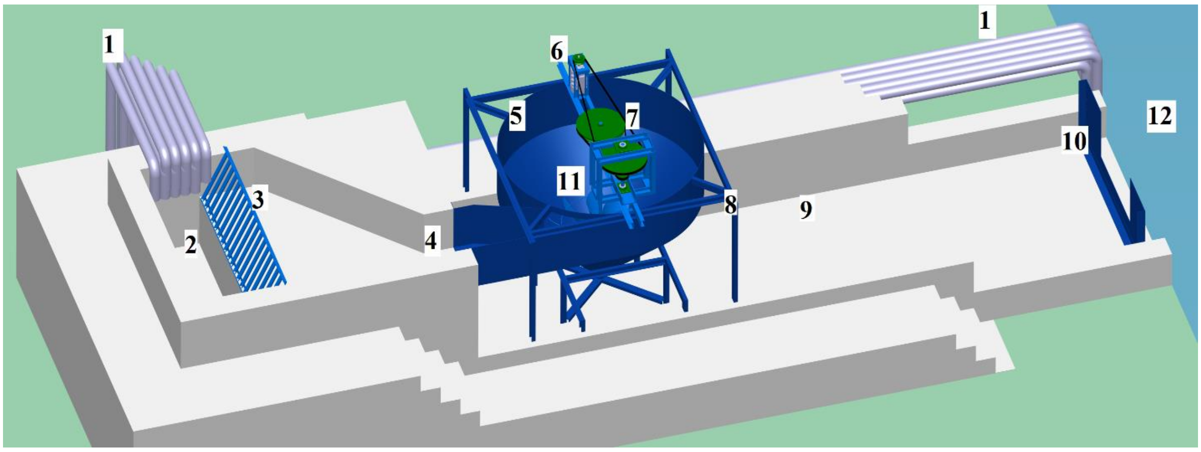

(c)

1) Intake	2) Drop chamber	3) Trash rack/Speed neutralizer
4) Inlet canal	5) Conical basin	6) Induction motor used as generator
7) Transmission pulley arrangement		8) Basin support structure
9) Tail race	10) Rectangular weir	11) Turbine runner with shaft
12) Pond	13) Power supply/Multipurpose control panel	

Figure 3 – (a) Experimental Facility: Plant installed at CES, IOE, (b) runner 3D model (c) plant layout

- Maximum Flow measured (Q_{max}) = 0.1175 m^3s^{-1}
- Head (H) = 0.9 m
- Input power (P_o) = ρgQH = 1031 W = 1.031 kW
- Turbine runaway speed = 88 RPM
- Generator Speed = 1750 RPM

The installed power plant is run under various flow rates by controlling water supply pumps and variable load by changing the electrical load. Several standard 100 W incandescent bulb has been used, and load has been varied in the step of 100 W from the control panel. Figure 4 shows the part-load electrical efficiency of the system under various flow rates. The best efficiency points are chosen and presented as part flow efficiency of the system.

Figure 5 shows the system in operation. The power generated from the vortex runner is glowing 100 W bulbs.

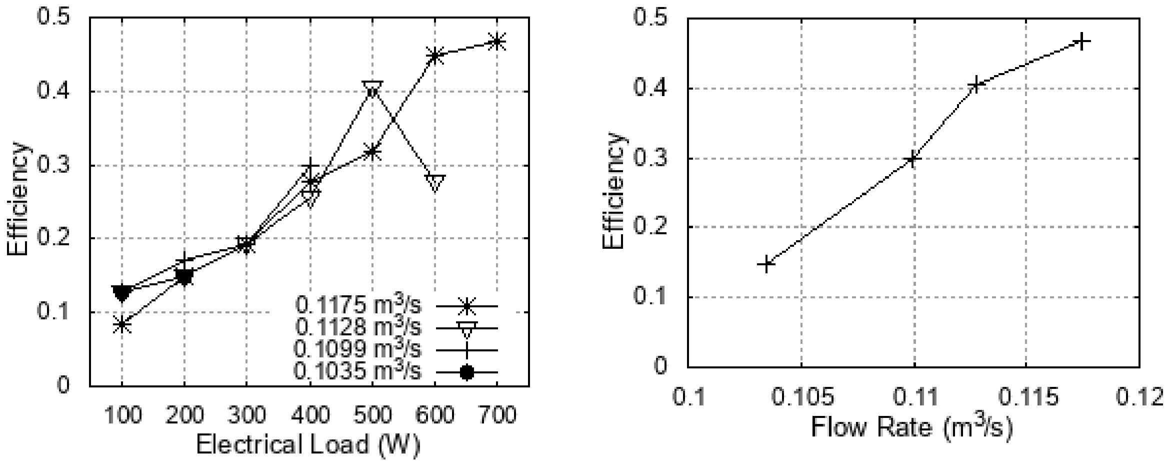

Figure 4 – On the left: Efficiency trend of the micro-hydro plant for various flow rates. On the right: Part flow efficiency of the micro-hydro plant

Figure 5 – Working of the Plant

Figure 4 shows that the maximum efficiency gradually decreases when subsequent pumps are turned off. This suggests that the plant should be operated nearer to its design condition, preferable to hydro turbines. However, a flat efficiency curve for some flow rates suggests that the plant can operate with relatively good efficiency like Pelton and Turgo turbines. Also, it gives us more insight into the operational nature of GWVPP itself. Overloading the plant under lower flow conditions can negatively affect power production, as shown by the dipping nature of the 0.1128 m^3/s curve in Figure 4. Also, a sweet spot exists for maximum efficiency, suggesting that flow regulation could help achieve better efficiency when the end load demand is lesser. After analysing the results, the following conclusions can be made about the pilot study and GWVHP in general:

(i) The system can be considered a suitable micro-hydro alternative where the availability of low head and high flow rate does not suit conventional turbine systems.
(ii) This type of system has a flat efficiency curve for a specific flow interval. The vortex formation is impossible, and the plant does not operate below a threshold flow rate or above the rated load.
(iii) The efficiency curve can be better understood by increasing the resolution of the loads.

4. DESIGN, ERECTION ASPECTS, AND GUIDELINES FOR GWVHP

This section is presented as a general guideline that can be helpful in successfully deploying a GWVHP. This section covers different aspects of GWVHP related to design, construction, material selection, transportability, cost-effectiveness, inspection, maintenance, etc. The guidelines presented here depend on the available literature, general practices, and experiences gained during the lab studies and prototype deployment.

- The inlet canal should be designed with a factor of safety that pertains to possible high flow in the intake canal. The canal width should be at least twice its height. A slight slope of a few degrees is preferred in the intake canal.
- The flow diversion from the river should be made at an angle closer to 90º. Also, the location should be chosen so that the headrace and tailrace span over longer lengths. This selection helps mitigate river currents and upstream river effects in the hydropower and settles the turbulent exit water before re-entering the river.
- Due to the sloshing effects, the plant is not beneficial to run above the designed flow rate due to spillage along the sides of the basin and canal closer to the basin.
- Small debris can easily pass through the hydropower plant, while larger debris needs a trash rack. Since sophisticated technology is not available at a remote place, the trash rack should be placed to be cleaned manually and less frequently.
- The cylindrical height of the basin is determined by canal height, whereas the available head determines cone height. The discharge coefficient determines the basin diameter. The exit diameter is taken as 18% of the basin diameter.
- Since using concrete to shape a cone can be costly and cumbersome, a metal basin, a concrete intake canal, and a concrete tailrace is preferred. The floors of the basin and intake canal should be made smooth to mitigate friction losses.
- Small panels should be developed into a cone and welded on-site to avoid the expensive transportation of a large basin. A metal basin makes it easier to couple all the mechanical components like pulley and shafts to the basin.
- Two bearings are needed to hold the shaft and runner in place. The lower bearing design needs special attention. A water-lubricated bearing is preferred, but a ball bearing properly sealed should suffice at the bottom of the shaft.
- Pulleys are preferred to gearboxes owing to low maintenance and cost-effectiveness. A two-stage or three-stage pulleys could be designed as per requirements. The selection of shaft, pulley, bearings, and belts are to be made based on available design guidelines.
- An induction motor can be used as a single-phase or three-phase generator. A standard ELC circuit with a proper current/voltage rating is suggested.
- Several components should be protected against wear and erosion. The metal components are to be coated against rust. Also, the s-metal coating is suggested for erosion if possible. The moving components are to be lubricated. The floor beneath the basin exit hole should be provided with means like a drop chamber to reduce the excavating effect of exit water.
- The control room should be secured against possible thefts and other hazards. A few spare parts should be kept in stock.
- Supervision from an engineer is suggested during installation. The issue of turbine eccentricity, basin–canal alignment, proper installation of all other moving components should be checked thoroughly. Also, a scheduled maintenance/inspection should be taught to locals.

5. CONCLUSION

The development of the 1 kW system provided a valuable experience regarding the successful development of a Gravitational water vortex power plant. The major problems encountered were transportation and installation. As the conical basin was fabricated in a single piece, it required large truck for transportation and a crane for erection at the installation site. To reduce this, it is recommended to develop basins in small sections and weld on site (or bolt) to form the entire basin. This would reduce both the transportation and erection cost. Evaluation of global systems of GWVHP (Timilsina et al. 2018) revealed that the average system efficiency is about 53%, and total efficiency of the system developed was 49% which can be considered competitive among similar technologies. From the tests performed and performance evaluation, it can be concluded that conical basin can successfully be deployed in site and with little considerations in design can be developed as an immediate energy relief device in disaster hit area.

6. ACKNOWLEDGMENTS

The authors are thankful to Ministry of Energy, Water Resources and Irrigation, Government of Nepal for funding, and Centre for Energy Studies for supporting this project. The authors would like to extend regards to all the personnel involved in materializing this pilot installation.

7. REFERENCES

Bajracharya T.R., Shakya S.R., Timilsina A.B., Dhakal J., Neupane S. and Gautam A. (2020), *Effects of Geometrical Parameters in Gravitational Water Vortex Turbines with Conical Basin*. Journal of Renewable Energy. Available at: https://doi.org/10.1155/2020/5373784.

Bajracharya, T.R. and Chaulagain, R.K. (2012), *Development and Testing of Gravitational Water Vortex Turbine*, Center for Energy Studies, Institute of Engineering, Tribhuvan University.

Bajracharya, T.R., Ghimire, R. and Timilsina, A.B. (2018), *Design and Performance Analysis of Water Vortex Powerplant in Context Of Nepal,* in *20th International Seminar on Hydropower Plants*.

Budynas, R.G. and Nisbett, J. (2011), *Shigley's Mechanical Engineering Design*, Tata McGraw-Hill Education.

Dhakal S., Timilsina A.B., Dhakal R., Fuyal D., Bajracharya T.R., Pandit H.P., Amatya N and Nakarmi A (2015), *Comparison of cylindrical and conical basins with optimum position of runner: Gravitational water vortex power plant*, Renewable and Sustainable Energy Reviews, 48(Supplement C), pp.662–669.

Dhakal S., Nakarmi S., Pun P., Thapa A.B. and Bajrachrya T.R. (2013), *Development and testing of runner and conical basin for gravitational water vortex power plant,* Journal of the Institute of Engineering, 10(1), pp.140–148.

Dhakal S., Timilsina A.B., Dhakal R., Fuyal D., Bajracharya T.R. and Pandit H.P. (2014), *Effect of dominant parameters for conical basin: Gravitational water vortex power plant,* In *Proceedings of IOE Graduate Conference*. p. 381.

Green J., Fuentes M., Rai K. and Taylor S. (2005), *Stimulating the picohydropower market for low-income households in Ecuador,* Energy Sector Management Assistance Programme (ESMAP) technical paper series, (090). Available at: https://openknowledge.worldbank.org/handle/10986/17995.

Heller, V. (2012), *Development of Wave Devices from Initial Conception to Commercial Demonstration,* in A. Sayigh, ed. "Comprehensive Renewable Energy", Oxford: Elsevier, pp. 79–110.

Mulligan, S. and Casserly, J. (2010), T*he Hydraulic Design and Optimisation of a Free Water Vortex for the Purpose of Power Extraction*, Undergraduate thesis, Institute of Technology, Sligo, Ireland.

Timilsina A.B., Mulligan S. and Bajracharya T.R. (2018), *Water vortex hydropower technology: a state-of-the-art review of developmental trends*, Clean Technologies and Environmental Policy, 20(8), pp.1737–1760.

Watson, J. and Johnson O. (2010), *Renewable energy technologies for rural development,* UNCTAD Current Studies on Science, Technology and Innovation, (01).

World Bank (2007), *Technical and Economic Assessment of Off Grid, Mini-Grid and Grid Electrification Technologies*. Energy Sector Management Assistance Programme (ESMAP) technical paper series, (ESM 121/07).

8th International Junior Researcher and Engineer Workshop on Hydraulic Structures
ISBN: 978-0-578-37416-1
https://doi.org/10.26077/74b4-2bbe

Galway, Ireland,
5th - 8th June 2021

Estimation of the Efficiency of Hydraulic Pumps

A. Martin-Candilejo[1], D. Santillán[1] and L. Garrote[1]
[1]Escuela Técnica Superior de Ingenieros de Caminos, Canales y Puertos of Madrid,
Departamento de Ingeniería Civil, Hidráulica, Energía y Medio Ambiente
Universidad Politécnica de Madrid
Profesor Aranguren 28040
SPAIN
E-mail: araceli.martin@upm.es

Abstract: *A sustainable design of water supply systems needs to account operational costs. When pumping is required, the energy consumed by the pumps plays a major part in the operational costs, and the efficiency of the pumps can greatly affect the energy expenses. How to properly estimate the value of pump efficiency is hence of great importance. The aim of this study is to study in depth the efficiency of hydraulic pumps, in relation with the other design variables (flow rate, pumping head, power, etc.). For that, 400 hydraulic pumps were analysed. A strong relationship between the flow rate and the pump efficiency was observed. This relationship was interpolated, and three empiric curves were defined (one for the average maximum and minimum expected value of pump efficiency). These curves can be easily used by designers in order to obtain an estimation of the efficiency of the hydraulic pumps.*

Keywords: *pump efficiency, water supply systems, design optimization, hydraulic pumps.*

1. INTRODUCTION

Under the threat of climate change, becoming energy efficient is of increasingly importance. In order to be more sustainable, the designing of a water supply system needs to consider both construction costs and operational costs, along its entire lifespan. When the facility requires pumping, investing little in construction costs will result in a much higher energy requirement. Therefore, addressing the operational expenses from the design stage is the sustainable approach.

Mala-Jetmarova et al (2018) well summarizes the different approaches to optimise the design of water supply systems. These approaches can be differentiated in single objective (e.g., Martin-Candilejo, 2020; Dziedzic et al 2015; Joong Hoon Kim & Mays, 1994; Sanchis et al 2019; Samani & Mottaghi, 2006; Kang et al 2013; Spiliotis & Tsakiris, 2007; or Costa et al 2000) or multi objective techniques (e.g., Vamvakeridou-Lyroudia et al 2005; Jin et al (2008). Either way, the most frequent objective is cost minimisation. In order to achieve a more precise assessment of all costs involved, multi-objective algorithms have started to incorporate in the optimization function costs of maintenance (Perelman & Ostfeld, 2007; Perelman et al 2008), greenhouse gas emissions (Wu et al 2010), among others. Multi-objective methods offer a very complete analysis of all costs, but many times they require very complex programming, resulting in computationally expensive and hard to use. That is the reason why single objective (cost optimization) remain as the most used approach in the practical scenario. Reed et al (2013) explains extensively the state-of-art of the multi-objective techniques. The most popular of these rely on iterative algorithms, such as genetic algorithm.

In any case, if a complete cost optimization (this includes operational expenses) is to be carried out, the estimation of the pump's efficiency μB is required, no matter the algorithm or the methodology of the optimisation. The value of the hydraulic pump efficiency has been typically estimated based on the experience of the designer; for instance, some of the most cited authors have made the following estimations: Alperovits & Shamir, (1977) estimated μB at 75%, and so did later Featherstone & El-Jumaily, (1983), Gessler & Walski, (1985) and Kapelan et al (2005); some more recent authors are Filion et al (2007) whose estimation is an interval between 81-84%. The energy cost is directly (inversely) proportional to μB. Hence the importance of a proper estimation of the pump efficiency Martin-Candilejo, et al (2020). This research analysed the values of the pump efficiency in order to provide designers some guidelines on how to choose the estimated value of µB.

2. METHODOLOGY

The aim of this research is to analyse the relationship of the pump efficiency and the other design parameters of a water supply system, such as the flow rate, the pumping head or the required power. For this task, a sample of 400 commercial hydraulic pumps was selected (Martin-Candilejo et al 2020). These pumps come from catalogues of different manufactures. These manufactures were IDEAL, WILO, ESPA and HASA. More specifically, the commercial models were:

- Split case pumps: CP/CPI/ CPR series.
- Horizontal pumps (normalized in the European Union): RNI/RN series.
- Multistage horizontal pumps: APM series.
- Vertical pumps: VS/VG series.
- Submersible vertical pumps: SVA/SVH series.

We discarded custom made pumps, and also those pumps for industrial or sanitary uses, since they have particular specifications, and the study focused on water supply pumps. In the end the sample consisted of 226 hydraulic pumps. All of the pumps differ from each other in their type, impeller, diameter, number of stages, rotation speed (electrical current frequency, number of poles), brand, etc. In the case of multistage pumps, for each flow rate, no matter the number of stages, they perform with the same efficiency. To avoid repetition and dispersion, it was decided only to use the operating point of a single stage. The data should be updated and completed in the fore coming years to fill in any bias and include more manufactures.

When the pumping station is designed, the pumps are chosen to best perform at the estimated operational point. This is the estimated flow rate and pumping head. Hence, the pumps are chosen so that this operating point is the closest to the optimum point of the pump, that is the point at which the pump will perform at its best efficiency. It is true that later in the operation, the pumps will vary the operating point according to the variable demand of water. But at the design stage, what interests the most is the optimum point (Martin-Candilejo et al 2021). For this reason, we registered the optimum value of the pump efficiency, with its correspondent flow rate, head, power consumption, frequency and speed. It should be clarified that this value of the pump efficiency μB refers to the hydraulic efficiency and does not include mechanical or electrical losses. With this collected data the study was carried out to analyze the variations of μB and the other design variables.

3. RESULTS AND DISCUSSION

3.1. Pump Efficiency and Flow Rate

The pump efficiency was first plotted against the flow rate in Figure 1. As it can be seen, a strong correlation can be observed. The minimum values of the optimum pump efficiency correspond to the smallest flow rates, somewhere over 65%. However, it soon starts to grow, and by 300 l/s, the pump efficiency has already reached a value of 85%. The curve continues to grow towards an asymptotic value of no more than 90%.

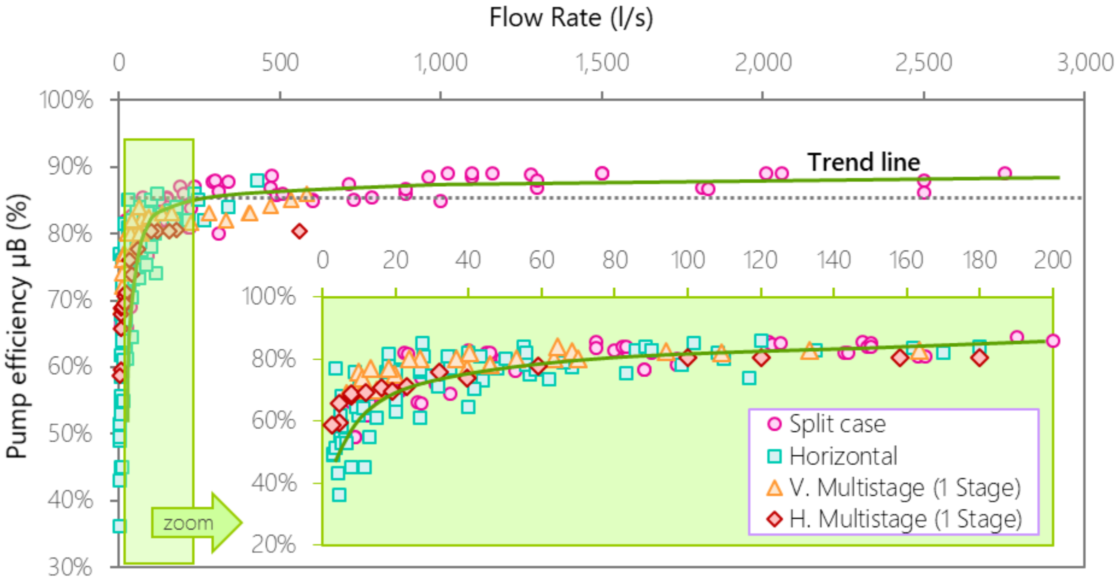

Figure 1 - Relationship between the flow rate and the pump efficiency.

Regarding the influence of the type of pump, split case pumps are the ones that are capable to work with the highest flow rates, and therefore, they are also correspondent to the highest pump efficiency. They are the predominant type for over 400 l/s and 85%. The rest of the regular horizontal pumps work for much smaller flow rates (under 250 l/s) and thus, lower values of the pump efficiency. Vertical and horizontal multistage pumps work in the same spectrum of flow rates (also under 250 l/s), but over all the vertical multistage pumps perform better for any flow rate than the horizontal multistage pumps. It should also be clarified that submersible vertical pumps are included in the vertical multistage category, since they were very few.

3.2. Pump Efficiency and Pumping Head

When the optimum pump efficiency is plotted against the pumping head in Figure 2, no relationship can be seen. The distribution of dots is too scattered to withdraw any conclusions. Therefore, it can be said that there is no relationship between the optimum pump efficiency and the pumping head.

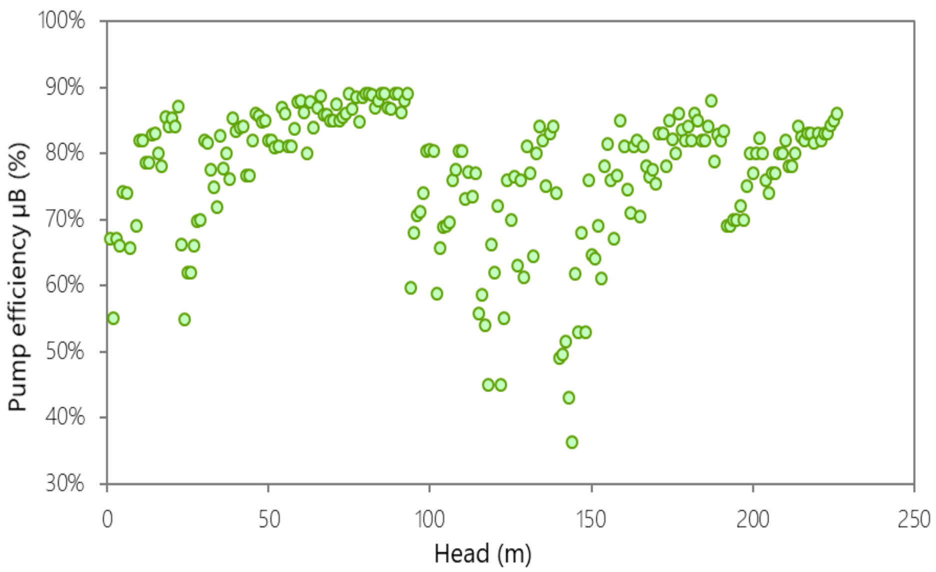

Figure 2 - Relationship between the pumping head and the pump efficiency.

3.3. Pump Efficiency and Power

The results for the relationship between the pump efficiency and the pumping power are very similar to those obtained with the flow rate: a clear relationship is observed in Figure 3. However, in this case the relationship is weaker since the distribution presents more dispersion. Nevertheless, the shape is very similar: it is a growing curve with an asymptote at almost 90%. For over 250 kWh, the pump efficiency can be expected to be higher than 85%. The reason of this slightly bigger dispersion can be explained by the fact that the pumping power is obtained from the flow rate, but also from the pumping head. The poor relationship between the pumping head and the pump efficiency could be responsible for the dispersion. Nevertheless, it can be concluded that there is a relationship between the pump efficiency and the power.

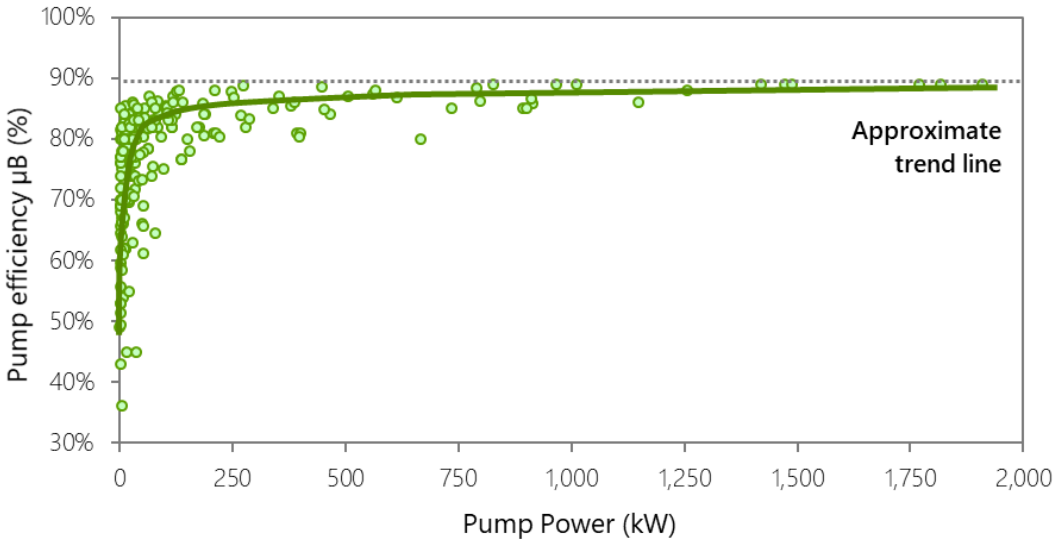

Figure 3 - Relationship between the pumping power and the pump efficiency.

3.4. Pump Efficiency and Speed.

It was also studied the relationship between the pump efficiency and the rotation speed (see Figure 4), the specific speed. The rotation speed of the pump is a discrete variable that depends on the frequency of the electrical network and the number of poles. The most common values are 1450 rpm and 2900 rpm. In either case, all range of values of the pump efficiency could be found. Therefore, no relationship between the pump efficiency and the rotation speed can be concluded.

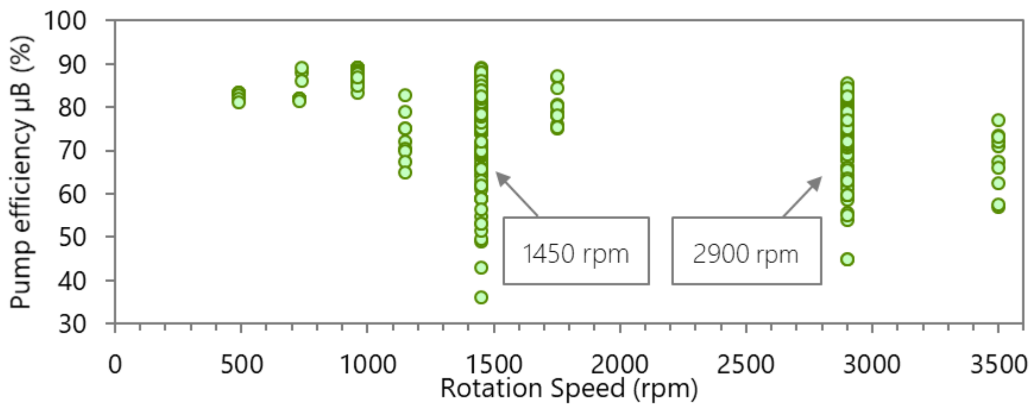

Figure 4 - Relationship between the rotation speed and the pump efficiency.

The specific speed is interpreted as the rotation speed that a homologous pump should have in order to elevate a discharge of 1 m^3/s at 1m height Martin-Candilejo,et al., (2020). The vast majority of the pumps showed a specific speed of 5-80 rpm. In that interval, the pump efficiency was also increasingly growing (see Figure 5), in a similar way as the flow rate or the power did; nevertheless, much more dispersion was observed. Thus, no sufficiently clear relationship was concluded.

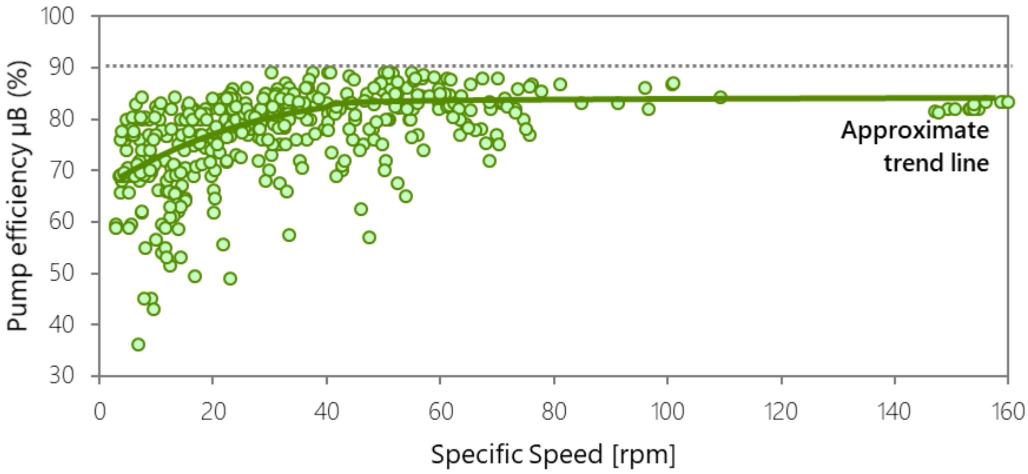

Figure 5 – Relationship between the pumping power and specific speed.

3.5. Average Pump Efficiency Depending on the Pump Type.

Overall, all the possible values of the pump efficiency can be seen in Figure 6, organised by the pump type. The average value is also marked for each type. It can be seen that in average, the split case is the type that offers the highest average values, and horizontal pumps are the ones that offers a wider range of pump efficiency. Once again, vertical multistage show better results than horizontal multistage.

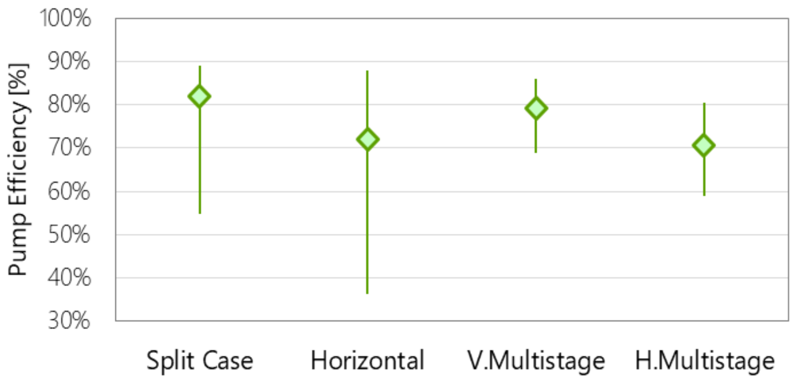

Figure 6 - Pump efficiency range and average values depending on the pump type.

3.6. Definition of the Relationship of the Pump Efficiency and Flow Rate.

Since the relationship between the optimum pump efficiency and the flow rate was the strongest observed, it was decided to properly define an interpolated empiric curve that could serve to estimate μ_B, from the design flow rate. The interpolation was carried out for the average and the maximum expected value of μB. The curve was fitted by sectioning the data in 14 sections. The values of each section were adjusted through a doubly logarithmic curve, and the curve fit very satisfactory. The curves can be seen in Figure 7. The empirical equations of the relationship between the flow rate and the expected optimum values of the pump efficiency are:

Average $\mu B \rightarrow \mu B = 0.1286 \cdot \ln(2.047 \cdot \ln(q) - 1.7951) + 0.5471 \quad r^2 > 98\%$ (1)
Maximum $\mu B \rightarrow \mu B = 0.0576 \cdot \ln(2.047 \cdot \ln(q) - 1.7951) + 0.741 \quad r^2 > 90\%$ (2)
Minimum $\mu B \rightarrow \mu B = 0.2074 \cdot \ln(2.047 \cdot \ln(q) - 1.7951) + 0.3161 \quad r^2 > 95\%$ (3)

where q the flow rate in litres per second (l/s).

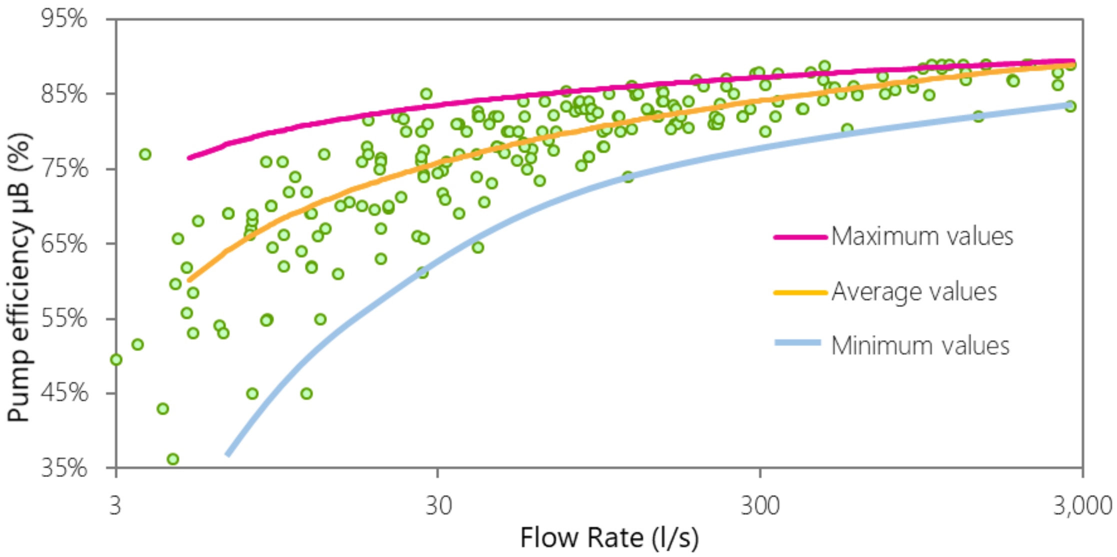

Figure 7 - Fitted curves of the flow rate and the pump efficiency.

4. CONCLUSION

The efficiency of the hydraulic pumps was analysed in depth, in relation with the other design variables. A relationship between the pump efficiency and flow rate or the pumping power was observed. Any relationship with the pumping head or the rotation speed was discarded. A slight relation with the specific speed was observed.

Since the relationship between the flow rate and the pump efficiency is very strong, an interpolated curve was fitted. This curve can be easily used by designers to estimate the value of the pump efficiency in the design of a water supply system that requires pumping. The curves only provide an orientate value of the hydraulic efficiency. The final value would depend on the pump selected by the designer. Entering with the design flow rate, the curve immediately returns the value of the estimated average or maximum optimum pump efficiency. Say that the supply system required a design flow rate of 300 l/s; the practitioner would enter the curves and see that the expected average value of the hydraulic efficiency of the pump would be 80% and the maximum that efficiency that could be found in the marked is around 85%. These empiric curves can be a great resource to properly incorporate the costs of pumping in the design of a water supply system. These results can be applied for the design stages of a water supply system, for instance, in agricultural purposes or in urban areas.

5. ACKNOWLEDGMENTS

This work was funded by Fundación Carlos Gonzalez Cruz; to whom we are deeply grateful.

6. REFERENCES

Alperovits, E. and Shamir, A. U. (1977) *Design of Optimal Water Distribution Systems*, Water Resources Research.

Costa, A. L. H., Medeiros, J. L. D. and Pessoa, F. L. P. (2000) *Optimization of pipe networks including pumps by simulated annealing*, Brazilian Journal of Chemical Engineering, 17.

Dziedzic, R., Karney, B. W. and Asce, M. (2015) *Cost Gradient-Based Assessment and Design Improvement Technique for Water Distribution Networks with Varying Loads*, Journal of Water Resources Planning and Management, 142(1).

Featherstone, R. E. and El-Jumaily, K. K. (1983) *Optimal Diameter Selection for Pipe Networks*, Journal of Hydraulic Engineering, 109(2), pp. 221–234.

Filion, Y. R., Adams, B. J. and Karney, B. W. (2007) *Stochastic Design of Water Distribution Systems with Expected Annual Damages*, Journal of Water Resources Planning and Management, 133(3), pp. 244–252.

Gessler, J. and Walski, T. (1985) *Water Distribution System Optimization.*

Jin, X., Zhang, J. and Gao, J. (2008) *Multi-objective optimization of water supply network rehabilitation with non-dominated sorting Genetic Algorithm-II*, Journal of Zhejiang University-Science A, 9(3), pp. 391–400.

Joong Hoon Kim, B. and Mays, L. W. (1994) *Optimal Rehabilitation Model for Water-Distribution Systems*, Journal of Water Resources Planning and Management, 120(5).

Kang, D., and Lansey, K. (2013) *Scenario-Based Robust Optimization of Regional Water and Wastewater Infrastructure*, Journal of Water Resources Planning and Management, 139(3), pp. 325–338.

Kapelan, Z. S., Savic, D. A. and Walters, G. A. (2005) *Multiobjective design of water distribution systems under uncertainty*, Water Resources Research, 41(11), pp. 1–15.

Mala-Jetmarova, H., Sultanova, N. and Savic, D. (2018) *Lost in optimisation of water distribution systems? A literature review of system design*, Water (Switzerland). doi: 10.3390/w10030307.

Martin-Candilejo, A., Santillán, D., Iglesias, A., and Garrote, L. (2020) *Optimization of the design of water distribution systems for variable pumping flow rates*, Water (Switzerland), 12(2), pp. 1–19.

Martin-Candilejo, A., Martin-Carrasco, F. J. and Santillán, D. (2021) *How to Select the Number of Active Pumps during the Operation of a Pumping Station: The Convex Hyperbola Charts*, Water, 13(11), p. 1474.

Martin-Candilejo, A., Santillán, D. and Garrote, L. (2020) *Pump efficiency analysis for proper energy assessment in optimization of water supply systems*, Water (Switzerland), 12(1).

Perelman, L. and Ostfeld, A. (2007) *An adaptive heuristic cross-entropy algorithm for optimal design of water distribution systems*, Engineering Optimization, 39(4), pp. 413–428.

Perelman, L., Ostfeld, A. and Salomons, E. (2008) *Cross Entropy multiobjective optimization for water distribution systems design*, Wiley Online Library, 44(9), p. 9413.

Reed, P. M. *et al.* (2013) *Evolutionary multiobjective optimization in water resources: The past, present, and future*, Advances in water resources, pp. 97–103.

Samani, H. M. V. and Mottaghi, A. (2006) *Optimization of Water Distribution Networks Using Integer Linear Programming*, Journal of Hydraulic Engineering, 132(5), pp. 501–509.

Sanchis, R. *et al.* (2019) *Solution approaches for the management of the water resources in irrigation water systems with fuzzy costs*, Water (Switzerland), 11(12).

Spiliotis, M. and Tsakiris, G. (2007) *Minimum Cost Irrigation Network Design Using Interactive Fuzzy Integer Programming*, Journal of Irrigation and Drainage Engineering, 133(3), pp. 242–248.

Vamvakeridou-Lyroudia, L. S., Walters, G. A. and Savic, D. A. (2005) *Fuzzy Multiobjective Optimization of Water Distribution Networks*, Journal of Water Resources Planning and Management, 131(6), pp. 467–476.

Wu, W., Simpson, A. R. and Maier, H. R. (2010) *Accounting for Greenhouse Gas Emissions in Multiobjective Genetic Algorithm Optimization of Water Distribution Systems*, Journal of Water Resources Planning and Management, 136(2), pp. 146–155.

8th International Junior Researcher and Engineer
Workshop on Hydraulic Structures
ISBN: 978-0-578-37416-1
https://doi.org/10.26077/d378-12f6

Galway, Ireland,
5th - 8th June 2021

Laboratory experiments on long waves interacting with rigid vertical cylinders

R. Basile[1], F. De Serio[1] and D. Raffaele[1]
[1] DICATECh, Department of Civil, Environmental, Land, Building Engineering and Chemistry
Polytechnic University of Bari
Bari BA 70125
ITALY
E-mail: rosangela.basile@poliba.it

Abstract: *The impact of waves caused by storm surges or floods could lead to significant damage to marine and fluvial structures. Hydraulic forces add significant hydrodynamic loads on bridges built in coastal and fluvial environments; therefore, the effect of the wave impact on bridge substructures must be properly considered for the safe and cost-effective design of the piers. The use of laboratory-scale models is a direct approach to investigate the effects of long waves on simple structures, mimicking bridge piers. The present study describes a laboratory-scale model, where the propagation of two different long waves in a flume, in the presence of two rigid cylinders, was investigated. The velocity measurements were acquired by the Particle Image Velocimetry (PIV) technique, providing instantaneous flow velocity vectors on 2D planes. For each experimental condition, the instantaneous velocity field close to the cylinders was analysed, in order i) to depict how it changes during the wave transit, and thus how the drag force acting on the cylinders could change, ii) to detect the spatial distributions of vorticity downstream. Some first interesting results have been obtained, showing a quite uniform distribution of the longitudinal velocity along the depth of the vertical plane upstream of the cylinders, with increasing values during the wave transit. No interactions in the central part of the flow downstream of the two cylinders was observed in the horizontal plane which are spaced approximately ten times their diameter. Finally, the vorticity has also been studied, displaying a phase-varying behaviour, which appears to lose symmetry during wave transit.*

Keywords: Long waves, wave-structure interaction, particle image velocimetry, velocity distribution, vorticity.

1. INTRODUCTION

In the fluvial and marine environment, fundamental civil infrastructures like bridges, are often exposed to serious environmental loads, in particular when subjected to wave impacts. The extent of the damage caused by extreme waves in bridge substructures suggests that wave forces were not adequately considered in the design of piers. Therefore, in recent years there has been considerable interest in the safety of such facilities in extreme wave conditions. Research on wave forces acting on the bridge pier is essential for structural design and for the investigation of bridge failure mechanisms.

The use of laboratory-scale models is a direct and effective approach to investigate the effects of long waves on simple structures. A certain amount of past literature focused on experimental studies of different kinds of waves impacting on a vertical cylinder. Antolloni et al. (2020) discussed experimental results of long and moderately long wave-induced vortex generation around a slender vertical cylinder, obtained from velocity flow measurements acquired using the Particle Image Velocimetry (PIV) technique. The results showed that vortex formation occurring in the long waves is attached to the cylinder in the form of thin vortex tubes which appear symmetrically at angles of 40º-45º off the wave propagation direction. Vested et al. (2020) performed an experimental study with the combined use of PIV and Laser Doppler Velocimetry in order to investigate the force distribution on a vertical circular cylinder exposed to shoaling regular waves. The force distribution was measured for twenty regular wave conditions and in all cases it was found that the maximum force did not occur simultaneously on the individual sections of the cylinder. Li et al. (2012) performed a wave basin experiment to examine the interactions between multi-directional focused waves and a vertical bottom-mounted cylinder, proving that the focused run-up is directly proportional to the wave parameters including wave steepness, frequency bandwidth, and the directional spreading index. Wei et al. (2018) performed an experiment to investigate the dynamic responses of a bridge tower subjected to ocean waves and wave-currents. Wave-induced base shear forces on the pile-group foundation and motion responses of the tower were analysed and the results showed that when a wave period is close to the natural period of the structure, an obvious resonance is induced on the structure. Furthermore, the longitudinal incident waves induced the largest longitudinal base shear forces on the foundation and the greatest dynamic motions on the upper tower of the structure. Mo et al. (2013) presented an experimental study of plunging solitary waves on a plane slope, with and without the interference of a vertical cylinder, using the PIV technique to record the time history of free surface elevations and temporal and spatial velocity variations in two fields of view.

Recent studies also focused on the flow behaviour around multi-cylinder structures, considered as obstacles necessary to mitigate the wave action. Tognin et al. (2019) exposed a peculiar experimental setup, designed to investigate the interaction between solitary waves and rigid emergent small-diameters cylinders representing rigid vegetation. Here it was observed observing that the cylinders strongly reduce the wave height based on their density.

The purpose of the present work is to describe a small-scale experiment representative of the propagation of long waves (such as for example flood waves due to heavy rains) on bridge piers. The experimental model reproduces the propagation of two long waves in a flume, in the presence of two rigid vertical cylinders simulating the bridge's piers. The velocity measurements are obtained with the use of the PIV technique, measuring instantaneous flow velocity vectors on different 2D planes. Specifically, the experiments consisted of flow velocity measurements: i) along the longitudinal plane of symmetry of both the cylinders, assessed upstream and downstream of each structure, and ii) on the horizontal plane at a specific distance from the flume bottom. Two solitary waves were released in the channel, overlapped on a uniform base flow, characterized by different values of flow rate, height, and period.

The aim of the present study is to provide some new benchmark data to improve the understanding of i) the time-varying vertical distribution of the drag and inertia forces acting on the cylinder during the wave transit, based on detailed measurements of the velocity distribution, ii) the time-varying velocity and vorticity field downstream of the cylinder in the horizontal plane.

2. EXPERIMENTAL SETUP

The experiments were performed at the Hydraulic Laboratory of the Polytechnic University of Bari (Italy). The rectangular flume, having a length of 25 m and a width of 0.4 m, was characterized by sidewalls and bottom constructed from Plexiglass which was well suited for optical measurements (see Figure 1).

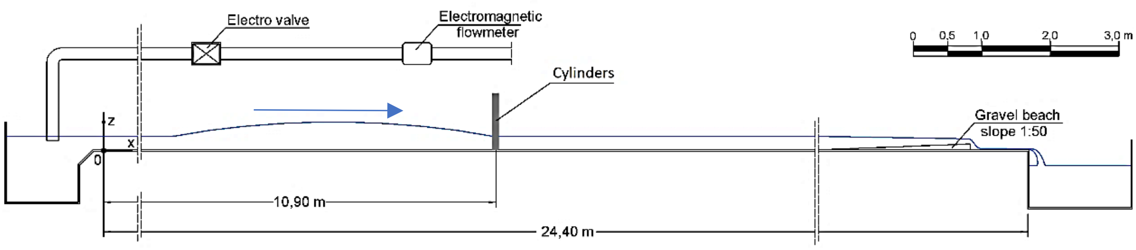

Figure 1 – Side view of the experimental setup, with the position of the cylinders.

The head tank could be fed by both a low-pressure and a high-pressure water circuit. The low-pressure main circuit provided constant flow conditions in the flume. The secondary high-pressure adduction pipe could release an additional water discharge in the head tank, controlled by an electronic actuated valve managed by a process PC with LabVIEW software. In this way, by properly tuning the added water release, the desired wave was generated in the channel, superimposed on the base flow.

At the downstream end of the channel, a secondary tank was located to receive the discharged flow. This was equipped with a triangular sharp-crested weir used to estimate the steady flow rate. The water level was controlled by a sloping gate at the end of the flume. In order to reduce the reflection of the generated waves, a structure with a high degree of porosity, consisting of a 2 m length metal cage with a 1 cm mesh filled with d_{50} = 1.50 cm gravel, was positioned on the bottom of the final part of the flume.

However, the measurements of the tested waves impinging on the model were acquired in a time period specifically chosen to avoid any reflection.

The model was designed according to Froude similitude, using a length scale factor equal to 1/10 (model/prototype). In this way we could evaluate the target phenomenon consistently with the lab available spaces. The experimental facility (Figure 1) consisted of two rigid cylinders having a diameter *d* = 20 mm, located along the *y* axis of the same transversal section, at a distance of *x* = 10.9 m from the header tank (being *x* the longitudinal axis of symmetry of the channel). They are positioned at equal distanced from the *x* axis, with *y* = 100 mm and *y* = -100 mm, respectively (Figure 2).

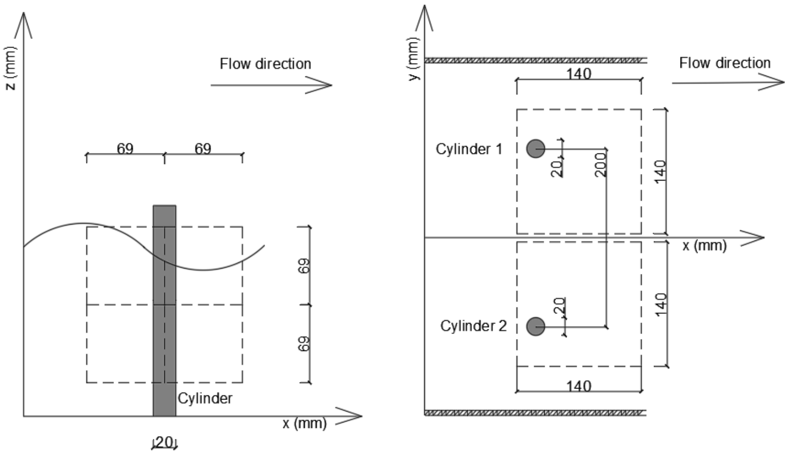

Figure 2 – Sketch illustrating the positions of the FoVs, in side-view (xz) on the left and plan-view (xy) on the right.

In order to obtain the flow velocity vectors on selected 2D planes, the velocity measurements were acquired by a PIV technique. The 2D PIV system was equipped with a FlowSense EO 4M-32 camera, a Bernoulli Laser (pulse energy of 200 mJ at 15 Hz) and a synchronizer controlled and monitored using a computer. The system was handled in double-frame mode, where the sampling frequency was settled to 13 Hz and the time interval between two frames of the same pair was 150 µs.

The data examined in the present work refers to the flow velocity measured in the horizontal plane (*x,y*) located at *z* = 30 mm from the bottom of the flume and containing both the cylinders, and in the longitudinal plane (*x,z*) passing through the centre of the first cylinder (located at *y* = -100mm).

In the horizontal plane, two field of views (FoVs) were properly selected (see Figure 2), each one containing a cylinder respectively. In the vertical plane, four FoVs were chosen: two filming below the free surface of the steady flow upstream and downstream of the cylinder respectively, and the other two filming in the upper part, to detect the passage of the solitary wave, again both upstream and downstream of the cylinder. In the present study, only data in the vertical plane upstream of the cylinder are shown for the sake of brevity.

After calibration, the obtained PIV images in the vertical plane had dimensions 69 × 69 mm, while the PIV images in the horizontal plane had dimensions 140 x 140 mm. The interrogation area of the images during adaptive correlation processing was 16×16 pixels; thus, the velocity vectors were assessed on points regularly spaced and distant 0.4 mm in the vertical plane and 0.8 mm in the horizontal plane, providing a very high spatial resolution.

The water depth in the flume was set to be 10.3 cm and the base flow rate, calculated using the flow rate scale for the Thomson-type triangular weir placed on the secondary tank, was 2.45 l/s.

In order to replicate, as an example, a flood propagation, two solitary waves, named O908 and O909, were used in the experiments. Each one was generated by linearly opening and successively closing the actuated valve of the high-pressure circuit for 19 s and 31 s (operating on a command PC in the Labview environment). Consequently, setting the maximum valve opening percentage to 70% for O908 and to 80% for O909, they had a wave height of 2.5 cm and 5 cm respectively and a wave period *T* = 20,000 ms.

The number of images acquired by PIV was limited by technical reasons related to storage size; therefore, the number of images per measurement was set to 150t. Consequently, the total acquisition time for each measurement was equal to 18,400 ms, that is lower than the entire wave period. Nevertheless, this was sufficient to capture the ascending and descending phase of both waves.

3. EXPERIMENTAL RESULTS AND DISCUSSION

The stationary conditions in the channel, typical of the base flow, i.e., the one characterized by h = 10.3 cm and q = 2.45 l/s, provided a reference average velocity equal to u_0 = 0.06 m/s. By setting the kinematic viscosity $\nu = 10^{-9}$ m^2/s, the flow Reynolds number was Re_f = 24000 and therefore the flow in the channel was turbulent. We also calculated the cylinder Reynolds number, $Re_{cyl} = u_0 * d/\nu$ = 1200, suggesting the presence of a laminar boundary layer on the cylinder front and a detachment of alternating vortices downstream it (Kirkil et al., 2015; Maraglino et al., 2019).

To evaluate the velocity vector field from pairs of particle images, the adaptive correlation method was used as first step of data processing. The resulting vector maps were examined and used also to extract the vorticity maps. Firstly, and for both O908 and O909 waves, the analysis focused on the vertical plane upstream of the cylinder (FoVs in Figure 2). The flow field was observed both in stationary conditions and in wave conditions, while varying during the passage of the long wave. Considering that the u velocity and the wave elevation are in phase, in Figure 3 the time series of the u horizontal velocity in a selected point close to the cylinder (located at x=10.87m and z=0.03m) is shown. In this graph, some specific values t/T are highlighted by a red line, referring respectively to the trough wave condition (*P1*), the peak of the wave (*P2*), two values (equi-spaced) in the descending phase of the wave (*P3, P4*) and the final value, approaching again the wave trough (*P5*).

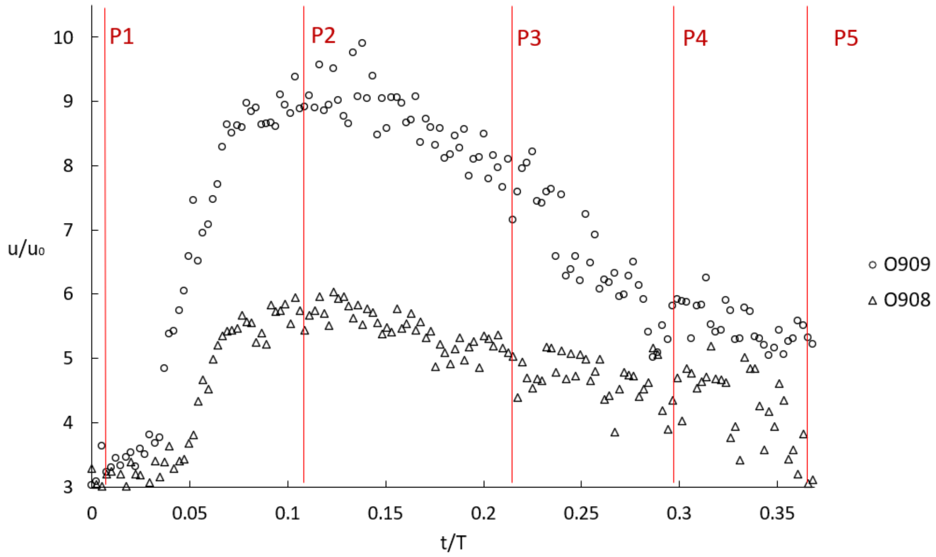

Figure 3 - Longitudinal velocity time series relative to point Q during the propagation of the waves.

The vertical profiles of u were extracted for each instant time mentioned above, at the selected point located at x = 10.87 m. Figure 4 displays the comparison between these five vertical velocity profiles of u, normalized by the average velocity u_0, for both the examined waves. The vertical profiles along z/h have been obtained by merging the instantaneous velocity maps of the two FoVs (upper and lower, as in Figure 2). In particular, for the O908 wave, the FoVs capture the image of the cylinder at 2 cm from the bottom of the flume, while for the O909 wave, the FoVs capture it at 4.5 cm from the bottom of the flume, in order to detect the entire height of the wave. It is evident that all the vertical profiles have a quite flat vertical trend, meaning that the distribution of the u velocity is quite uniform along the depth. Rather, we observe increasing values of u/u_0 due to the wave transit, which reach a maximum at the wave peak, as expected (u/u_0 = 6.15 for O908 and u/u_0 = 9.3 for O909). Moreover, the transit of the wave is evidently proved also by the increased relative heights z/h where the velocities are detected, with respect to z/h, close to 0.9 in the P1 profile. For the wave O908, a maximum relative wave height

z/h = 1.13 is reached in P2, while for wave O909, the maximum relative height in P2 is z/h = 1.3. Coherently with the descending branch of the wave, P3, P4 and P5 profiles show lower velocities and heights gradually. The P3, P4 and P5 profiles for the O908 wave have similar u/u_0 velocity values, being the descending branch of the time series (Figure 3) less sloped than for the O909 wave.

Knowing the distribution of the longitudinal components of the longitudinal velocity u in both wave conditions, may allow us to detect the force acting on the cylinder per unit height. In fact, expressions like the Morison's equation can be adopted in this case, considering the sum of the inertia and drag contributions (1):

$$F(t) = C_M \rho \frac{\pi d^2}{4} \frac{du}{dt} + C_D \frac{1}{2} \rho d u|u| \qquad (1)$$

where ρ is the water density, C_D is the drag coefficient and C_M is the inertia coefficient (both can be assumed ~ 1 in our case). It is evident that in the case of the O909 wave, the cylinder is expected to be affected by higher force values e than in the case of the O908 wave, due to the higher u peak velocity and greater variation in the time period of the u velocity.

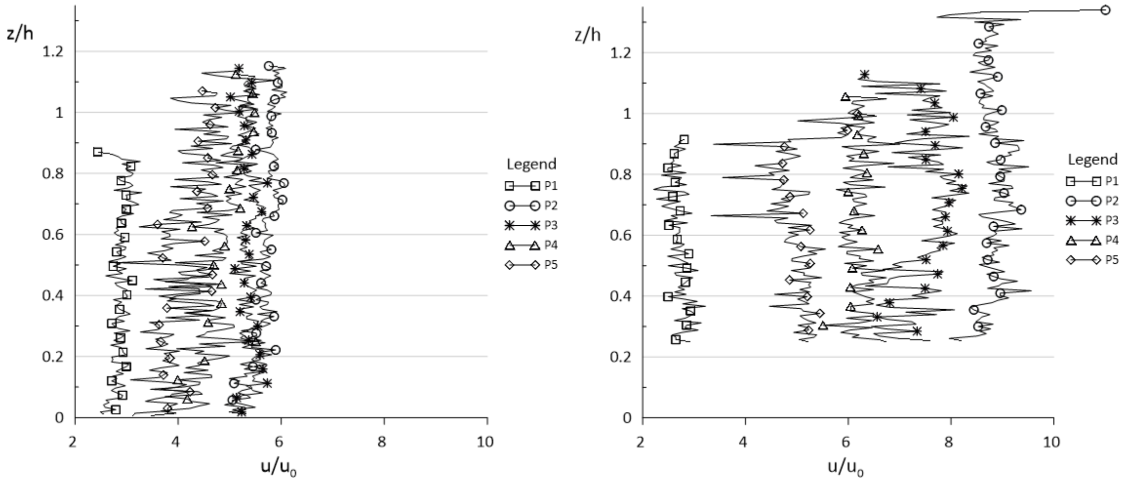

(a) (b)

Figures 4 - Comparison between the vertical profiles of the longitudinal velocity u normalized by the average velocity u_0, as measured at five instant times related to wave trough: (P1), wave peak (P2), descending wave (P3 and P4), approaching trough (P5) for (a) wave O908 and (b) wave O909.

As a second step, the results obtained from the FoVs in the horizontal plane, at z = 0.03 m, downstream of the two cylinders (Figure 2) were analysed for both O909 and O908 waves. In this case we chose four instant times as been significant to describe the wave behaviour such as wave trough, ascending branch, wave peak and descending branch.

For the O908 wave, Figure 5 shows the instantaneous velocity horizontal maps in the two selected FoVs, each one containing a cylinder respectively, during the wave transit. The analogous plot is shown in Figure 6 for the O909 wave. In such plots the reference system used refers to the frame (x_f, y_f). It is necessary to point out the presence of a shaded region up to x_f = 40 mm, due to the shadow caused by the laser light source on the two cylinders. It is evident that, being the two cylinders spaced along y ~ 10d, no interaction is observed in the central part of the flow, which remains quite undisturbed.

The horizontal velocity vectors (having components u along x, and v along y) gradually increase from 0.1 m/s to 0.4 m/s for the O908 wave and up to 0.5 m/s for the O909 wave, while going from the trough condition to the peak one. This is observed generally in points far from the wake of the cylinder. Figures 5 and 6 in fact highlight the presence of a wake behind the cylinders, where the velocity magnitude abruptly decreases (up to values from 0 m/s to 0.1 m/s) as expected and where a detachment of eddies occurs.
To evaluate the vorticity W_z, we have computed the vorticity maps, plotted in Figure 7 and 8 respectively for O908 and O909 waves, always for the selected four instant times. For the case of the wave trough, opposite values of vorticity are observed (and quite symmetrical) downstream of each cylinder: anticlockwise (negative) on the left side of the cylinder wake and clockwise (positive) on the right side.

This is consistent with the stationary case of a flow impacting a cylinder. During the three successive time steps (ascending, peak, descending) the symmetry seems lost, and the negative vorticity affects also the right side, while the positive vorticity spreads more downstream. In the peak condition, the most intense vorticity values are observed with values in the range from W_z = -0.1 s^{-1} to W_z = 0.1 s^{-1} for O908 wave and in the range from W_z = -0.2 s^{-1} to W_z = 0.2 s^{-1} for O909 wave.

Finally, we have examined how the presence of the two cylinders influences the velocity distribution in the transverse direction. Figures 9 and 10 illustrate the transverse profiles of the longitudinal *u* velocity during the trough, the ascending branch, the peak and the descending branch for the O908 and O909 waves. For each profile, the *u* velocity is normalized by its maximum value U_{max} measured along the profile itself. Moreover, we compare the transversal profiles at five different positions, at increasing distances from the cylinders (x_f = 50.4 mm, x_f = 70.4 mm, x_f = 90.4 mm, x_f = 110.4 mm, x_f = 130.4 mm).

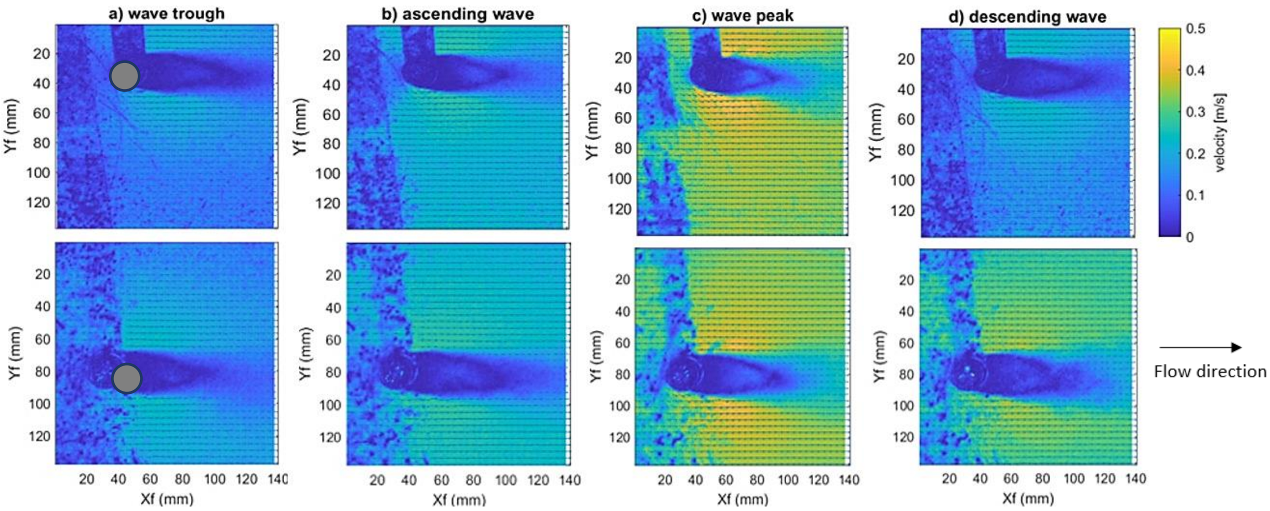

Figures 5 - The velocity in the horizontal plane during the wave transit: (a) trough, (b) ascending phase, (c)peak and (d) descending phase of O908 wave.

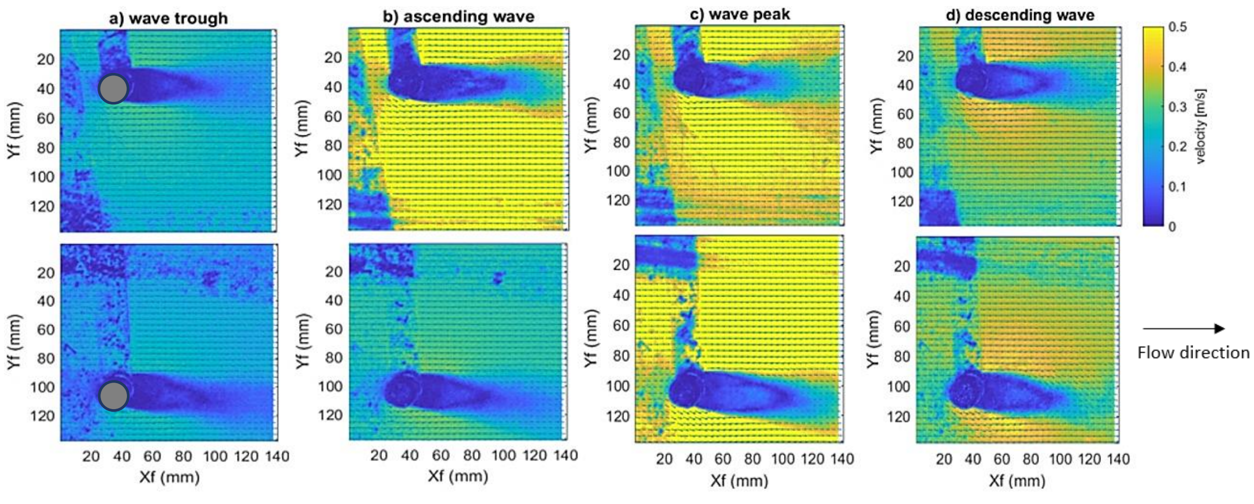

Figures 6 - The velocity in the horizontal plane during the wave transit: (a) trough, (b) ascending (c) phase, peak and (d) descending phase of O909 wave.

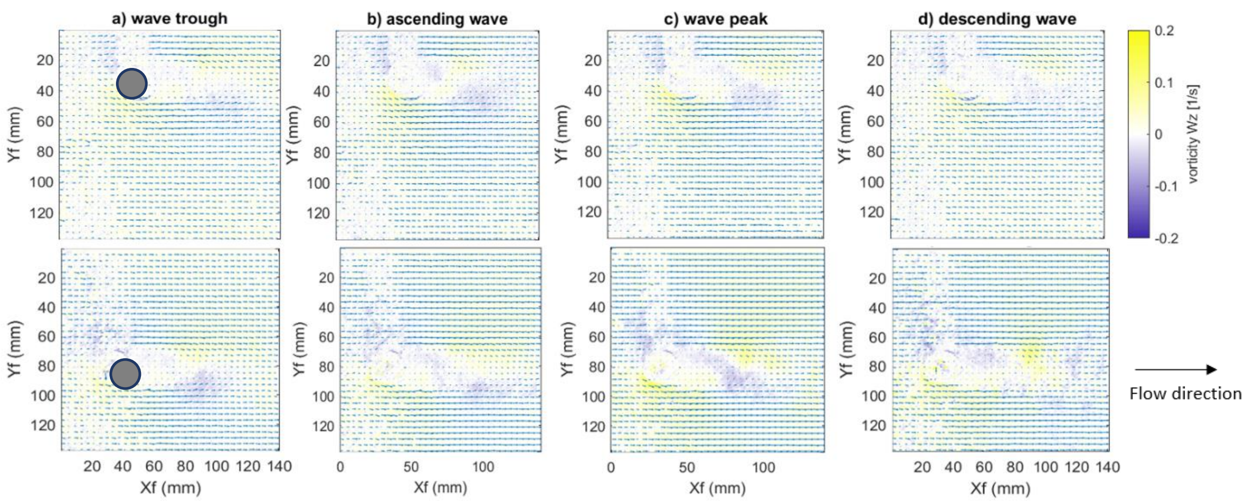

Figures 7 - Vorticity in the horizontal plane during the wave transit: (a) trough, (b) ascending phase, (c) peak and (d) descending phase of O908 wave.

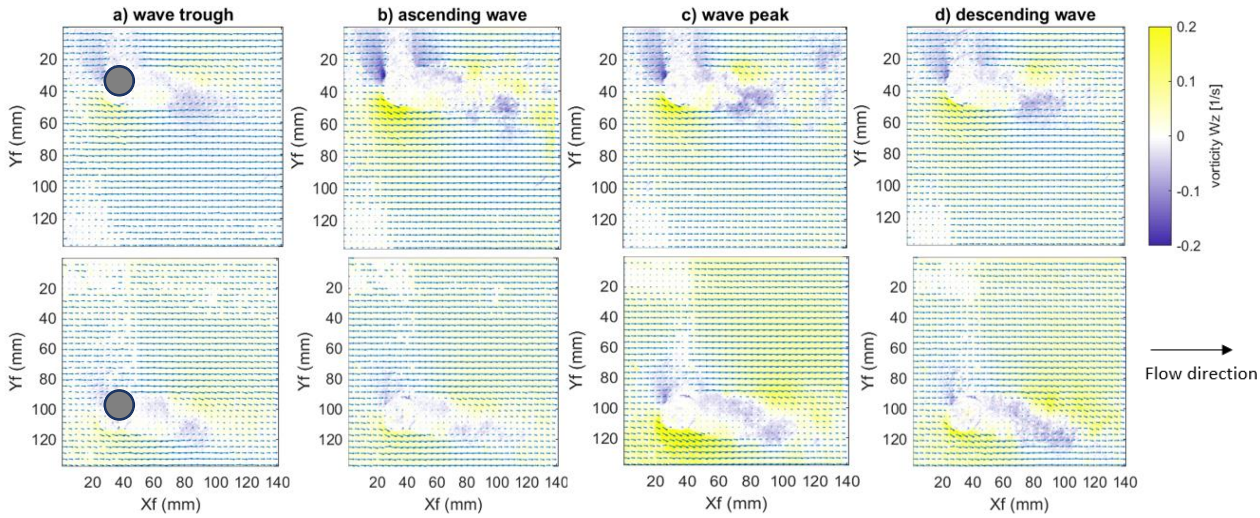

Figures 8 - Vorticity in the horizontal plane during the wave transit: (a) trough, (b) ascending phase, (c) peak and (d) descending phase of O909 wave.

At the same distance from the cylinders, the transversal profiles of the two waves show a similar trend, meaning that in the region between the two cylinders and outside the wake, the velocity is quite uniform with a magnitude of approximately 80% of the maximum value. A relevant velocity reduction is noted downstream of the cylinders, passing from u/U_{max} = 0.6 to u/U_{max} = 0.01 in the case of the wave O908 in x_f = 50.4 mm, and from u/U_{max} = 0.7 to u/U_{max} = -0.2 in the case of the wave O909, at the same distance.

When a negative sign is observed for u/U_{max}, the presence of a vortex should be assumed. With increasing x_f distances, the velocity in the cylinders' wakes gradually increase tending to represent the original base flow.

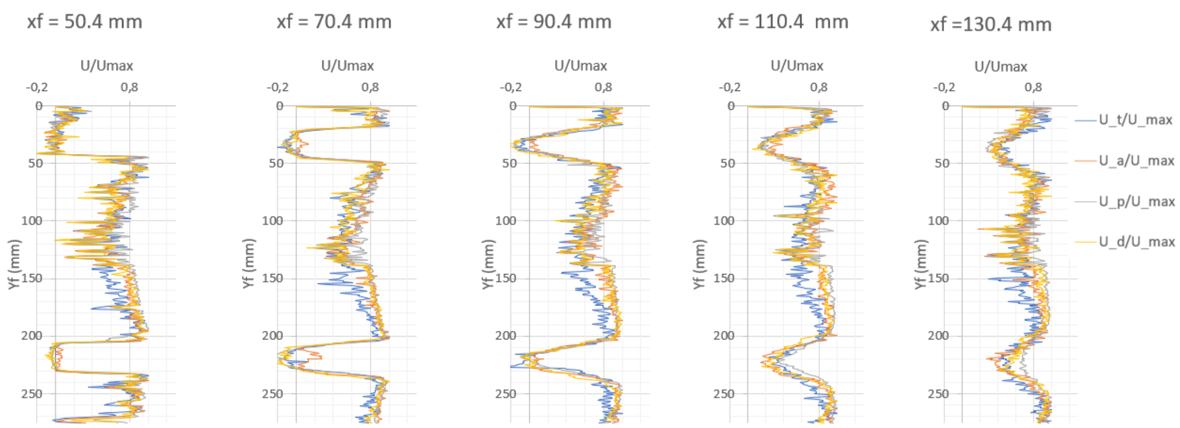

Figures 9 – Transverse profiles during the trough, the ascending branch, the peak and the descending branch of O908 wave, at selected distances x_f.

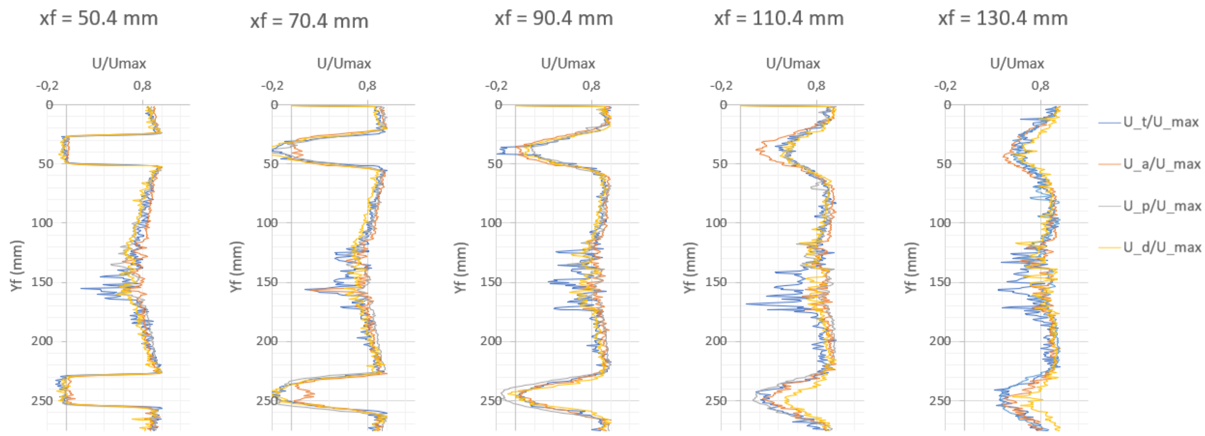

Figures 10 – Transverse profiles during the trough, the ascending branch, the peak and the descending branch of O909 wave, at selected distances x_f

4. CONCLUSION

This study describes a laboratory-scale model, where the propagation of two different long waves in a flume in presence of two rigid cylinders, mimicking bridge piers, is investigated using Froude similtude. The velocity measurements acquired by the PIV technique have provided the following results.

The vertical profiles of the longitudinal velocity *u* upstream of each cylinder, normalized by the average velocity u_0, for both the examined waves, show a quite flat vertical trend, meaning that the distribution of the *u* velocity is quite uniform along the depth. Increasing values of u/u_0 are observed due to the wave transit, reaching a maximum at the wave peak, as expected (u/u_0= 6.15 for O908 and u/u_0 = 9.3 for O909). Furthermore, the presence of the wave transit is evident also from the increased relative heights *z/h* at the position where the velocities are detected.

Downstream of both cylinders, the velocities in the horizontal plane at the transverse distance of ~10d between the two cylinders highlights that no interactions are observed in the central part of the flow which remains quite undisturbed. In points far from the cylinders' wakes, the horizontal velocity gradually increases from 0.1 m/s to 0.4 m/s for the O908 wave and up to 0.5 m/s for the O909 wave, during their transits. In the wakes behind the cylinders, the velocity abruptly decreases as expected and a detachment of vortices occurs. During the wave trough, opposite values of vorticity are observed, and which are quite symmetrical downstream of each cylinder. During the three successive examined time steps, the symmetry seems to reduce, and the negative vorticity prevails close to the cylinders, while the positive vorticity spreads further downstream.

The velocity distribution in the transverse direction observed at five different positions, shows a similar trend at the same distance from the cylinders for both waves, meaning that in the region between the two cylinders and outside the wake the velocity, is quite uniform generally around 80% of the maximum value. With increasing distances from the cylinders, the velocity in the cylinders' wakes gradually increase, tending to re-establish the original flow.

5. REFERENCES

1. Antolloni, G., Jensen, A., Grue, J., Riise, B. and Brocchini, M. (2020), *Wave-induced vortex generation around a slender vertical cylinder,* Physics of Fluids, 32, 1-10
2. Bradner, C., Schumacher, T., Cox, D. and Higgins, C. (2011), *Experimental setup for a large-scale Bridge superstructure model subjected to waves*, Journal of waterway, port, coastal and ocean engineering, 137, 3-11
3. Chella, M.A., Bihs, H., Myrhaug, D. and Muskulus, M. (2017), Breaking solitary waves and breaking wave forces on a vertically mounted slender cylinder over an impermeable sloping seabed, J. Ocean Eng. Mar. Energy, 3, 1-19
4. Guo, A., Liu, J., Chen, W., Bai, X., Liu, G., Liu, T., Chen, S. and Li, H. (2016), *Experimental study on the dynamic responses of a freestanding bridge tower subjected to coupled actions of wind and wave loads*, Journal of wind engineering and industrial aerodynamics, 159, 36-47
5. Kirkil, G. and Constantinescu, G. (2015), *Effects of cylinder Reynolds number on the turbulent horseshoe vortex system and near wake of a surface-mounted circular cylinder*, Physics of Fluids, 27, 1-25
6. Li, J., Wang, Z. and Liu, S. (2012), *Experimental study of interaction between multi-directional focused wave and vertical circular cylinder, part I: Wave run-up*, Coastal Engineering, 64, 151-160
7. Li, J., Wang, Z. and Liu, S. (2014), *Experimental study of interaction between multi-directional focused wave and vertical circular cylinder, part II: Wave force*, Coastal Engineering, 83, 233-242
8. Liu, C., Zhang, S. and Hao, E. (2017), *Joint earthquake, wave and current action on the pile group cable-stayed bridge tower foundation: an experimental study*, Applied Ocean Research, 63, 157-169
9. Malavasi, S. and Guadagnini, A. (2003), *Hydrodynamic Loading on River Bridges*, Journal of Hydraulic Engineering, 129, 854-861
10. Maraglino, D., Meftah, M.B., De Serio, F., Mossa, M. (2019), *Fields measurements in a flow around a hydrofoil: some preliminary results*, in International Workshop on Metrology for the Sea, Genoa, October 3-5, 2019, pp. 270-275
11. Mo, W., Jensen, A. and Liu, P. (2013), *Plunging solitary wave and its interaction with a slender cylinder on a sloping beach*, Ocean Engineering, 74, 48-60
12. Park, H., Tomiczek, T., Cox, D.T., van de Lindt, J. W. and Lomonaco, P. (2017), *Experimental modeling of horizontal and vertical forces on an elevated coastal structure*, Coastal Engineering, 128, 58-74
13. Seiffert, B., Hayatdavoodi, M. and Ertekin, R.C. (2014), *Experiments and computations of solitary-wave forces on a coastal-bridge deck, part I: Flat Plate*, Coastal Engineering, 88, 194-209
14. Tognin, D., Peruzzo, P., De Serio, F., Meftah, M.B., Carniello, L., Defina, A. and Mossa, M. (2019), *Experimental setup and measuring system to study solitary wave interaction with rigid emergent vegetation*, Sensors, 19
15. Vested, M. H., Carstensen, S. and Christensen, E. D. (2020), *Experimental study of wave kinematics and wave load distribution on a vertical circular cylinder*, Coastal Engeneering, 157, 1-18
16. Wei, C., Zhou, D. and Ou, J. (2018), *Wave and wave-current actions on a bridge tower: an experimental study*, Advanced in Structural Engineering, 1-12
17. Zhu, D. and Dong, Y. (2020), *Experimental and 3D numerical investigation of solitary wave forces on coastal bridges*, Ocean Engineering, 2019, 1-15

8th International Junior Researcher and Engineer
Workshop on Hydraulic Structures
ISBN: 978-0-578-37416-1
https://doi.org/10.26077/2d19-80a4

Galway, Ireland,
7th - 10th June 2020

Streamflow Duration Curves: Focus on Low Flows

E.Carcano[1], and M.Betasolo[2]
[1,2] Civil Engeneering Department
Unitech, Lae Morobe Province
PAPUA NUOVA GUINEA
E-mail: elena.carcano@pnguot.ac.pg

Abstract: *Flow duration curves (FDCs) express the link between a selected streamflow and the percentage in time such value is exceeded. The curves provide a graphical insight into hydrological regimes, though, the absence of time-series data is a significant shortcoming. Conversely to what happens with hygrograms, flows in FDCs are represented without regard of sequence of occurrence. This paper explores FDCs of 19 catchments for which, at least, 10 years of daily discharges are available. FDCs can be built for any temporal scale (i.e. daily, weekly, monthly). In this study daily discharges have been adopted because daily scale better represents the variation in flow. A particular focus is on low flow data which are useful to the design: fish ladders, environmental passages and low flow diversions. The work also introduces a unique hydrological area having the inner catchments similar response among themselves in terms of low flow data. For such an hydrologically homogeneous area, environmental flow, namely the amount of water released uniquely for biological requirements, is appropriately detected.*

Keywords: *Biological demands, characteristic durations, environmental structures, fish passages, flow duration curves, low flow data.*

.

1. INTRODUCTION

Analysis of watercourse regimes, with a focus on low flows and droughts, is important for designing storage and capture works, managing regulation devices and dealing with qualitative standards for the ecosystem. Runoff data would ideally be obtained from the hydrometrical gauges but in most cases is obtained through regional analysis that extrapolates available data at a number of measured sites to the rest of a catchment. Searcy (1959) demonstrated that with a sufficiently long record of reliable information curves can be derived that represent the cumulative frequency and enable data analysis that can inform probabilistic modelling of future scenarios. Other work on Flow Duration Curves (FDCs) is attributed to Vogel and Fennesey (1994,1995) who provide a brief history of their widespread use in hydrology. More recent efforts tend to focus on the problem of curve regionalization. Vogel and Fennessey (1994) introduced the idea of annual flow duration curves which have shown to be quite useful for drawing probabilistic considerations on wet and dry years and for computing confidence intervals associated with the curves. Following these conclusions, Castellarin et al. (2004a) modelled the relationship between FDCs and Annual Flow Duration Curves (AFDCs) built on daily streamflow series. His results provide an evaluation of the reliability of the regional FDCs for ungauged sites and show that the reliability of the three best performing regional models are similar to one another. A generation of time series of daily streamflows for ungauged sites has been also detected. Castellarin (2004) tested the procedure over three catchments varying from 400 to 3000 km^2 of size. LeBoutillier and Waylen (1993) tried to relate FDCs to AFDCs through a five-parameter stochastic model of daily streamflows. Albeit a widespread application of different forms of FDCs, curves based upon daily discharges seem yet to be of principal use. This work provides a focus on low flow data dealing with FDCs expressed in the form of ''*characteristic durations*'' detailing a procedure explained by Searcy (1959). In more recent efforts attributed to Claps (1997) and Verma et al (2017) there are attempts to estimate environmental flow (EF) using FDCs. Verma made use of two different approaches, the former one based on a period of record and the second on stochastic approaches for daily: 7-, 30-, 60-day moving averages, and 7-daily mean annual flows. The procedure has been tested on 6 Indian catchments. The results of the study presented here demonstrate a practical and appropriate tool for assessing adequate EF for river courses characterized by similar precipitation pattern but different catchments responses.

2. STUDY AREA AND DATA

The study area, known as Liguria region, is located along the north eastern side of Italy (see Figure 1). Major city is Genova which separates the eastern from the western river courses. The analysis considers a group of 19 catchments for which at least 10 concurrent years of daily data are available. The period of analysis belongs to 1951-1971. After 1977 the dismantlement of the *Ufficio Idrografico Statale* , namely the National Bureau in charge with hydrometrical information, has limited data only to level observations and streamflows are no longer at disposal.

Figure 1 - Liguria Region with highlighted monitored catchments.

This area is characterized by river courses of intermittent and torrential flow regime where major flash floods occur about twice a year, namely, in: November and April. During summer period, conversely, flows are a consequence of a long sequence of non-rainy days (roughly more than 90) which highly limit the water availability necessary for irrigation and potable purposes. The intermittent behavior is entailed in those courses which are sharply dry almost all the yearlong and rebirth after intensive precipitation events, thus flowing for several days before vanishing again. Torrential river courses have an extremely variable flow regime with stream flows going from negligible values along the year to high peaks of hundreds of m^3/s in half a day. The floods, coupled with the high urbanizations, cause severe havoc in the cities located next to their delta, both in term of moral and material damages. A paradigmatic example of high damages is expressed by the photo below.

Figure 2 - Flood in Genova: November 2011

High slopes, short concentration times during the floods (generally in less than 8 hours the flood reaches the delta at sea level originating from 700 m of height) and fast continuous alternation of sediment and erosion areas along the riverbeds characterize hazardous and highly unpredictable response to sudden precipitations.

In general, all 19 catchments have average slope varying from 3 up to 8% and catchment sizes around 150 km^2 and river lengths less than 80 km. Three courses have been selected (see 'Table 3') being representative of: extreme eastern (Roya), eastern (Argentina) and western (Petronio) rivers respect the city of Genova. The former one closed at the hydrometrical section is 480 km^2 squared and origins from 3050 m of height and reaches the delta after 60 km. The river course is located at the extreme eastern side of the region next to the French border. Only one third of its total catchment is in Italian territory and the remaining part has been acquired by France after the Italian defeat of WWII. Its delta is in Ventimiglia. Argentina catchment (total size S=220 km^2) stretches along 39 km from Mountain Saccarello (2000 m of height) to its delta at sea level near the city of Sanremo. Major tributaries have intermittent patterns. In the upper part of the valley there are many slates, limestone and conglomerates quarries. Average overall slope equals to 5.6 %. Petronio is located near the city of Genova and has mean slope of 3.4% with highest altitude of 870 m above sea level.

Table 1 lists the 19 catchments under study. Columns report, respectively: the catchment's area, the period of absent information detected inside the total period considered, the driest month in the year and the corresponding minimum flow value.

Table 1 - Catchments studied from 1951 to 1971, in * catchments with missing data.

Catchment's number	**Catchment's name and area (km^2)**	**Missing Data between 1951-1971**	**Month with lowest rainfall and minimum corresponding flow Q (m^3/s)**
1	Roya*; 477.78	1960-1961	September; *5.264*
2	Bevera*; 155.40	1951-1956; 1960-1963; 1971	September; 0.419
3	Nervia*; 123	1956	September; *0.217*
4	Argentina; 192	No missing data	September; *0.474*
5	Impero*; 69	1951	August; *0.111*
6	Arroscia*; 202	1959: December 1960: January-February 1962: July-September	September; *0.442*
7	Lerrone*; 47	1951-1955; 1967; 1970-1971	September; *0.117*
8	Neva*; 124	1955-1964 1954: October, December	September; *0.31*
9	Sansobbia*; 32	1966	August; *0.033*
10	Bisagno*; 34	1955-1963 1954: September-December	August; *0.09*
11	Lavagna*; 163	1969-1971	August; *0.229*
12	Graveglia*; 41	1953: September-December; 1955-1959 1960: January-March	August; *0.193*
13	Entella; 364	No missing data	August ; *0.497*
14	Petronio*; 57	1951-1956; 1960: May-December 1961	August; *0.0431*
15	Piccatello*; 77	1951-1956	August; *0.369*
16	Bagnone; 51	No missing data	August; *0.432*
17	Aulella*; 208	1951-1954 1955: June-July 1959: May-December 1960-1961 1963: January-August	August; *1.692*
18	Calamazza*; 939	No missing data	August; *5.340*
19	Vara* ; 206	1954: November-December; 1958: August-November	August; *0.768*

3. ADOPTED METHODOLOGY

For each of the above-mentioned catchments the FDC with duration referred to such known long-*term period* has been built having ranked the daily recorded streamflows for ten years at disposal into a descendent order. FDCs are synthesized at official *characteristic durations* (according to the National Hydrographic Bureau custom, Annali Idrologici (1951, 1971)) which correspond to runoff values available: 10, 91, 182, 274 and 355 days/year. To these values the National Hydrographic Bureaus attribute the meaning of: runoff Q10 as maximum flood of reference, namely: the value available (or exceeded) 10 days a year, Q355 is minimum drought of reference, Q91 and Q274 being ordinary flood threshold and ordinary drought threshold. Q182 is the semipermanent flow, namely, the streamflow available half the year. The remaining durations: 10, 91, 274, 355 are specularly complementary within a year. Shape factors are obtained from the ratio of streamflows set at the characteristic durations and briefly describe the shape of the plotted FDCs. Durations between 274 and 355 deal with droughts going from ordinary 274 to extraordinary 355-day limits. Q335 has been here additionally inserted as the complementary runoff value of the month with minimum flow a year. Q335 represents, on the plot of FDC, a pivot point for most of the 19 catchments which have the remaining data (Q336-to Q365) all recorded into the driest month of the year. Results show that for the tail of FDCs the hypothesis that low flow values follow the corresponding chronological sequence of observations is respected. The novelty of the work is to introduce a link between the bottom part of FDCs and the corresponding temporal sequence of low streamflows, which is known to lack by nature. Table 2 summarizes FDCs information reporting: Q335 as the low flow value available, or exceed, 335 days/year in the hydrological year *of long term period* (1951-1971), the shape factors (Q182/Q335 and Q274/Q335) evaluated in respect of Q335 as the value of reference and the number of day/year the average minimum flow (reported in column 4 of Table 1) is available on FDCs. In case such minimum flow (column 4 of Table 1) matches totally to Q335 (column 2 of Table 2) the days/ year (column 5 of Table 2) naturally equal to 335. Such coincidences have been highlighted in bold. The corresponding basins are, therefore, identified as a unique homogeneous hydrographic area in respect of low flows. Shape factors can be detected for any duration of reference and briefly summarize the shape of FDCs. However, the comparisons among Q335 to Q10 and Q91 have been disregarded for lack of useful information since Q335 and Q10, Q91 belong to different hydrological regimes.

Table 2 - FDCs set at *characteristic durations*. Discharges expressed in m^3/s.

Catchment's number	**Q(335)**	**Q(182)/Q(335)**	**Q(274)/Q (335)**	**Duration (days/year)**
1	**5.26**	**1.869**	**1.3118**	**335**
2	**0.38**	**3.39**	**1.58**	**333-335**
3	**0.22**	**3.955**	**1.773**	**335**
4	**0.47**	**3.745**	**1.723**	**335**
5	**0.11**	**4.637**	**2**	**335**
6	0.53*	3.811	1.811	343
7	0.06	4.50	2.333	= 296- 306= 338
8	0.39	3.333	1.872	=350-351
9	**0.03**	**10**	**2.667**	**335**
10	0.1	5.10	1.70	=340-354
11	0.15	13.933	4.667	322
12	0.16	5.188	2.438	327
13	0.66	8.485	3.182	342
14	0.06	12.33	4.33	348
15	0.38	4.132	1.579	340
16	0.42	3.048	1.738	333
17	1.82	3.028	1.643	343
18	5.5*	3.709	1.735	338
19	0.65	5.539	2.431	322

It can be noticed that eastern catchments have similar low flow (catchment number: 1-5) behavior conversely to western catchments (catchment number: 14-18) where the minimum flow is experienced at the very tail of the curves. The formers have flatter slopes which denote (see Figure 3) the presence of ground water storage able to balance flow especially during summer periods while the latter (see Figure 4) have steeper slopes which reveal that flows are highly from direct runoff. A flat slope at the very lower end reveals, in general, a large amount of storage while a steep slope indicates a negligible amount.

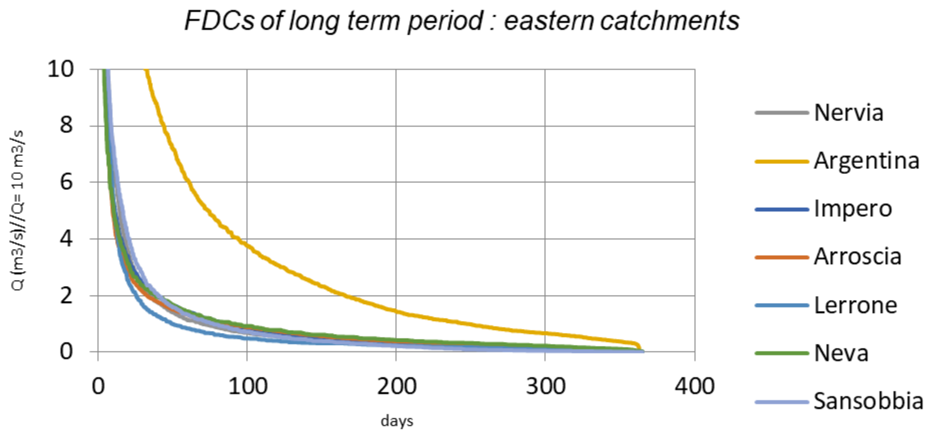

Figure 3 - FDCs extract: eastern catchments respect city of Genova.

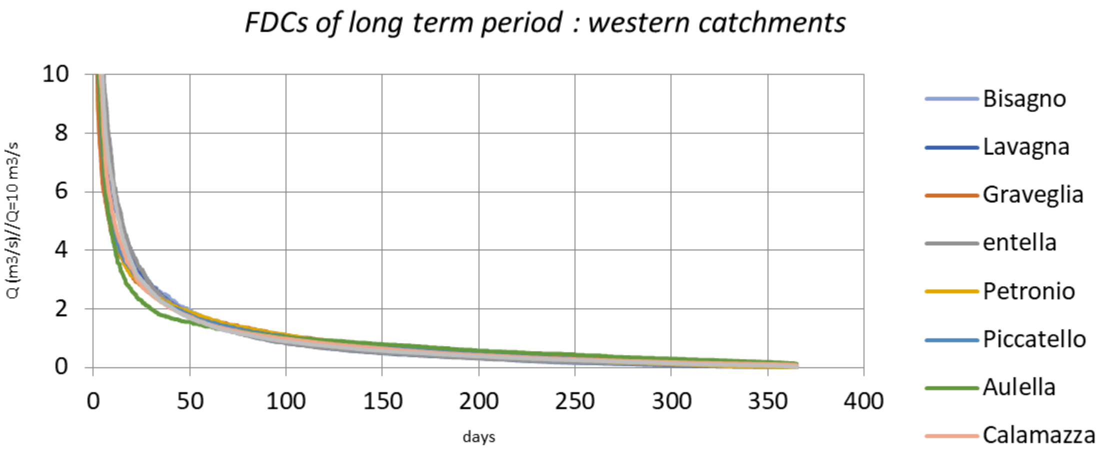

Figure 4 - FDCs extract: western catchments respect city of Genova.

Table 3 reports: maximum, mean and minimum average monthly flow for three selected catchments groups during the period of study which comprehends: 1951-1971. Values are expressed in m^3/s. Roya is the unique catchment intensively fed by snow precipitation while Argentina and Petronio are sorted examples of eastern and western catchments.

Table 3 - Monthly averaged stream flows. Discharges expressed in m^3/s.

ROYA (1st group)											
J	***F***	***M***	***A***	***M***	***J***	***Jul***	***A***	***S***	***O***	***N***	***D***
21.93	26.51	37.41	43.62	33.18	28.95	13.30	12.03	18.11	51.53	84.40	46.96
10.93	11.23	14.50	18.64	19.97	16.19	9.66	7.32	7.16	10.16	16.74	13.13
7.24	7.49	8.90	11.50	13.74	10.98	7.14	5.76	5.26	5.38	6.43	7.86
ARGENTINA (sorted example in 2nd group of similar catchments)											
35.70	32.46	47.84	38.70	20.57	8.61	1.94	4.32	17.23	29.60	85.93	55.31
6.63	6.75	8.57	7.21	4.55	2.52	1.03	0.84	1.46	3.68	10.54	7.20
1.96	2.05	2.64	2.82	1.73	1.13	0.72	0.48	0.48	0.68	1.36	1.86
PETRONIO (sorted example in 3rd group of similar catchments)											
9.99	7.65	6.60	4.91	3.07	1.36	0.59	0.41	2.87	4.51	11.41	7.66
2.04	2.41	2.12	1.78	1.02	0.59	0.25	0.14	0.35	0.92	1.98	2.18
0.66	0.68	0.96	0.83	0.50	0.31	0.10	0.04	0.09	0.17	0.45	0.75

Figures 5 and 6 show monthly discharges values which express the hydrological regime of the catchments.

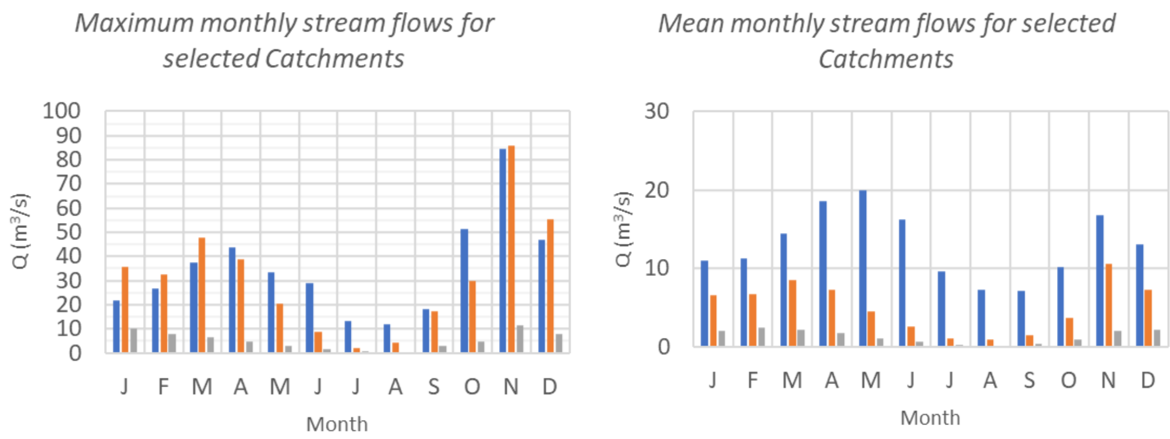

Figures 5 - Averaged monthly maximum (left) and mean (right) discharges for Roya, Argentina and Petronio.

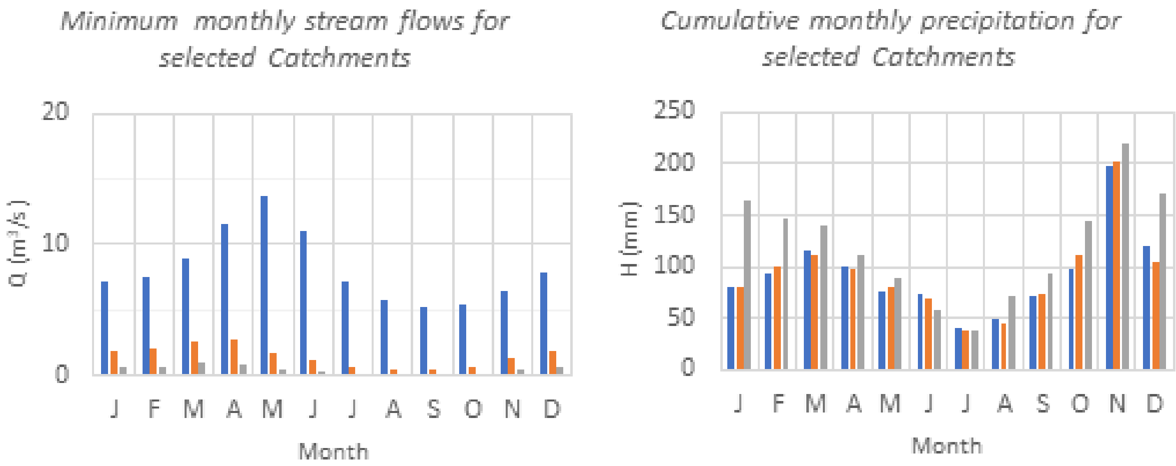

Figure 6 - Averaged monthly minimum discharges (left) and cumulative precipitations (right) for Roya, Argentina and Petronio.

Table 4 displays FDCs synthesized at *characteristic durations*. Q, average is evaluated summing all the observed stream flows for each catchment (record length's equal to 3650+) and dividing the result by the amount of data. Incidentally it must be noticed that the duration associated to Q, average is never known *a priori* but can be stated after its calculation, only. The curves are built according to the *total period* method which requires that all discharges are ranked according to their magnitude and values are, thereafter, sorted to set durations of 10, 30…274 and 355 days. This method is mostly transparent in terms of final curve construction.

The other procedure is known as *calendar year* method which consists in considering the discharges of each singular year ranked according to the magnitude. Subsequently, the discharges of each ordered number are averaged. Shortcoming of this method, although very practical and used also in *Annali Idrologici* is that the final averaged curve has the crest lowered (Q10—Q91) and the tail (Q274-Q355) lifted up. Final values may slightly differ from the more accurate values reported in the *total year's* procedure.

Table 4 - Streamflow data expressed in m^3/s and synthesized at characteristic durations.

Catchment's number	Q(10)	Q(30)	Q(60)	Q(91)	Q(135)	Q, average	Q(182)	Q(274)	Q(355)
1	36.30	25.10	18.90	15.50	11.90	13.14	9.83	6.90	4.61
2	12.20	5.03	3.49	2.60	1.77	2.51	1.29	0.60	0.21
3	19.60	6.41	3.12	2.07	1.38	2.77	0.87	0.39	0.16
4	31.3	11.20	6.18	4.08	2.73	4.98	1.73	0.81	0.36
5	8.09	3.64	2.12	1.42	0.87	1.49	0.53	0.22	0.07
6	21.80	9.60	6	4.37	2.93	4.50	1.99	0.96	0.32
7	5.47	1.65	0.84	0.55	0.35	0.83	0.27	0.15	0.03
8	14	6.27	3.88	2.69	1.30	2.68	1.30	0.73	0.29
9	7.72	2.82	1.41	0.86	0.5	1.06	0.30	0.08	0.5
10	8.04	3.75	2.19	1.29	0.81	1.34	0.51	0.17	0.08
11	35	16	8.32	5.30	3.21	5.66	2.09	0.70	0.07
12	6.73	3.76	2.46	1.77	1.24	1.49	0.83	0.39	0.10
13	103	42.30	22.20	14.10	8.60	15.21	5.60	2.10	0.40
14	6.60	3.43	2.27	1.62	1.09	1.36	0.74	0.26	0.02
15	12.9	7.03	4.37	3.18	2.30	2.79	1.57	0.6	0.31
16	11.7	5.53	3.38	2.46	1.80	2.31	1.28	0.73	0.31
17	37.50	17.7	11.7	9.12	7.05	8.24	5.50	2.85	1.39
18	221	105	61.9	44.6	30.9	42.03	20.4	9.54	4.46
19	52.20	21.3	12	8.04	5.34	8.25	3.60	1.58	0.44

These data, for all catchments, confirm that monthly average stream flows approximately related to Q91 are higher than the corresponding median value Q182 of reference. This is always true for highly skewed data as daily stream flows is much emphasized in case of river of torrential regime whereas the floods squeeze the average value toward shorter days.

Therefore, having the average value toward high flood (Q91) identifies all the Ligurian catchments being typical of torrential regime and differences consist in catchments sizes, slopes, and precipitations patterns.

Figure 7 show the average FDCs built according to the *calendar year* method.

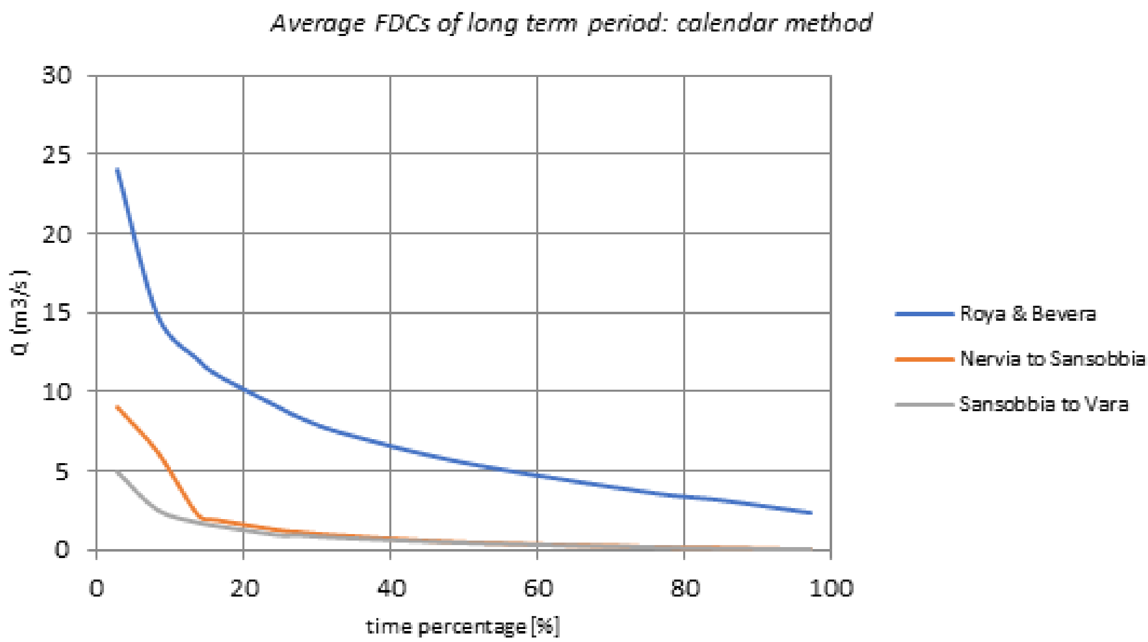

Figure 7 - FDCs represented in long term period and later synthesized at characteristic durations

4. RESULTS AND COMMENTS

The information detected from FDCs is more complete in respect to the one corresponding to only streamflow data. FDCs not only provide information about water availability but also about percentage in time such resource is present or generally exceeded either in a singular year, namely, *immediate hydrological scenario*, or in a long-term year of reference, namely, *general hydrological scenario*. As a matter of fact, in practical circumstances comparing a generic withdrawal to the available mean streamflow has very poor strength in terms of water quality and quantity defense of the river body since it is not known *a priori* the duration in a year (either short or long year of reference) associated to such value and furthermore, it is not guaranteed that the streamflow record is thereafter depleted accordingly to the streamflow withdrawn. Although FDCs disregard temporal sequence upon observations the hypothesis that high flow values are independent while low flows are more likely to be strongly timely correlated among themselves is supported by the results. The tails of the curves (from Q335 up to Q365) show that a generic low flow into this last interval is generally followed by a subsequent low flow observed the day after or two days after and all values (into the interval Q335 to Q365) belong to the driest month of the year. (see 'Table 2' highlighted values). The authors suggest the use of Q335 as a proper minimum EF useful to design fish passages and other biological requests. Additional increases initial EF of 10% up to 20% can be added thus introducing a hydrological modulation along the year to better comply the variation of needs. The benefit of the procedure is the detection of a specific duration (335 days/year) whose corresponding streamflow datum, namely Q335, becomes the keystone between non temporal consequential flows (Q1-Q335) to very likely consequential flows (Q335-Q365). Such a value enables a better estimation of EF respect the one achieved using pre-defined formulas based upon catchment's overall: area, precipitation and slope.

5. CONCLUSIONS

The study considers the analysis on low flow values for FDCs of long-term period built for 19 catchments under study. The paper is able to provide mean streamflow value estimation for rivers of intermittent and torrential regime having such a value roughly sitting on the Q91 or, in other words, the discharge available almost three months a year (not necessarily 91 consecutive days). A particular focus on the tail of the curve is also provided through the evaluation of shape factors: Q182/Q335 and Q274/Q335 of FDCs. Still, the novelty of the research is that five catchments have the Q335 of long-term period exactly coincident with the average value of minimum flow observed in the driest month of the year. For almost all the catchments the tail of FDCs is represented by likely consecutive observations and in particular the first five nearby catchments represent a unique hydrographic singularity which have similar minimum precipitation pattern and similar minimum catchments responses. This study is a primary and useful example of temporal information on low flows in FDCs.

REFERENCES

Annali Idrologici (1951,1971), *Ministero dei Lavori Pubblici, Servizio Idrografico Sezione autonoma del Genio Civile con sede di Genova, Bacini con foce nel litorale tirrenico dal Roya al Magra,* Roma.

Castellarin A., Vogel R.M., Brath A., (2004a), *A stochastic index flow model of flow duration curves*, Water resources research, 40 (3), pp. 1-10.

Castellarin A., Galeati G., Brandimarte L., Montanari A., Brath A., (2004), *Regional Flow duration curves:* Reliability for ungauged basins, Journal of Hydrology 27, pp 953-965.

Claps P. Fiorentino M., (1997), *Probabilistic flow duration curves for use in environmental planning and management*, NATO-ASI seies, pp. 255-266

LeBoutillier D.V., Waylen P.R., (1993*), A stochastic model of flow duration curves*, Water Resource s Research, 29(10) pp. 3535-3541.

Searcy James K., (1959), *Flow duration curves, Manual of Hydrology: Part 2 Low Flow Tecniques,* Geologica Survey Water Supply Paper, United States Government Printing Offiuce, pp. 1-33.

Verma R. K., Murthy S. (2017), *Design flow duration curves for environmental flow estimation in Damodor River Basin India,* Applied Water Science*,* pp. 283-293.

8th International Junior Researcher and Engineer Workshop
on Hydraulic Structures
ISBN: 978-0-578-37416-1
https://doi.org/10.26077/996a-823d

Galway, Ireland,
5th - 8th July 2021

Calibration of a Hydraulic Model for Seasonal Flooding in a Lowland River with Natural Diversions and Bathymetric Uncertainty, for Dam Downstream Impact Assessment

Getachew E. Mamo[1], Davide Motta[1] and Martin Crapper [1]
[1]Department of Mechanical and Construction Engineering
Northumbria University
Newcastle upon Tyne, NE1 8ST
UNITED KINGDOM
E-mail: g.mamo@northumbria.ac.uk

Abstract: *A method is developed to generate bank-full river main channel geometry, to complement an open-source Digital Elevation Model (DEM) and produce a calibrated hydraulic model reproducing the extent of historically observed overbank flooding. This approach relies on limited surveyed cross section and flow rate information and is potentially suitable for projects in developing countries where the availability of measured data is limited. The method presented is applied to the case of the seasonal flooding of the Baro River in the Gambela floodplain in Ethiopia, modelled with a two-dimensional hydraulic model. The simulated flooding extent for the 1990 wet season is compared with the observed flooding from 1990 satellite imagery and the expected flow interaction patterns with the near Alwero River, showing good agreement. The calibrated model is also used to show the impact of the planned TAMS hydropower dam on the Baro River flooding.*

Keywords: *dams, downstream impact, river bathymetry, seasonal flooding, hydraulic modelling, remote sensing.*

1. INTRODUCTION

Dams are instream structures providing a wide range of services, including energy supply, drought and flood hazard mitigation, water supply, and recreation services (Graf, 1999, Bednarek, 2001, Biswas, 2012, Ansar et al., 2014). In particular, the importance of dams cannot be understated for developing countries (IRENA, 2020), where dam construction is expected to increase in the future to mitigate uneven distribution of fresh water in space and time (ICOLD, 2019) and to support economic and social development (Biswas, 2012).

On the other hand, the construction and operation of dams can cause different hydrological, social, economic, environmental, geomorphological and ecological impacts (Power et al., 1996, Magilligan and Nislow, 2005, Merritt and Wohl, 2006, Poff and Zimmerman, 2010, Marcinkowski and Grygoruk, 2017, Bejarano et al., 2019). Focusing on the area downstream of a dam, the hydrological impact, that is, the change, caused by the dam presence and operation, of the patterns of flooding magnitude, extent and duration, drives all the other types of impact (e.g., decrease in overbank flooding reduces wetland recharge). Energy production maximization while minimizing the negative downstream impact is the main evaluation principle in a hydropower dam project feasibility study; therefore, quantifying the dam downstream impact, particularly the hydrological impact, is crucial for hydropower project decision makers.

Numerical hydraulic models are keys to understand the hydrodynamics of a river system and its flooding patterns, before and after dam construction, to quantify and map the hydrological impact. On the other hand, model input uncertainties affect the accuracy of hydraulic models (Merwade et al., 2008, Bales and Wagner, 2009), and consequently affect the accuracy of the overbank flooding prediction. The availability of open-source Digital Elevation Models (DEMs) from remote sensing is crucial when developing hydraulic models for dam projects located in developing countries, where most of the hydropower projects are currently being designed and built. However, such DEMs do not contain accurate elevation information for the underwater river main channel. Typically, river main channel bathymetric information is collected by conducting topo-bathymetric surveys, and this information complements the elevation information from a DEM for the overbank areas. However, river bathymetry data collection is often expensive and time-consuming (Bures et al., 2019, Chénier et al., 2018) and, within specific projects in certain remote areas and with budget constraints, simply unfeasible.

Different methods have been proposed to estimate river bathymetry (longitudinal slope and cross-section geometry), based on different sources and techniques and the amount of information available. Some authors investigated the use of satellite images, such as assimilation of synthetic Surface Water and Ocean Topography (SWOT) water surface elevation to determine the channel depth and calibrate the roughness coefficient (Yoon et al., 2012, Häfliger et al., 2019) or the use of band ratio and multi-band models to extract satellite driven bathymetry from high-resolution satellite images (Chénier et al., 2018). These approaches, though promising, are still characterized by uncertainty, especially in absence of survey data for verification. Hostache et al. (2015) used a particle filter assimilation algorithm to extract the river bathymetry from GPS-equipped buoys, reporting a Root Mean Square Error (RMSE) of 36 cm; however, the study did not consider the effect of abrupt changes of topography in bathymetric estimation. Domeneghetti (2016) used a channel bank-full depth and slope break approach to generate the 140 km Po River (Italy) reach bathymetry from a 90m Shuttle Radar Topography Mission (SRTM) DEM, using linear statistical relationships to estimate both bank-full discharge and slope breaks from drainage area-bank-full depth and flow width-water surface elevation relationships, respectively. However, this method is not replicable for areas where there is not enough gauge station data to establish statistical relationship between channel bank-full discharge and drainage area as well as in the case of absence of high-resolution satellite data to establish flow width and water surface elevation. Caviedes-Voullième et al. (2014) proposed an algorithm to generate cross sections from 25 field surveyed cross sections and a 1m resolution LiDAR-based DEM available for the floodplain. Though the proposed algorithm is promising, the inconsistencies between DEM and the interpolated riverbed produced using the algorithm challenge its applicability. Bures et al. (2019) developed a mathematical model to represent the bathymetry of the Otava River (Czech Republic), with parameters estimated from 375 measured cross sections along the 1.75 km Otava River. Though the bank-full discharge is one of the most critical parameters in river bathymetry estimation, the study failed to consider the bank-full discharge and used instant Otava River flow as design discharge. The approach needs a significant amount of surveyed data to estimate the parameters of the model.

This paper presents and applies a method to calibrate a hydraulic model for flooding prediction that combines an open-source DEM and a procedure for bank-full cross-section geometry generation. The streamwise variation of the cross-sectionally-averaged depth is based on bank-full discharge estimation from stream gauge flow data, river width digitization from aerial imagery, streamwise river slope estimation from the DEM and uniform-flow calculations with friction coefficient determined from limited surveyed cross-section geometry, river photos and (Jarrett, 1985)'s method. The reconstructed main river bathymetry is then used to modify the available DEM within the river main channel region, to conduct two-dimensional (2D) hydrodynamics simulations. The reconstructed bathymetry is opportunely adjusted (calibrated) against historically observed river flooding extent. An application is presented for the Baro River in southwest Ethiopia, characterized by seasonal flooding (we focus here on the wet season) and complex overbank flow patterns in a lowland are where the absence of a clearly defined drainage divide in the left overbank area leads to water exchange between Baro River and Alwero River systems (natural river “diversions”).

2. MATERIALS AND METHODS

2.1. The study area

The Baro River in southwest Ethiopia is part of the Baro-Akobo river basin system, which contributes to the flow of the Sobat River, which in turn provides 48% of the White Nile flow (Wood et al., 2016). Except for the Baro River and the Alwero River, which joins the Baro River downstream of the Ethiopia-South Sudan border, all the other major rivers in the Baro-Akobo system, notably the Akobo River and the Gilo River, join the Pibor River, which is a tributary of the Sobat River.

Figure 1 shows the 29256 km^2 catchment of the Baro River, upstream of its confluence with the Alwero River. Figure 1 also shows the Baro River catchment location within the larger River Nile catchment.

While the upper part of the Baro River catchment is mountainous and forested, in the lower part of the catchment, starting from approximately 45 km downstream of the planned TAMS dam location, the river flows through lowland areas with meandering patterns. The Baro River right overbank area is relatively well constrained. On the contrary, the left overbank area is characterized by complex flooding patterns, also due to the vicinity of the Alwero and Adura rivers with the absence of a well-defined drainage divide, resulting in the natural water transfer (natural "diversions") between catchments during the wet season.

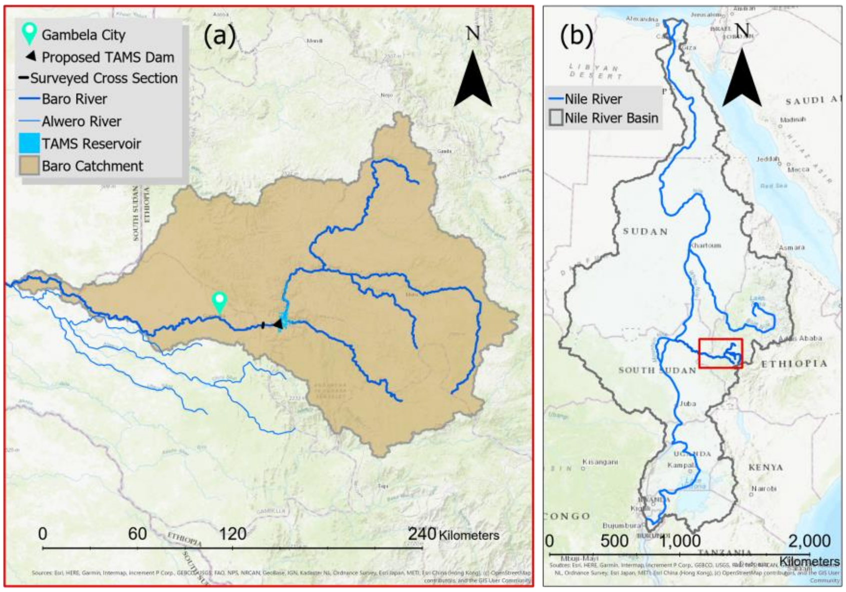

Figure 1 – (a) Baro River catchment and (b) its location within the Nile River catchment.

The weather in the Baro River region is significantly affected by tropical monsoons from the Indian Ocean; as a result, there is abundant rainfall during the wet season (May/early June to September/early October) and low precipitation in the dry season (December to April). The region presents a wide variety of ecosystems, such as wetlands, and activities such as navigation and recreation (Gambela National Park) (Wood et al., 2016). The average annual flow (1928-2009) of the Baro River, as measured at the stream gauge at Gambela (Figure 1) is 395 m^3/s, a value equalled or exceeded 39% of the year.

A number of hydropower and irrigation projects are either constructed or planned on the Baro-Akobo basin (Sileet et al., 2013). Notably, the hydropower TAMS dam (Figure 1) is planned for construction on the Baro River around 45 km upstream of Gambela. The dam height is 248 m, with a top-of-dam elevation of 730 m a.s.l. and length of 1335 m. The maximum and minimum pool elevations are 726 and 625 m a.s.l., respectively. The total storage capacity is estimated as 5868 Mm^3. The expected hydropower output is 2000 MW (≈ 5.5 GWh/year), provided by eight turbines. In addition to hydropower generation, the dam is planned to provide irrigation water during the dry season to the fertile Gambela floodplain.

2.2. The hydraulic model

The Hydrologic Engineering Center's River Analysis System (HEC-RAS) (Brunner, 2021) was used to develop a two-dimensional (2D) HEC-RAS hydraulic model (based on volume and energy conservation principles) for a longitudinal section of the Baro River stretching from the site of the planned construction of the TAMS hydropower dam to the Baro-Alwero river confluence, located about 243 km further downstream. This long reach of the Baro River was considered to model the area that will be affected by the construction of the TAMS dam, through overall flooding reduction, downstream of Gambela, and to capture the water exchange between Baro River and Alwero River catchments. The use of a 2D numerical modelling approach, instead of 1D, is important for the Baro River, characterised by overbank flooding during the wet season and complex flow patterns, especially in the lowland areas.

The freely available Shuttle Radar Topography Mission (SRTM) 30m DEM from the U.S. Geological Survey (USGS) was used as input for the model. A two-dimensional computational mesh, made of 100 m X 100 m computational elements, was used for the simulations. The finite volume solution scheme implemented by the HEC-RAS 2D modelling has the capability to use unstructured computational cells that may occur at the border of the computational domain. The default iterations number (20) for solution was used for each computational time step in the model setup. Breaklines were traced along both banks of the Baro River to capture the width variation of the river and refine the computational mesh in the river main channel area.

2.3. Estimation of bank-full discharge

Observed river flows (discharge at daily interval) in the Baro River flow are available at a stream gauge at Gambela for a period of 82 years, from 1928 to 2009, obtained from the Ethiopian National Meteorological Agency (NMA) and the Ministry of Water, Irrigation and Electricity (MoWIE) (ELC, 2017). A single, surveyed cross section is also available (Figure 2a), located about 5 km downstream of the proposed TAMS dam at Bonga (ELC, 2017). The measured river flow at Gambela was “transferred” to the measured cross section location using the drainage area ratio method (Williams, 1986, Emerson, 2005)

$$Q_U = Q_N * (A_U/A_N)^k \tag{1}$$

where Q_U is the unknown flow at the location of the surveyed cross section (m^3/s), Q_N is the known flow at Gambela (m^3/s), A_U is the catchment area at the location of the surveyed cross section (km^2), A_N is the catchment area at Gambela (km^2) and k = 0.82 is a region-specific exponent obtained from the analysis of 13 gauging stations located in the Baro River catchment upstream and downstream of the planned TAMS dam (ELC, 2017). Based on the flow rate time series generated at the measured cross section location, the bank-full discharge was estimated using flood frequency analysis techniques, as the value corresponding to a return period of two years, obtaining a value of 1179 m^3/s.

2.4. Reconstruction of the river main channel depth

As mentioned, a single Baro River cross section was surveyed by (ELC, 2017) 5 km downstream from the proposed TAMS dam location using an echo sounder Ohmex SonarLite (Figure 2a). This cross section was taken as reference to reconstruct the river main channel cross section, not provided by remote sensing techniques, at different locations (cross sections) in five different sub-reaches of the Baro River, each characterized by an average slope obtained from the available SRTM 30m DEM (Figure 2b).

At different locations along the Baro River, the bank-full discharge was estimated using Eq. (1) and the known value of bank-full discharge at the location of the surveyed cross section. For each of the five sub-reaches, a roughness Manning’s coefficient was assigned based on Manning’s values estimated for uniform flow based on the only surveyed cross section, literature values based on the river characteristics (Chow, 1959), or Jarrett (1985)’s equation. The latter equation was used for bed gradient higher than 0.002, as follows

$$n = 0.39 * S_b^{0.38} * R^{-0.16} \tag{2}$$

where S_b (ft/ft) is the riverbed slope and R *(ft)* is the hydraulic radius of the stream.

The width of the channel was estimated at each cross section considered along the River Baro from the DEM and satellite imagery. Finally, knowing riverbed slope, channel width, Manning's coefficient, and bank-full discharge, the reconstructed bank-full depth was computed for each cross section considered along the river reach. The river channel was assumed to be rectangular, because the channel carrying capacity is of interest here, more than the bathymetry-driven flow properties gradients within a given cross section. Additional interpolated scaled cross sections were generated to increase the number of cross sections (Caviedes-Voullième et al., 2014). From the reconstructed cross sections, a new terrain GeoTIFF was created in HEC-RAS Mapper and merged with the original terrain DEM to carry out the 2D simulations.

2.5. Model calibration

The inevitable uncertainty associated to the Manning's coefficient estimation, reflecting upon the river main channel bathymetry reconstruction, was finally mitigated by adjusting the resulting bathymetry from the steps described in sections 2.2 and 2.3 in a few sub-reaches. This was done by trial and error, to calibrate the simulated maximum flooded area against the historically observed flooded area for the flood event considered (in this case, the 1990 wet season). In this sense, the bathymetry produced, specifically the bank-full depth along the Baro River, was used as a calibration parameter for the hydraulic model to match the inundation maximum extent extracted from the Landsat 5 satellite imagery dated 4th October 1990.

3. RESULTS AND DISCUSSION

Five different sub-reaches of the Baro River were identified, each characterized by an average slope obtained from the available SRTM 30m DEM, ranging from 0.0001 m/m at the downstream end, towards the Baro-Alwero confluence, to 0.003 m/m upstream, at the TAMS dam location (Figure 2b). The dotted lines in Figure 2b are the linear best fit curves, and the points represent the minimum elevation of the cross section in the main channel. Using the procedures and inputs discussed above, the reach-wise Baro river main channel roughness coefficient was estimated, obtaining values in the range 0.024-0.053. The calculated Manning's coefficients were compared with typical Manning's coefficient values (0.025-0.06) suggested in the literature (Chow, 1959) for similar streams and showed good agreement.

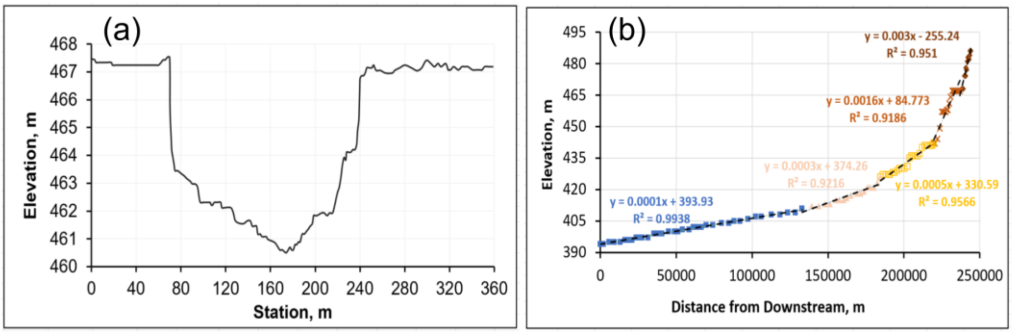

Figure 2 – (a) Surveyed cross section in the Baro River (ELC, 2017) and (b) Baro River bed profile.

As mentioned, the 1990 wet season was considered for our simulations. The 1990 wet season was the one characterised by the largest flows in the period 1928-2009. Our procedure was calibrated against satellite imagery from Landsat 5, dated 4th October 1990, from which the maximum extent of the flooded area was digitized, for comparison with the modelled maximum flooding extent.

Figure 3 shows a good agreement between modelled and observed maximum flooded areas. The figure focuses on the area downstream of Gambela In the right overbank area, the extent of flooding is relatively constrained by the floodplain topography, which is what is observed from the historical satellite imagery (Figure 3a). In the left overbank area, the absence of a drainage divides between Baro and Alwero causes water from the Baro River to flow into the Alwero system (Figure 3b). This is confirmed by the feasibility study conducted by Selkhozpromexport (1990), describing the area as "partially impounded" for large, low frequency, flood events, such as the one considered in this analysis, therefore suggesting communication between the different river systems in the lowlands downstream of Gambela.

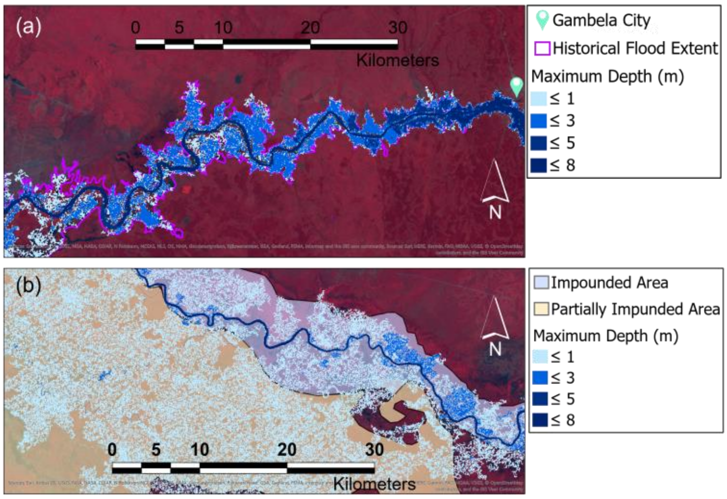

Figure 3 - Baro River 1990 flood extent in the Gambela floodplain. (a) Comparison of historically observed maximum flooded area from Landsat 5 imagery vs simulated flooded area downstream of Gambela and (b) Flooding in the left overbank downstream of Gambela, associated with Baro-Alwero water exchange.

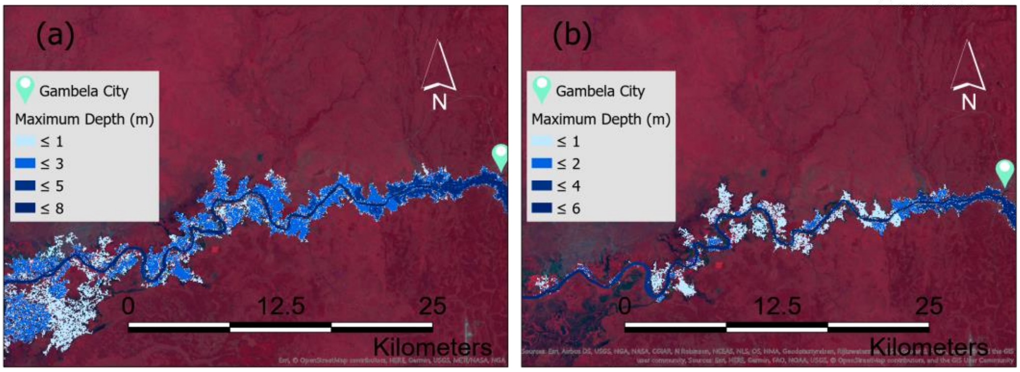

Figure 4 – Maximum flood extent comparison (a) without and (b) with the TAMS dam for the 1990 wet season.

Once a calibrated model is produced for the river in absence of dam, different TAMS dam operation scenarios (involving the opening/closing of spillways, bottom outlets, turbines) can be evaluated to model their impact on the downstream flooding (downstream dam hydrological impact). To illustrate this, the scenario with three spillways working simultaneously was considered here. The outflow hydrograph from the dam, developed using level pool routing techniques, was used as input hydrograph for the 2D model to simulate downstream flooding in presence of the dam. The peak flow rate from the dam decreased by 55% compared to the natural hydrograph in absence of dam and Figure 4 shows the resulting maximum flood extent comparison without or with dam for the reference 1990 wet season. As expected, the presence of the dam reduces the overbank flooded area, possibly having a negative ecological impact on wetlands along the Baro River; it also stops the water transfer from the Baro to the Alwero river system, at least for the protocol of dam operation considered here.

4. CONCLUSIONS

The method presented in this paper to reconstruct river main channel bathymetry uses limited data and considers bank-full depth as a calibration parameter for a hydraulic model simulating river flooding. The method was applied to the modelling of the seasonal flooding of the Baro River in the Gambela floodplain in Ethiopia, in lowlands characterised by multiple river systems and complex flow patterns including natural river diversions. The approach was shown to be able to capture the conveyance of the main channel, which is key to reproduce historically observed flooding extent. The agreement between simulated and observed maximum inundation area is satisfactory especially in the area immediately downstream of Gambela (Figure 3a); further downstream the agreement remains visually good, and deviations are explained by observing that the historical inundation extent was digitized from satellite imagery as a single polygon (in reality high ground areas exist, therefore not all areas inside the polygon will be flooded) and that some flooding downstream of Gambela is also due to sheet flow from the right side of the river (not captured by the model).

The hydraulic model produced in this study will be used to quantify and map the hydrological impact of the TAMS dam construction and operation and the consequent impact on the downstream wetlands and recession agriculture and fishing activities, all relying on the seasonal overbank flooding of the Baro River. A preliminary simulation of the impact of the dam on the downstream flooding extent has shown a significant reduction of the maximum inundation area (Figure 4b), with most of the flow contained within the main channel and generally lower main channel flow depths (30% less), compared with the scenario without dam.

5. ACKNOWLEDGEMENTS

This work was conducted in collaboration with ELC Electroconsult S.p.A. (Italy). Their support and data provision are greatly appreciated.

6. REFERENCES

Ansar, A., Flyvbjerg, B., Budzier, A. & Lunn, D. (2014). *Should we build more large dams? The actual costs of hydropower megaproject development*. Energy Policy 69, 43-56.

Bales, J. D. & Wagner, C. R. (2009). *Sources of uncertainty in flood inundation maps*. J. Flood Risk Manag. 2(2), 139-147.

Bednarek, A. T. (2001). *Undamming rivers: a review of the ecological impacts of dam removal*. Environ Manage 27(6), 803-14.

Bejarano, M. D., Sordo-Ward, A., Gabriel-Martin, I. & Garrote, L. (2019). *Tradeoff between economic and environmental costs and benefits of hydropower production at run-of-river-diversion schemes under different environmental flows scenarios*. J. Hydrol. 572, 790-804.

Biswas, A. K. (2012). *Impacts of large dams: Issues, opportunities and constraints. In Impacts of large dams: A global assessment*.) Springer, pp. 1-18.

Brunner, G. W. (2021). *HEC-RAS River Analysis System 2D User's Manual. Version 6.0.* US *Army Corps of Engineers - Hydrologic Engineering Center: Davis, CA, USA, 2016. Available online:* https://www.hec.usace.army.mil/confluence/rasdocs/r2dum/latest. (accessed on 15 May 2021).

Bures, L., Sychova, P., Maca, P., Roub, R. & Marval, S. (2019). *River Bathymetry Model Based on Floodplain Topography*. Water 11(6), 1287.

Caviedes-Voullième, D., Morales-Hernández, M., López-Marijuan, I. & García-Navarro, P. (2014). *Reconstruction of 2D river beds by appropriate interpolation of 1D cross-sectional information for flood simulation*. Environ Model Softw 61, 206-228.

Chénier, R., Faucher, M.-A. & Ahola, R. (2018). *Satellite-derived bathymetry for improving Canadian Hydrographic Service charts*. ISPRS International Journal of Geo-Information 7(8), 306.

Chow, V. T. (1959). *Open-channel hydraulics.* McGraw-Hill Book Company, Inc.

Domeneghetti, A. (2016). *On the use of SRTM and altimetry data for flood modeling in data-sparse regions*. Water Resour. Res. 52(4),2901-2918.

ELC (2017). *Hydrology-Volume-2. Prefeasibility and Feasibility Study of TAMS Hydropower Project in Gambela Region. Doc. No. 1745-E-3-R-GE-0002-02.* ELC Electroconsult, Milan, Italy.

Emerson, D. G., Vecchia A. V. And Dahl A. L. (2005). *Evaluation of Drainage-Area Ratio Method Used to Estimate Streamflow for the Red River of the North Basin, North Dakota and Minnesota*.

Graf, W. L. (1999). Dam nation: *A geographic census of American dams and their large-scale hydrologic impacts*. Water Resour. Res. 35(4), 1305-1311.

Häfliger, V., Martin, E., Boone, A., Ricci, S. & Biancamaria, S. (2019). *Assimilation of synthetic SWOT river depths in a regional hydrometeorological model*. Water 11(1), 78.

Hostache, R., Matgen, P., Giustarini, L., Teferle, F. N., Tailliez, C., Iffly, J. F. & Corato, G. (2015). *A drifting GPS buoy for retrieving effective riverbed bathymetry*. J. Hydrol. 520,3 97-406.

ICOLD (2019). *International Commission on Large Dams. Position Paper Dams and Environment. https://www.icold-cigb.org/userfiles/files/DAMS/Position_paper.pdf.* Accessed no April-26, 2020.

IRENA (2020). *Global Renewables Outlook: Energy transformation 2050 (Edition: 2020), International Renewable Energy Agency, Abu Dhabi. ISBN 978-92-9260-238-3*.

Jarrett, R. D. (1985). *Determination of roughness coefficients for streams in Colorado (Vol. 85, No. 4004).* US Department of the Interior, Geological Survey.

Magilligan, F. J. & Nislow, K. H. (2005). *Changes in hydrologic regime by dams*. Geomorphology 71(1-2), 61-78.

Marcinkowski, P. & Grygoruk, M. (2017). *Long-term downstream effects of a dam on a lowland river flow regime*: Case study of the Upper Narew. *Water* 9(10), 783.

Merritt, D. M. & Wohl, E. E. (2006). *Plant dispersal along rivers fragmented by dams*. River Res Appl 22(1), 1-26.

Merwade, V., Olivera, F., Arabi, M. & Edleman, S. (2008). *Uncertainty in Flood Inundation Mapping: Current Issues and Future Directions*. J. Hydrol. Eng. 13(7),608-620.

Poff, N. L. & Zimmerman, J. K. H. (2010). *Ecological responses to altered flow regimes: a literature review to inform the science and management of environmental flows*. Freshw. Biol. 55(1), 194-205.

Power, M. E., Dietrich, W. E. & Finlay, J. C. (1996). *Dams and Downstream Aquatic Biodiversity: Potential Food Web Consequences of Hydrologic and Geomorphic Change*. Environ. Manage. 20(6), 887-95.

Selkhozpromexport (1990). *Baro-Akobo basin master plan study of water & land resources of the gambela plain final report. Vol III Climatology and Hydrology. Soyuzgiprovodkhoz Institute USSR, Moscow*.

Sileet, T. M., M. El Shamy, Aty, M. A. & Sharaky, A. M. (2013). *The Development of the Baro-Akobo-Sobat sub basin and its Impact on Downstream Nile Basin Countries*. Nile Water Sci. Eng. 6(2), 38-53.

Williams, G. P. (1986). *River Meanders and Channel Size*. J. Hydrol. 88, 14-164.

Wood, A., Sutcliffe, J. P. & Dixon, A. (2016). *Baro-Akobo River Basin Wetlands: Livelihoods and Sustainable Regional Land Management (Ethiopia)*. In The Wetland Book, pp. 1-8.

Yoon, Y., Durand, M., Merry, C. J., Clark, E. A., Andreadis, K. M. & Alsdorf, D. E. (2012). *Estimating river bathymetry from data assimilation of synthetic SWOT measurements*. J. Hydrol. 464-465, 363-375.

8th International Junior Researcher and Engineer Workshop on Hydraulic Structures
ISBN: 978-0-578-37416-1
https://doi.org/10.26077/6f4d-62c1

Galway, Ireland,
5th - 8th June 2021

Effect of Boundary-Layer Development on the Water-Surface Fluctuations of Supercritical Flow below a Sluice Gate

R. Satoh[1], M. Takahashi[1] and I. Ohtsu[2]
[1]Department of Civil Engineering
Nihon University, College of Science and Technology
Tokyo
JAPAN
[2] Nihon University
Tokyo
JAPAN
E-mail: satou.ryugen@nihon-u.ac.jp

Abstract: *Hydraulic structures with a sluice gate are commonly used for control of the flow. In supercritical flow below a sluice gate, an accurate estimation of the water depth and boundary layer thickness is important for the hydraulic design of a horizontal apron. The relation between water-surface fluctuations and boundary-layer development has not been clarified. The aim of this paper is to experimentally demonstrate the effect of boundary-layer development on water-surface fluctuations of supercritical flow below a sluice gate. It is shown that water surface begins to fluctuate slightly upstream of the critical point. The water-surface fluctuations and turbulence intensities downstream of the critical point are also obtained, which demonstrates the length required for the water-surface fluctuations and turbulence intensity distributions to nearly equal uniform open-channel flow.*

Keywords: *Supercritical flow, boundary-layer development, water-surface fluctuations, turbulence intensity.*

1. INTRODUCTION

Hydraulic structures with a sluice gate are commonly used for control of the flow. For supercritical flow downstream of a sluice gate in a horizontal rectangular channel, the velocity distribution at the section of the vena contracta becomes almost constant (Ohtsu & Yasuda, 1994; Roth & Hager, 1999). A boundary layer develops from the vena contracta section and reaches the water surface. The point where the boundary layer reaches the water surface is known as the critical point. The supercritical flow between the section of the vena contracta and that of the critical point is referred to as the developing flow, as shown in Figure 1.

In the supercritical flow below a sluice gate, an accurate estimation of the water depth and the boundary-layer thickness is important for the hydraulic design of a horizontal apron because the location of the toe of a hydraulic jump is very sensitive to the supercritical flow depth. Recently, Takahashi & Ohtsu (2017; 2009) showed that the boundary-layer development and the water-surface fluctuations at the jump toe have important effects on the characteristics of air entrainment and the velocity fields in hydraulic jumps. Additionally, for a given Froude and Reynolds numbers, Takahashi & Ohtsu (2017) showed that the flow condition for the water surface in the supercritical flow depends on the boundary-layer development. Further study may be required to quantitatively clarify the relation between the water-surface fluctuations and the boundary-layer development of the supercritical flow below a sluice gate.

The aim of this paper is to experimentally demonstrate the effect of the boundary-layer development on the water-surface fluctuations of the supercritical flow below a sluice gate. A method for analytical calculation of the boundary-layer thickness and the supercritical flow depth is examined for the developing flow by using the presented data. Using high-speed video camera images and the measured values of the water-surface fluctuations, it is found that the water-surface fluctuations begin to occur in the developing flow region. The water-surface fluctuations and the turbulence intensities in the section downstream of the critical point are also obtained, determining the region where the distribution of the turbulence intensity is similar to that of uniform open-channel flow.

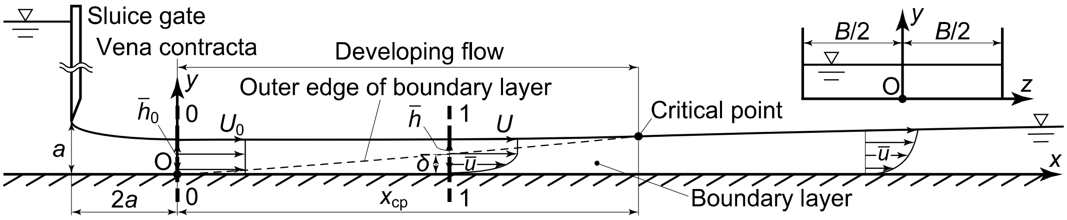

Figure 1 – Definition sketch for a supercritical flow below a sluice gate.

2. EXPERIMENTS AND EXPERIMENTAL SET-UP

The experiments were performed in a horizontal rectangular channel with channel width B = 0.40 m under Fr_0 = 8.0 and $Re = 7.2 \times 10^4$, where Fr_0 [$= U_0/(g\bar{h}_0)^{1/2}$] is the Froude number at the vena contracta section (section 0 in Figure 1), U_0 is the depth-averaged velocity at section 0, g is the acceleration due to gravity, $\bar{h}_0$ is the time-averaged depth at section 0, Re ($= \rho q/\mu$) is the Reynolds number, ρ is the water density, q is the water discharge per unit width, and μ is the dynamic water viscosity. The water was pumped from a basin to a constant head tank. The water discharge was controlled with a valve and that was measured with an accuracy of ±2% using a sharp-edged weir. The supercritical flow depth was controlled by a sluice gate which composed of a 4 mm thick stainless-steel plate with a sharp lower edge.

The instantaneous water depth h ($= \bar{h} + h'$) and the water-surface fluctuation $(\overline{h'^2})^{1/2}$ were obtained by using an ultrasonic water-level sensor (U.L.S.) of ±1% accuracy with a sampling frequency of 100 Hz and a sampling time of 200 s, where $\bar{h}$ is the time-averaged depth and h' is the fluctuating depth. This measurement was conducted 10 times for each section. It was confirmed that the values of the time-averaged depth determined by using the U.L.S. were equal to those obtained by using a point gauge with a reading accuracy of ±0.1 mm. Additionally, the experiments undertaken confirmed that the vena contracta section is located at a distance 2a downstream the sluice gate (Rajaratnam, 1977; Ohtsu & Yasuda, 1994; Roth & Hager, 1999; Castro-Orgaz & Hager, 2014) and $\bar{h}_0 = 0.64a$ (Rajaratnam, 1977; Ohtsu & Yasuda, 1994), where a is the gate opening. The flow conditions for the water-surface fluctuations were observed using a high-speed video camera recording at 1000 fps. To determine the velocity characteristics, the instantaneous velocity u ($= \bar{u} + u'$) was measured by using a one-dimensional laser Doppler velocimeter (L.D.V.), where $\bar{u}$ is the time-averaged velocity in the x-direction, u' is the fluctuating velocity in the x-direction, and x is the horizontal coordinate from the vena contracta. Data were collected at a frequency of up to 4 kHz for each point. The Doppler signals were processed with a sampling frequency of 25 Hz and a sampling time of 164 s. These measurements were carried out along the centerline of the channel (z = 0), where z is the coordinate of a cross section.

3. ANALYSIS OF WATER DEPTH AND BOUNDARY-LAYER THICKNESS

3.1. Developing flow

To show the methods used for analytical calculations of the time-averaged depth and the boundary-layer thickness, it is assumed that the flow is two dimensional and that the loss of energy outside the boundary layer is negligible. Bernoulli's equation for the streamline along the water surface between the vena contracta section (section 0 in Figure 1, x = 0) and the section of the developing flow region (section 1 in Figure 1, $x = x$) is expressed as

$$\frac{U_0^{\,2}}{2g} + \bar{h}_0 = \frac{U^2}{2g} + \bar{h} \tag{1}$$

where U is the velocity outside the boundary layer in the developing flow region. Using the dimensionless quantity J ($= U_0/U$), Eq. (1) can be written as (Ohtsu & Yasuda, 1994)

$$\frac{\bar{h}}{\bar{h}_0} = \frac{1}{2}Fr_0^{\,2}\left(1 - J^{-2}\right) + 1. \tag{2}$$

The continuity equation between sections 0 and 1 is written as

$$U_0\bar{h}_0 = U\left(\bar{h} - \delta_1\right) \tag{3}$$

where δ_1 is the displacement thickness, defined as

$$\delta_1 = \int_0^{\bar{h}} \left(1 - \frac{\bar{u}}{U}\right) \mathrm{d}y \tag{4}$$

where y is the vertical coordinate from the channel bed. If the velocity distribution for $\bar{u}$ in the boundary layer is approximated by a one-seventh power law, the relative velocity $\bar{u}/U$ can be expressed as

$$\bar{u}/U = (y/\delta)^{1/7} \quad \text{for} \quad 0 \le y \le \delta \tag{5}$$

where δ is the thickness of the boundary layer, and the velocity distribution $\bar{u}/U$ outside the boundary layer is constant:

$$\bar{u}/U = 1 \quad \text{for} \quad \delta \le y \le \bar{h}\,. \tag{6}$$

Using Eqs. (5) and (6), the displacement thickness δ_1 is written as

$$\delta_1 = \delta/8\,. \tag{7}$$

Or, equivalently,

$$\delta = 8\delta_1. \tag{8}$$

Substituting Eqs. (2) and (7) into Eq. (3), the relative boundary-layer thickness is expressed as (Ohtsu & Yasuda, 1994)

$$\frac{\delta}{\bar{h}_0} = 8\left[\frac{1}{2}Fr_0^{\,2}\left(1 - J^{-2}\right) + 1 - J\right]. \tag{9}$$

For the boundary layer in the open-channel flow, the momentum integral equation for two-dimensional flow can be expressed as

$$\frac{\mathrm{d}\delta_2}{\mathrm{d}x} + \frac{2\delta_2 + \delta_1}{U}\frac{\mathrm{d}U}{\mathrm{d}x} = \frac{C_\mathrm{f}}{2} \tag{10}$$

where δ_2 [$= \int_0^{\bar{h}}(1 - \bar{u}/U)(\bar{u}/U)\,\mathrm{d}y$] is the momentum thickness, C_f [$= \tau_0/(\rho U^2/2)$] is the local skin friction coefficient, and τ_0 is the shear stress on the channel bed. Using Eqs. (5) and (6), the momentum thickness δ_2 is written as

$$\delta_2 = 7\delta/72\,. \tag{11}$$

Substituting Eqs. (7), (9), and (11) into Eq. (10), the following equation is obtained as

$$\mathrm{d}x = \frac{2}{9C_\mathrm{f}}\left[-\frac{37U}{2g} + \frac{23}{U}\left(\frac{U_0^{\,2}}{2\mathrm{g}} + \bar{h}_0\right) - \frac{16U_0\bar{h}_0}{U^2}\right]\mathrm{d}U\,. \tag{12}$$

The local skin friction coefficient C_f may be expressed as that for a turbulent boundary layer along a smooth flat plate with a zero pressure gradient (Schlichting, 1979):

$$C_\mathrm{f} = 0.0592(\rho Ux/\mu)^{-1/5} \quad \text{for} \quad 3\times10^5 \le \rho Ux/\mu \le 1\times10^7. \tag{13}$$

After substituting Eq. (13) into Eq. (12) and integrating this with respect to x under the condition of the vena contracta section ($U = U_0$ at $x = 0$), the relative distance $x/\bar{h}_0$ is expressed as (Ohtsu & Yasuda, 1994)

$$\frac{x}{\bar{h}_0} = 194Re^{1/4}\left[\frac{37}{99}Fr_0^{\,2}\left(1 - J^{-11/5}\right) + \frac{23}{9}\left(2 + Fr_0^{\,2}\right)\left(J^{-1/5} - 1\right) - \frac{8}{9}\left(1 - J^{4/5}\right)\right]^{5/4}. \qquad (14)$$

Thus, for a given Fr_0 and Re, the water-surface profile of the developing flow is calculated by using Eqs. (2) and (14), and the boundary-layer development is calculated by using Eqs. (9) and (14). Furthermore, the value of the critical point x_{cp} is determined by using Eqs. (2), (9), and (14) under the condition at the critical point ($\bar{h}/\bar{h}_0 = \delta/\bar{h}_0$) for a given Fr_0 and Re.

3.2. Supercritical flow downstream of the critical point

In the section downstream of the critical point, the gradually varied flow equation in a horizontal rectangular channel is expressed as

$$\frac{\mathrm{d}\bar{h}}{\mathrm{d}x} = \left(-\frac{f}{4}\frac{1}{R}\frac{V^2}{2g}\right)\bigg/\left(1 - \frac{\alpha BQ^2}{gA^3}\right) \qquad (15)$$

where f is the skin friction coefficient, R is the hydraulic radius, V is the depth-averaged velocity, Q is the discharge, A is the cross-sectional area, and $\alpha\left[= \int_0^{\bar{h}}(\bar{u}/V)^3\,\mathrm{d}y/\bar{h}\right]$ is the energy coefficient. For a smooth rectangular channel, the skin friction coefficient f can be presented as (Knight *et al*., 1984)

$$1/\sqrt{f} = 1.81\log\left[(4\rho VR/\mu)\sqrt{f}\right] - 0.35 \quad \text{for} \quad 5.3\times10^3 \le \rho VR/\mu \le 1.9\times10^5. \qquad (16)$$

If $R = \bar{h}$, Eq. (16) can be represented as

$$1/\sqrt{f} = 1.81\log\left(4Re\sqrt{f}\right) - 0.35. \qquad (17)$$

After substituting $R = \bar{h}$ into Eq. (15), assuming $\alpha = 1$, and integrating this with respect to x under the condition at the section of the critical point ($\bar{h} = \bar{h}_{cp}$ at $x = x_{cp}$) gives (Ohtsu & Yasuda, 1994)

$$\frac{x}{\bar{h}_0} = \frac{8}{f\,Fr_0^{\,2}}\left[Fr_0^{\,2}\left(\frac{\bar{h}}{\bar{h}_0} - \frac{\bar{h}_{cp}}{\bar{h}_0}\right) + \frac{1}{4}\left(\frac{\bar{h}_{cp}}{\bar{h}_0}\right)^4 - \frac{1}{4}\left(\frac{\bar{h}}{\bar{h}_0}\right)^4\right] + \frac{x_{cp}}{\bar{h}_0} \qquad (18)$$

where $\bar{h}_{cp}$ is $\bar{h}$ at the section of the critical point. For a given Fr_0, Re, and $x/\bar{h}_0$, the water-surface profile downstream of the critical point is calculated by using Eqs. (17) and (18). In Eq. (18), the relative value of $\bar{h}_{cp}/\bar{h}_0$ and that of $x_{cp}/\bar{h}_0$ can be obtained from Eqs. (2), (9), and (14) as noted in Section 3.1.

4. RESULTS

4.1. Velocity distributions

For a given Fr_0 and Re, Figure 2(a) shows the velocity distributions for the developing flow, and the solid line in Figure 2(a) illustrates the calculated values obtained with Eq. (5). In the present study, the boundary-layer thickness δ is determined by substituting the displacement thickness δ_1 into Eq. (8). As shown in Figure 2(a), in the range of $0 \le y/\delta \le 1$, the velocity distributions in the boundary layer of the developing flow can be approximated by a one-seventh power law. For the outside of the boundary layer ($y/\delta \ge 1$), the values of the relative velocity $\bar{u}/U$ become constant ($\bar{u}/U = 1$). Additionally, the effects of

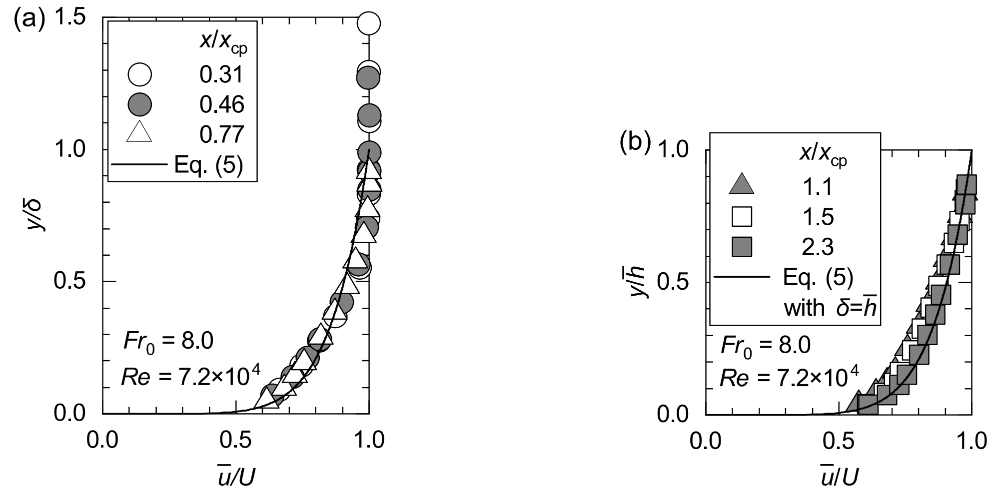

Figure 2 – Velocity distributions for (a) the developing flow; (b) a section downstream of the critical point.

the relative distance x/x_{cp} on the velocity distribution of the developing flow are negligible. Figure 2(b) shows the velocity distributions in the section downstream of the critical point, and the solid line in Figure 2(b) illustrates the calculated values obtained by using Eq. (5) with $\delta = \bar{h}$. The relative velocity distributions in the section downstream of the critical point are approximated by a one-seventh power law, and the effects of x/x_{cp} on the relative velocity distribution are negligible.

4.2. Water-surface profile and boundary-layer development

The water-surface profile and the boundary-layer development in accordance with $\bar{h}/\bar{h}_0$ = f(x/x_{cp}) and $\delta/\bar{h}_0$ = f(x/x_{cp}) are presented in Figure 3 under a given Fr_0 and Re. The dashed line in Figure 3 shows the values of the boundary-layer thickness calculated using Eqs. (9) and (14). The solid line in Figure 3 shows the values of the water depth for the developing flow calculated using Eqs. (2) and (14), and the dotted-dashed line in Figure 3 shows the values of the water depth for the section downstream of the critical point calculated using Eqs. (17) and (18). As shown in Figure 3, in the developing flow ($0 < x/x_{cp} < 1$), the boundary-layer thickness $\delta/\bar{h}_0$ and the time-averaged depth $\bar{h}/\bar{h}_0$ increase with the relative distance x/x_{cp}. At the critical point ($x/x_{cp} = 1$), the boundary-layer thickness is equal to the time-averaged depth. In the section downstream of the critical point ($x/x_{cp} > 1$), $\bar{h}/\bar{h}_0$ increases with the relative distance x/x_{cp}. Additionally, the calculated values of the water depth $\bar{h}/\bar{h}_0$ and the boundary-layer thickness $\delta/\bar{h}_0$ are in agreement with the experimental values of $\bar{h}/\bar{h}_0$ and $\delta/\bar{h}_0$, respectively.

4.3. Turbulence intensity distributions

For a given Fr_0 and Re, the turbulence intensity distributions for the developing flow ($0 < x/x_{cp} < 1$) in accordance with $(\overline{u'^2})^{1/2}/U = \mathrm{f}(y/\delta)$ are shown in Figure 4(a). In the boundary layer ($0 < y/\delta \lesssim 1$), as shown in Figure 4(a), the values of the turbulence intensity $(\overline{u'^2})^{1/2}/U$ become small with increasing the relative height y/δ. Outside the boundary layer for $y/\delta \gtrsim 1.2$, the values of $(\overline{u'^2})^{1/2}/U$ are smaller than those in the boundary layer, and the values of $(\overline{u'^2})^{1/2}/U$ outside the boundary layer are nearly constant. Klebanoff (1955) indicated that the instantaneous position of the edge of the turbulent boundary layer has a random character, and the edge rarely extends outside the region of $0.4 \leq y/\delta \leq 1.2$. This discussion means that the fully turbulent region and the intermittent region are formed in $y/\delta < 0.4$ and $0.4 \leq y/\delta \leq 1.2$, respectively. Therefore, in the supercritical flow below a sluice gate, it may be considered that the region in $0.4 \leq y/\delta \leq 1.2$ is intermittently turbulent.

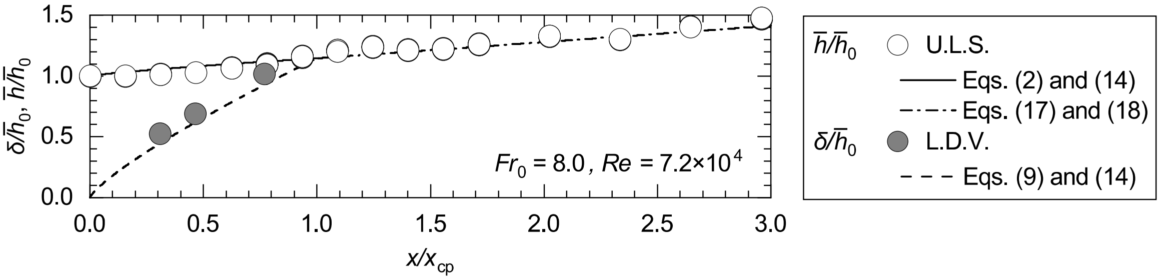

Figure 3 – Water-surface profile and boundary-layer development.

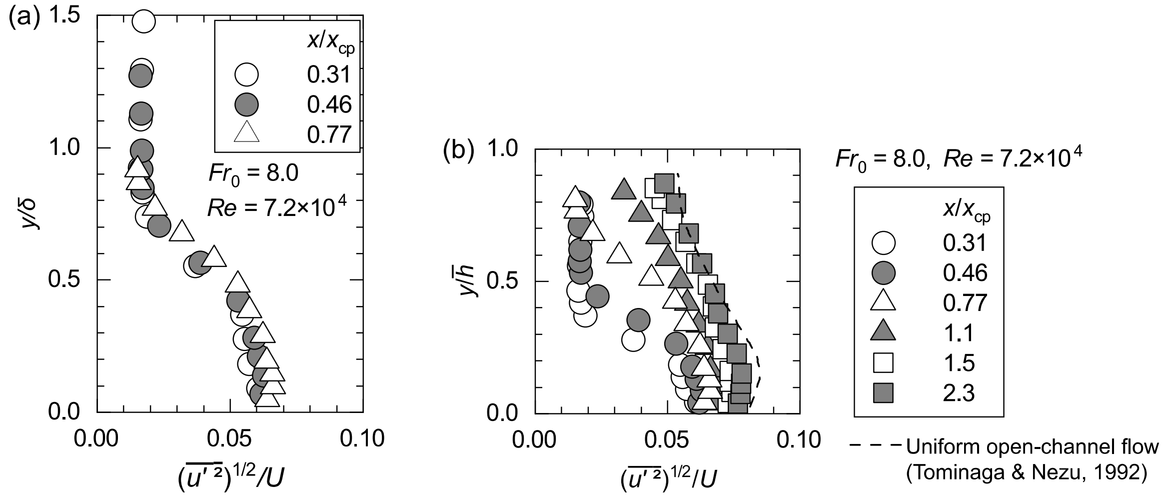

Figure 4 – Turbulence intensity distributions for (a) the variation of y/δ with $(\overline{u'^2})^{1/2}/U$; (b) the variation of $y/\bar{h}$ with $(\overline{u'^2})^{1/2}/U$.

For a given Fr_0 and Re, Figure 4(b) shows the variation of the turbulence intensity $(\overline{u'^2})^{1/2}/U$ with the relative height $y/\bar{h}$ in the supercritical flow below a sluice gate. In Figure 4(b), the dashed line is the distribution of the turbulence intensity for uniform open-channel flow (Tominaga & Nezu, 1992). In the range of $0 < x/x_{cp} \lesssim 0.8$, as shown in Figure 4(b), the measured values of $(\overline{u'^2})^{1/2}/U$ near the water surface ($y/\bar{h} \approx 1$) are small and independent of the relative distance x/x_{cp}. In the range of $1 < x/x_{cp} \lesssim 1.5$, the measured values of $(\overline{u'^2})^{1/2}/U$ near the water surface ($y/\bar{h} \approx 1$) increase with the relative distance x/x_{cp}. In the range of $x/x_{cp} \gtrsim 1.5$, the magnitude and distribution of the turbulence intensity is independent of x/x_{cp}. It is shown that the distributions for the turbulence intensity in the range of $x/x_{cp} \gtrsim 1.5$ are nearly equal to those in the uniform open-channel flow, as shown by the dashed line in Figure 4(b). Therefore, in the supercritical flow below a sluice gate, it is considered that the fully developed flow is formed in the range of $x/x_{cp} \gtrsim 1.5$.

4.4. Water-surface fluctuations

The high-speed video camera images for the water-surface fluctuations for a given Fr_0 and Re are shown in Figure 5. In Figure 5, the values of x/x_{cp} and those of the boundary-layer development $\delta/\bar{h}$ are calculated by using Eqs. (2), (9), and (14). As shown in Figure 5(a), the water surface in the range of $0 \leq x/x_{cp} \lesssim 0.2$ ($0 \leq \delta/\bar{h} \lesssim 0.3$) is smooth like transparent glass. This is because the turbulence in the boundary layer does not reach the water surface. As shown in Figure 5(b), the water surface begins to fluctuate slightly in the range of $0.6 \lesssim x/x_{cp} \lesssim 0.8$ ($0.7 \lesssim \delta/\bar{h} \lesssim 0.8$). This result might show that the boundary layer reaches the water surface intermittently in the range of $0.6 \lesssim x/x_{cp} \lesssim 0.8$ ($0.7 \lesssim \delta/\bar{h} \lesssim 0.8$). As shown in Figure 5(c), the water-surface fluctuations at the critical point (x/x_{cp} =1) are large compared with Figures 5(a) and 5(b). As shown in Figure 5(d), the water-surface fluctuations in the range of $1.6 \lesssim x/x_{cp} \lesssim 1.7$ are larger than those shown in Figures 5(a), 5(b), and 5(c).

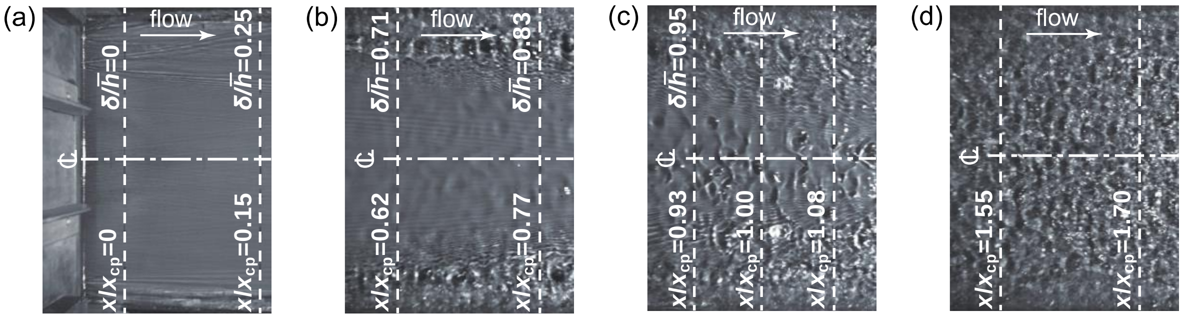

Figure 5 – Flow condition of water-surface fluctuations with Fr_0 = 8.0 and Re = 7.2×10^4 for (a) 0 ≤ $x/x_{cp} \lesssim 0.2$; (b) $0.6 \lesssim x/x_{cp} \lesssim 0.8$; (c) $0.9 \lesssim x/x_{cp} \lesssim 1.1$; (d) $1.6 \lesssim x/x_{cp} \lesssim 1.7$.

For a given Fr_0 and Re, Figure 6 shows the relation between the water-surface fluctuations $(\overline{h'^2})^{1/2}/\bar{h}$ and the boundary-layer development $\delta/\bar{h}$ in the developing flow region, and the values of $\delta/\bar{h}$ are calculated by using Eqs. (2), (9), and (14). The dashed line in Figure 6 indicates the trend for the water-surface fluctuations with boundary-layer development $\delta/\bar{h}$. As shown in Figure 6, the measured values of $(\overline{h'^2})^{1/2}/\bar{h}$ in the range of $0 \le \delta/\bar{h} \lesssim 0.6$ are small. However, the measured values of $(\overline{h'^2})^{1/2}/\bar{h}$ in the range of $0.7 \lesssim \delta/\bar{h} \lesssim 1.0$ increase with $\delta/\bar{h}$, illustrating that water-surface fluctuations may begin to occur if $0.7 \lesssim \delta/\bar{h} \lesssim 0.8$. This is because the water surface begins to fluctuate slightly in the range of $0.7 \lesssim \delta/\bar{h} \lesssim 0.8$ ($0.6 \lesssim x/x_{cp} \lesssim 0.8$), as shown in Figure 5(b). It may be similar to air flow on a flat plate in the turbulent boundary layer intermittently reaching y/δ = 1.2 (Klebanoff, 1955).

Figure 7 shows the streamwise change of water-surface fluctuations in the supercritical flow below a sluice gate for a given Fr_0 = 8.0 and Re = 7.2×10^4. The dashed line in Figure 7 indicates the trend for the water-surface fluctuations with the relative distance x/x_{cp}. The values of the water-surface fluctuations $(\overline{h'^2})^{1/2}/\bar{h}$ in the range of $0 \le x/x_{cp} \lesssim 0.5$ are small, and these results correspond with Figure 5(a). The values of $(\overline{h'^2})^{1/2}/\bar{h}$ in the range of $0.5 \lesssim x/x_{cp} \lesssim 1.5$ increase with the relative distance x/x_{cp}. The water surface, as shown in Figures 5(b) and 5(c), changes from smooth to uneven in the range of $0.5 \lesssim x/x_{cp} \lesssim 1.5$. Whereas, as shown in Figure 7, the values of $(\overline{h'^2})^{1/2}/\bar{h}$ in the range of $x/x_{cp} \gtrsim 1.5$ are nearly constant, and the values of $(\overline{h'^2})^{1/2}/\bar{h}$ in the range of $x/x_{cp} \gtrsim 1.5$ are larger than those in the range of $0 \le x/x_{cp} < 1.5$. These results might demonstrate that the water-surface fluctuations in the range of $x/x_{cp} \gtrsim 1.5$ are similar to those obtained for uniform open-channel flow because the distributions of the turbulence intensity in $x/x_{cp} \gtrsim 1.5$ are nearly equal to those in uniform open-channel flow, as noted in Section 4.3. Therefore, it is considered that the water-surface fluctuations

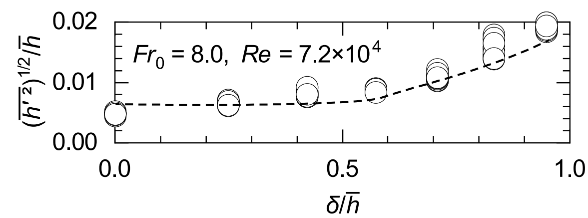

Figure 6 – Relation between water-surface fluctuations and boundary-layer development.

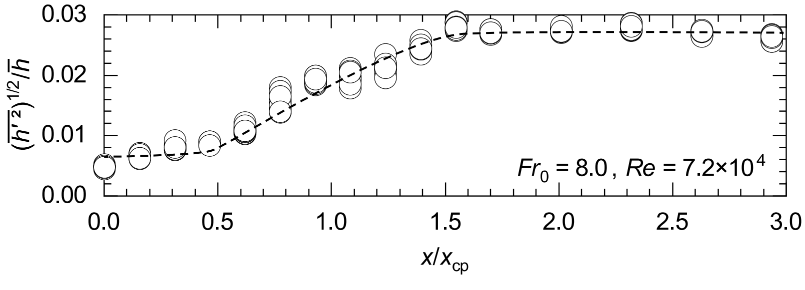

Figure 7 – Streamwise change of water-surface fluctuations.

in the range of $x/x_{cp} \gtrsim 1.5$ are fully developed for Fr_0 = 8.0 and $Re = 7.2\times10^4$. To clarify the water-surface fluctuations of the supercritical flow below a sluice gate, further measurements for a wide range of Fr_0 and Re are needed.

5. CONCLUSIONS

The effect of the boundary-layer development on the water-surface fluctuations of the supercritical flow below a sluice gate in a horizontal rectangular channel was experimentally demonstrated for Fr_0 = 8.0 and $Re = 7.2\times10^4$. The results in this paper are summarized as follows:

(i) The time-averaged velocity distributions in the boundary layer for the developing flow and a section downstream of the critical point can be approximated by a one-seventh power law.

(ii) For a given Fr_0 and Re, the water-surface profile and the boundary-layer development in the developing flow region can be calculated by using Eqs. (2), (9), and (14). The water-surface profile downstream of the critical point is obtained by using Eqs. (17) and (18).

(iii) In the developing flow region, high-speed video camera images show that the water-surface fluctuations begin to occur if the boundary-layer development $\delta/\bar{h}$ becomes equal to 0.7–0.8.

(iv) The water-surface fluctuations and the turbulence intensities in a section downstream of the critical point are nearly equal to those in uniform open-channel flow if the relative distance x/x_{cp} is greater than 1.5.

6. ACKNOWLEDGEMENTS

The second author was financially supported by the Japan Society for the Promotion of Science (JSPS), Grant Number 19K04624.

7. REFERENCES

Castro-Orgaz, O. and Hager, W.H. (2014), *Transitional flow at standard sluice gate*, Journal of Hydraulic Research, IAHR, 52 (2), 264–273.

Klebanoff, P.S. (1955), Characteristics of turbulence in a boundary layer with zero pressure gradient, NACA Technical Report 1247, National Advisory Committee for Aeronautics, Hampton, NASA-Langley Research Center.

Knight, D.W., Demetriou, J.D. and Hamed, M.E. (1984), *Boundary shear in smooth rectangular channels*, Journal of Hydraulic Engineering, ASCE, 110 (4), 405–422.

Ohtsu, I. and Yasuda, Y. (1994), *Characteristics of supercritical flow below sluice gate*, Journal of Hydraulic Engineering, ASCE, 120 (3), 332–346.

Rajaratnam, N. (1977), *Free flow immediately below sluice gates*, Journal of the Hydraulics Division, ASCE, 103 (4), 345–351.

Roth, A. and Hager, W.H. (1999), *Underflow of standard sluice gate*, Experiments in Fluids, Springer, 27, 339–350.

Schlichting, H. (1979), *Boundary-layer theory*, seventh edition, McGraw-Hill, New York.

Takahashi, M. and Ohtsu, I. (2009), *Effect of inflow condition on air entrainment characteristics in hydraulic jump*, *Proceedings of the 33rd IAHR congress*, Vancouver, BC, Canada, 4917–4924.

Takahashi, M. and Ohtsu, I. (2017), *Effects of inflows on air entrainment in hydraulic jumps below a gate*, Journal of Hydraulic Research, IAHR, 55 (2), 259–268.

Tominaga, A. and Nezu, I. (1992), *Velocity profiles in steep open-channel flows*, Journal of Hydraulic Engineering, ASCE, 118 (1), 73–90.